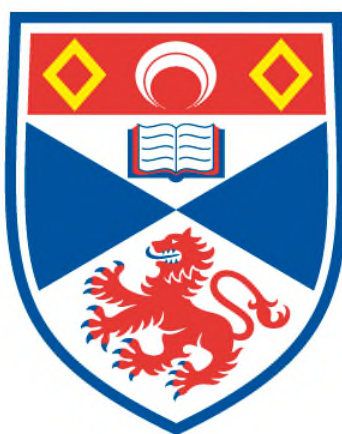


**PROBING THE INFLUENCE OF BIMETALLIC
COMPOSITION ON THE Pd/Au CATALYSED SYNTHESIS
OF VINYL ACETATE MONOMER**

Andrew Richard Haire

**A Thesis Submitted for the Degree of PhD
at the
University of St Andrews**



2010

**Full metadata for this item is available in
St Andrews Research Repository
at:**

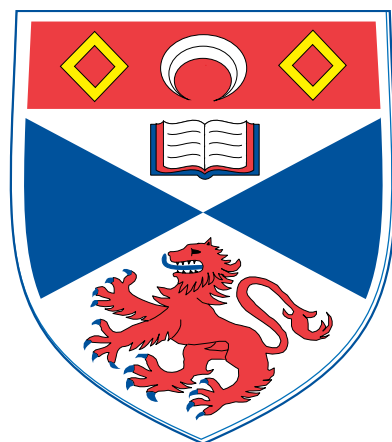
<http://research-repository.st-andrews.ac.uk/>

Please use this identifier to cite or link to this item:

<http://hdl.handle.net/10023/1018>

This item is protected by original copyright

**This item is licensed under a
Creative Commons Licence**



University
of
St Andrews

**Probing the Influence of Bimetallic Composition on the
Pd/Au Catalysed Synthesis of Vinyl Acetate Monomer**

Thesis submitted in accordance with the requirements
of the University of St. Andrews for the degree
of Doctor of Philosophy

Andrew Richard Haire

February 2010

Acknowledgements

I would like to thank my supervisor, Dr. Chris Baddeley for giving me the opportunity to work on this project and for his support, advice and enthusiasm throughout. Thanks must also go to Johan Gustafson for his vital contribution to the analysis of the MEIS data and to Steve Francis, Tim Jones, Alex Murdoch and Aoife Trant for their help with the experimental side of the project.

I would like to thank the St Andrews Surface Science Group and the Baddeley research group – Johan Gustafson, Sean Jensen, Tim Jones, Alex Murdoch, Nicola Toma, Karen Wilson and especially Aoife Trant for all of their help over the last few years and for making my time in St Andrews so enjoyable.

Thanks also to my family, especially my parents, for all of their support throughout.

Additional thanks to STFC Daresbury for providing MEIS beamtime and Tim Noakes and Paul Bailey for their assistance with data acquisition. Thanks also to Bruce Williams of BP Chemicals Hull for a number of useful discussions.

I am grateful to BP Chemicals Hull and EPSRC for funding and to the University of St Andrews for hosting me during the last nine years of my studies.

Probing the Influence of Bimetallic Composition on the Pd/Au Catalysed Synthesis of Vinyl Acetate Monomer

Abstract

Scanning Tunnelling Microscopy (STM) was utilised together with the high resolution depth-profiling capabilities of Medium Energy Ion Scattering (MEIS), a technique traditionally associated with single crystal substrates, to probe the mean size and depth dependent composition profile of bimetallic PdAu nanoparticles on planar oxide surfaces as functions of the starting composition and annealing temperature.

In order to fit composition profiles to experimental MEIS data, a new analysis tool has been designed that models the particles as flat-topped structures with a hexagonal base which can be divided into a number of shells, each shell corresponding to a particular ion pathlength inside the material. The reliability of this method will be discussed in detail. Fitting results show that the surface layers are always significantly enriched in Au compared to the bulk alloy composition. By comparing MEIS data for clean surfaces data for modified surfaces it was found that Pd generally segregates towards the particle surface on adsorption of acetic acid.

The interaction of potassium acetate with Au/Pd{111} alloy surfaces of varying composition has been investigated using Temperature Programmed Desorption (TPD) and Reflection Absorption Infra Red Spectroscopy (RAIRS). At lower coverage, potassium acetate reacts reversibly with the surface to form CO and carbonate. Formation of surface acetate is observed on Pd-rich surfaces only. At higher coverage, acetate is the major surface species formed on all samples examined.

Abbreviations

AcOH	Acetic acid
AcOK	Potassium acetate
AES	Auger Electron Spectroscopy
AFM	Atomic Force Microscopy
DFT	Density Functional Theory
DRIFTS	Diffuse Reflectance Infra-red Fourier Transform Spectroscopy
fcc	face-centred cubic
FTIR	Fourier Transform Infra-Red
hcp	hexagonal close packed
(HR)EELS	(High Resolution) Electron Energy Loss Spectroscopy
(HR)TEM	(High Resolution) Transmission Electron Microscopy
L, Langmuir	$= 1 \times 10^{-6}$ Torr.s
LEED	Low Energy Electron Diffraction
LEIS	Low Energy Ion Scattering
MEIS	Medium Energy Ion Scattering
ML	Mono-Layer
NP	Nanoparticle
RAIRS	Reflection-Absorption Infra-Red Spectroscopy
RBS	Rutherford Backscattering Spectroscopy
STFC	Science and Technology Facilities Council
STM	Scanning Tunnelling Microscopy
TPD	Temperature Programmed Desorption
UHV	Ultra-High Vacuum
VA/VAM	Vinyl acetate / vinyl acetate monomer
XPS	X-ray Photoelectron Spectroscopy

Table of Contents

<u>Chapter 1 - Introduction and Literature Survey</u>	1
1.1 – Introduction to Surfaces and Heterogeneous Catalysis	1
1.2 – Synthesis of Vinyl Acetate Monomer (VAM)	2
1.3 – VAM Formation Over Pd Catalysts	3
1.4 – Surface Studies on Model PdAu Systems	11
1.5 – Bimetallic Catalysts	17
1.6 – VAM formation Over Pd/Au Alloy Catalysts	19
1.7 – Model Nanoparticles on Oxide Surfaces	21
1.8 – References	26
<u>Chapter 2 – Experimental Techniques</u>	32
2.1 – Auger Electron Spectroscopy (AES)	33
2.2 – Low Energy Electron Diffraction (LEED)	35
2.3 – Temperature Programmed Desorption (TPD)	37
2.4 – Reflection-Absorption Infrared Spectroscopy (RAIRS)	38
2.5 – Scanning Tunneling Microscopy (STM)	40
2.6 – Medium Energy Ion Scattering (MEIS)	42
2.7 – References	43
<u>Chapter 3 – Model PdAu Nanoparticles on Oxide Surfaces</u>	44
3.1 – Experimental	44
3.2 – Medium Energy Ion Scattering (MEIS) – Basic Theory	45
3.3 – Data Preparation	50
3.4 – Spectrum Simulation	54
3.5 – Growth of Model Nanoparticles on SiO ₂ /Si{100}	64
3.6 – St Andrews Particle Fitting Method	75
3.7 – TPD – CO on Pd/Au/Al ₂ O ₃ /NiAl{110}	93

3.8 – Interaction With AcOH	95
3.9 – Summary and Conclusions	119
3.10 – References	121

Chapter 4 – AcOK on Au/Pd{111} **125**

4.1 – Experimental	125
4.2 – Results	126
4.3 – Discussion	156
4.4 – Summary	175
4.5 – Conclusions	177
4.6 – References	178

Chapter 5 – Summary, Further Work and Publications **181**

5.1 – Summary	181
5.2 – Suggested Further Work	184
5.3 – Publications	184

Chapter 1 - Introduction and Literature Survey

1.1 – Introduction to Surfaces and Heterogeneous Catalysis

A catalyst, from the Greek *catalytes*, is defined as a substance which when present in small amounts increases the rate of a chemical reaction or process but which is itself chemically unchanged by the reaction [1]. Although the catalyst will play a part in the formation of reaction intermediates, it is neither product nor reactant and can be recovered unchanged at the end of a reaction cycle. This may proceed by either a homogeneous (reactants and catalysts both in the same phase e.g. liquid/liquid) or a heterogeneous (reactants and catalysts both in different phases e.g. gas/solid) mechanism.

Heterogeneous catalysis is an important commercial and industrial process, particularly in the petrochemical industry where it accounts for around 90% of product output [2]. Solid phase catalysts usually consist of a finely dispersed metal or alloy, often in the form of nanoparticles supported on an oxide surface or within a zeolite framework, where the metallic component provides an active surface on which the reaction can take place. The development of new heterogeneous routes has several economical advantages. Although such catalysts are usually composed of precious metals, the high dispersion maximises the available reaction surface area per unit mass and the catalyst can be much more easily recovered, regenerated and recycled at the end of a reaction than a homogeneous alternative.

Despite being widely used, both in industry and in the laboratory, most heterogeneous catalysts are highly complex materials [3]. It has been well established that the surface of a given solid material will have different physical and chemical properties to the bulk of the same material. This is because atoms in the bulk are constrained by three-dimensional interactions, while atoms at the surface have lower coordination numbers so are able to relax from their ideal bulk positions. This gives rise to distinct electronic states at the surface, leading to an increased free energy which leads to a greatly increased reactivity. Since the surface is the first part of the material to come into contact with any external species, an understanding of reactions and processes

occurring at surfaces plays a pivotal role in the understanding of heterogeneous catalysis as well as many other fields in material, optical and electronic sciences.

Since the surface atoms are not held as rigidly as bulk atoms surface processes tend to be highly dynamic. It has been observed that certain crystal planes may be more or less active towards a particular species than others. Although the close packed, and normally less reactive, crystal planes are thermodynamically favoured in UHV chemisorption can cause relaxation or reconstruction of surface atoms to expose more reactive planes. This leads to the observation that the structure of metal surfaces in particular will be highly dependent upon the immediate environment.

For a supported metal catalyst, the reaction kinetics are known to be strongly dependent on the size, structure and composition of the particles. The support material may or may not be involved in the active phase, but the extent of particle aggregation and intermixing will depend on the ability of the metal to diffuse across the support material. The presence of poisons and promoters will also affect the catalysis. Although such factors are obviously critical to catalyst performance, relatively little is known about their origins on the microscopic scale. This is mainly due to the complexity of heterogeneous systems and the difficulties in applying modern surface science techniques to their study.

Most current research involves the use of idealised model systems, such as metal or alloy single crystal systems or model nanoparticles supported on a suitable oxide in ultrahigh vacuum (UHV) conditions, to probe surface-adsorbate interactions on a fundamental level in a controlled environment. This allows us to study the effects of the substrate on the kinetic and mechanistic properties of a given reaction, giving information on the position and nature of catalytically active sites.

1.2 – Synthesis of Vinyl Acetate Monomer (VAM)

VAM ($\text{CH}_3\text{COOCHCH}_2$) is an important part of the polymer industry and is produced on a massive scale. It can be polymerised directly to form polyvinyl acetate (PVA) for use in paints, adhesives and coatings or can be readily co-polymerised with a range of other monomers [4] including vinyl chloride, ethylene and styrene as well as various

acrylics and alcohols to form a wide range of moulding, sheeting, coating, adhesive and insulation materials.

Two separate processes, both relying on Pd-based catalysts, are currently used to form VAM by acetoxylation of ethene. Gas-phase heterogeneous processes account for around 75% of total VAM production, while the remaining 25% is produced by liquid-phase homogeneous methods [5]. Although the basic aspects of the reaction were studied in the early 1970's [6-9], there is still no agreement regarding the reaction mechanism, and the nature of the reaction sites and intermediates is still debated.

The reaction stoichiometry is known to follow the equation [10]:



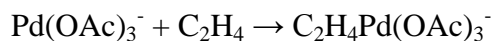
The heterogeneous process is usually operated between 413 and 453 K at pressures between 5 and 10 atm [11]. The catalyst is Pd or Pd/Au on silica, often modified by addition of potassium acetate (AcOK) [12]. The reaction rate has been found to depend on many factors, including reactant partial pressures, contact times, Pd particle dispersion and the presence of additives. Addition of Au and AcOK to the Pd catalyst is known to increase the selectivity for VAM formation from around 80-89% to as high as 96% [12-15] as well as doubling the reaction rate, however the details of this effect are not well understood. Selectivity for Pd-based catalysts is generally limited by secondary decomposition, leading to the combustion of acetic acid and ethylene. Since Au has a high affinity for sulphur, the effects of catalyst poisoning by impurities in the reactor feed can be reduced by modification with Au [16].

1.3 – VAM Formation Over Pd Catalysts

In the early 1960s, Moiseev et al. investigated the homogeneous liquid phase synthesis of VAM using a $[\text{PdCl}_2(\text{C}_2\text{H}_4)]_2$ complex as a catalyst [6]. They concluded that vinyl acetate is formed by the reaction of ethylene with Pd acetate in acetic acid solution, accompanied by the reduction of Pd to Pd black as shown below.



The following reaction scheme has been proposed, with the final step being rate limiting.



The presence of alkali metal acetates, usually AcOLi, AcONa or AcOK, was found to greatly increase the rate of vinyl acetate formation. The Pd catalyst can be regenerated by addition of copper chloride to form the redox system:



Around the same time, it was reported that vinyl acetate formation can be carried out in the vapour phase using a palladium based catalyst deposited on a suitable oxide support along with an alkali metal acetate activator [7-9]. The less corrosive nature of the vapour phase process as well as the elimination of chlorine from the reaction were seen as major advantages. It is this system that was eventually commercialised by Bayer [17] among others for the large-scale production of vinyl acetate.

The vapour phase oxidation of ethylene and acetic acid on SiO₂ and Al₂O₃ supported Pd catalysts was studied by Samanos et al. [9]. The effects of Pd dispersion as well as the partial pressures of reactants and water were studied. Yasui and Nakamura studied the mechanism of vinyl acetate synthesis on Pd-based catalysts [7, 8]. The reaction orders for acetic acid and ethylene were studied, along with the promotional effect of alkali metal acetates. It was concluded that VAM synthesis proceeds via a Langmuir-Hinshelwood type mechanism where the rate-determining step takes place within the adsorbed layer. Contrary to the conclusion of Moiseev et al. [6] that the catalytic site has Pd present as Pd⁰, it was suggested that the active site involves Pd²⁺ as an acetate species Pd(OAc)₂ formed from adsorption of acetic acid on the catalyst surface. Two possible reaction mechanisms have been proposed.

The first possible mechanism involves the adsorption and subsequent activation of ethylene to form a vinyl species, which then couples with the co-adsorbed acetate species to form vinyl acetate [7]. This is thought to proceed via the seven step mechanism shown:

1. $C_2H_4(g) \rightarrow C_2H_3(ads) + H(ads)$
2. $O_2(g) \rightarrow 2O(ads)$
3. $CH_3COOH(g) \rightarrow CH_3COOH(ads)$
4. $CH_3COOH(ads) \rightarrow CH_3COO(ads) + H(ads)$
5. $CH_3COO(ads) + C_2H_3(ads) \rightarrow CH_2=CHOCOCH_3(ads)$
6. $CH_2=CHOCOCH_3(ads) \rightarrow CH_2=CHOCOCH_3(g)$
7. $2H(ads) + O(ads) \rightarrow H_2O(g)$

The combination of the dissociatively adsorbed acetic acid with vinyl in stage 5 is thought to proceed by a β C – H bond scission mechanism as shown in figure 1.1.

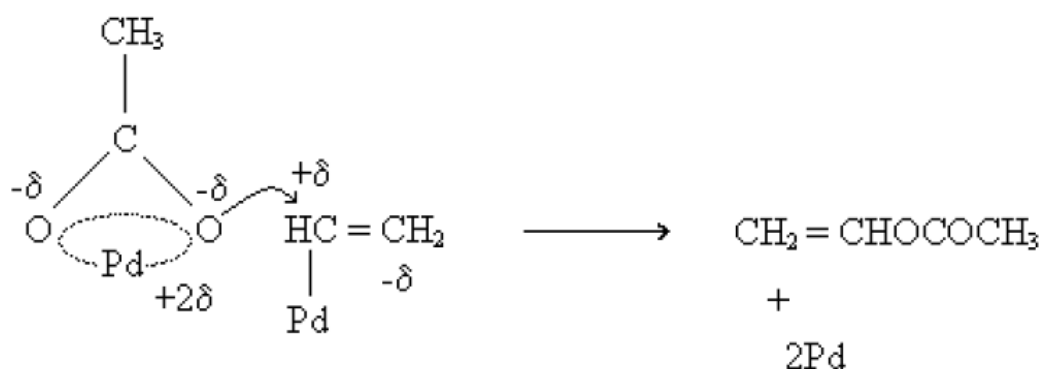


Figure 1.1 - Combination of dissociatively adsorbed acetic acid with vinyl via a β C – H bond scission mechanism [7].

The second method involves the reaction of adsorbed ethylene with an adsorbed acetate nucleophile to form an ethyl acetate species. This intermediate species then undergoes β C – H elimination to form vinyl acetate [9, 18].

Both mechanisms involve coupling of acetate and ethylene species as rate-determining steps [7, 9, 18]. In addition, unselective side reactions involving the

oxidation of some of the dissociatively adsorbed ethylene and acetic acid by O_{ads} results in the formation of CO and CO_2 , which are then desorbed from the surface.

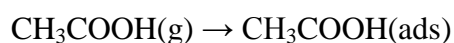
The adsorption of acetic acid has been studied on various metal surfaces including Rh{111} [19], Ru{0001} [20], Cu{110} [21], Ni{110} [22], Pd{110} [23], Pd{111} [24] and Pd/Au{111} [25] among others. Adsorption is usually found to be dissociative, resulting in the formation of surface acetates. A number of possible surface structures including monodentate [18], bidentate chelating [20] and bidentate bridging [20, 21] conformations have been reported along with various decomposition pathways.

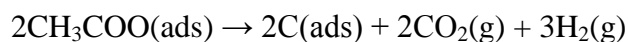
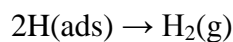
Surface science investigations of the adsorption and subsequent decomposition of carboxylate species on various Pd surfaces [23, 24, 26-29] show that the preferred adsorption mode is bidentate through both of the oxygen atoms, with the OCO plane perpendicular to the surface. In this case, the two O atoms would be equidistant from the surface plane, a result that has been verified by the absence of an O-C-O asymmetric stretching mode in High Resolution Electron Energy Loss Spectroscopy (HREELS) measurements [24, 25].

Plane-wave Density Functional Theory (DFT) calculations [27] have shown that the most stable binding state for acetate has the O-C-O in an atop-bridge-atop site configuration with the OCO plane aligned along the surface normal as shown in figure 1.2 below, where the C-C bonding distance between the methyl group and the carboxylate carbon has been estimated at around 1.54 Å.

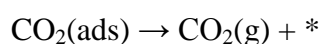
Catalytic decomposition of acetate, known to be one of the possible unselective pathways in the vinyl acetate synthesis reaction, has been studied on several metal surfaces [18, 21, 23] and has been concluded to proceed via an autocatalytic mechanism to yield CO_2 , H_2 and C_{ads} .

The decomposition pathway can be summarised as follows:





The narrow CO_2 desorption peaks observed in TPD analysis are consistent with surface explosion kinetics. The desorption process is thought to proceed as shown [19]:



The symbol * represents a vacant active site, which in this case would correspond to a free Pd ensemble. The extra reactive sites freed by the decomposition process are the reason for the surface explosion. It should be noted that the blocking of decomposition sites by co-adsorbed species such as O_{ads} , C_{ads} and K_{ads} has been seen to cause substantial changes in the desorption kinetics [25, 12, 30]. A detailed discussion of the mechanisms of acetate decomposition on metal surfaces will be given in Chapter 4.

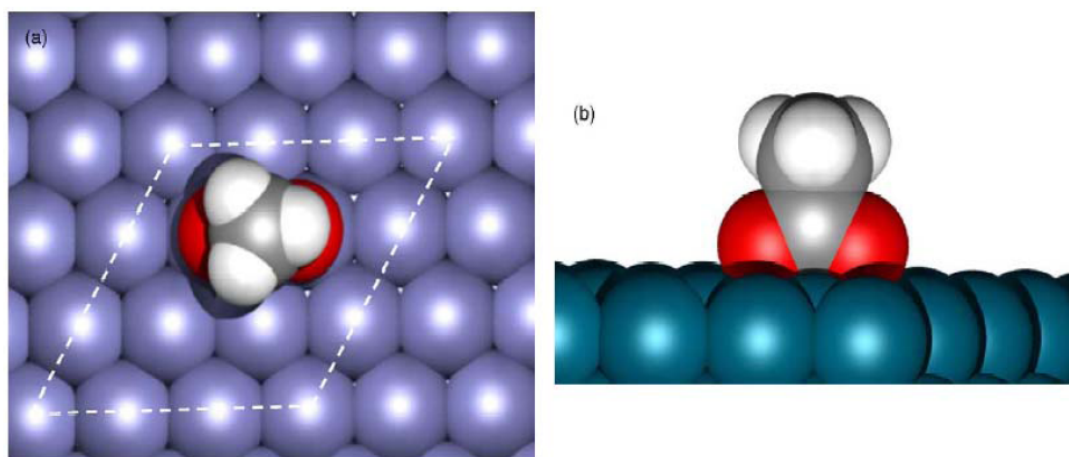


Figure 1.2 – Top (a) and side (b) view of the preferred geometry of acetate on Pd{111} as determined from DFT calculations [27]. The dotted line in part (a) represents the unit cell used in the calculations.

The reaction order with respect to acetic acid is a subject of some debate, with quoted values ranging from 0 to 1 [9, 31, 32]. Goodman and co-workers found that Pd catalysts on SiO_2 gave reaction orders close to zero [31], with a similar reaction mechanism to that observed on Pd{110} [11].

The reaction order with respect to oxygen has been reported to be positive for supported Pd catalysts [7, 31]. Adsorption of O₂ on the Pd surface is thought to be dissociative, leading to oxidation of the Pd. It is thought that surface oxide species may be present during the vinyl acetate synthesis reaction, although the existence of a bulk oxide cannot be ruled out [14]. The use of surface techniques by Voogt and co-workers [33] identified three possible phases in the interaction of O₂ with Pd{111}. These can be summarised as follows:

1. Dissociative adsorption of oxygen with a saturation coverage of 0.25 ML above 470 K.
2. Diffusion of O atoms into Pd.
3. Oxide nucleation and growth of an oxide layer.

The O₂ adsorption is suppressed by the presence of adsorbed ethylene and CO on the surface. This is thought to give rise to the negative reaction orders observed for CO and ethylene. Adsorbed oxygen species are thought to play a role in the activation of the C-H bond, or to act as a thermodynamic sink for any hydrogen produced in the reaction. Either way, the net result is the evolution of water as a by-product [18]. An increase in oxygen partial pressure had been seen to increase the coverage of surface oxygen, giving rise to an increase in the vinyl acetate formation rate [11].

Molecular adsorption of ethylene on Pd{111}, {110} and {100} has only been observed below ~150 K [14]. At increased adsorption temperatures, the ethylene appears to isomerise to ethylidene (CH=CH₂) with a subsequent dehydrogenation to ethylidyne (C≡CH). The effect will differ slightly depending on the adsorption face. On Pd{111}, ethylidene forms at room temperature and then desorbs below 350 K. On the {100} face, ethylene was found to adsorb reversibly and then dehydrogenate directly to CH_x at temperatures greater than 400 K.

Adsorption studies of ethylene and oxygen on Pd single crystal surfaces and clusters identified two possible adsorption types. These are the π -type adsorption on a site atop a Pd atom and the di- σ -type adsorption on bridging sites, which is associated with the adsorption of sp^3 - sp^2 rehybridised ethylene molecules [14]. LEED studies by Tysoe and co-workers have confirmed the existence of di- σ -bonded ethylene on the Pd{111}

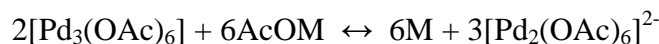
surface at low temperatures [34]. When the surface is pre-treated with hydrogen, only π -bonded species are observed, presumably due to isolation of the Pd sites. RAIRS investigations of either clean or CO covered Pd{111} after exposure to pressurised ethylene has identified a third possible configuration [35]. This spectral evidence in combination with molecular beam experiments showed the formation of ethylene multilayers, with coverages of up to 1.3 ethylene species per Pd atom.

It is assumed that most of the CO produced during the reaction comes from the catalytic oxidation of ethylene [29], since ethylene is more easily oxidised over Pd than acetic acid and since the selectivity towards vinyl acetate formation has been seen to increase along with the ratio of acetic acid to ethylene [7]. Combustion of ethylene on a high surface area Pd catalyst is likely to proceed by the oxygen activated method, where the oxygen atom abstracts a hydrogen atom then attacks the C atom on the ethylene. Indirect combustion, whereby the O_{ads} combines with C_{ads} and H_{ads} produced by the decomposition of surface species, is also possible. However, since $Pd(OAc)_2$ has been proposed as a possible intermediate in vinyl acetate formation, it is likely that CO is produced by more complex method involving both ethylene and acetate under reaction conditions [14].

As an alternative to Langmuir-Hinshelwood type gas-solid kinetics, the model proposed by Samanos et al. [9] suggests that there is a strong possibility of a liquid-phase-like mechanism also occurring under reaction conditions. In this model the reaction would be similar to that seen in the liquid phase using colloidal catalysts, where the ethylene is inserted into the Pd-OAc bond in a palladium/alkali metal/acetate complex. Adsorption of acetic acid and water on the support can be significant under industrial conditions. Transient kinetic studies have identified the existence of an adsorbed layer of acetic acid, approximately 2-3 monolayers in depth, under typical reaction conditions on Pd/Cd/SiO₂ and Pd/Au/SiO₂ model catalysts [36]. TPD studies showed that the presence of alkali metal acetates, particularly AcOK helped to retain this layer.

Kragten and co-workers studied the interaction of palladium and potassium acetates dissolved in acetic acid [37]. In the absence of alkali metal acetates, the palladium acetate was found to exist as $Pd_3(OAc)_6$ trimers. On addition of alkali metal acetates

to the solution, these trimers were converted to $[\text{Pd}_2(\text{OAc})_6]^{2-}$ dimers via the equilibria shown, where M represents an alkali metal:



The decomposition of palladium acetate trimers is believed to involve an S_N2 attack by either acetate ions, acetic acid molecules or by a bidentate bridging acetate. The possible acetate surface structures are shown in figure 1.3 below.

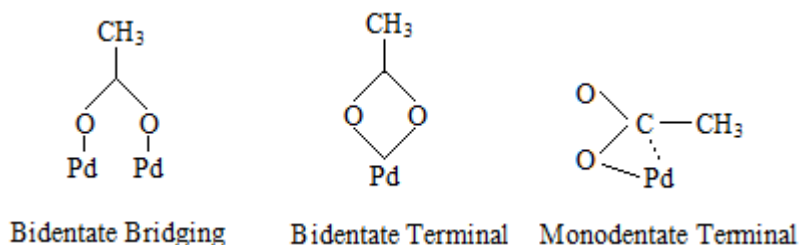


Figure 1.3 – Structures of possible Pd acetate surface species [38].

Of these, the monomer will have only terminal acetates, while the trimer will have only bridging acetates. The dimer form will have both terminal and bridging acetates. The different surface species will have different catalytic activities with respect to vinyl acetate formation.

The catalyst activity was found to increase in proportion to the palladium acetate and alkali acetate concentrations, peaking at the concentrations for which the trimers were converted to dimers [37]. Above this level the activity decreases with alkali acetate concentration. This would suggest that the alkali metal acetate initially forms, or allows formation of the catalytically active species, but that the acetate ions begin to function as inhibitors at higher concentrations. The explanation given was that low alkali metal concentrations cause conversion of the inactive trimers to the more active dimer form. In this case, the Pd trimers were found to be completely converted to dimers on addition of either 0.5 M AcOLi or 0.2 M AcONa. Increasing the concentration leads to the formation of other less active species, possibly monomers

or Pd dimers that are fully coordinated to acetate ligands. This would be unfavourable if the ethylene is proposed to coordinate to terminal positions on the dimer.

The alkali metal acetate, which is known to form a dimer with acetic acid, is thought to be essential for immobilizing the acid on the catalyst surface to create the liquid phase layers. This in turn increases the reaction rate for vinyl acetate. In addition, due to the comparatively low solubility of ethylene in acetic acid, the rate of ethylene combustion is suppressed [9, 12, 39].

In Raman studies of palladium and potassium acetates, a band observed at 1730 cm^{-1} was assigned to monodentate terminal acetate bound to the palladium in an ester-like configuration [12]. However, as a similar band was seen in HREELS analysis of AcOH adsorbed on Pd{111}, this spectral evidence alone is not enough to confirm the existence of dissolved Pd in the liquid layer.

1.4 - Surface Studies on Model PdAu Systems

The modification of Pd catalysts with Au has been investigated in detail. As well as vinyl acetate synthesis [12-15], Pd/Au alloy catalysts are used in a variety of other applications including pollution control [40] oxidation processes [41] and novel hydrogen fuel cells [42]. Catalyst stability, activity and selectivity were found to be significantly enhanced by the addition of Au in all cases. Studies of the surface structure and composition of PdAu alloys and their interactions with adsorbates can hopefully give an insight into the nature of this promotional effect.

Because the lattice mismatch between Pd and Au is small (~4.9%), PdAu alloys are completely miscible at 300 K at all compositions, with lattice parameters varying linearly from 0.389 nm for pure Pd to 0.408 nm for pure Au with increasing Au composition [5, 43]. Single crystal studies have been carried out on Pd deposited on Au surfaces [44-54], Au deposited on Pd surfaces [43, 55-59], PdAu alloy crystals [60-64] and PdAu alloy surfaces grown on a bulk substrate [65]. A number of studies have been carried out on more complex systems involving deposition of Pd [66], Au [67] and PdAu alloy nanoparticles on various oxide surfaces [68].

It has long been accepted that the composition of the surface of a bimetallic alloy will be different from the bulk composition of the same material by thermodynamic arguments. The composition at the surface is known to be dynamic and may be affected by temperature or by the presence of the gas phase, provided certain kinetic conditions can be satisfied. The surface composition of binary alloy in UHV can be estimated by considering the relative enthalpies of sublimation of the component metals [69]. The Modern Thermodynamic Calculation of Interface Properties (MTCIP) theory [70, 71] shows that the surface composition is also highly dependent on the exposed crystal plane.

While estimating the composition of clean bimetallic surfaces is itself a complex task, the presence of adsorbates adds further complications. Thermodynamic considerations would suggest that segregation due to an adsorbate X at a bimetallic surface AB would be determined by the relative bonding strength of $A-X$ in comparison to $B-X$ [72].

Currently, the technique of medium energy ion scattering (MEIS) provides one of the most successful methods for studying segregation behaviour on single crystal substrates [25, 73-76]. The theory and applications of this technique will be discussed in detail in chapter 3.

1.4.1 - Pd on Au{111}

Conventionally, there are two main methods of depositing Pd onto Au - UHV vapour deposition or electrochemical deposition, which will not be discussed here. Shen et al. [44, 45] studied the growth of Pd on Au{111}, proposing epitaxial Pd monolayer growth at room temperature. This is in contrast to thermodynamic calculations of segregation effects, which would suggest that monolayer growth is not feasible even at moderate temperatures. Due to the importance of Pd Au alloy catalysts in industry, a number of investigations on this system were carried out in the late 70's and early 80's. Some of these reported no segregation of Au to the surface [46, 47], while others observed enrichment of Au on sputtered and annealed surfaces [48, 49]. Varga et al. [50] reported enrichment of Au in the first layer at room temperature, with extensive segregation of Au on annealing to 500 °C. The formation of alloys at room temperature was also verified by Poppa et al. [51].

Koel et al. [52] concluded from LEIS studies that the growth mode of Pd on Au{111} depends strongly on the Pd deposition temperature. Although layer-by-layer Pd growth was observed at 150 K, monolayer growth was concluded to be impossible at 300 K due to alloying, either by Pd diffusion into the crystal or Au segregation. Deposition at higher temperatures resulted in more substantial Pd/Au intermixing, giving an Au rich surface layer.

Lambert and co-workers used STM imaging to study the structure of Pd on Au{111} [53, 54]. They found that at low coverages Pd tends to nucleate in islands at the elbow sites of the Au{111} – $(22 \times \sqrt{3})$ “herringbone” reconstruction as shown in figure 1.4 below [54].

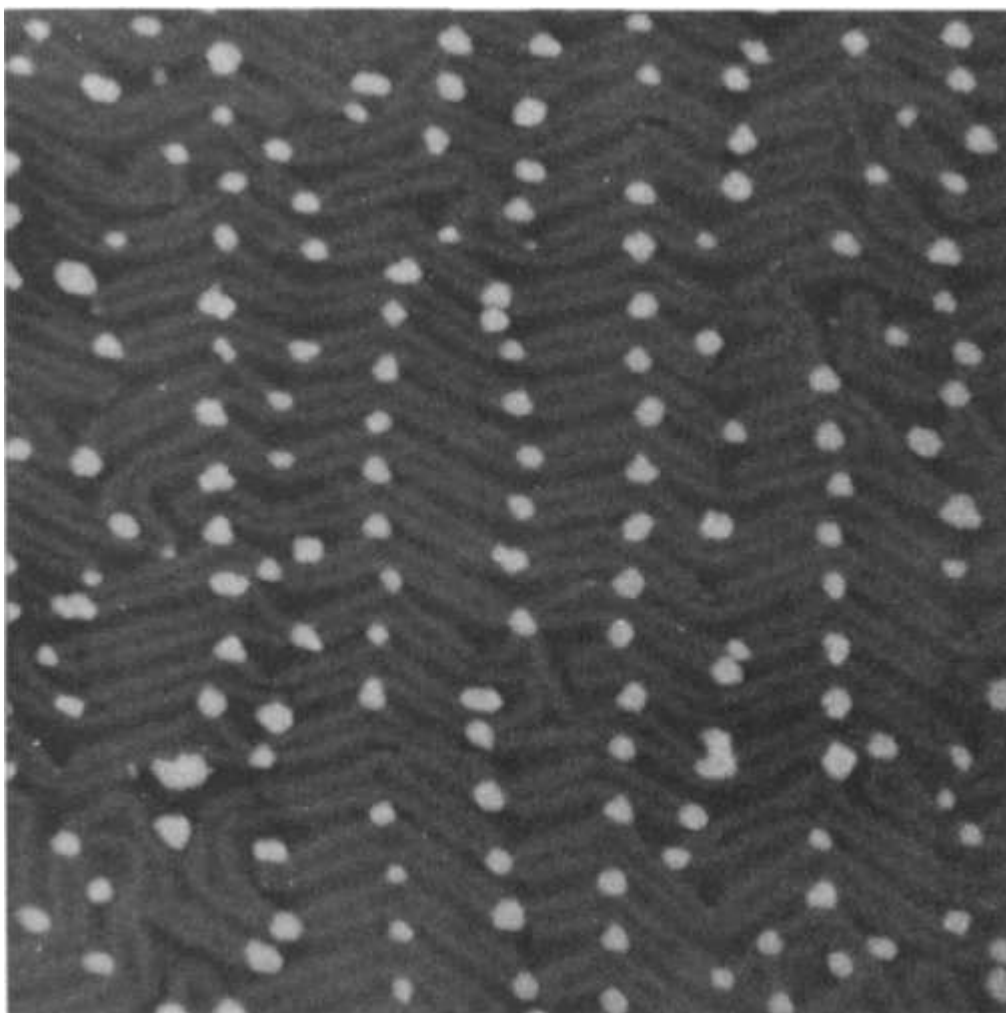


Figure 1.4 - Nucleation of Pd clusters in the elbow sites of the Au{111} – $22 \times \sqrt{3}$ “herringbone” reconstruction. Taken from reference [54].

This growth method has also been seen for a number of metals e.g. Ni [77], Fe [78], Co [79] and Rh [80] evaporated onto Au{111}. The start of the second layer growth commences at around 0.5 ML Pd coverage. At higher coverages the Pd grows as rough multilayers. The morphology of these layers was found to affect the catalytic behaviour of the system in the acetylene cyclisation reaction [43].

In contrast to Koel's work [62], Pd/Au intermixing was not observed at 300 K, but an ordered Pd₂Au surface alloy was formed and found to be stable between 450 and 700 K. This discrepancy was rationalised by considering that the second layer growth begins before completion of the monolayer. A LEIS spectrum would therefore show a signal due to the remaining bare Au, so that the presence of an Au surface signal in this case does not necessarily imply intermixing.

1.4.2 - Au on Pd{111}

For the system to be used in Chapter 4 of this study, Au will be evaporated onto Pd{111} in UHV. Kuk [55] investigated the growth of Au on Pd{111}. Initial growth was found to be pseudomorphic layer-by-layer with a lattice parameter similar to that of Pd, with little 3-dimensional islanding. Little interdiffusion was observed at room temperature, leading to the observation of sharp interfacial regions. After a critical coverage of around 1 ML the lattice parameter was seen to slowly increase to the normal Au value.

In studies carried out at around the same time, Weissmann-Wenocur et al. [56] investigated the formation of a Pd/Au alloy surface on Pd{111} using photoemission. A new structure was identified for around 0.1 ML Au coverage with a lattice parameter that evolved steadily with increasing Au coverage, eventually giving a structure characteristic of bulk Au. The valence band structure for 0.3 ML Au on Pd{111} was found to be similar to that of a 30% Au alloy.

Lambert and co-workers conducted a study of acetylene trimerisation on a range of Au/Pd{111} surfaces [43]. Ordered surface alloys were not found when Au was deposited on Pd{111}. Instead, by depositing 4 ML Au onto Pd{111} and varying the annealing temperature, a range of disordered Pd/Au alloys be formed. The Au was

found to intermix with the substrate at around 600 K, suggesting a higher activation barrier than is seen for the inverse system. In contrast to the inverse Pd/Au{111} system, there was no temperature range over which the alloy composition was found to be stable. Instead segregation of Pd to the surface results in a continuous range of alloy compositions being formed on annealing, while the lattice parameter was found to vary linearly between the value expected for Au{111} to a value just above the clean Pd{111} spacing. This makes the Au/Pd{111} system ideal for surface science investigations, since a wide range of alloy compositions can easily be prepared in a single experiment just by heating the sample.

Behm investigated the adsorption of CO as a probe molecule on well-defined Au/Pd{111} surfaces [57, 58], identifying three distinct surfaces. Deposition of ~0.25 ML Au covered the Pd{111} terraces in islands of around 20 Å average diameter and 9×10^{-12} atoms/cm⁻² density with a structure reminiscent of a relaxed dendritic shape. It was concluded that these islands consisted of Au adatoms and dissolution of Au into the substrate was deemed to be unfeasible under the conditions used. Of the total number of Au atoms deposited, around 40% were calculated to occupy sites at the island edges and that 14% of the available Pd surface atoms were adjacent to island edges.

Deposition of 0.2 ML Au at 300 K resulted in a similar structure, although the islands this time were much larger (~300 Å diameter) and the island density dropped by two orders of magnitude. This is due to the higher mobility of the Au atoms at 300 K. The number of atoms in edge sites was calculated to be 7% with 2% of Pd atoms adjacent to the Au edges, although the mobility of the edge atoms was not enough to allow them to assume their equilibrium shape.

The third surface was prepared deposition of 1.3 ML Au at 300 K, followed by stepwise annealing up to 925 K. Dissolution of Au was found to take place at around 450 K, becoming more pronounced as the temperature rose above 650 K. By this point, the Au Auger signal had dropped to 11% of its original value and the surface showed a flat step-terrace morphology with no islands on the terraces and no additional material nucleated at the step edges. Quantitative STM measurements gave

a surface concentration of 17% Au, although this method gives no information on the subsurface layers.

Baddeley and co-workers investigated the growth of Au on Pd{111} using STM and MEIS [25]. Initial growth was found to be dendritic, nucleated at the step edges. Second layer Au growth was found to take place before completion of the monolayer. The overlayer islands were seen to grow with increasing annealing temperature. At the highest annealing temperature the surface showed flat terraces separated by well-defined steps. MEIS experiments were carried out on 4 ML Au deposited on Pd{111} as a function of pre-annealing temperature. The top two layers were shown to be Au rich at 300 K. However, it was reported that the Au overlayer does not completely cover the Pd substrate at 300 K, even after the depositing the equivalent of several layers of Au, meaning that bare Pd is still accessible. Intermixing was observed at 600 K, producing a more homogeneous bimetallic surface and the surface composition was seen to vary smoothly with increasing annealing temperature. Most of the Au was dissolved into the crystal bulk by around 900 K, giving a Pd-like surface.

Tysoe investigated the formation of Au/Pd alloys on Pd{111} [59]. It was concluded that the Au film grows in a Frank-van der Merwe mode, intermixing with the Pd substrate at 600 K. XPS detected the formation of a Pd/Au alloy at 600 K and above in agreement with Owens et al. and Baddeley et al. [25, 43], showing that a full range of Pd/Au surface compositions can be achieved by adsorbing Au on Pd{111} and then annealing as required.

1.4.3 - Pd/Au Alloy Surfaces

There have been few detailed studies on Pd/Au alloy single crystals. Early studies on Pd/Au polycrystals identified segregation of Au to the bimetallic surface [60, 61]. Heiland and co-workers carried out structural studies on Au₃Pd {110} [62] and {113} [63] surfaces, concluding that the top layer in each case contained 100% Au. Piccolo et al. [64] investigated the selective hydrogenation of 1, 3-butadiene on Pd₇₀Au₃₀ fcc {111} and {110} single crystal surfaces. Both surfaces were found to exhibit 1×1 structures. Heating the samples to ~250 °C was enough to activate significant

segregation of Au to the surface. Annealing to 450° C gave top layer compositions of 75% and 85% respectively for the {111} and {110} surfaces.

Studies carried out by Nieuwenhuys and co-workers [81, 82] using a PdAg{111} alloy single crystal showed that a bulk 67% Pd/ 33% Ag alloy crystal exhibits a surface concentration of around 10% Pd. Further investigations using STM confirmed that the surface consisted of isolated Pd sites surrounded by Ag [83].

Goodman recently investigated the properties of a thin AuPd {111} alloy film created by evaporation of 5 ML Au and 5 ML Pd onto a Mo {110} single crystal surface [65]. Stable alloys were found within the annealing range 700-1000 K. Significant Au surface enrichment was observed, with a 1:1 Pd/Au alloy giving a stable alloy surface of composition Pd₂₀Au₈₀ after annealing to 800 K regardless of the metal deposition sequence. The most prevalent surface ensemble was proposed to consist of an isolated Pd atom surrounded by Au. The concentration of such surface sites can be altered by controlling the bulk alloy composition.

1.5 – Bimetallic Catalysts

Bimetallic catalysts attract extensive attention because they often exhibit drastically different properties from either of the constituent metals. Advances in UHV surface preparation methods and analysis techniques mean that the preparation and characterisation of bimetallic surfaces has become routine procedure, allowing the creation of tailor-made surfaces with specific properties. The chemistry of bimetallic surfaces is predominantly controlled by the composition of the outermost layer, and to a lesser extent by the composition of the immediate sub-surface.

Two reasons have been proposed for the enhanced performance of bimetallic catalysts compared to monometallic systems. These are the so called ensemble effects, a result of structural modification of the surface of one metal by the other, and ligand effects, where the electronic states of the catalytic metal are altered by the presence of the promoter metal [84]. In general however, differentiation between ensemble and ligand effects is not always possible and there is often a contribution from both.

1.5.1 – Ensemble Effects

The importance of surface studies in understanding the chemistry of bimetallic systems arises from the concept of an active site for a particular reaction. Taking the {111} surface as an example, if one reaction requires coordination to three-fold hollow sites while a competing reaction requires only single sites, then dilution of the active metal by a second catalytically inert metal would dramatically reduce the number of available three-fold sites. The number of available single sites would not be depleted as rapidly, resulting in a shift in the catalyst selectivity with composition.

Detailed investigation of the trimerisation of ethyne to benzene over Pd{111} suggests that the active site is a relatively large Pd₇ ensemble consisting of a central Pd atom surrounded by a hexagonal array [43], although this same ensemble was found to catalyse competing decomposition and dehydrogenation reactions giving selectivity of only 25% on Pd{111}. Upon alloying with Au, the activity of the Au_xPd_{100-x} surface varied dramatically as a function of surface composition, peaking at a composition of Au₁₅Pd₈₅. This was found to be close to the composition that results in the highest density of AuPd₆ ensembles (1 Au atom surrounded by a hexagonal array of Pd atoms), which were found to be 100% selective for ethyne trimerisation.

1.5.2 – Ligand Effects

The ligand effect originates from the assumption that the electronic properties of one element can be altered by the presence of another. This in turn modifies the chemisorption of adsorbates and their reaction properties. The Rigid Band Model assumes that a group *VIII* metal (e.g. Pd) will retain its original Brillouin Zone structure upon dilution by a group *IB* metal. The effect is that one extra electron is added to the common band structure for each atom of *IB* element added, altering the density of occupied states at the Fermi energy as a function of alloy composition. In the case of pure Pd where the d-band is around 95% filled, there is a high density of states at the Fermi energy. Using this model and adding Au, the adsorption properties would be expected to alter dramatically at the composition where the d-band became completely filled due the extra electrons supplied by Au.

This has been supported by investigations into the conversion of ortho to para-hydrogen over PdAu alloys [85]. A distinct change was observed in the activation energy near the point predicted by the Rigid Band Model. The rate limiting step was proposed to be the dissociative chemisorption of hydrogen. Since this involves transfer of electrons to the alloy, the rate should be higher in a Pd rich alloy when the density of states (*DOS*) near the Fermi energy is high and lower for an Au rich alloy where the *DOS* near the Fermi energy is low.

The major disadvantage of Rigid Band theory is that the elements comprising the bimetallic surface lose their individual chemical identity, so that the composition of the bimetallic surface is assumed to be static.

1.6 – VAM formation Over Pd/Au Alloy Catalysts

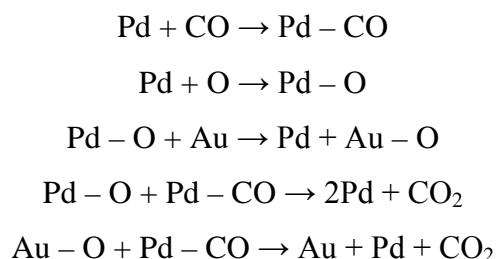
Since the rate of vinyl acetate formation on pure Au surfaces is so low, it is appropriate to consider reaction kinetics purely in terms of the availability of Pd sites [27]. The role of Au is thought to be in modifying the Pd surface by ligand effects as in the case of ortho to para-hydrogen conversion [85], or by ensemble effects as observed in ethyne trimerisation on PdAu [43] or by a combination of both.

Theoretical models proposed by Neurock [18] suggest that the activation of ethylene to vinyl and the subsequent coupling of vinyl to acetate have the highest activation energies and may be the rate controlling steps in VA synthesis. Ethylene adsorption was found to require an ensemble of four or five Pd atoms, with a six atom ensemble required for O assisted activation of the C-H bond. The vinyl-acetate coupling phase was also found to require a six atom ensemble. Unselective side reactions, the most prominent being the autocatalytic decomposition of bidentate acetate discussed previously, were found to require much larger Pd ensembles. The presence of Au disperses the surface Pd sites, giving an estimated 5% increase in VA selectivity [18].

Goodman and co-workers investigated the effects of CO and C₂H₄ on VA formation on a series of Pd and Pd/Au alloy surfaces [13], suggesting that the modification of the Pd ensembles on addition of Au is the key to the change in the kinetics of VA synthesis and CO oxidation. The negative reaction order with respect to C₂H₄/CO and

the positive order with respect to O₂ observed on Pd catalysts indicate that both reactions proceed by Langmuir-Hinshelwood kinetics, with O₂ adsorption as the rate-determining step [13, 86-88]. This is not the case on the Pd/Au catalyst, where the reaction order for C₂H₄ changes to a positive value while the reaction order for CO becomes less negative [13]. This may be due to a change in C₂H₄ binding energy, which leads to the observation of a below saturation coverage of C₂H₄ on Pd/Au. This may actually enhance the adsorption and subsequent mobility of oxygen on the surface, despite the reduction in oxygen capacity of Pd/Au compared to Pd [89].

Gossner et al. [90] studied electrochemical oxidation of CO, suggesting that the high reaction rate over Pd/Au may be due to migration of O_{ads} from Pd onto Au as shown in the scheme below. It was thought that this would enhance the adsorption of oxygen. It is not clear whether this migration also occurs in VA synthesis over Pd/Au or whether this is the origin of the improved selectivity [13].



A more recent study by Goodman and co-workers [91] has shown that the rate of VA synthesis is significantly enhanced over Pd/Au{100} compared to Pd/Au{111}. After carrying out UHV characterisation followed by in-situ activity tests they proposed that the critical site for VA synthesis is a pair of suitably spaced, non-contiguous Pd monomers. Larger Pd ensembles were found to be less selective as had been predicted previously. The role of Au in this case is to isolate these single Pd sites that facilitate the coupling of critical species, while suppressing the formation of undesirable by-products. However, the method used in this investigation assumes that the composition of the catalyst surface remains constant under reaction conditions, which is not generally true due to segregation effects as will be discussed in Chapter 3.

1.7 - Model Nanoparticles on Oxide Surfaces

It is known that catalysts consisting of oxide-supported bimetallic nanoparticles often show enhanced activity and/or selectivity compared to monometallic systems [92]. The catalytic properties of the system are inextricably linked to the surface composition of the alloy particles. We have so far discussed the characterisation of single-crystal bimetallic surfaces and their interactions with adsorbates. Although it has been shown that the characterisation of extended metallic surfaces can be useful from a catalysis viewpoint, a number of problems can arise when trying to correlate results obtained on single crystal systems with those obtained on bimetallic nanoparticles.

Since we are no longer dealing with extended crystal planes, the finite size and basic structure of the particle must be taken into account. In a typical catalyst, metals are present as nanoparticles exposing the most thermodynamically favourable atomic arrangements. For an fcc metal, a typical particle shape would be a cuboctahedron exposing {111} and {100} facets. Since segregation effects are face-sensitive [69], this means that the surface composition of a bimetallic nanoparticle can differ from that observed on single-crystal samples and will be strongly dependent on the particle size and shape [92].

The interaction of the catalyst particles with the support should also be taken into consideration. The catalyst support can modify the electronic properties of the metal particles [93-95] and, in the case of the strong metal-support interaction (SMSI), can migrate over the particles [96]. Particle aggregation and intermixing will depend on the ability of metal particles to diffuse across the oxide support. It is often unclear whether complete intermixing occurs to form alloy clusters, whether core-shell type structures with a depth-dependent composition are formed or whether segregation results in the formation of clusters of pure metallic components [97].

The so-called materials gap between single-crystal and nanoparticle surfaces has been partly overcome by the introduction of the supported model catalyst – metal nanoparticles deposited onto a suitable oxide surface which can then be characterised

in UHV in the same way as a single-crystal system. The properties of such systems have been investigated in detail (see [98-101] and references therein).

In this case an ordered substrate would be preferred, but the insulating nature of many bulk oxides may introduce severe experimental limitations. As an alternative, it has been shown that an ultra-thin oxide film grown on a metallic substrate can display the characteristic physical properties of the bulk oxide [102]. Such a film can be created by direct oxidation of the native metal, although this method often results in the creation of amorphous or polycrystalline overlayers or films with a high defect density, e.g. [103-104]. Other possibilities include evaporation of metal or Si onto a refractory metal host crystal in an ambient oxygen environment [105] or oxidation of an alloy single crystal containing the desired metal. A well documented example of the latter is the creation of well-ordered Al₂O₃ films on low-index NiAl surfaces [106-108].

The oxidation of NiAl {110} results in a characteristic LEED pattern with a number of sharp extra spots in addition to the {110} substrate spots [98]. The two-fold symmetry of the substrate allows the formation of two separate domains which are rotated by 48° with respect to each other. Closer examination of the pattern reveals that the oxide grows commensurately along the [110] and incommensurately along the [001] direction of the NiAl {110} surface. It has been proven that oxide films prepared in this way do not contain any Ni [109]. Although the thin alumina film possesses a well-defined structure and a high degree of long range order, STM and SPA-LEED measurements have identified a number of characteristic line defects occurring at the boundaries between the two rotational domains [110]. It is these defect sites that will play a role in the nucleation and growth of metal particles.

Nanoparticles of various transition metals including Rh [111], Pd [54], Co [110], Pt [112] and V [113] have been grown on alumina films on NiAl. Freund and co-workers studied Pd nanoparticles created by vapour deposition of Pd onto Al₂O₃/NiAl{110} in UHV [114, 115]. Upon deposition at 90 K, small particles nucleate on the point defects and a narrow size distribution is observed. Deposition at 300 K increases the mobility of Pd on the surface so that nucleation on the line defects between the substrate domains is now favoured. In this case, all of the deposited

material nucleates on the steps and at the reflection and antiphase domain boundaries [114]. Particle size was found to be fairly uniform, depending on the amount of material deposited. TPD and vibrational spectroscopy experiments on Pd particles on Al₂O₃/NiAl{110} have shown that both {111} and {100} facets are present [115].

Freund and co-workers studied PdAg model nanoparticles on alumina [115]. Although preferential surface segregation of Ag was observed, XPS analysis confirmed the formation of Pd-Ag alloy particles rather than core-shell structures. For Pd rich particles, the observed surface species at 2105-2085 cm⁻¹ desorbing at 100-300 K and at 1900-1800 cm⁻¹ desorbing at 400-500 K were identical to those observed for the pure Pd particles, and were attributed to CO adsorption on extended Pd islands or domains on the nanoparticle surface. This was confirmed by the reduction in intensity of these features with increasing Ag composition.

Goodman and co-workers used IRAS and TPD to investigate the adsorption of CO on 1:1 Pd:Au alloy nanoparticles grown on a thin silica film on Mo{112} [68]. Significant alloying was observed when Au was deposited on top of ready-formed Pd clusters and then annealed. For 0.1 ML Au/1 ML Pd, a surface composition of 85% Pd was observed by LEIS analysis. For 1 ML Au/1 ML Pd the atop CO desorption peaks remained, although attenuated to around 30%, but no 3-fold or bridging CO desorptions were observed, suggesting isolation of Pd surface sites by Au. In this study, we will investigate the structural properties of PdAu nanoparticles grown on silica films on Si{100}.

As well allowing us to study the structural properties of nanoparticles, the use of supported model catalyst systems in UHV allows us to observe the interaction of the particles with the support material itself, often on an atomic scale. Such interactions give rise to behaviour that cannot be observed using the traditional metal single-crystal methods as will now be discussed.

TiO₂ supports have attracted much interest in recent years as a support for model metal catalysts. Haruta et al. [116] have demonstrated that Au acts as a catalyst for low-temperature CO oxidation when dispersed as nanoclusters on a TiO₂ support, despite the fact that no prior evidence had been found for the adsorption of CO on

planar Au surfaces at 300 K. Besenbacher and co-workers studied the interaction of Au nanoparticles with the {110} surface of reduced rutile TiO₂ [67]. Using a combination of Scanning Tunnelling Microscopy (STM) imaging and DFT calculations, they were able to show that the nucleation and growth of Au clusters on the rutile TiO₂{110} surface is strongly related to the presence of oxygen vacancies.

Bowker and co-workers have studied the behaviour of Pd nanoparticles deposited on TiO₂ surfaces using STM [117, 118]. The strong metal-support interaction (SMSI) effect was identified at atomic resolution from the appearance of partially oxidised Ti layers at the surface of the Pd particles [117]. It has been proposed that the spill-over of reactants from an active metal centre to an otherwise inert ceramic support material could explain many unusual kinetic observations in catalysis [119, 120]. Bowker and co-workers have recently used STM to image this process in-situ during the course of a reaction [121, 122]. For Pd particles on TiO₂, the spillover effect was found to depend strongly on the morphology of the metal particles [117].

An alternative solution is to attempt to create and characterise models as close as possible to the industrial catalyst by the use of wet chemical methods, but in this case the structure and morphology of the deposits can be difficult to control.

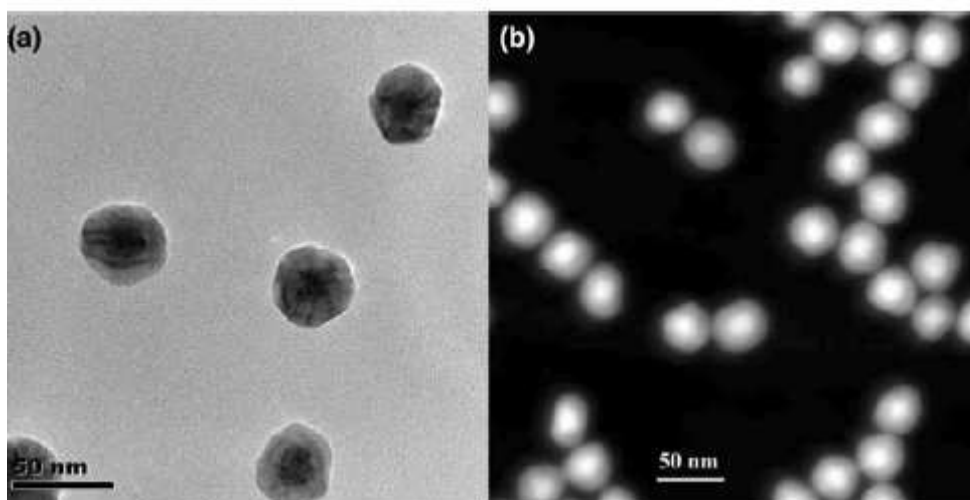


Figure 1.5 - TEM images of Pd Au nanoparticles on Pt using (a) HRTEM and (b) STEM in dark field mode showing a dense inner core of material surrounded by an outer shell [123].

Figure 1.5 above shows High Resolution Transmission Electron Microscopy (HRTEM) and Scanning Transmission Electron Microscopy (STEM) images of Pd Au nanoparticles prepared by chemical deposition of Pd over pre-formed Au seeds on a polished Pt electrode surface [123]. Both images show a dense Au core surrounded by a Pd outer shell.

Thin-shelled nanoparticles are interesting from a catalysis viewpoint because the properties of the Pd shell are more than likely to be perturbed by the underlying core and alloying of the metals resulting from thermally induced intermixing gives altered catalytic behaviour compared to pure Pd [124]. EDS analysis of supported alloy nanostructures has shown Au enrichment in the Pd Au surface [13], supporting this core shell model.

Ferrer et al. have recently studied the growth mode of Pd/Au core/shell nanoparticles [124]. For particles above a critical diameter of 5 nm, they were able to confirm the existence of complex three-phase particles, as shown in figure 1.6, consisting of an inner core containing an even mixture of Pd and Au, an intermediate layer consisting of an Au-rich alloy phase and a surface layer consisting of a Pd-rich alloy. This three-shell model had previously been predicted by Baletto et al. [125].

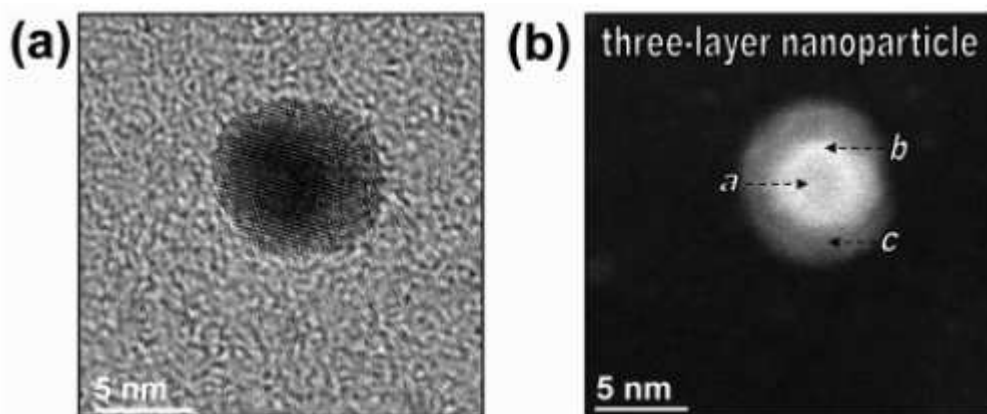


Figure 1.6 – High-resolution (a) and scanning (b) TEM images confirming the presence of a three compositional domains in the core/shell structure of typical single nanoparticles. From reference [123].

1.8 - References

1. <http://www.oed.com/>
2. R. M. Lambert, G. Pacchioni (Eds.), “*Chemisorption and Reactivity on Supported Clusters and Thin Films*”, Kluwer Academic Publishers, 1996.
3. J. Libuda, H.-J. Freund, Surf. Sci. Reports **57** (2005), 157.
4. <http://www.dow.com/vam.htm>
5. D. Kumar, M. S. Chen, D. W. Goodman, Cat. Today **123** (2007), 77.
6. I. I. Moiseev, M. N. Vergaftic, Y. K. Syrkin, Dokl. Akd. Nauk. Az. SSR **133** (1960), 377.
7. S. Nakamura, T. Yasui, J. Cat. **17** (1970), 366.
8. S. Nakamura, T. Yasui, J. Cat. **23** (1971), 315.
9. B. Samanos, P. Boutry, R. Montarnal, J. Cat. **23** (1971), 19.
10. M. Neurock, W. D. Provine, D. A. Dixon, G. W. Coulston, J. J. Lerou, Chem. Eng. Sci. **51** (1996) 10, 1691.
11. D. Kumar, Y.-F. Han, M. S. Chen, D. W. Goodman, Cat. Lett. **106** (2006), 1.
12. N. Macleod, J. M. Keel, R. M. Lambert, Appl. Cat. A **261**, 1 (2004), 37.
13. Y.-F. Han, J. H. Wang, D. Kumar, Z. Yan and D. W. Goodman, J. Cat. **232**, (2005) 467.
14. Y.-F Han, D. Kumar, C. Sivadinarayana and D. W. Goodman, J. Cat. **224** (2004), 60.
15. Y.-F. Han, D. Kumar, D. W. Goodman, J. Cat. **230** (2005), 362.
16. B. Pawelec, A. M. Venezia, V. La Parola, E. Cano-Serrano, J. M. Campos-Martin, J. L. G. Fierro, Appl. Surf. Sci. **242** (2005), 380.
17. M. Nakamura, Y. Fujiwara, T. Yasui, U. S. Patent No. 4,087,622, 1978.
18. M. Neurock, J. Cat. **216** (2003), 73.
19. G. Hoogers, D. C. Papageorgopoulos, Q. Ge, D. A. King, Surf. Sci. **340** (1995), 23.
20. A. R. Garcia, J. L. da Silva, L. M. Lharco, Surf. Sci. **415** (1998), 138.
21. S. L. Silva, T. M. Pham, A. A. Patel, S. Haq, F. M. Leibsle, Surf. Sci. **452** (2000), 79.
22. R. J. Madix, J. L. Falconer, A. M. Suszko, Surf. Sci. **54** (1976), 6.
23. M. Bowker, C. Morgan, J. Couves, Surf. Sci. **555** (2004) 145.
24. J. L. Davis, M. A. Barteau, Surf. Sci. **256** (1991), 50.

25. T. G. Owens, T. E. Jones, T. C. Q. Noakes, P. Bailey, C. J. Baddeley, *J. Phys. Chem. B* **110** (2006) 21152.
26. E. Hansen. M. Neurock, *J. Phys. Chem. B* **105** (2001), 9218.
27. J. James, D. K. Saldin, T. Zheng, W. T. Tysoe, D. S. Scholl, *Cat. Today* **105** (2006), 74.
28. F. Calaza, D. Stacchiola, M. Neurock, W. T. Tysoe, *Surf. Sci.* **598** (2005), 263.
29. F. T. Thomas, R. I. Masel, *Surf. Sci.* **573** (2004), 169.
30. M. Bowker, Y. Li, *J. Cat.* **142** (1993) 630.
31. Y.-F. Han, D. Kumar, D. W. Goodman, *J. Cat.* **230** (2005) 353.
32. S. M. Augustine, J. P. Blitz, *J. Cat.* **142** (1993) 312.
33. E. H. Voogt, A. J. M. Mens, O. L. J. Gijzeman and J. W. Geus, *Surf. Sci.* **373** (1997), 210.
34. T. Zheng, D. Stacchiola, H. C. Poon, D. K. Saldin, W. T. Tysoe, *Surf. Sci.* **564** (2004), 71.
35. D. Stacchiola, L. Burkholder, W. T. Tysoe, *Surf. Sci.* **511** (2002), 215.
36. E. A. Crathorne, D. MacGowan, S. R. Morris, A. P. Rawlinson, *J. Cat.* **149** (1994), 254.
37. D. A. Kragten, R. A. van Santen, M. K. Crawford, W. D. Provine, J. J. Lerou, *J. Inorg. Chem.* **38** (1999), 31.
38. R. G. Brown, J. M. Davidson, C. Triggs, *Am. Chem. Soc. Div. Petrol. Chem. Prep.*, **14**, B23 (1969).
39. W. D. Provine, P. Mills, *Stud. Surf. Sci. Cat.* **101** (1996), 191.
40. M. Bonarowska, A. Maliniowski, W. Juszczak, Z. Karpinski, *Appl. Cat. B* **30** (2001), 187.
41. J. K. Edwards, B. E. Solsona, P. Landon, A. F. Carley, A. Herzing, C. J. Kiely, G. J. Hutchings, *J. Cat.* **263** (2005), 69.
42. R. Larsen, S. Ha, J. Zakzeski, R. I. Masel, *Journal of Power Sources* **157** (2006), 78.
43. C. J. Baddeley, M. S. Tikhov, C. Hardacre, J. R. Lomas, R. M. Lambert, *J. Phys. Chem.* **100** (1996), 2189.
44. X. Y. Shen, D. J. Frankel, J. C. Hermanson, R. J. Smith, G. J. Lapeyre, *Phys. Rev. B.* **32** (1985), 2120.

45. X. Y. Shen, D. J. Frankel, J. C. Hermanson, R. J. Smith, G. J. Lapeyre, *Phys. Rev. B* **33** (1986), 5372.
46. B. J. Wood, H. Wise, *Surf. Sci.* **52** (1975), 151.
47. L. Hilaire, P. Legare, Y. Hull, G. Maire, *Surf. Sci.* **103** (1981), 105.
48. A. Jablonski, S. H. Overbury, G. A. Somorjai, *Surf. Sci.* **65** (1977), 578.
49. M. J. Kelley, S. B. Ziemacki, D. G. Schwartzfager, *J. Vac. Sci. Technol.* **19** (1981), 185.
50. P. Varga, G. Hetzendorf, *Surf. Sci.* **162** (1985), 544.
51. H. Poppa, E. Bauer, H. D. Shih, *Surf. Thin Solid Films* **88** (1982) L21.
52. B. E. Koel, A. Sellidj, *Phys. Rev. B.* **46**, 12 (1992), 7846.
53. C. J. Baddeley, R. M. Lambert, A. W. Stephenson, M. S. Tikhov, *Surf. Sci.* **398** (1998), 172.
54. C. J. Baddeley, R. M. Lambert, A. W. Stephenson, M. A. Ormerod, *J. Phys. Chem.* **99** (1995), 5148.
55. Y. Kuk, L. C. Feldman, P. J. Silverman, *Phys. Rev. Lett.* **50**, (1982), 511.
56. D. L. Weissman-Wenocour, P. M. Stefan, B. B. Pate, M. L. Shek, I. Lindau, W. E. Spicer, *Phys. Rev. B* **27** (1983) 3308.
57. B. Gleich, M. Ruff, R. J. Behm, *Surf. Sci.* **386** (1997), 48.
58. M. Ruff, S. Frey, B. Gleich, R. J. Behm, *Appl. Phys. A* **66** (1998), S513.
59. Z. Li, F. Gao, Y. Wang, F. Calaza, L. Burkholder, W. T. Tysoe, *Surf. Sci.* **601** (2007), 1898.
60. A. Jablonski, S. H. Overbury, G. A. Somorjai, *Surf. Sci.* **65** (1977), 57.
61. D. G. Schwartzfager, S. B. Ziemecki, S. J. Kelly, *J. Vac. Sci. Technol.* **19** (1981), 185.
62. M. Aschoff, S. Speller, J. Kuntze, W. Heiland, E. Platzgummer, M. Schmid, P. Varga, B. Baretzky, *Surf. Sci.* **425** (1998), L1051.
63. M. Aschoff, G. Piaszenski, S. Speller, W. Heiland, *Surf. Sci.* **402** (1998), 770.
64. L. Piccolo, A. Piednoir, J.-C. Bertolini, *Surf. Sci.* **592** (2005), 169.
65. C.-W. Li, K. Luo, T. Wei, D. W. Goodman, *J. Phys. Chem. B* **109** (2005), 18535.
66. T. Schalow, B. Brandt, M. Laurin, S. Schaueremann, J. Libuda, H.-J. Freund, *J. Cat.* **242** (2006) 58.
67. E. Wahlström, N. Lopez, R. Schaub, P. Thostrup, A. Rønnau, C. Africh, E. Lægsgaard, J. Nørskov, F. Besenbacher, *Phys. Rev. Lett.* **90** (2003) 026101.

68. K. Luo, T. Wei, C.-W. Yi, S. Axnada, D. W. Goodman, *J. Phys. Chem. B* **109** (2005) 2357.
69. G. A. Somorjai, “*Introduction to Surface Chemistry and Catalysis*”, J. Wiley and Sons, 1994.
70. P. Wynblatt, R. C. Ku, *Surf. Sci.* **65** (1977), 511.
71. L. Z. Mezey, *Surf. Sci.* **234** (1990), 210.
72. D. Tomanèk, S. Mukherjee, V. Kumar, K. H. Bennemann, *Surf. Sci.* **114** (1982), 11.
73. S. Deckers, F. Habraken, W. F. Vanderweg, A. W. D. Vanderagon, J. F. Van der Veen, J. W. Geus, *Appl. Surf. Sci.* **45** (1990), 121.
74. C. J. Baddeley, L. H. Bloxham, S. C. Laroze, R. Raval, T. C. Q. Noakes, P. Bailey, *Surf. Sci.* **435** (1999), 827.
75. C. J. Baddeley, L. H. Bloxham, S. C. Laroze, R. Raval, T. C. Q. Noakes, P. Bailey, *J. Phys. Chem. B* **105** (2001), 2766.
76. T. E. Jones, T. C. Q. Noakes, P. Bailey, C. J. Baddeley, *J. Phys. Chem. B* **108** (2004), 4759.
77. D. D. Chambliss, R. J. Wilson, S. Chiang, *Phys. Rev. Lett.* **66** (1991) 1721.
78. B. Voigtlander, G. Meyer, N. M. Amer, *Surf. Sci.* **255** (1991) L529.
79. B. Voigtlander, G. Meyer, N. M. Amer, *Phys. Rev. B.* **44** (1991) 10353.
80. E. I. Altman, R. J. Colton, *Surf. Sci* **304** (1994) L400.
81. A. Nordermeer, G. A. Kok, B. E. Nieuwenhuys, *Surf. Sci* **165** (1986) 375.
82. G. A. Kok, A. Nordermeer, B. E. Nieuwenhuys, *Surf. Sci.* **152** (1985) 505.
83. P. T. Wouda, M. Schmid, B. E. Nieuwenhuys, P. Varga. *Surf. Sci.* **417** (1998) 292.
84. C. J. Baddeley, “*The Chemical Physics of Solid Surfaces, Volume 10, Surface Alloys and Alloy Surfaces*”, Elsevier, 2002.
85. A. Couper, D. D. Eley, *Disc. Farad. Soc.* **8** (1950), 172.
86. J. Szanzi, W. K. Kuhn, D. W. Goodman, *J. Phys. Chem.* **98** (1994) 2972.
87. J. Szanzi, W. K. Kuhn, D. W. Goodman, *J. Phys. Chem.* **98** (1994) 2978.
88. N. W. Cant, P. C. Hicks, B. S. Lennon, *J. Cat.* **54** (1978) 372.
89. D. L. Weissman-Wenocur, W. E. Spicer, *Surf. Sci.* **133** (1983) 499.
90. K. Gossner, E. Mizera, *J. Electroan. Chem.* **98** (1979) 37.
91. M. S. Chen, K. Luo, T. Wei, Z. Yan, D. Kumar, C.-W. Yi, D. W. Goodman, *Cat. Today* **117**, (2006) 37.

92. J. H. Sinfelt, *Accounts of Chemical Research* **20** (1987) 134.
93. C. C. Kao, S. C. Tsai, M. K. Bahl, Y. W. Chung, W. J. Lo, *Surf. Sci.* **95** (1980), 1.
94. S. Ogawa, S. Ichikawa, *Phys. Rev. B* **51** (1995), 17231.
95. G. Pacchioni, N. Rösch, *Surf. Sci.* **306** (1994), 169.
96. D. A King, D. P. Woodruff (Eds.), “*The Chemical Physics of Solid Surfaces Vol. 8. Growth and Properties of Ultrathin Epitaxial Layers*”, Amsterdam, Elsevier, 1997.
97. W. Bente, N. Nilus, N. Ernst, H.-J. Freund, *Phys. Rev. B* **72** (2005) 054403.
98. M. Bäumer, H.-J. Freund, *Prog. Surf. Sci.* **61** (1999), 127.
99. C. T. Campbell, *Surf. Sci. Rep.* **27** (1997), 1.
100. C. R. Henry, *Surf. Sci. Rep.* **31** (1998), 231.
101. J. Libuda, H.-J. Freund, *Surf. Sci. Rep.* **57** (2005), 157.
102. H.-J. Freund, *Phys. Status Solidi (b)* **192** (1995), 373.
103. J. G. Chen, J. E. Crowell, J. T. Yates Jr., *Surf. Sci.* **185** (1987) 373.
104. D. N. Belton, S. J. Schmieg, *Surf. Sci.* **199** (1988), 373.
105. D. W. Goodman, *J. Vac. Sci. Technol. A* **14** (1996) 1526.
106. M. Yoshitake, B. Mebarki, T. T. Lay, *Surf. Sci.* **511** (2002) L313.
107. W. Song, M. Yoshitake, *Thin Solid Films* **464-465** (2004) 52.
108. Y. Lykhach, V. Moroz, M. Yoshitake, *Appl. Surf. Sci.* **241** (2005) 250.
109. J.-P. Jacobs, S. Reijne, R. J. M. Elfrink, S. N. Mikhailov, H. H. Brongersma, M. Wuttig, *J. Vac. Sci. Technol. A.* **12** (1994) 2308.
110. S. Stempel, Ph. D. Thesis, Freie Universität, Berlin, 1998.
111. J. T. Stuckless, D. E. Starr, D. J. Bald, C. T. Campbell *J. Chem. Phys.* **107** (1997) 5547.
112. Th. Bertrams, F. Winkelmann, Th. Uttich, H.-J. Freund, H. Neddermeyer *Surf. Sci.* **331-333** (1995) 1515.
113. M. Bäumer, J. Biener, R. J. Madix, *Surf. Sci.* **432** (1999) 189.
114. H.-J. Freund, M. Bäumer, J. Libuda, T. Risse, G. Rupprechter, S. Shaikhutdinov, *J. Cat.* **216** (2003), 223.
115. N. A. Khan, A. Uhl, S. Shaikhutdinov, H.-J. Freund, *Surf. Sci.* **600** (2006) 1849.
116. M. Haruta, S. Tsubota, T. Kobayashi, H. Kageyama, M. J. Genet, *J. Cat.* **144** (1993) 175.

117. M. Bowker, E. Fourre, *Appl. Surf. Sci.* **254** (2008) 4225.
118. M. Bowker, R. D. Smith, R. A. Bennett, *Surf. Sci.* **478** (2001) L309.
119. S. Khoobiar, *J. Phys. Chem.* **68** (1964) 411.
120. J. H. Sinfelt, P. J. Lucchesi, *J. Am. Soc.* **85** (1963) 3365.
121. R. A. Bennett, P. Stone, M. Bowker, *Farad. Discuss.* **114** (1999) 267.
122. R. A. Bennett, P. Stone, M. Bowker, *Cat. Lett.* **59** (1999) 99.
123. J.-W. Hu, Y. Zhang, J.-F. Li, Z. Liu, B. Ren, S.-G. Sun, Z.-Q. Tian, T. Lian, *Chem. Phys. Lett. A.* **408** (2005), 354.
124. D. Ferrer, A. Torres Castro, X. Gao, S. Sepulveda-Guzman, U. Ortiz-Mendez, M. Josè-Yacama, *Nano. Lett.* **7** (2007) 1701.
125. F. Baletto, C. Mottet, R. Ferrando, *Phys. Rev. Lett.* **90** (2003) 135504.

Chapter 2 – Experimental Techniques

All experiments described were carried out under ultrahigh vacuum (UHV) conditions. The reason for this is that the experimental and characterisation techniques involving ion/electron beams are not viable above the 10^{-7} mbar range, since they depend on the mean free paths of the relevant species. Operation under high vacuum ($\sim 10^{-9}$ mbar) is still not enough to prevent coverage of the test crystal with contaminants from the residual gas atmosphere. In order to maintain a clean surface for times of one hour or more, residual gas pressure must be in the range of around 10^{-10} mbar. Obviously, real heterogeneous systems under real operating conditions cannot be characterised in this way, but fundamental adsorption and structural studies on a suitable well defined model surface, such as a single crystal surface or a model nanoparticle/support system, can be related to the properties of the real catalyst.

Three UHV systems were used in this study. Chamber 1, used for temperature-programmed desorption (TPD) experiments, has a base pressure of around 10^{-10} mbar and contains facilities for Ar^+ ion bombardment for sample cleaning, an Omicron 4-grid optics system for low energy electron diffraction (LEED) and Auger Electron Spectroscopy (AES) and a Spectra Microvision Plus quadrupole mass spectrometer for use in TPD analysis. The sample was attached to the manipulator by Ta wires for resistive heating. Sample temperature was monitored by means of a K-type thermocouple attached directly to the crystal.

Scanning tunneling microscopy (STM) and reflection-adsorption infra-red spectroscopy (RAIRS) experiments were carried out Chamber 2, an Omicron variable temperature STM system (10^{-10} mbar base pressure) containing facilities for sample cleaning, LEED and STM measurements. Attached to this is a secondary chamber for RAIRS characterisation using a Nicolet Nexus spectrometer with a mercury cadmium telluride detector.

All MEIS experiments were carried out in Chamber 3 at the UK national MEIS facility at STFC Daresbury Laboratory. The system, described in detail in [1], comprises an accelerator designed to operate at energies up to 400 keV, a beamline

for transport of the positively charged ion beam and multi-chamber UHV end station consisting of a scattering chamber, a separate sample preparation chamber equipped with AES/LEED facilities for surface characterization and a fast entry vacuum load – lock system. The ion source and beamline supplies are controlled remotely from a computer console in the experiment station. The main scattering chamber houses a toroidal electrostatic analyzer fitted with a 2-dimensional position sensitive detector to allow parallel detection of a range of scattering angles and ion energies. Samples are mounted on a triple-axis high precision manipulator allowing rotation of the sample in azimuth about the surface normal, in incidence angle about a vertical axis perpendicular to the horizontal scattering plane and in tilt angle about a horizontal axis.

2.1 - Auger Electron Spectroscopy (AES)

Both Auger electron spectroscopy and the closely related technique of X-ray photoemission spectroscopy (XPS) can be used to gain quantitative measurements in UHV by exploiting the short mean free pathlength of low energy electrons in solids. Photoemission forms the basis of both techniques and Auger peaks can be easily seen along with core level peaks in an XPS spectrum. The sample is irradiated with a high energy beam (1-10 keV electrons in AES or monochromatic 1.5 keV X-rays in XPS). When an incident photon of energy $h\nu$ penetrates the sample and collides with an inner shell electron with a given binding energy E_B , relative to the vacuum level, the electron will be ejected from the surface with a resulting kinetic energy given by Koopman's Equation:

$$E_{\text{Koopman}} = h\nu - E_B \quad (\text{Eqn. 2.1})$$

This means that the original binding energies can be easily determined, giving a spectrum which is unique to each particular element. It is these binding energies that are analysed in XPS. The atom has now become a positively charged ion with an inner shell electron vacancy. This energetic ion can relax by dropping a higher level electron of energy E_X down to fill the core level E_C , resulting in the emission of a photon with energy:

$$h\nu = E_C - E_X \quad (\text{Eqn. 2.2})$$

Secondary or Auger electron emission can occur if this photon is of sufficient energy to cause a second valence level electron of energy E_S to be ejected from the surface, creating a 2^+ positive ion. The kinetic energy of the Auger electron will be:

$$\text{KE} = E_C - E_X - E_S \quad (\text{Eqn. 2.3})$$

Our equipment allows the detection of Auger electrons with kinetic energies in the range of 10 – 1000 eV. Although the incident beam will be able to penetrate multiple crystal layers, the ejected low energy Auger electrons will have mean free paths of the order of a few Angstroms within the crystal lattice. The limited penetrating power and element specificity of the Auger electrons means that AES is a highly surface sensitive technique, and will allow the acquisition of a surface fingerprint for any given surface composition. An advantage of AES compared to other techniques is that the Auger peaks for a particular element will always appear at the same energy in the spectrum, irrespective of the incident beam energy.

Auger spectra are usually presented in differentiated form. This leads to greater sensitivity by removing most of the background contribution. AES is extremely useful for measurements on overlayers, since the change in intensity of a principal peak can be used to calculate the amount of that particular element in the surface. For a metal B deposited onto a substrate crystal of metal A :

$$I = I_0 e^{-d/\lambda \cos\theta} \quad (\text{Eqn. 2.4})$$

where I is the intensity of the attenuated metal A peak after deposition, I_0 is the metal A peak intensity for the clean metal A surface, d is the depth of the metal B layer, λ is the electron mean free path of electrons in metal B and θ is the angle. This provides a way to quantitatively determine the composition of the bimetallic surfaces used in this work.

2.2 - Low Energy Electron Diffraction (LEED)

Low Energy Electron Diffraction (LEED) is a technique that can be used to probe the long range order of atoms on the surface of a crystalline sample. It can be shown that the de Broglie wavelength of a low energy (20 – 200 eV) electron is sufficiently short to allow the electron to be diffracted by the ordered crystal lattice in much the same way as X-ray diffraction, which is commonly used to probe 3-dimensional ordering in crystal lattices. In contrast to XRD which uses high energy X-rays, the use of low energy electrons in LEED means the penetration depth is much shorter and that the diffraction pattern observed will be primarily due to atoms in the surface region so will give information on the 2-dimensional ordering of atoms at the surface.

It can be shown that a periodic 1-dimensional chain of atoms with a given lattice spacing a will interact with a low energy electron beam in the same way as a conventional diffraction grating provided the electron source is sufficiently distant from the sample so that the beam can be considered as a series of plane waves of de Broglie wavelength λ at normal incidence to the sample as shown in figure 2.1 below.

If the beam backscatters from two adjacent atoms at an angle θ from the surface normal then the distances traveled by each beam from the sample to the screen will be separated by the pathlength d , which can be shown by simple trigonometry to be equal to $a \sin \theta$. The Laue condition states that in order for constructive interference to take place, this difference in pathlength must be equal to an integer number of wavelengths, that is:

$$d = a \sin \theta = n \lambda \quad (\text{Eqn. 2.5})$$

For convenience, this can be rewritten as:

$$\sin \theta = \frac{2\pi n}{ka} \quad (\text{Eqn. 2.6})$$

The vector \underline{k} with magnitude $|\underline{k}| = 2\pi/\lambda$ describes the wave – particle duality of the electron beam and is known as the wavenumber.

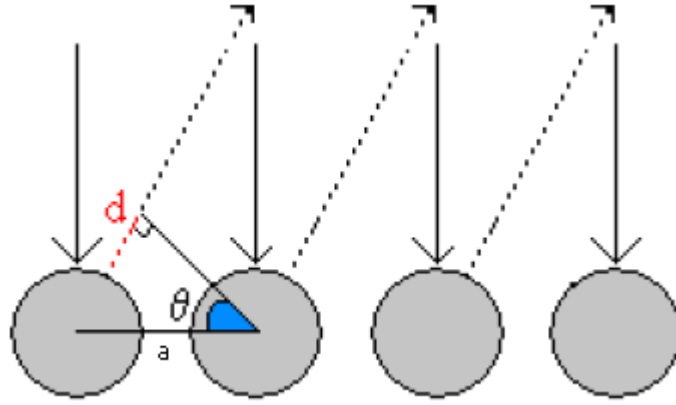


Figure 2.1 – Backscattering of electron beam from a 1-D chain of atoms.

For an isolated pair of adjacent objects the diffracted beam intensity would vary between zero (complete destructive interference at $d = (n + \frac{1}{2})\lambda$) and a maximum value when the condition $d = n\lambda$ is satisfied. For an extended 2-dimensional periodic array of objects, such as an array of atoms on a surface, the diffracted intensity is only significant when the Laue condition is satisfied exactly. The backscattered electrons pass through a series of charged hemispherical grids in order to filter out any inelastically scattered electrons and are then accelerated to a phosphor-coated screen biased to 5 keV. Points of constructive interference will show up as bright spots on the luminescent screen. The special condition $n = 0$ implies that the scattering angle θ must also be equal to zero, giving rise to the zero order or specular diffraction which is the origin of the bright central spot.

It can be shown by simple geometrical arguments that the spacing between the diffraction spots as they appear on the screen is inversely proportional to the lattice parameter a . In terms of the crystal surface, the LEED pattern observed is the reciprocal of the surface net. Large separations in the diffraction pattern correspond to small interatomic separations and vice versa. In mathematical terms, the diffraction pattern is the Fourier transformation of the surface lattice, a periodic array of physical objects in real space, to its equivalent representation in momentum or k -space [2]. It is this inverse lattice that is accessible to the quantum electron waves.

In practice, LEED analysis can be used to obtain information on the periodicity and dimensions of the surface unit cell, however it will not give information on the number of atoms in the unit cell in complex cases, or on their location with respect to

the substrate. The main use of LEED in this investigation will be as a probe of general surface cleanliness and ordering.

2.3 - Temperature Programmed Desorption (TPD)

Temperature programmed desorption (TPD), also known as thermal desorption spectroscopy involves adsorbing molecules onto a model surface and then heating the sample while simultaneously monitoring the residual gas in the vacuum chamber. It is a useful technique for measuring the surface coverage and bonding strengths of adsorbates.

The sample temperature is raised slowly and linearly over several minutes and the residual gas in the chamber is monitored by use of a quadrupole mass spectrometer. As the temperature rises, certain adsorbed species will gain enough energy to desorb from the surface and will be detected as an increase in partial pressure at a particular mass. As the temperature rises further the amount of species on the surface will be reduced. Provided the pumping rate is constant then the partial pressure will begin to fall again when the supply of molecules on the surface is exhausted, giving rise to a characteristic desorption peak when partial pressure is plotted against temperature.

The desorption kinetics are known to follow Arrhenius type behaviour, so that the rate constant for desorption k_d can be expressed as:

$$k_d = A e^{-E_d/RT} \quad (\text{Eqn. 2.7})$$

It can be shown that the desorption flux will depend on both the sample temperature T and the desorption activation energy E_d .

The results of the TPD experiment are produced as plots of partial pressure vs. sample temperature for each species present. Studying the positions and profiles of the peaks can give an insight into the type and strength of bonding between adsorbate and surface and the desorption activation energies E_d can be approximated by using the Redhead Equation [3]:

$$E_d = k_B T_{max} [\ln(v T_{max}/\beta) - 3.64] \quad (\text{Eqn. 2.8})$$

where T_{max} is the position of the desorption peak maximum, v is a pre-exponential frequency factor and β is the heating rate assuming a linear temperature ramp. If the pumping rate is known and remains constant throughout the experiment then the absolute surface coverage can be determined from the peak integral. Care must be taken when analyzing the data, as desorption pathways and activation energies are likely to be dynamically influenced by both decreasing coverage and increasing temperature.

2.4 - Reflection-Absorption Infrared Spectroscopy (RAIRS)

The use of vibrational spectroscopies gives a powerful method for the characterization of molecular species, allowing a particular molecule to be identified by a unique absorption fingerprint. Photon absorption spectroscopies are not inherently surface-sensitive but can be made so by analyzing the beam reflected from a thin surface on a reflective material, such as a single crystal surface.

The Fresnel equations [4] describe the behaviour of a photon beam at an incident angle θ_i to an interface between two media with refractive indices η_1 and η_2 – in this case, the interface between the vacuum ($\eta_1 = 1$) and the crystal surface η_2 . The reflection coefficients R for the incident waves are dependent on their polarisations, labeled as p - (E-field parallel to plane of incidence) polarization, with reflection coefficient R_p and s - (E-field perpendicular to plane of incidence) polarisation with reflection coefficient R_s .

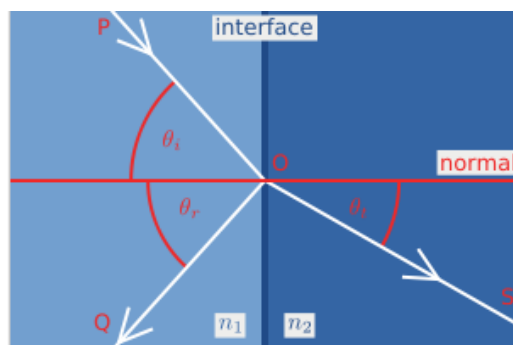


Figure 2.2 – Photon beam at the interface of two media at incident angle σ [5].

$$R_s = \left[\frac{\sin(\theta_t - \theta_i)}{\sin(\theta_t + \theta_i)} \right]^2 = \left[\frac{n_1 \cos(\theta_i) - n_2 \cos(\theta_t)}{n_1 \cos(\theta_i) + n_2 \cos(\theta_t)} \right]^2 \quad (\text{Eqn. 2.9})$$

$$R_p = \left[\frac{\tan(\theta_t - \theta_i)}{\tan(\theta_t + \theta_i)} \right]^2 = \left[\frac{n_1 \cos(\theta_t) - n_2 \cos(\theta_i)}{n_1 \cos(\theta_t) + n_2 \cos(\theta_i)} \right]^2 \quad (\text{Eqn. 2.10})$$

The Fresnel equations predict that *s*-polarised light will be almost eliminated by reflection at grazing incidence (usually $\sim 75\text{-}85^\circ$), while *p*-polarised light is almost doubled in intensity. If the incoming IR beam is aligned at grazing incidence, then only *p*-polarised light will be reflected towards the detector. This means that the surface signal can be easily distinguished from gas-phase absorptions.

The observation of vibrational modes for adsorbates bound to a surface is determined by the surface dipole selection rule. The electric field generated by the oscillating dipole moment of the adsorbed molecule will induce an equal and opposite image charge at the surface as shown in figure 2.3.

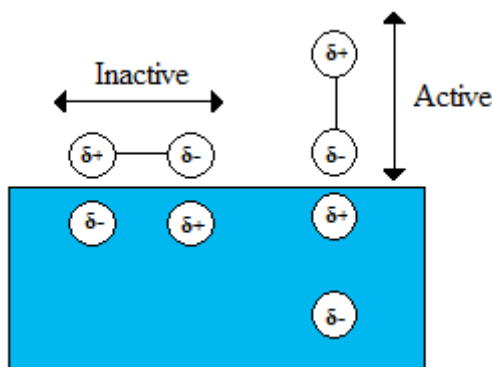


Figure 2.3 – Active and inactive vibrational modes according to the surface selection rule.

In practice, this means that dipole moments parallel to the surface will be cancelled and only those vibrations whose dipole moments are perpendicular to the substrate will give absorption bands in the IR spectrum. By using a suitable theoretical model it is possible to predict which vibrations will have components in the *x*, *y* and *z* directions, allowing us to predict the absorption bands for a given molecule in a given orientation.

One potential problem with RAIRS is that the small number of absorbing molecules usually gives rise to a weak signal. The sampled area is typically around 1 cm^2 , with less than 10^{15} adsorbed molecules (around 1 nmol). Since the absorbance is proportional to E^2 and the area of surface sampled is inversely proportional to $\cos\theta_{\text{incident}}$, it follows that the sensitivity is proportional to $E^2 / \cos\theta_{\text{incident}}$. With modern FTIR spectrometers these small absorption signals, usually in the range of 0.01 – 2 % absorption can still be recorded at relatively high resolution ($\sim 1 \text{ cm}^{-1}$).

For practical reasons, low frequency modes are not easily observable so the vibrations of the metal-adsorbate bond cannot be studied with any accuracy. Attention is usually focused on the intrinsic vibrations of the adsorbed species in the range 600-3600 cm^{-1} .

2.5 - Scanning Tunneling Microscopy (STM)

Scanning tunneling microscopy is a technique developed in the early 1980s by Binnig and Rohrer at IBM. It allows the atomic structure of surfaces to be accurately studied via quantum tunneling effects between a conducting surface and a specially sharpened metallic tip [6].

The phenomenon of quantum tunneling can be explained by considering an electron constrained by finite energetic barrier. The overlapping of multiple atomic orbitals within the crystal lattice leads to the creation of a continuous electronic band structure. The class of material - metal, insulator or semiconductor - will depend upon the positioning, overlap and filling of these bands, particularly the energy gap between the highest occupied level E_F , known as the Fermi energy, and the lowest unoccupied state. The specific electronic structure of a surface is slightly different to the bulk electronic structure. The work function ϕ is defined as the energy required to excite an electron from E_F to the vacuum level E_V as shown in figure 2.4 below.

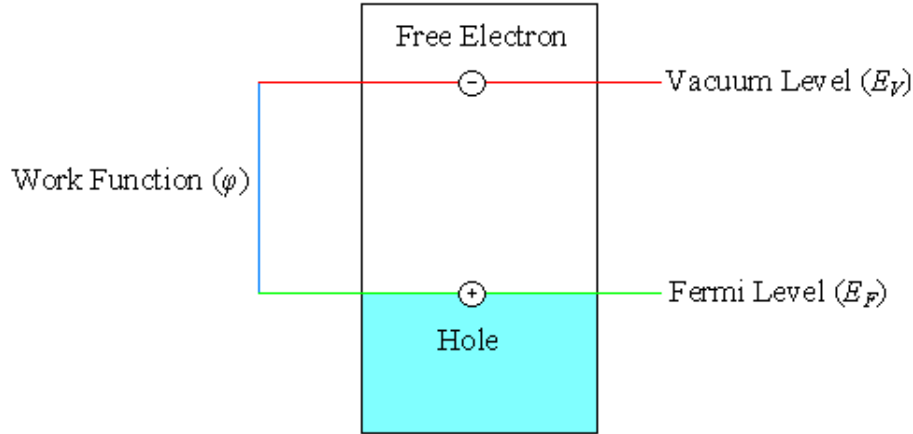


Figure 2.4 – Electronic band structure showing the Fermi and Vacuum Levels.

The work function will vary between materials and between different surfaces of the same material and is influenced by reconstructions or adsorbates at the surface. An electron at the surface can be modeled as a wavefunction constrained by a finite potential well of depth ϕ . The Schrödinger equation will have two separate parts:

$$\begin{aligned}
 -\left(\frac{\hbar}{2m}\right) \frac{d^2\Psi}{dx^2} &= E\Psi && \text{inside solid} \\
 -\left(\frac{\hbar}{2m}\right) \frac{d^2\Psi}{dx^2} + \phi\Psi &= E\Psi && \text{outside solid}
 \end{aligned}
 \tag{Eqn. 2.11}$$

The solutions to these are:

$$\begin{aligned}
 \Psi_{\text{in}} &= A e^{ikx} + A' e^{-ikx} && k = \sqrt{\frac{2mE}{\hbar^2}} \\
 \Psi_{\text{out}} &= B e^{jx} + B' e^{-jx} && j = \sqrt{\frac{2m(V-E)}{\hbar^2}}
 \end{aligned}
 \tag{Eqn. 2.12}$$

The wavefunction outside the solid will be complex when $E < \phi$. Otherwise it describes an exponential decay curve. This can be quantified by the inverse decay length K , which is defined as the reciprocal of the distance from the surface at which the electron density falls to $1/e$. The value of K for a typical metal is around $1\text{-}2 \text{ \AA}^{-1}$. If two metals are brought sufficiently close so as to allow their electron densities to

overlap then electrons can tunnel between them. The flow direction can be controlled by applying a potential V_{ext} to one of the metals so that electrons from the filled states within a range V_{ext} of E_F in the biased metal travel to the empty states just above E_F in the second metal. It is this tunneling current I_T that STM relies on to form images.

The STM can be operated in one of two modes. Constant height mode involves fixing the distance between the tip and the sample so that the image is built up by monitoring changes in I_T . This method allows rapid scanning, but is suitable for atomically flat surfaces only. In constant current mode, the tunneling current is kept constant by continually adjusting the height by means of a piezoelectric feedback loop. Topographical images can be recorded by monitoring changes in the tip's z movement. This is a slower method but it can be used successfully for rougher surfaces so it is the more common of the two modes, and is preferred here in studies of alloy nanoparticles on oxides.

The image quality will depend on the ability to mechanically damp the effect of external vibrations and on the sharpness of the tip. The most common tip materials are W or Pt/Ir. If a perfect atomically sharp tip can be achieved by cutting and chemical etching then I_T will be dominated by the contribution from the end of the tip, resulting in a high lateral resolution.

Provided experimental conditions are optimized, STM can be used to gain an accurate picture of the topography down to atomic resolution on flat conducting samples. This is useful for the study of alloying behaviour, adsorbate overlayer formation, surface reconstruction and nanoparticle growth among other processes.

2.6 - Medium Energy Ion Scattering (MEIS)

An in-depth discussion of the principles of the MEIS technique is given in Chapter 3, which describes the formulation of a new computational method that will allow us to analyse MEIS data from complex supported nanoparticle samples.

2.7 – References

1. P. Bailey, T. C. Q. Noakes, D. P. Woodruff, *Surf. Sci.*, **426** (1999), 358 - 372.
2. J. R. Hook, H. E. Hall, *Solid State Physics 2nd Edition*, J. Wiley and Sons, 1991.
3. <http://www.diss.fu-berlin.de/2004/162/Chapter3.pdf>
4. <http://physics.tamuk.edu/~suson/html/4323/prop-em.html>
5. http://en.wikipedia.org/wiki/Fresnel_reflection
6. G. Binnig, H. Rohrer, *Rev. Modern Physics*, **59**, 3 (1987), part I.

Chapter 3 – Model PdAu Nanoparticles on Oxide Surfaces

3.1 – Experimental

All experiments were carried out under ultrahigh vacuum (UHV) conditions. Three UHV systems were used in this study as described in Chapter 2. All TPD experiments were carried out in Chamber 1. STM measurements were carried out in Chamber 2. All MEIS measurements were carried out during allocated beamtime at the UK national MEIS facility at STFC Daresbury Laboratory in Chamber 3 [1].

In each set of experiments, model catalyst systems of Pd/Au alloy particles were prepared on two different oxide surfaces, silica films grown on a Si{100} substrate for STM and MEIS investigations and alumina films grown on a NiAl{110} substrate for TPD experiments, according to the following standard procedures.

Samples cut from a Si{100} wafer were cleaned by repeated cycles of flash heating to 1273 K and annealing at 1023 K until no impurities were detected by AES analysis. A thin oxide layer was grown by exposing samples to 2700 L O₂ at 873 K.

The NiAl{110} single crystal substrate was prepared by repeated cycles of argon ion bombardment and annealing to 1173 K until a sharp {110} LEED pattern was observed and no impurities were detected by AES analysis. A thin ordered alumina layer was created by cycles of annealing to 573 K in 2.5 x 10⁻⁶ mbar O₂ followed by annealing in UHV at 1123 K [2]. The thickness and cleanliness of the oxide layer were monitored by AES analysis using the ratio of the 503 eV oxide AES peak to the 57 eV substrate peak and the ordering was confirmed by the observation of a characteristic oxide LEED pattern [2].

Au followed by Pd were evaporated from droplets on separate resistively heated Ta filaments onto the oxide surfaces in varying molar ratios. The Au deposition rate was calibrated by dosing Au onto a clean Pd{111} single crystal and estimating the coverage from the attenuation of the 330 eV Pd_{MNN} AES peak and the growth of the 69 eV Au_{NOO} AES peak. For our STM measurements, we were able to estimate the Pd

deposition rate by monitoring the growth of small Pd clusters in the elbows of the Au{111} “herringbone” reconstruction as in [3]. Otherwise, the Pd deposition rate was determined by dosing Pd onto Ni{111} and monitoring the attenuation of the 61 eV Ni_{MNN} AES peak and the growth of the 330 eV Pd_{MNN} AES peak. The calibration point used in each case was 1 monolayer equivalent (MLE) Au, or 1.38×10^{15} Au atoms/cm². Au was always deposited first followed by Pd unless otherwise stated.

Samples were flash-annealed to a series of different temperatures in order to induce intermixing of the metal components and changes in the particle morphology. STM and MEIS data were taken after each annealing step. MEIS data were taken at both normal incidence and 15° off-normal in each case using a dose of 2×10^{15} ions/cm². The MEIS beam has a footprint of 0.5 mm² compared to a typical sample size of 100 mm². In order to minimise the effects of beam damage, each MEIS data set was taken from a fresh region of the sample.

In order to investigate the reaction of acetic acid (AcOH) with the surface, a small glass bulb of liquid AcOH was mounted onto the vacuum lines and purified by several freeze-pump-thaw cycles before dosing 30 L AcOH (AnalR, 100%) onto the sample at 300 K via a leak valve. The glass bulb was isolated from the chamber by a PTFE Young’s tap valve to minimise decomposition of AcOH. MEIS data from samples exposed to AcOH were then taken at normal and 15° off-normal incidences. Used samples were discarded between experiments.

CO and AcOH TPD experiments were carried out on the Pd/Au/alumina/NiAl{110} samples by dosing 30 L CO (Aldrich 99.99%) or AcOH onto the sample at 300 K through a leak valve. The CO feed was passed through a liquid nitrogen and acetone cold trap before dosing into the chamber in order to prevent contamination by volatile metal carbonyls formed by reaction of the CO with the stainless steel gas lines.

3.2 - Medium Energy Ion Scattering (MEIS) – Basic Theory

Medium Energy Ion Scattering (MEIS) is a refinement of the more commonly used Rutherford back scattering (RBS), but with a significantly enhanced energy resolution. The MEIS technique occupies an energy regime between low energy ion

scattering and RBS, typically between 50 and 500 keV, where detectors with high spatial and energy resolution are available. 100 keV H⁺ or He⁺ ions are typically used as the scattering species. The heavier He⁺ ions give better depth resolution than H⁺, but may cause more damage to softer samples. MEIS is increasingly used in studies of the compositional and structural aspects of the near-surface structure of solids.

As in RBS, the energy of the back-scattered ions is dependent on two processes – an elastic recoil energy loss, which can be modelled by billiard ball physics and is dependent on the mass of the scattering atom, and an inelastic energy loss due to interaction with the crystal lattice, which is determined from the distance travelled by the ions through the solid and the stopping power of the material, which is unique to any particular material for a given ion species and beam energy. The scattered ion energy spectrum will therefore contain information on the elemental identity of atoms in the near-surface region as well as their depth below the surface.

The basic model for elastic collisions follows conventional billiard ball physics as follows. An incident ion of mass m_1 and atomic number z_1 travelling with velocity v_1 undergoes a collision with a stationary atom of atomic number z_2 and mass m_2 and is deflected through a scattering angle θ . The kinetic energy of the scattered ion after the collision is given by:

$$E_1 = k^2 E_0 \quad (\text{Eqn. 3.1})$$

where the kinematic factor k^2 is given by [4]:

$$k^2 = \left[\frac{(m_2^2 - m_1^2 \sin^2 \theta)^{1/2} + m_1 \cos \theta}{m_1 + m_2} \right] \quad (\text{Eqn. 3.2})$$

During the collision, the ion may be scattered over any angle. The scattering probability density can be given by:

$$\frac{d\sigma}{d\Omega} = F \left[\frac{z_1 z_2 e^2}{4E \sin^2(\theta/2)} \right]^2 g(\theta, m_1, m_2) \quad (\text{Eqn. 3.3})$$

where the relativistic term $g(\theta, m_1, m_2)$ arises from the conversion from the centre of mass to the laboratory frame of reference.

$$g(\theta, m_1, m_2) = 1 - 2 \left(\frac{m_1}{m_2} \right)^2 \sin^4(\theta/2) \quad (\text{Eqn. 3.4})$$

For most purposes, we can assume that $m_2 \gg m_1$ and $\sin^4(\theta/2)$ will be small for $\theta < 130^\circ$, so that the value of $g(\theta, m_1, m_2)$ can be taken as 1. The factor F is a correction factor arising from the Molière approximation, which takes account of the screening of the nucleus by the surrounding electron cloud [4].

$$F = 1 - \frac{0.042 z_1 z_2^{4/3}}{E} \quad (\text{Eqn. 3.5})$$

It is this effect that is responsible for the small low energy tail seen in the ion intensity vs. ion energy plots. It is important to note that the elastic energy loss depends strongly on the scattering angle.

The extent of inelastic energy losses will depend on the ion species and energy, the sample composition and structure and the depth to which the ion has travelled below the surface. The depth-dependency of the inelastic energy loss is the key feature that enables depth-profiling experiments using MEIS. The total path travelled by the ion beam from source to detector is shown in figure 3.1 below.

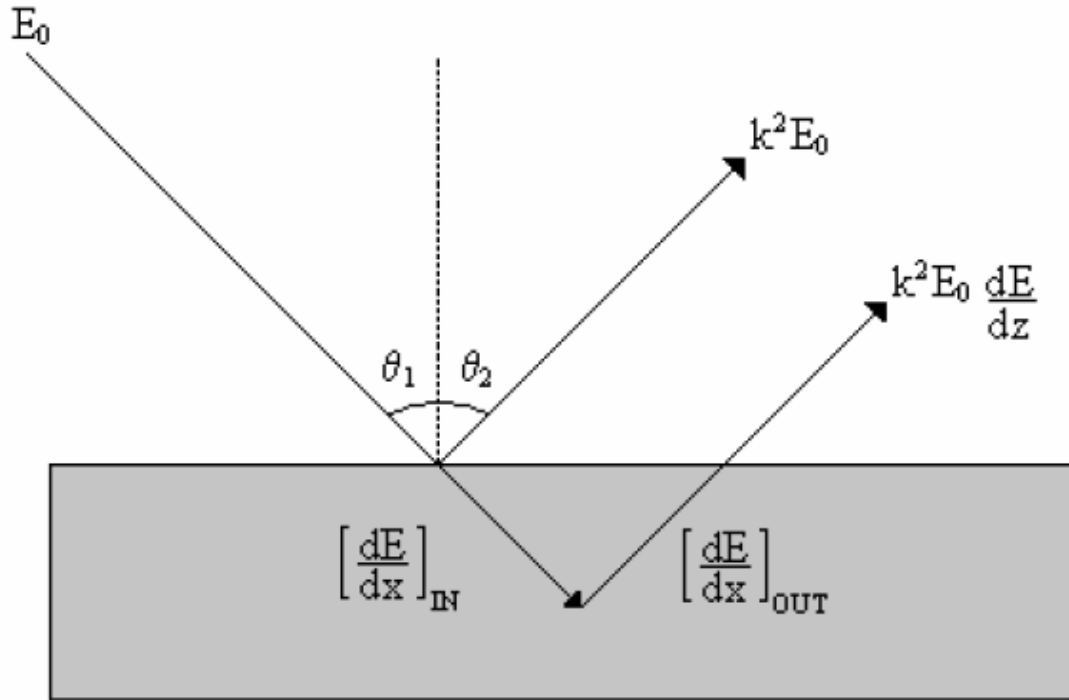


Figure 3.1 – Path travelled by ion beam incident on entering surface at angle θ_1 and exiting at angle θ_2 .

The energy loss per unit length for an ion beam striking the surface at an angle θ_1 and leaving at angle θ_2 as in figure 3.1 above can be calculated as follows. The stopping power for a particular solid is defined as the rate of energy retardation with distance travelled for an ion inside the crystal lattice. Since we are dealing with collisions close to the surface, inelastic energy losses will be small enough so that the stopping powers on the ingoing (pre-collision) and outgoing (post collision) paths can essentially be treated as a pair of constants $[dE/dx]_{E_{in}}$ and $[dE/dx]_{E_{out}}$ respectively.

Now the total stopping power dE/dz for the entire trip can be given by:

$$\frac{dE}{dz} = \frac{k^2}{\cos \theta_1} \left(\frac{dE}{dx} \right)_{E_0} + \frac{1}{\cos \theta_2} \left(\frac{dE}{dx} \right)_{k^2 E_0} \quad (\text{Eqn. 3.6})$$

This means that an ion scattered from a depth t below the surface will suffer an inelastic energy loss per unit length within the surface according to:

$$E_{loss} = \frac{dE}{dz} t \quad (\text{Eqn. 3.7})$$

Using this linear dependence, the inelastic energy losses can be directly related to the penetration depth, giving compositional information as a function of depth below the surface.

If the beam is aligned along a low index crystallographic plane, it can be made to illuminate only the near-surface region as shown in figure 3.2 below. Now, deeper-lying atoms are shielded from the ion beam and hence will not contribute to the spectrum.

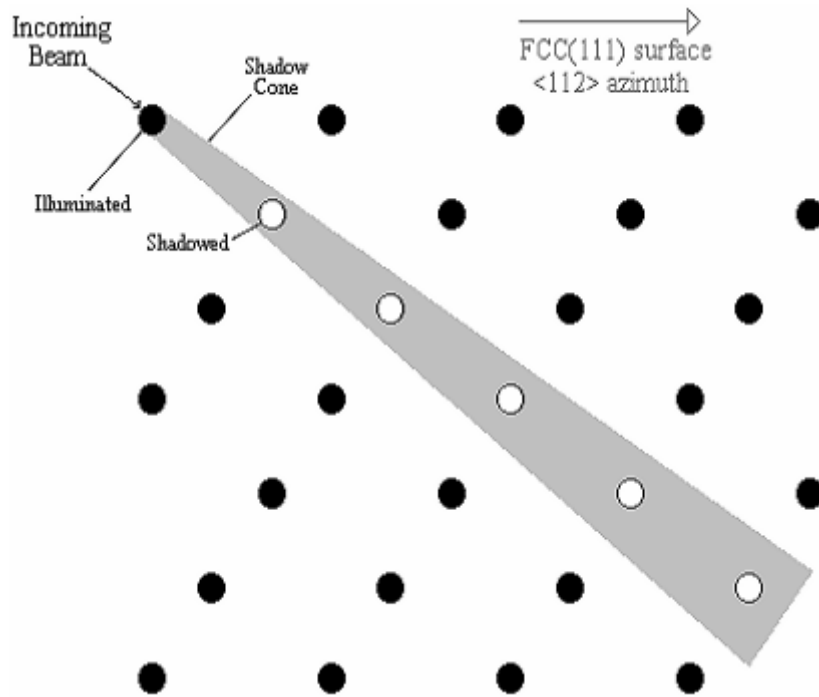


Figure 3.2 – Shadow cone of radius r_{sc} leads to shielding of lower-lying layers from the incident beam.

The radius of the shadow cone r_{sc} is related to the beam energy E by:

$$r_{sc} = 2 \sqrt{\frac{dz_1 z_2 e^2}{4\pi\epsilon_0 E}} \quad (\text{Eqn. 3.8})$$

where d is the separation between metal centres along the ion beam trajectory and Z_1 and Z_2 are the atomic numbers of the incident ion and the scattering atom respectively. This model assumes that the atoms in the crystal are both perfectly ordered and

completely static. In reality, static disorder within the crystal as well as periodic vibrations within the lattice can lead to the unwanted illumination of lower layers by the incoming ion beam.

3.3 - Data Preparation

The MEIS measurements yield data in the form of 2-dimensional tiles. Ion energy is plotted against scattering angle and the ion count intensity at each point is shown on a false-colour contour map. Figure 3.3 below shows MEIS data for PdAu nanoparticles on SiO₂/Si{100}. For clarity, only the Pd and Au surface features are shown here. The silicon and oxygen peaks would also be visible if the tile extended to lower scattered ion energies. However, since the scattering cross-section depends on z^2 , the Si and O peaks are considerably weaker in intensity than the Pd and Au features. As such, the signal to noise ratio is relatively poor and these peaks were not used in our analysis. It would be possible to improve the signal to noise ratio by acquiring data over a longer period of time, but it was decided that it was more important to focus on the Pd and Au signals.

Conventionally, it is not the entire data set but two specific cuts that are analysed. The first section is a plot of the scattered ion intensity against the scattering angle, integrated over a small range of energies. This will give crystallographic information on the relative locations of atoms in the near-surface region through the effects of shadowing and blocking. For single crystal samples, it is possible to follow relaxation and reconstruction processes occurring at the surface from change in the positions of the blocking dips.

In order to obtain compositional information, the scattered ion intensity can be plotted against ion energy over a limited range of scattering angles to give intensity vs. energy plots.

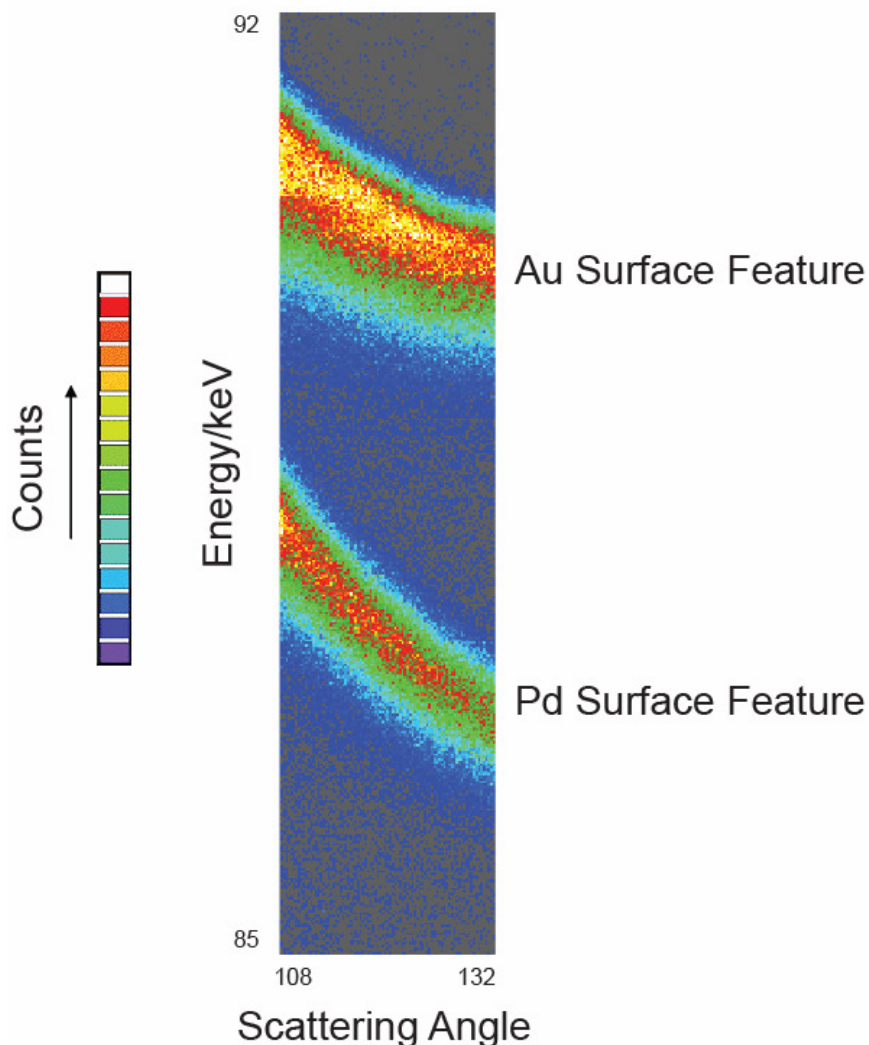


Figure 3.3 – 2-D MEIS tile of Pd/Au alloy nanoparticles on $\text{SiO}_2/\text{Si}\{111\}$.

Figure 3.4a below shows an intensity vs. energy plot for ~ 2 ML Au on Pd{111} from a previous study [5]. The effects of shadowing and blocking have been utilised by careful selection of the ingoing and outgoing ion trajectories in order to limit the contribution from deeper layers. This means only the immediate surface region is illuminated, giving rise to sharp, well-defined peaks. For comparison, Figure 3.4b shows similar data for Pd/Au particles on $\text{SiO}_2/\text{Si}\{100\}$. It is important to note that, unless the particles are aligned in a very specific way, which is unlikely here, a range of different incident geometries exists. Even using a normal incidence geometry (with respect to the Si{100} substrate), deeper lying Pd and Au atoms will contribute to the scattered ion signal, giving rise to broadening of the peaks.

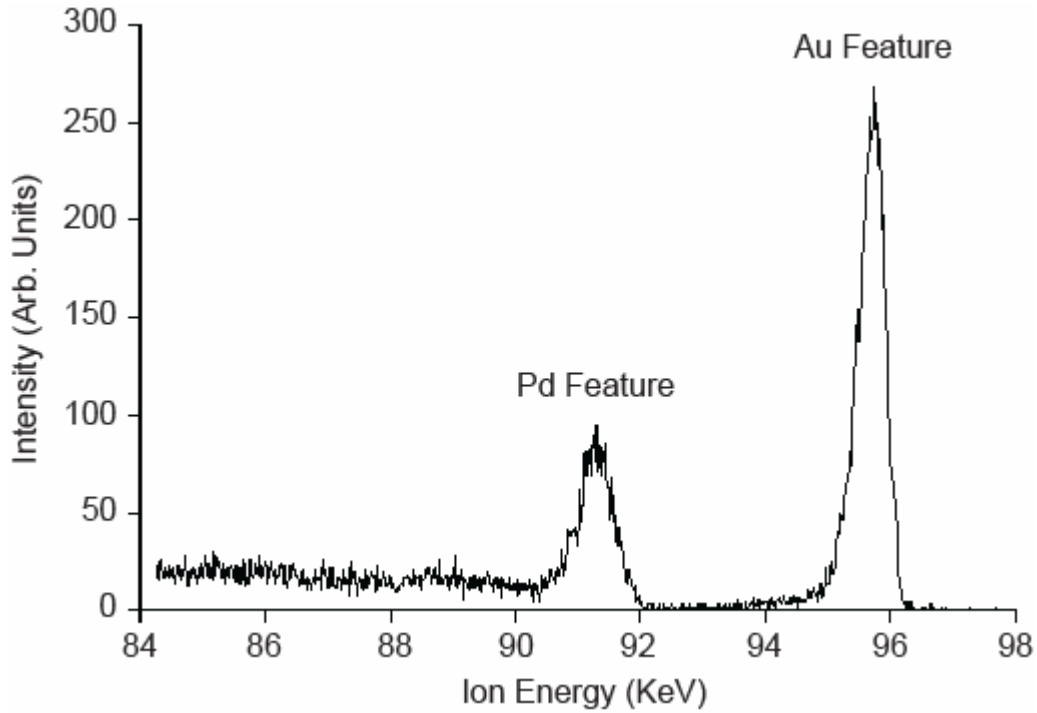


Figure 3.4a – Intensity vs. energy plot for Au/Pd{111} showing only contributions from near-surface layers [5].

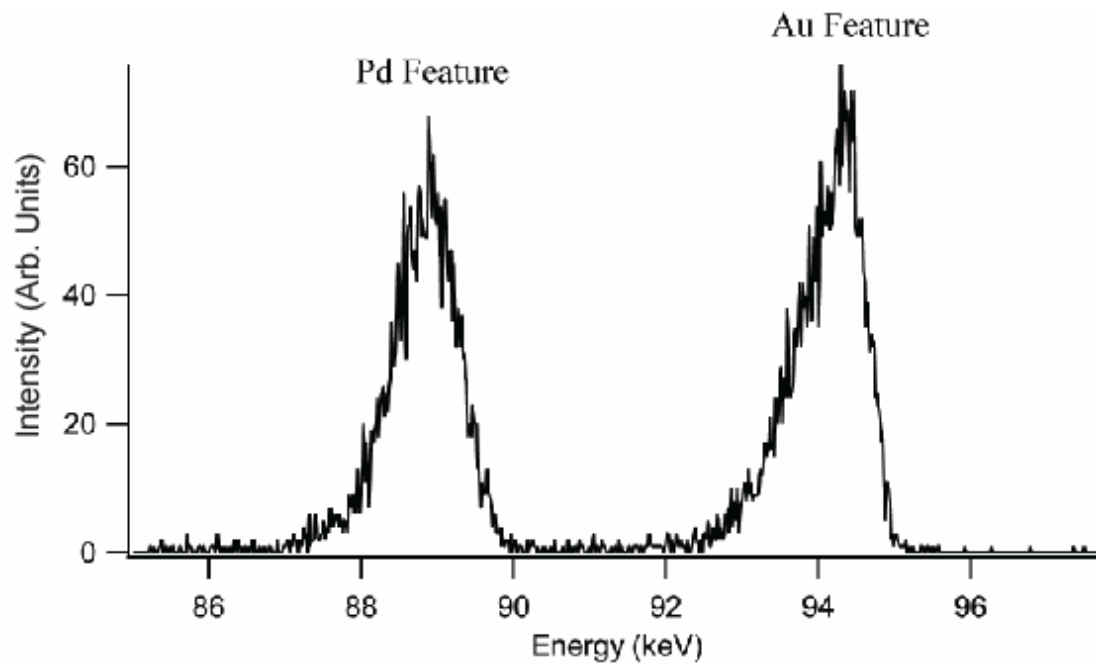


Figure 3.4b – Intensity vs. energy plot for Pd/Au nanoparticles.

Assuming conservation of energy and momentum in a two-body collision, the kinetic energy of the scattered ion after the collision, E_1 , can be derived from the incident ion energy E_0 using Eqn. 3.1 above. We can therefore assign the Pd and Au peaks based on their positions on the energy scale.

For a system containing more than one type of metal atom, it is possible to obtain relative compositions from the relative peak integrals after carrying out a series of normalisation processes on the raw data. It is common practice to first normalise peak areas by multiplying by $\sin^4(\theta/2)$. Since the scattered ion intensity depends strongly on the charge on the scattering nucleus, the peak integral from the raw data must be divided by Fz^2 where z is the nuclear charge of a particular element and F is the Molière correction factor as given in Eqn. 3.5.

Finally, the effect of the beam footprint is removed by multiplying by $\cos\phi$, where ϕ is the incident angle of the ion beam on the surface with respect to the surface normal. The footprint correction takes account of the increase in the illuminated area when the sample is tilted away from normal incidence. The result is a normalised count value for each element which can be compared in order to determine the relative composition of each in the entire volume illuminated by the beam.

In order to gain more detailed compositional analysis, the experimental intensity vs. energy data can be fitted using suitable theoretical models to derive information on the layer-by-layer composition of the sample. MEIS has been widely and successfully used in depth profiling and structural experiments on well ordered bimetallic single-crystal surfaces to follow effects such as alloying and segregation [5-8]. We will now attempt to apply similar solutions to study near-surface compositional effects on supported bimetallic nanoparticles in the first study of its kind.

The compositional data shown in figure 3.4b above were acquired over a small range of scattering angles. In preparing our raw data for fitting it is useful to improve the signal to noise ratio by including a large number of channels around the chosen scattering angle. However, the dependence of the scattered ion energy on the kinematic factor k and hence the scattering angle, means that increasing the angular range causes the energy resolution to decrease. The solution is to perform a k^2 correction, which removes the scattering-angle dependence. This allows us to sample data for a larger range of scattering angles without compromising the energy resolution. Since the kinematic factor also depends on the mass of the target atom it is obviously element specific, meaning that the k^2 correction must be carried out separately for the parts of the spectrum corresponding to each specific element and

the different parts then merged together to create the overall spectrum. An inverse k^2 correction can be performed in order to recover the original experimental data that will be used in the next stage.

3.4 - Spectrum Simulation

Compositional information can now be obtained by simulating theoretical spectra and fitting them to the experimental data by the following general method.

The first step is to select a suitable basic structural model of the sample being investigated, in our case this will be some form of nanoparticle structure. In a typical catalyst, metals are present as nanoparticles exposing the most thermodynamically favourable atomic arrangements. For an fcc metal, a typical particle shape would be a cuboctahedron exposing {111} and {100} facets. A truncated cuboctahedral structure has previously been observed for Pd deposits on $\text{Al}_2\text{O}_3/\text{NiAl}\{110\}$ [9].

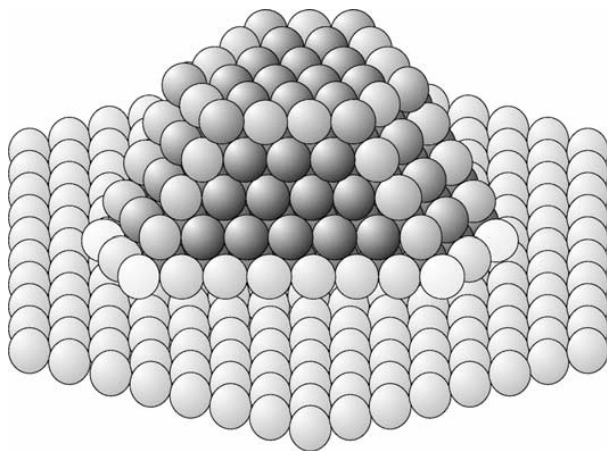


Figure 3.5 – Schematic representation of a cuboctahedral metal cluster on a substrate [9].

Next, scattered ion spectra for all atoms in the model are simulated separately and these are combined to give a spectrum corresponding to the entire particle. Bimetallic systems are simulated by combining two spectra, one for each element, whose relative intensities are weighted according to the relative composition of each element. An inhomogeneous composition can be simulated by performing this weighting shell by shell. Spectra from a number of different particle sizes are calculated in order to

account for a particle size distribution. Finally, the effects of shadowing and blocking are considered and the detected ion yield adjusted accordingly.

The basic theory involves separating the sample into a number of slices or shells. When incident He ions are scattered by the atoms of the i^{th} element in a small volume dv in a metal or alloy shell, the yield of detected ions $H_i(E_{out}) dE$ is described by [10]:

$$H_i(E_{out}) dE = x_i Q \Omega \sigma_i(E_{in}, \theta) N dv \quad (\text{Eqn. 3.9})$$

where

$$E_{in} = E_0 - E_{lossin}(x, y, z) \quad (\text{Eqn. 3.10})$$

$$E_{out} = E_{in} - E_{lossout}(x, y, z) \quad (\text{Eqn. 3.11})$$

where x_i is the composition of the i^{th} element, E_0 is the incident ion energy, E_{in} is the ion energy just before scattering, $E_{lossin}/E_{lossout}$ are the inelastic energy losses before/after scattering from an atom at position (x, y, z) within the sample, Q is the dose of He ions, Ω is the solid angle subtended by the detector, $\sigma_i(E_{in}, \theta)$ is the differential scattering cross-section for an atom of the i^{th} element and N is the atomic density within the sample. By integrating over all the atoms of element i within the alloy shell and summing up over all elements present, the total MEIS spectrum $H(E)$ for a single shell is obtained.

The main aim of our investigation is to develop a reliable method for depth-profiling bimetallic nanoparticles and to examine the influence of adsorbates on our model catalyst system.

Obviously, the key to successfully fitting our experimental data will be the selection (or creation) of a suitable structural model for the bimetallic nanoparticles. Three different approaches will be discussed in detail below. The first example is of data analysis from a single-crystal sample. It should be noted that MEIS is primarily used for the analysis of single crystals and standard procedures are generally used to analyse compositional data [6]. Most published MEIS studies deal with well-defined single crystal substrates where the sample is split into a number of flat slabs (usually

single atomic layers) in the direction of the surface normal. Since the sample has a well defined structure and the interlayer spacing is well known, inelastic energy losses on the ingoing and outgoing paths can be easily calculated for a given scattering geometry.

A few recent attempts have been made to characterise more complex supported monometallic nanoparticle [11] or binary nanoparticle systems [12, 13] by adapting commonly used single-crystal fitting procedures. However, the currently published work is concerned only with the structural properties of pre-prepared samples. This will be the first study of segregation effects on bimetallic nanoparticle systems using MEIS.

3.4.1 - Single Crystal Approach

At the ion energies used during MEIS experiments, a randomly directed ion beam is able to penetrate tens of nm into the sample. In order to simplify data analysis, the beam is often aligned with the bulk of the single crystal sample. The alignment scans plot scattered ion intensity against scattering angle for each of the three goniometer axes in turn. The resulting plot of integrated ion counts will show minima at particular scattering angles that correspond to the bulk blocking channels. The size and intensity of a blocking channel will depend primarily on the size of the shadow cone and the distance between atoms in the chosen direction. Stereographic projections can be used to assign particular blocking axes [14].

For example, in an analogous experiment to ours, where MEIS is used to investigate adsorbate-induced segregation on Au/Pd{111}, the same incident angle could be used to acquire data in the 1-, 2- and 3- layer geometries as shown in figure 3.6 [15].

Compositional information from the surface layer can be obtained by aligning the beam along the $[\bar{1}\bar{1}\bar{4}]$ channel and detecting along the $[110]$ channel as in figure 3.6a so that contributions from lower lying layers are blocked from reaching the detector (to a first approximation). Information on both the 1st and 2nd atomic layers can be obtained by aligning along the same $[\bar{1}\bar{1}\bar{4}]$ channel and this time measuring

along the $[3\bar{3}2]$ channel as in figure 3.6b. Similarly, data on the top 3 atomic layers can be obtained by detecting along the $[2\bar{2}\bar{1}]$ channel as in figure 3.6c. In theory, the same methodology can be applied to any well-ordered single-crystal sample.

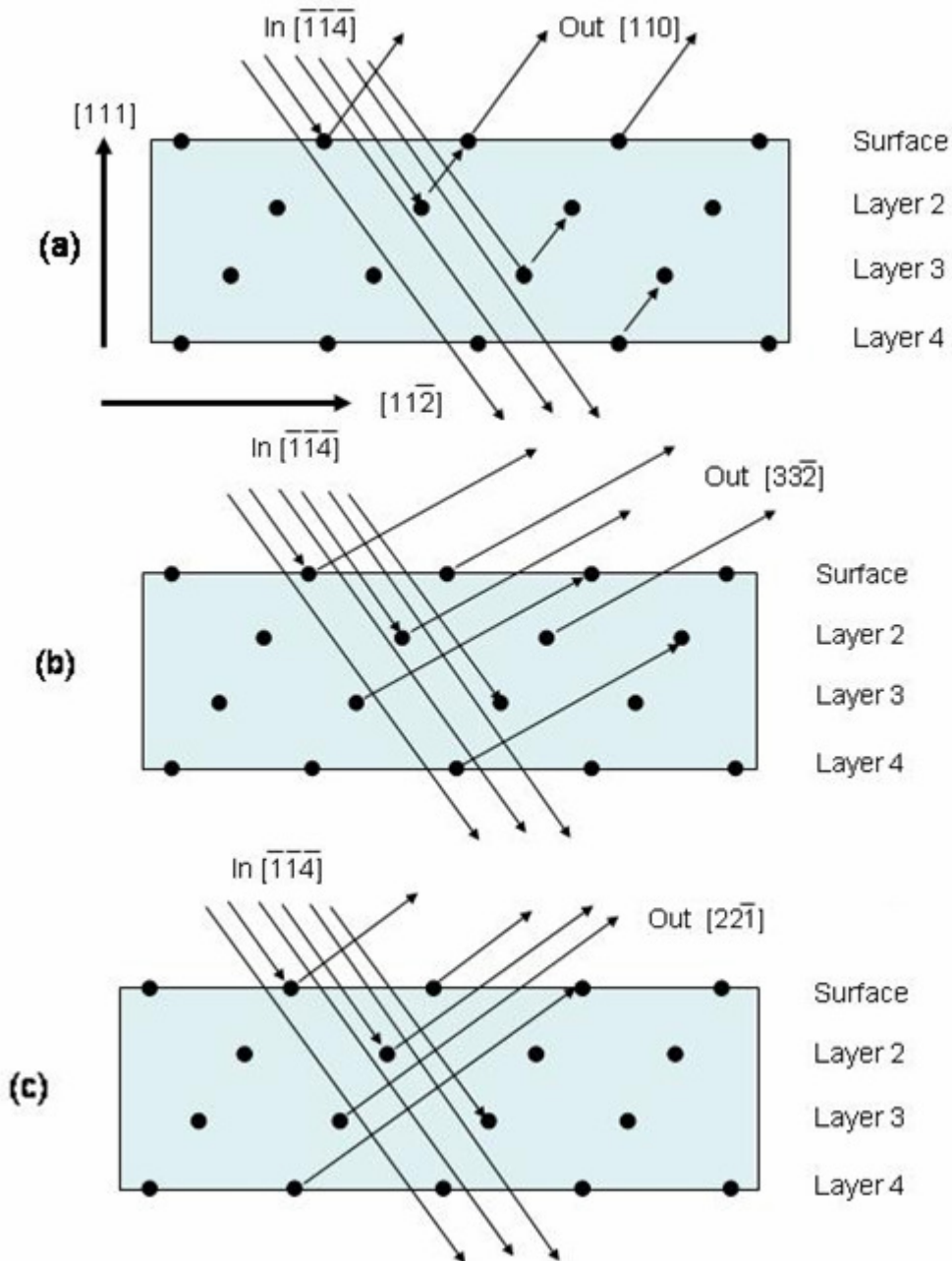


Figure 3.6 –Shadowing and blocking configurations giving rise to 1-, 2- and 3-layer geometries.

As has been discussed, there are now two types of data that can be obtained from the raw single-crystal MEIS plots – structural information is given in ion intensity vs.

scattering angle curves and compositional information is given in ion intensity vs. ion energy plots.

Going back to the previous example of Au on Pd{111}, a blocking dip is observed at $\sim 110^\circ$, which corresponds to the exit blocking direction in the 1st layer geometry. If shadowing and blocking are assumed to be perfect, then by plotting the integrated ion intensity against energy for a small angular range around the base of this dip and applying normalisation calculations we can estimate the ratio of Au to Pd in the top layer. However, in general it is not the case that we can take the ratio of Au to Pd as the absolute composition of each layer. Since the 100 keV ions have a relatively narrow scattering cone, thermal vibration, relaxation and/or reconstruction of the surface atoms are likely to lead to some illumination of lower lying layers.

In order to get an estimate of the number of layers contributing to the scattered ion spectrum for a given scattering geometry we can carry out simulations using the VEGAS code [16]. A starting lattice structure is input in terms of atomic coordinates along with separate values for the vibrational amplitudes of the bulk and surface atoms. Surface relaxations are taken into account as necessary. Incident and scattering angles are input and Monte Carlo simulations are carried out using the basic scattering theory detailed above in order to calculate the contribution of each atomic layer to the overall MEIS spectrum.

Returning to our experimental MEIS data, we now have an estimate of the contribution of each atomic layer from VEGAS. The next step is to estimate the composition of each layer as a function of depth from:

$$H_i(E_{out}) dE = x_i Q\Omega\sigma_i(E_{in}, \theta) Ndv \quad (\text{Eqn. 3.12})$$

But first we must make some further approximations. Previously, energy of the outgoing ion was given as the value E_{out} , derived from:

$$E_{out} = E_{in} - E_{lossout}(x, y, z) \quad (\text{Eqn. 3.13})$$

In practice, however, the outgoing energy is known to have a distribution centred on this calculated value of E_{out} due to energy straggling [17]. The basic lineshape of a peak corresponding to a single layer of material has recently been described in great detail by Grande et al. [18]. Woodruff and co-workers [19] have used a combination of precise experiments and theoretical calculations to confirm the existence of loss features caused by electronic excitations within the target atoms induced by the incident ions that are manifest as a tail on the low-energy side of the peak. This is the reason for the asymmetric lineshape. It is usually sufficient to approximate the peak shape to an asymmetric Gaussian function.

Since the ions are detected by an electrostatic analyser, a further multiplier $F^+(E)$ must be introduced to account for the small proportion of ions that are neutralised on contact with the sample surface (and are thus invisible to the detector) if the simulated spectrum is to be properly compared with the experimental data. The yield of ions detected after scattering from the i^{th} element is now:

$$H_i(E_{out}) dE = x_i Q\Omega\sigma_i(E_{in}, \theta) NdV F^+(E) \quad (\text{Eqn. 3.14})$$

where $F^+(E)$ is formulated according to the experimental observations of Marlon and Young [10, 20]:

$$F^+(E) = 0.02045 (E - 12.3388)^{2/3} \quad (\text{Eqn. 3.15})$$

With these approximations in place, the expected ion yield corresponding to the i^{th} element in the top layer of the sample can be calculated. The expected *FWHM* of this peak can be estimated using data from a 1-layer-geometry spectrum acquired from a single crystal sample. The peak due to the second layer will then be offset from the surface layer peak by a value that can be calculated from the stopping power given by the SRIM code [21]. The scattered ion yield for the i^{th} element in the 2nd layer is calculated and then further modified by the probability of scattering from layer 2 as generated by the VEGAS simulation.

The same process is repeated for each layer illuminated by the ion beam, and the single-layer spectra are convoluted to generate the total MEIS spectrum for the i^{th}

element. The entire process is repeated for each element present and the individual elemental spectra summed to create a total calculated MEIS spectrum for the sample. This calculated spectrum can then be fitted to the experimental data by varying the composition of each layer individually, giving an estimate of the layer-by-layer composition of the sample.

The aim of this work is to extend the current single-crystal methodology to allow the analysis of data from supported bimetallic nanoparticles. While the basic experimental procedure is essentially unchanged, our approach will require extensive modification of the data analysis step compared with the analysis of single-crystal data.

Clearly, the direct application of single crystal methods to nanoparticle data is not a valid solution for a number of reasons. In contrast to a well-defined single-crystal surface which can reasonably be assumed to be atomically flat within the footprint of the beam, the particles in the present study exist as discrete clusters of material on an otherwise bare oxide surface. We can assume that the oxide surface is homogeneous and that the Au/Pd coverage is similar across the surface, so that our 0.5 mm^2 scan area is representative of the sample as a whole. However, STM data tell us that the particles are not of uniform size and that the oxide surface is not atomically flat so that while the particles may be similar, there is evidence that they are not uniformly orientated with respect to the incoming beam. Furthermore, the existence of a large number of discrete particles within the beam footprint, each of which will have corners and edges visible to the ion beam, means that multiple crystal facets may be presented at any given time and that the entry and exit pathways and path-lengths will vary from particle to particle. If we are to fit data from nanoparticles, we must first create a model that can account for complex shadowing and blocking conditions.

Fortunately, it has been shown that the basic theory behind the single-crystal methods can be adapted for use with nanoparticle systems with some success as the following examples prove.

3.4.2 - Particle Model 1 – Hemispherical Particles [12]

In a recent study by Konomi et al., H^+ MEIS data from Pt/Rh bimetallic nanoparticles on α -alumina have been interpreted by use of a Monte Carlo method with a hemispherical particle model as shown in figure 3.7 [12]. The method used is summarised below.

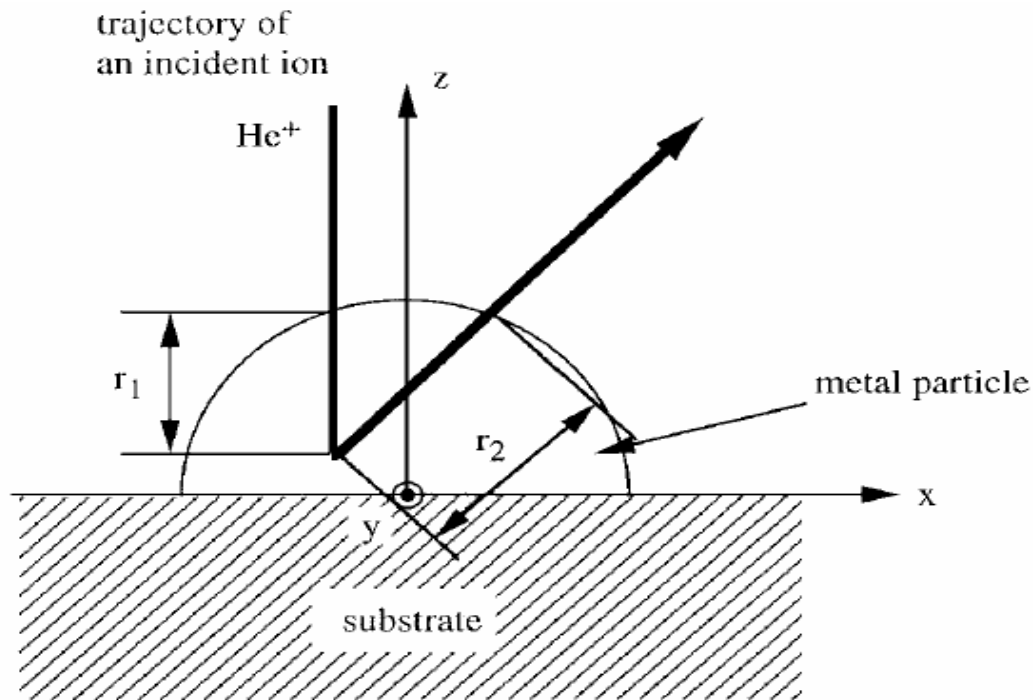


Figure 3.7 – Hemispherical particle model showing incident and outgoing ion beam trajectories [12].

For simplicity, the particle is modelled as a hemisphere of radius r and the position within the particle where scattering occurs is given by (x, y, z) , where x , y and z are randomly generated numbers. Since the probability of scattering is proportional to the elemental composition and the scattering cross section, the number of scattered ions is weighted by $x_i \sigma_i(E_{in}, \theta)$.

For probe ions in the high energy region (~ 500 keV), a Rutherford scattering cross section can be calculated using a Coulomb potential. As the incident ion energy decreases and the number of electrons in the target atoms increases, the screening effect of the electrons causes the real scattering cross section to deviate from the

Rutherford cross section. In the simulation program, $\sigma(E)$ was calculated as a function of energy by fitting the real cross section.

The distance between the incident site and the scattering site is calculated and the inelastic energy loss E_{lossin} before scattering is calculated using Ziegler's formula for stopping power [17]. The elastic energy loss due to scattering is calculated according to kinematic factors. The inelastic energy loss on the outgoing path $E_{lossout}$ is then calculated from the stopping power and the outgoing energy E_{out} is determined.

The outgoing energy E_{out} is known to have a distribution centred on the average energy E_{out} due to energy straggling [17], so that the energy straggling in the incoming and outgoing paths has to be calculated. This is assumed to be a Gaussian distribution $f(E - E_{out}, \Gamma)$ with a Full Width at Half Maximum (FWHM) Γ . In the simulation the straggling was calculated with Chu's value [21], with the energy distribution of detected ions expressed as:

$$f(E) = 2\sqrt{\ln 2}/\sqrt{\pi}\Gamma(r) \exp(-4\ln 2(E - E(r))^2/\Gamma(r)^2) \quad (\text{Eqn. 3.16})$$

where E is the energy, r is the path length if the ion inside the sample and $E(r)$ and $\Gamma(r)$ are the average energy and the FWHM of the energy distribution after passage through a distance r in a metal particle. The FWHM $\Gamma(r)$ is described as:

$$\Gamma^2(r) = \Gamma_0^2 + K^2 \Gamma_{in}^2 + \Gamma_{out}^2 \quad (\text{Eqn. 3.17})$$

where Γ_0 is the FWHM of the energy spread due to the instrument resolution and Γ_{in} and Γ_{out} are the FWHM of the energy straggling associated with the ingoing and outgoing paths.

At this point, the $F^+(E)$ multiplier is introduced to account for those ions that are neutralised on contact with the sample surface. The yield of ions detected after scattering from the i^{th} element is now:

$$H_i(E) = x_i \sigma_i(E_{in}, \theta) f(E - E_{out}, \Gamma) F^+(E) \quad (\text{Eqn. 3.18})$$

where $F^+(E)$ is formulated according to the experimental observations of Marlon and Young [10, 20].

$$F^+(E) = 0.02045 (E - 12.3388)^{2/3} \quad (\text{Eqn. 3.19})$$

The calculation is repeated for a large number of incident ions and each spectrum is convoluted to generate the MEIS spectrum $H_i(E)$ for the i^{th} element. Summing up the $H_i(E)$ for all the elements generates the MEIS spectrum $H_r(E)$, which corresponds to the spectrum for an alloy particle of radius r .

Since the real sample consists of many particles of various sizes, particles are divided into several groups of similar sizes and the spectrum for each group calculated. The synthesized spectrum is now:

$$H_s(E) = \sum n_i H_{ri}(E) \quad (\text{Eqn. 3.20})$$

where n_i is the number of particles whose size is r_i , $H_{ri}(E)$ is spectrum for particle whose size is r_i and $H_s(E)$ is the total spectrum which can be directly compared to the experimentally obtained spectrum.

Changes in the size and composition of the nanoparticles can be calculated, but the contribution from the substrate is not taken into consideration meaning that the program is applicable only to heavy metal/ light substrate systems.

3.4.3 - Particle Model 2 – Stacked Semiconductor Particles [13]

Quinn and co-workers [13] have shown that it is possible to use MEIS to study the composition profile along the <001> growth direction of low-growth-rate InAs-GaAs semiconductor quantum dots (QDs) created by deposition of InAs on GaAs{001}. In this case, AFM measurement showed that the QDs being investigated were discrete 3-dimensional structures with an average diameter of 2.8 nm and an average height of 27 nm. Because of this, a range of different path lengths, and hence stopping and straggling losses, are possible for backscattering from a nucleus at a particular depth. The energy loss process is simulated by placing a single model QD of idealised shape,

whose size was determined by AFM, in the centre of a section of substrate, whose area was again determined by AFM via the QD number density.

The simulation method employed is similar to that used by Konomi et al. [12] as described above. The whole structure is divided into a grid of 400 possible entry points and the energy spectrum for each of the resulting ion trajectories calculated. The simulated spectrum is then the sum over all those paths. Stopping powers were calculated using the SRIM code and analytic formulae [21]. The total ion yield from the i^{th} element is now [10, 22]:

$$Y = x_i \sigma_i f(E - E_{out}, \Gamma) N(E) \Omega \quad (\text{Eqn. 3.21})$$

where x_i and σ_i describe the atomic density and scattering cross-section respectively. The Gaussian f is centred on the energy E_{out} of the ion as it leaves the surface as given by the appropriate stopping powers and elastic energy loss. The Gaussian width Γ is the sum of the inward and outward straggling terms [23] and the instrumental resolution, which is determined by experiments on clean surfaces [24]. The neutralisation probability $N(E)$ is determined from tabulated data [10].

It was found that it is possible to produce satisfactory fits to the experimental MEIS data by using such a method with an indium composition that varied linearly with depth.

3.5 - Growth of Model Nanoparticles on SiO₂/Si{100}

We can conclude that the use of single-crystal MEIS analysis methods are not directly applicable to data from supported bimetallic nanoparticle systems. It has been shown that it is possible to adapt existing analysis procedures to deal with supported nanoparticle data provided an appropriate model is chosen. The examples above describe two such models – hemispherical particles and tall stacked semiconductor structures and the successful use of each in a given situation. However, it should be stressed that these are specific solutions to specific problems. In order to obtain layer-by-layer compositional data from our own samples, we must first investigate the

morphology of our particles and then select an appropriate structural model for our calculations.

3.5.1 – Au on SiO₂/Si{100}

Figure 3.8 below shows intensity vs. energy profiles for ~0.6 ML Au on SiO₂/Si{100} taken at normal and 15° off-normal incident angles.

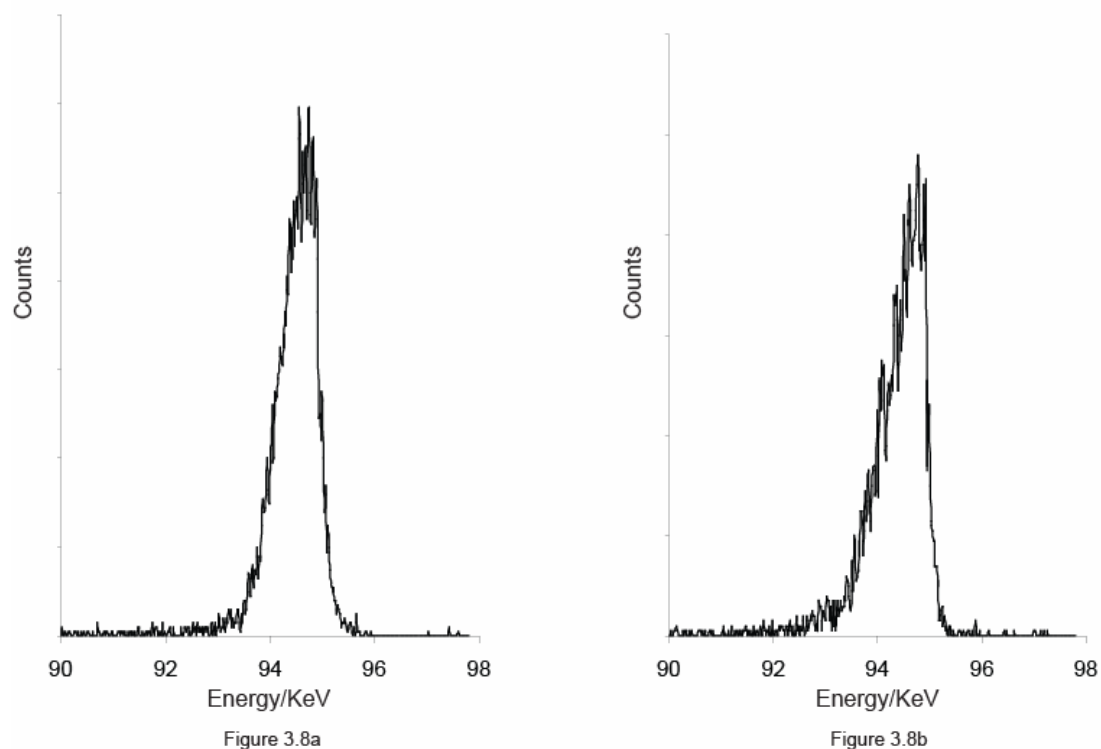


Figure 3.8 – Intensity vs. energy profiles for ~0.6 ML Au/SiO₂/Si{100} taken at (a) normal and (b) 15° off-normal incidence.

Prior to each MEIS run, two days of set-up time were used to prepare and carefully calibrate our Pd and Au deposition sources using AES. By appropriately normalising the total integrated ion yield and comparing the result to 1-layer geometry MEIS data from Au{111}, we can estimate the relative volume of material illuminated by the ion beam. Thus, comparing data for normal and 15° off-normal incidences will give some indication of the extent of shadowing and blocking effects. In general, we observed that the total normalised ion yield is unchanged on moving from normal to 15° off-normal incidence.

This is an extremely important point in the interpretation of the data. If the particles were oriented in a well-defined way with respect to the underlying Si surface, such that, for example, hexagonal planes of metal atoms were parallel to the Si surface, one would expect relatively fewer metal atoms to be visible in a normal incidence geometry than in the more random 15° off-normal incident geometry. For a {111} surface of an fcc metal, only the top three layers are visible at normal incidence, while at 15° a large number of layers are visible. The fact that the total illumination changes little from normal incidence to 15° off normal implies that either all particles are well oriented and just a few layers deep or, more likely, that the particles are not well oriented with respect to the underlying Si substrate. Since the oxide surface is not atomically flat, one would not anticipate that the particles would be well oriented with respect to the substrate. In our models, we assumed that some shadowing and blocking would occur and estimated this by carrying out a VEGAS simulation for a {111} surface with an ion beam incident 7° off-normal – a pseudo-random incidence geometry.

The growth of sub-monolayer quantities of Au on SiO₂ on Si{100} was studied by STM and MEIS. Figure 3.9 below shows a typical STM image of ~0.5 ML Au/SiO₂/Si{100}.

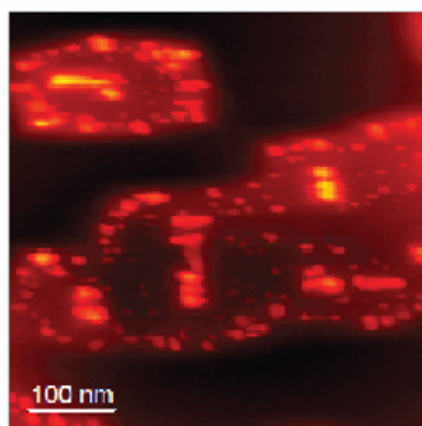


Figure 3.9 - ~0.5 ML Au/SiO₂/Si{100}.

Because of the difference in electrical conductivity between the oxide film and the metallic particles, the electronic height measured by the STM tip is unlikely to accurately reflect the geometric height of the nanoparticles [25]. We will need another

method of determining the true particle height. We have used the *Igor Pro* program together with software developed in-house by Dr Renald Schaub to analyse the particle size distribution in detail. Each individual particle is identified and then fitted by an ellipse. The area, major and minor axes of the ellipses were tabulated and weighted averages calculated for use in MEIS spectrum simulation. Our analysis of a typical image as shown in figure 3.9 below, shows that ~11% of the visible surface area is covered by particles. The Au source has been carefully calibrated so that we can be confident that there is ~ 0.5 MLE material on the surface in total. Assuming the particle coverage is uniform across the surface, this would mean an average particle has a height of ~4 atomic layers, or ~1 nm and an average base area of 197 nm², so that the particles are much broader than they are tall. A previous STM study by Goodman and co-workers [26] has suggested that Au nanoparticles grown on a thin SiO₂ film on Mo{112} are generally not spherical.

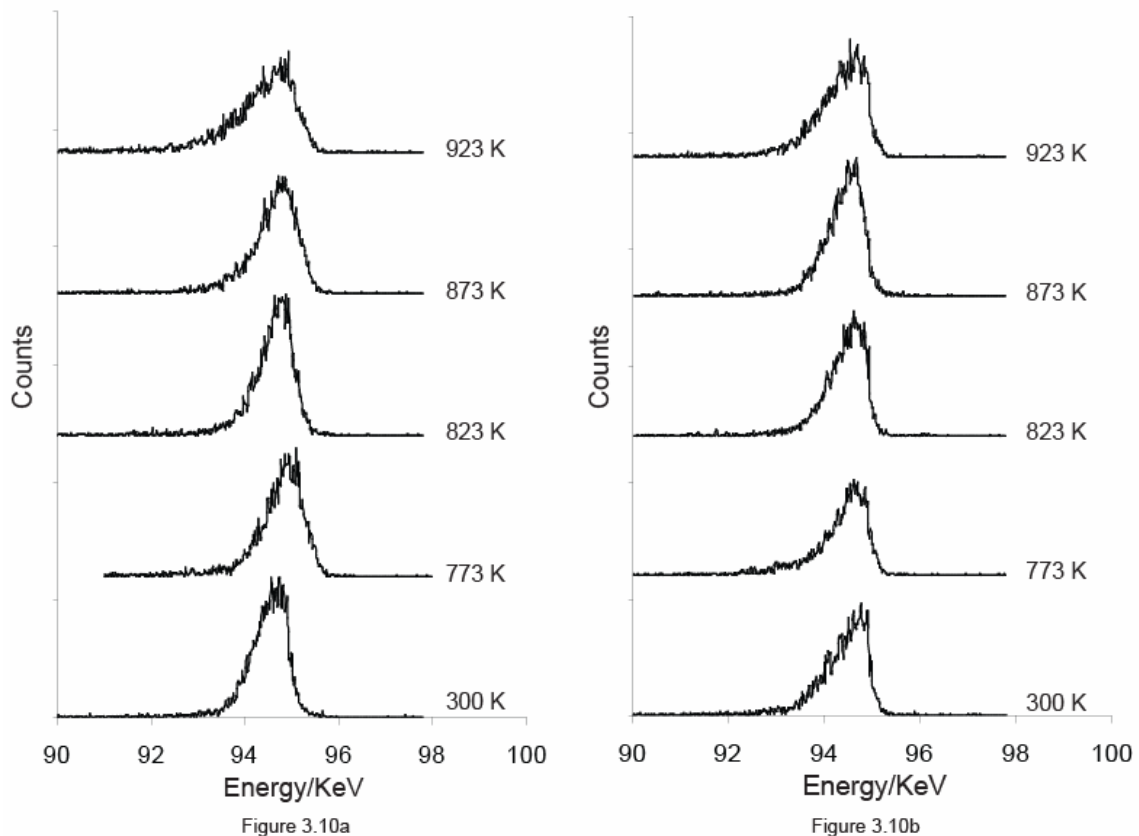


Figure 3.10 – Intensity vs. energy profiles for ~0.6 ML Au/SiO₂/Si{100} taken at (a) normal and (b) 15° off-normal incidence as a function of pre-annealing temperature.

Figure 3.10 above shows intensity vs. energy profiles for ~ 0.6 ML Au on $\text{SiO}_2/\text{Si}\{100\}$ at normal and 15° off-normal incident angles for a series of annealing temperatures. The broadening of the peaks at high temperature indicates an increase in particle size. Comparing the total normalised ion yields shows that the amount of material illuminated does not change with increasing annealing temperature. If the particle height were to increase dramatically on annealing, then we would expect the total normalised ion yield to decrease as the contribution from lower lying layers is reduced due to shadowing and blocking effects. The fact that this does not occur suggests that particle height does not increase significantly on annealing up to 923 K and that the short, broad particle structure is retained.

3.5.2 – PdAu on $\text{SiO}_2/\text{Si}\{100\}$

It is known that the catalytic properties of the Pd/Au system are inextricably linked to the surface composition of the bimetallic particles, which, in turn is strongly dependent on the particle size and shape. In addition, particle aggregation and intermixing depend on the ability of the metal particles to diffuse across the oxide support. In cases such as this, it is often unclear whether complete intermixing of the metallic components occurs to form homogeneous alloy clusters or whether core-shell type structures with a depth-dependent composition profile are formed or whether segregation occurs, resulting in pure metal clusters [27]. We will now attempt to address these issues using a combination of MEIS, STM and TPD analysis.

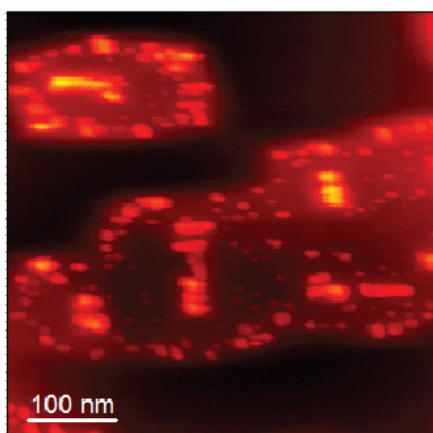


Figure 3.11a

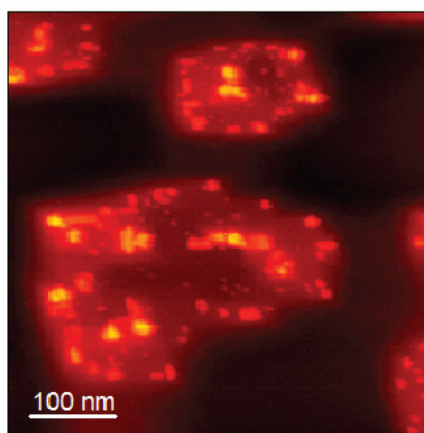


Figure 3.11b

Figure 3.11 – STM images showing (a) 0.5 ML Au/ $\text{SiO}_2/\text{Si}\{100\}$ and (b) 0.5 ML Pd/0.5 ML Au/ $\text{SiO}_2/\text{Si}\{100\}$ as deposited at 300 K.

The first step is to determine whether we are forming monometallic clusters of Pd and Au or bimetallic Pd/Au structures. Figure 3.11a above shows 0.5 ML Au deposited onto SiO₂/Si{100} at 300 K. Figure 3.11b shows the result of depositing 0.5 ML Pd on top of this system to give 0.5 ML Pd/0.5 ML Au/SiO₂/Si{100}.

We observe that the distribution of particles on the surface does not appear to change significantly after deposition of Pd onto the existing Au clusters. Our area analysis shows that the average particle footprint increases from 197 to 593 nm² after deposition of Pd. This suggests that the Pd grows primarily on the existing Au clusters, forming mixed Pd/Au particles. This result is not unexpected, since the lattice mismatch between Pd and Au is small and the Gibbs free energy for mixing of Pd and Au is negative for all compositions [28, 29]. We can estimate the average particle height in figure 3.11b in the same way as for the pure Au particles. This gives a value of ~6 atomic layers or ~1.4 nm.

Figure 3.12 shows a set of STM images of 0.5 ML Pd/0.5 ML Au/SiO₂/Si{100} taken from a single sample annealed to a series of increasing annealing temperatures.

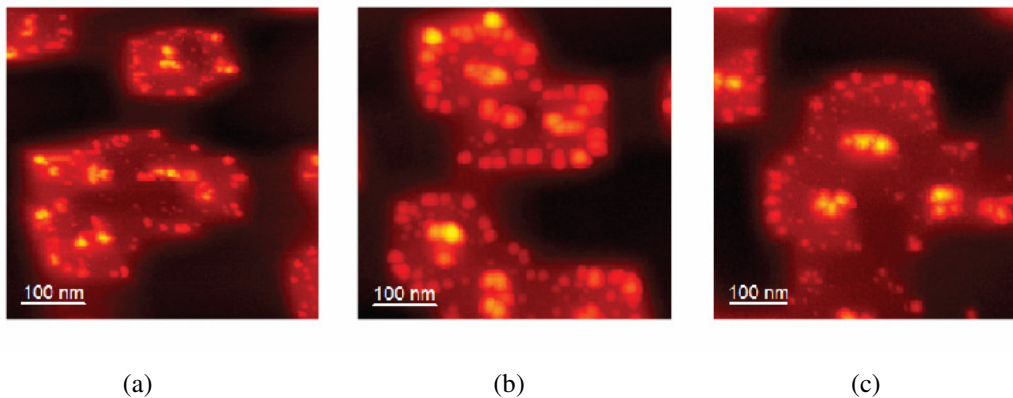


Figure 3.12 - from left to right - STM images showing 0.5 ML Pd/0.5 ML Au/SiO₂/Si{100} (a) as deposited, (b) annealed to 573 K and (c) annealed to 673 K.

By creating 3-dimensional images from the STM data (see figure 3.13) we can see that the nanoparticles seem similar in structure to the pure Au particles – broad based with flat tops. We can therefore assume that hemispherical particle model like the one used by Konomi et al. [12] is unlikely be an appropriate fit for our system.

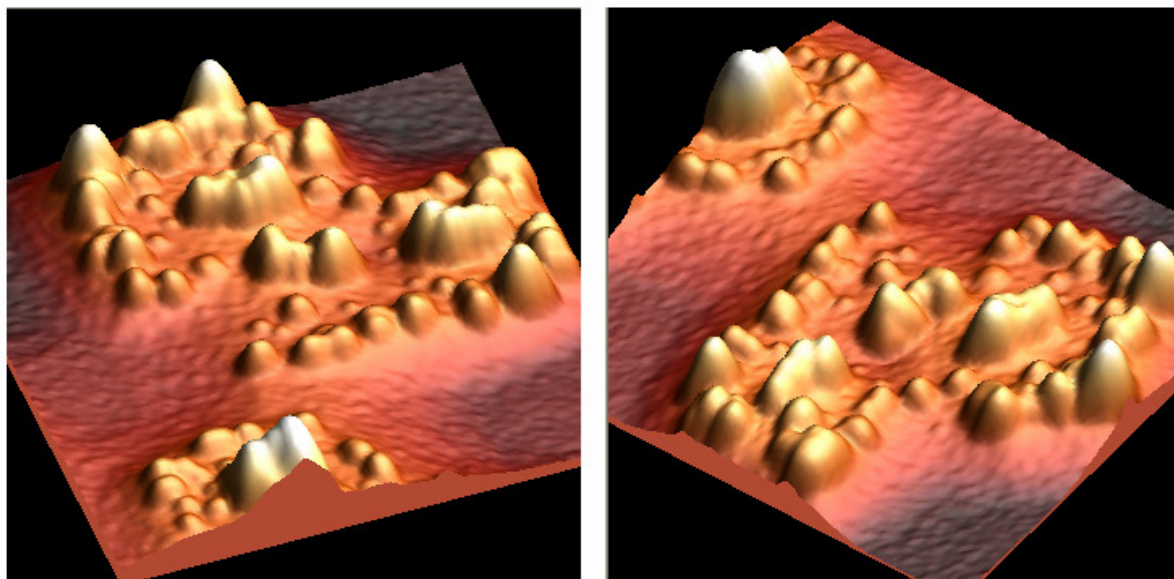


Figure 3.13 – 3-dimensional representation of a typical STM image (100 nm x 100 nm) showing 0.5 ML Pd/0.5 ML Au/SiO₂/Si{100} annealed to 573 K showing flat-topped structures.

Figure 3.14 below shows the variation of average particle base area as a function of annealing temperature for 1 ML of material on SiO₂/Si{100} for different compositions. The data show that the particle growth method is strongly linked to the Au content. We will now attempt to use MEIS in order to study the layer-by-layer composition profiles of Pd/Au nanoparticles on SiO₂/Si{100}.

For a binary alloy of metals *A* and *B*, the basic driving force behind segregation is the difference in the binding energies between the two metal atoms *A-B* and the binding energies in the pure components *A-A* and *B-B*. In practice, atomic size, surface and sublimation enthalpies, particle size and exposed crystal planes will all have an effect on the segregation behaviour [30]. The change in chemical bonding gives rise to a change in the surface tension in the bimetallic system compared to the pure metal systems. There is a strong correlation between the surface tension and the enthalpy of sublimation.

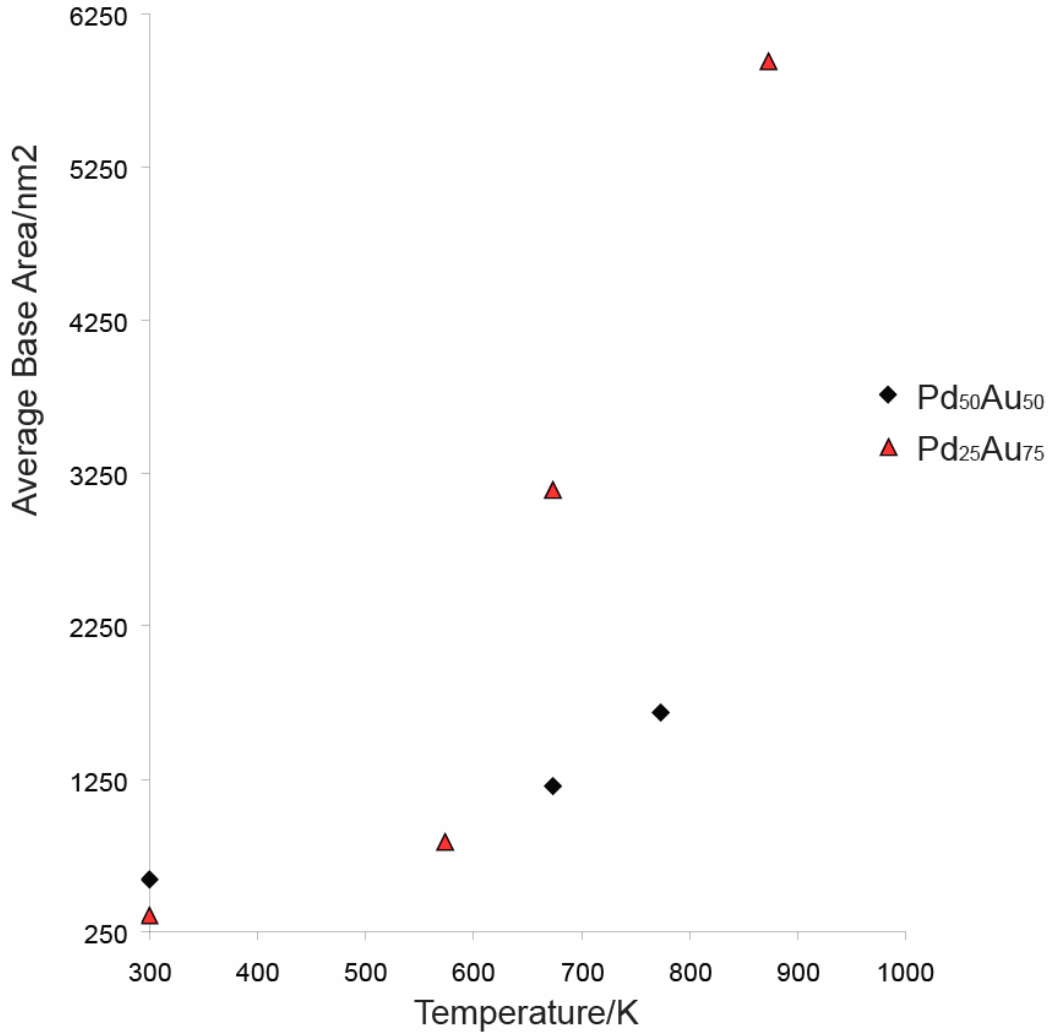


Figure 3.14 – particle growth as a function of annealing temperature for a number of starting compositions.

For an fcc {111} surface for example, atoms in the surface layer will have a coordination number of 9, while bulk atoms will be 12-coordinate. The enthalpy of sublimation ΔH_{sub} can be thought of as the energy required to convert a bulk atom to an isolated gas phase atom. The difference in energy between bulk and surface states will be the energy required to break 3 of the metal-metal bonds, which is proportional to ΔH_{sub} . A value of $0.16 \Delta H_{sub}$ has been obtained experimentally for the {111} metal face. Somorjai [31] showed that the ratio of the mole fraction of surface atoms of *A* compared to surface atoms of *B* can be expressed as:

$$\chi_B^s / \chi_A^s = \chi_B^b / \chi_A^b \exp [0.16(\Delta H_{subA} - \Delta H_{subB})/RT] \quad (\text{Eqn. 3.22})$$

where χ_B^s and χ_B^b are the surface and bulk compositions of metals *A* and *B* respectively. The main implications of this theory are, firstly, that the surface and bulk compositions are different, with the element with the lower heat of sublimation likely to be the dominant surface species. It can also be seen that the surface composition will vary exponentially with temperature. For the purposes of the derivation, the alloy was treated as an ideal solid solution. In reality, the alloy has a finite heat of mixing, which can be introduced into the model [32]. The surface composition can then be seen to be strongly dependent on both the sign and magnitude of the mixing enthalpy.

So far, we have considered the lower coordination numbers of the surface sites as the major driving force for segregation. In solid alloys and solutions, solute atoms that differ in size from the solvent atoms create strain in the solid lattice. The solute atoms can create space and reduce strain by migrating to the open sites available at the grain boundaries.

Although this relatively simple approach does explain the important features of segregation, problems can be encountered with the calculations when trying to predict surface compositions even for simple adsorbate-free systems. In order to solve this, Mezey developed a theory known as the Modern Thermodynamic Calculation of Interface Properties (MTCIP) [33, 34]. In this theory the conditions of the thermodynamic equilibrium state of an interface separating two homogeneous bodies are represented by a system of coupled non-linear equations. Good agreement with experimental data was found in all examined cases, giving correct prediction of face-dependent behaviour.

The data in figure 3.15 show intensity vs. energy profiles for a typical annealing temperature series for Pd₆₀Au₄₀/SiO₂/Si{100}. The data behave similarly to the pure Au data, in that the total normalised ion yield does not change with increasing annealing temperature, but the broadening of both the Pd and Au peaks at higher annealing temperatures suggest changes in the particle shape as we have observed from our STM data in figure 3.12.

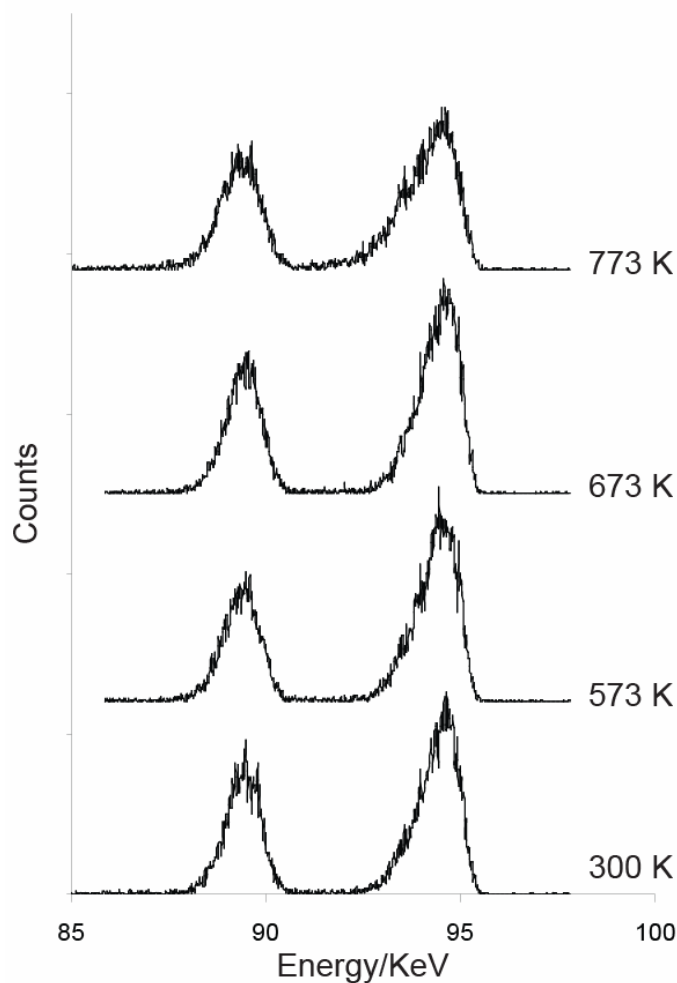


Figure 3.15 – Intensity vs. energy profiles for Pd₆₀Au₄₀/SiO₂/Si{100} as a function of annealing temperature.

In order to investigate the effect of shadowing and blocking, data were taken at normal and 15° off-normal as before. We find that, for samples with ~1-2 ML material on SiO₂/Si{100}, the total normalised ion yield from the Pd and Au peaks is not significantly affected by the incident beam angle, implying that we are sampling all of the layers in the particle in both cases. While STM evidence clearly shows that the particle base area is dependent on annealing temperature, we can conclude that the average particle height does not increase beyond the point where deeper lying layers are not observed.

This last point can be illustrated by considering the effect of the incident beam angle on larger clusters of material. We have increased the metal loading tenfold by depositing ~0.5 ML Au followed by ~9.5 ML Pd onto SiO₂/Si{100}. Figure 3.16

shows intensity vs. energy data for ~9.5 ML Pd/0.5 ML Au/SiO₂/Si{100} at normal and 15° off-normal incidence geometries.

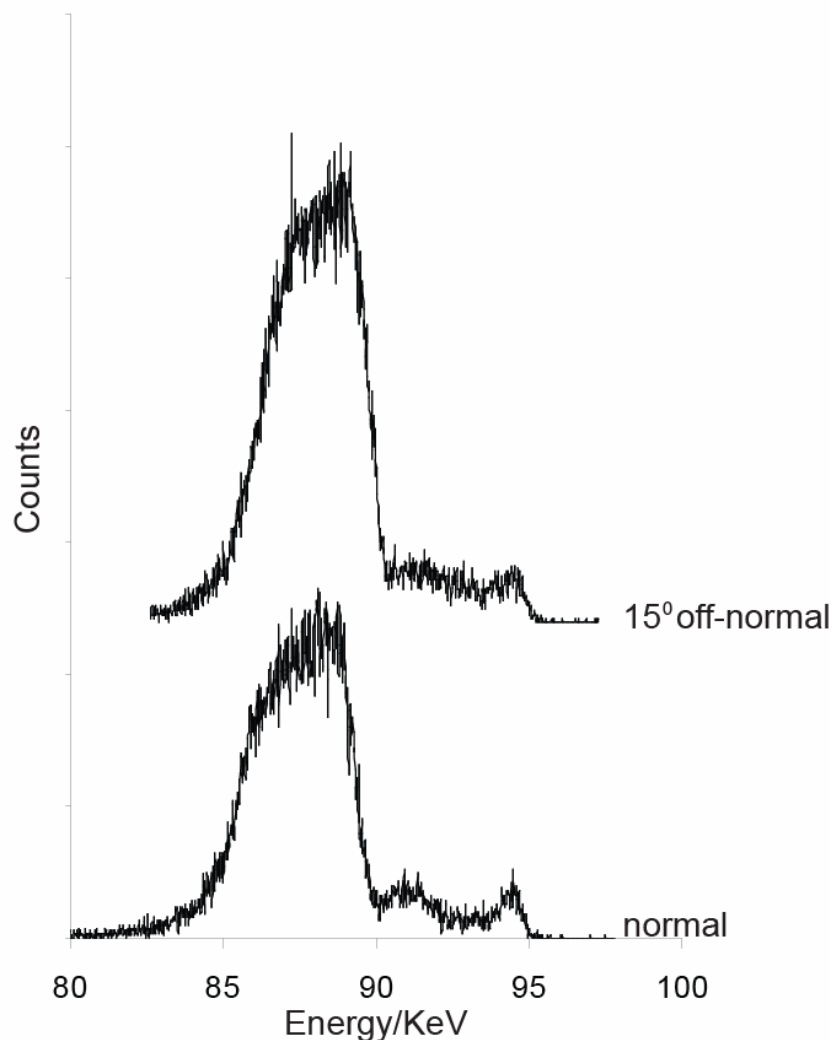


Figure 3.16 – MEIS data for ~9.5 ML Pd/0.5 ML Au/ SiO₂/Si{100} at normal and 15° off-normal incidences.

By normalising the total ion yield in each case, we can calculate the volume of material illuminated in each spectrum. In this case, the total normalised ion yield is increased by a factor of 1.3 on moving to 15° off-normal, implying that shadowing and blocking effects are significant at normal incidence in this case. In both cases, the Au feature is split into a pair of maxima at 91.1 and 94.5 eV, implying that we have high concentrations of Au at the surface and again deep within the particle with little Au in the intermediate layers. Whether this is a general trend will be further investigated by fitting our MEIS data.

In the light of our STM observations, which show that our Pd/Au particles are broad, flat-topped structures, it would not be appropriate to use a hemispherical model of the kind utilised by Konomi et al. [12]. In addition, Konomi's model approximates the clusters as amorphous lumps of material, an approach that is more likely to work with large particles rather than smaller ones.

The model employed by Quinn et al. [13] describes an ion beam directed down a tall, narrow structure at normal incidence. Clearly, moving 15° off-normal in this case would have a significant effect so this model does not describe our system well either, unless we restrict the particle height to a few layers. While an early attempt was made to characterise our system using a program based on the model of Quinn et al. [13], the imposition of either a linear or an exponentially decreasing composition profile meant that the results were unsatisfactory and that segregation effects involving swapping of atoms between the near-surface layers could not be modelled at all.

In order to overcome these difficulties, we have created a new theoretical model based on our experimental observations. This new process is described in detail in [35].

3.6 - St Andrews Particle Fitting Method [35]

We have attempted to extract compositional information by creating theoretical spectra and fitting them to the experimental data as follows.

First of all we need a basic model of the sample being investigated, in our case nanoparticles. Scattered ion spectra for all atoms in the model are simulated separately and these are combined to give a spectrum corresponding to the entire particle. Bimetallic systems are simulated by combining two spectra, one for each element, whose relative intensities are weighted according to the relative composition of each element. An inhomogeneous composition can be simulated by performing this weighting shell by shell. Spectra from a number of different particle sizes are calculated in order to account for a particle size distribution. Finally, the effects of shadowing and blocking are considered.

The particle model can be adjusted separately in order to fit different kinds of samples. For our purposes, we will model the particles as flat-topped truncated hexagonal pyramids as shown in figure 3.17 below.

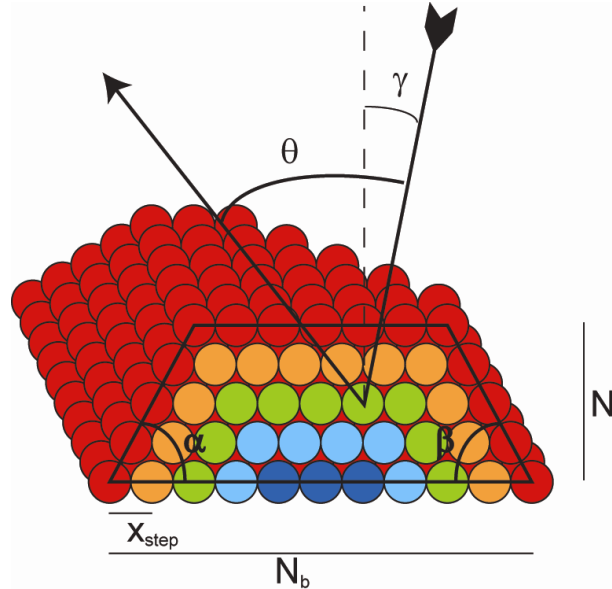


Figure 3.17 – Cross-sectional diagram of the particles used in the analysis and definition of the simulation parameters used in the model.

The starting point is a slice with N_b atoms in the base consisting of N_l layers. As new layers are added, the number of atoms in each layer is reduced by 1. The position of each layer is chosen so that the interatomic distance between each layer is constant and the side angle of the particle is defined by α as shown in figure 3.17. Similar slices are added on either side, with N_b reduced by 1 with each shell until the top of the particle is hexagonal. Now N_l is reduced by 1 with each step until the point where $N_l = 0$ and the model is complete.

From this model, the path length (i.e. the distance travelled by a scattered ion inside the sample) to each atom is calculated to be used in the simulation. For the sake of simplicity, all ion trajectories are assumed to be in the plane of the slices.

3.6.1 - Spectra of Monometallic Systems

The basic line-shape of a MEIS spectrum has been discussed for some time and has recently been described in great detail by Grande et al. [18]. For our purposes, the

line-shape can be represented by an asymmetric Gaussian such that the left and right sides of the function are described by half Gaussians of different widths. This can be described by introducing the parameters σ and a , corresponding to the total *FWHM* and the ratio between the left and right half-widths respectively. For our simulations we have calculated values for σ and a by fitting data from a sample created by depositing Au onto Ni{111} and subsequently annealing to 900 °C, which causes the gold to diffuse into the bulk except for 1/3 ML that is found exclusively in the top layer [36]. This basic line-shape is then assumed to be valid for all elements studied within the error margins of the rest of the analysis.

To a first approximation, we can treat the scattering as being elastic. The energy of the outgoing ion is then given by equation 3.1 above, using the kinematic factor k^2 as defined in equation 3.2. In order to find out how much the actual scattering differs from the elastic approximation we have fitted a well known Au/Pd{111} sample, yielding a shift of 0.39 keV between the elastic peak and the top of the basic peak.

For target elements with more than one abundant isotope, the basic peak is split into one peak per isotope with an energy shift relative to that of the average mass given by equation 3.1 and an intensity corresponding to the isotope abundance. Pd has five major isotopes; ^{104}Pd , ^{105}Pd , ^{106}Pd , ^{108}Pd and ^{110}Pd present at natural abundances of 11.14%, 22.33%, 27.53%, 26.46% and 11.72% respectively. Au has only one major isotope, ^{197}Au [37].

The resulting line-shape is used in the simulation of the spectra of atoms at the surface, where the beam does not enter the sample and the path-length is zero. For non-zero path lengths within the sample, the line profile is shifted to lower energies due to the stopping power and broadened due to energy straggling. The magnitudes of both these effects are described by the SRIM tool [21].

By adding together the spectra of all individual atoms, the spectrum corresponding to the complete model can be simulated. The distribution of particle sizes in the real sample is accounted for by combining spectra from particles of different sizes.

One of the key features of MEIS is the effect of shadowing (where atoms closer to the surface prevent the beam from reaching lower lying layers) and blocking (where atoms in the upper layers block the backscattered ions on their path between the target atom and the detector). This is a major influence on the detected intensity and is extremely useful in quantitative structure determination in single-crystal samples. In our study, however, the oxide support surface is not completely flat and we have shown that the orientation of the particles with respect to the ion beam is essentially random. Hence, any shadowing and blocking effects will also be random. In order to include this in our simulation, the shadowing and blocking in a Pd{111} single crystal along a pseudo-random trajectory is simulated using the VEGAS code [16]. The resulting signal from each layer is translated to signal vs. path length using the scattering parameters from the present simulation and the shadowed/unshadowed intensity ratio spectrum is calculated. Finally, the unshadowed simulation is multiplied by this ratio spectrum in order to produce a new simulation that includes shadowing and blocking.

3.6.2 - Extension to bimetallic systems

A bimetallic system is simulated by combining two spectra, calculated as described above, corresponding to scattering by each individual element. We can simulate a certain composition by weighting the relative intensity of each spectrum. A layer-by-layer composition is simulated by setting the weights shell-wise instead of using the same weights for the whole sample. The relative intensity of the spectra must be adjusted according to the difference in scattering cross-section.

3.6.3 - Simulation Parameters

A list of the parameters used in the simulation is given in table 3.1 below along with a brief description of each. Most of these have already been described above. The value of each to be used in our example is also given.

Of these, the last five are used as free parameters in the fitting procedure and will be described in detail here. I_0 is a multiplier used to normalise the overall intensity of the simulation to match that of the experimental data. E_{ion} is the energy of the ions before

the scattering event. This is used in the simulation to calculate the position of the elastic peaks of each element using equation 3.1.

The value of E_{ion} in our experiments was originally set by the MEIS equipment to be ~ 100 keV, but unfortunately this value cannot be directly measured during the experiment. The absolute value of E_{ion} can be calculated from the experimental tiles by extrapolating back from the energies of the Pd and Au peaks taking into account the scattering angle. Once the beam has been created each day, the beam energy is constant throughout the day. The beam energy is found to fluctuate slightly (by $\sim 0.1\%$) from day to day. We found it convenient to treat E_{ion} as an unknown quantity to be fitted during the analysis. The value obtained from the fit is then compared from experiment to experiment to ensure consistency.

d_{size} defines the particle size distribution. We assume the size distribution to be Gaussian so that d_{size} consists of two values corresponding to the peak position and the FWHM of the Gaussian function respectively. The Gaussian distribution of particle size agrees well STM data for Au particles on $\text{SiO}_2/\text{Mo}\{112\}$ collected by Goodman and co-workers [26].

Before combining the spectra of different particle sizes, they are normalised according to the number of atoms in each particle. Hence, the distribution does not describe the number of particles of each size, but instead the total number of atoms found in particles of each size. For technical reasons, only the particle height N_l is allowed to vary through the size distribution, while N_b is kept at a constant value obtained from STM data.

In the simulations, the composition of each atom shell in each particle size is described individually. For the fitting, however the composition of all particles has to be described in as simple a way as possible. We have chosen to define a composition profile such that the top $p_{top}\%$ of each particle has the composition c_{top} , the bottom $p_{bottom}\%$ has a composition c_{bottom} and the rest of the atoms, found in the core of the particles, have a composition c_{core} .

Parameter	Description	Value in our example
N_b	The number of atoms across the bottom layer.	55
N_l	The maximum height of particles included in the size distribution.	20
α	The angle of the side of the particles.	62.6°
x_{step}	The distance between atoms within each layer.	2.804 Å
$Stop$ $stragg$	The stopping power of the atoms in the particles. Parameter describing the amount of straggling – the broadening effect of 1 Å material.	0.0381 keV/Å 0.20 keV
R_l	The ratio between the scattering cross-sections of the two elements.	2.45
m	The atomic mass of the elements simulated.	197 amu, 108.6 amu
m_{ion}	The mass of the probe ions.	4 amu
Γ	Angle of the incoming beam relative to the surface normal.	0°
Θ	Scattering angle.	124°
Σ	FWHM of the basic line shape.	0.69
A	Ratio in width between the left and right sides of the basic lineshape.	1.56
I_0	Overall intensity multiplier.	109.1
E_{ion}	Energy of the incident ions. This is used to calculate the position of the elastic peaks for each element.	101.5 keV
$c_{top, core, bottom}$	The composition, given as the Au mole fraction, of the top, core and bottom parts of the composition profile.	0.62, 0.20, 1.0
$p_{top, bottom}$	The ratio of the particles considered to belong to the top and bottom in the composition profile.	0.20, 0.14
d_{size}	Definition of the size distribution.	4.19 layers, 4.13 layers

3.6.4 – Fitting of Experimental Data

Once the simulation has been defined, it is relatively straight-forward to fit a simulated spectrum to the experimental data. For this purpose, we have chosen to use MATLAB and the built-in function *fminsearch* on a standard laptop computer. However, there are many parameters that can be fitted, which makes it very easy to obtain a good fit but much harder to judge whether the final result is sensible. Therefore, we have performed our fits carefully, increasing the number of free parameters in a stepwise manner.

The parameters x_{step} , *stop* and *stragg* are dependent on the total composition so should also vary during the fit. Unfortunately, this would require too much computer power so the analysis is instead done in an iterative manner, where the fit and updating of these parameters are repeated until no significant change is found.

We will now illustrate the analysis method and its capabilities with a number of examples. PdAu nanoparticles were created on an oxidised Si{100} substrate by depositing ~0.4 ML Au followed by 0.6 ML Pd at room temperature. The sample was then annealed to 673 K before MEIS data were taken at normal incidence and a scattering angle of 124°. STM data taken from a similar sample indicate an average particle base diameter of 150 Å ($N_b = 55$). The simulation parameters provided in the last column of table 1 above are the fitted parameters corresponding to the final result shown in figure 3.18d below.

Figure 3.18 shows the step-wise analysis where the complexity is gradually increased from panels *a* to *d*. In panels *a-c*, the sample is approximated as a flat surface in order to reduce the computational workload. In panel *a*, we have further simplified the analysis by using a homogeneous composition throughout the particle and a fixed size distribution, where the main contribution to the spectrum comes from 5 layer high particles and the Gaussian describing the size distribution has a FWHM of 5 layers. Looking at the plot in figure 3.18a, it is clear that this fit puts too much intensity at the high energy edge (surface) of the Pd peak and too little intensity at the low energy edge (bottom) of the Au peak.

Between figures 3.18a and 3.18b we have in three steps fitted the size distribution as well as the compositions of the top, bottom and core regions individually. The sizes of these regions are fixed such that the top and bottom regions each correspond to 20% of the total volume and the core region corresponds to the remaining 60%. Now the fit is rather good with surface and bottom regions enriched in Au (62% and 78% respectively) compared to the average composition of 40% and the core is correspondingly depleted to 20% Au. In figure 3.18c we have also fitted the volume of the sample to be treated as surface and bottom, but the difference compared to 3.18b is small ($p_{top} = 21.4\%$, $p_{bottom} = 19.6\%$).

Finally, figure 3.18d below shows the result when the simulation is built on a particle-shaped model instead of a flat surface. This gives slightly different lineshapes, but both the quality of the fits and the end results are close to identical, with the exception that the bottom region is now found to be pure Au.

Figure 3.19 shows the final fit in greater detail. All parameters are as described in table 3.1 above. This above example raises a number of interesting points. Firstly, we can see that the estimated particle height is only a few atomic layers as we had previously predicted on the basis of our STM analysis. By comparing the full particle model fits to the single-crystal-like fits we can see that fitting using some single-crystal approximations is an appropriate shortcut for the special case of short, broad particles where the contribution from edge effects is small.

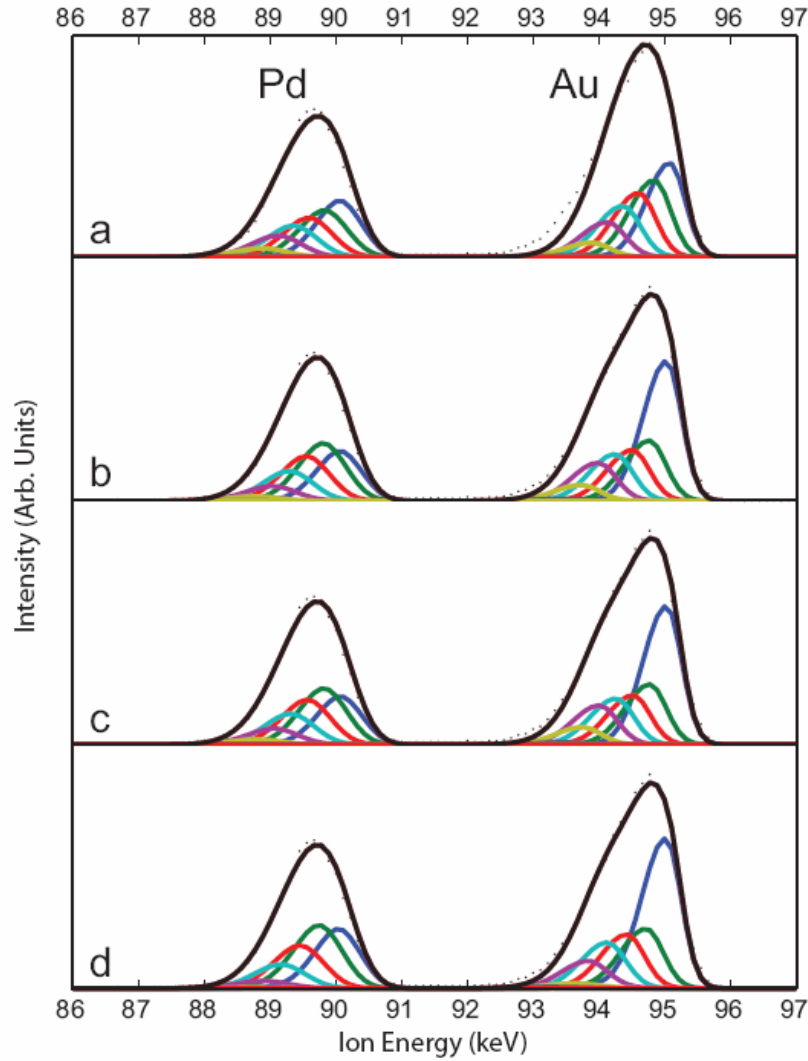


Figure 3.18 – The steps followed in the analysis of a sample with PdAu particles on SiO₂. Panel *a* shows the fit assuming a homogeneous composition profile. In *b* the composition profile is divided into 3 regions; the top 20%, the bottom 20% and the remaining 60% core. In *c*, the borders between these fitting regions were included as well. While *a-c* use a model where the sample is described as a flat surface, *d* finally uses a particle model as described in figure 3.17. Otherwise, settings are the same as in *c*.

The bottom layer is found to be rich in Au ($c_{bottom} = 100\%$), as would be expected when Pd is deposited on top of Au clusters. The observation that the surface is significantly enriched in Au ($c_{top} = 62\%$ compared to an average composition of 40%) is less intuitive. This suggests that intermixing of Pd and Au is taking place even at room temperature, to the extent that Au is able to migrate to the particle surface.

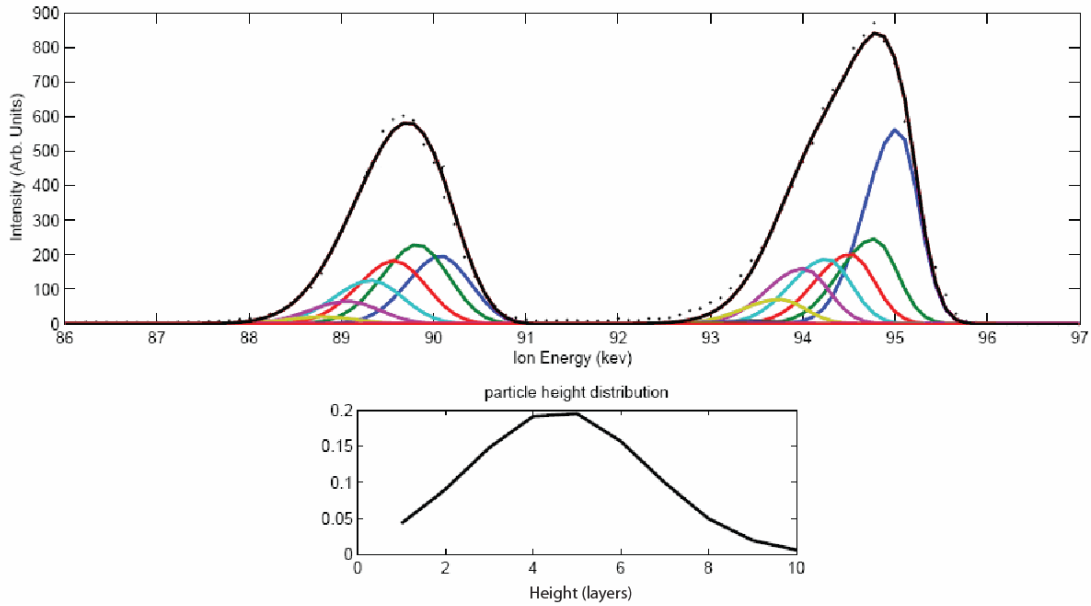


Figure 3.19 – Final fitting result from Pd₆₀Au₄₀/SiO₂/Si{100} showing fitted composition profiles and particle size distributions.

Going back to Somorjai’s model [31], the ratio of the mole fraction of Au to Pd at the surface can be expressed as:

$$\chi_{\text{Au}}^s / \chi_{\text{Pd}}^s = \chi_{\text{Au}}^b / \chi_{\text{Pd}}^b \exp[0.16(\Delta H_{\text{subPd}} - \Delta H_{\text{subAu}}) / RT] \quad (\text{Eqn. 3.23})$$

By inputting appropriate values for ΔH_{subPd} and ΔH_{subAu} [38, 39], we estimate that the {111} surface of a Pd₆₀Au₄₀ alloy sample at 300 K alloy should contain ~55% Au, so that the surface is still enriched in Au but less so than we observe experimentally.

If we plot the fitted surface Au composition against pre-annealing temperature for our Pd₆₀Au₄₀/SiO₂/Si{100} sample as in figure 3.20, we can see that the absolute compositional values given by the single-crystal like model are similar to, if not exactly the same as those given by the particle model. In both cases, we find that our results follow a similar general trend as that predicted by Somorjai [31], but the surface Au compositions are systematically higher in each case than the theoretically predicted values. We can conclude that, in the special case of broad, short, flat topped particles, we are able to use some single-crystal approximations in order to reduce the required computing power and calculation time. This allows us to fit large quantities of data quickly and efficiently using a standard personal laptop computer.

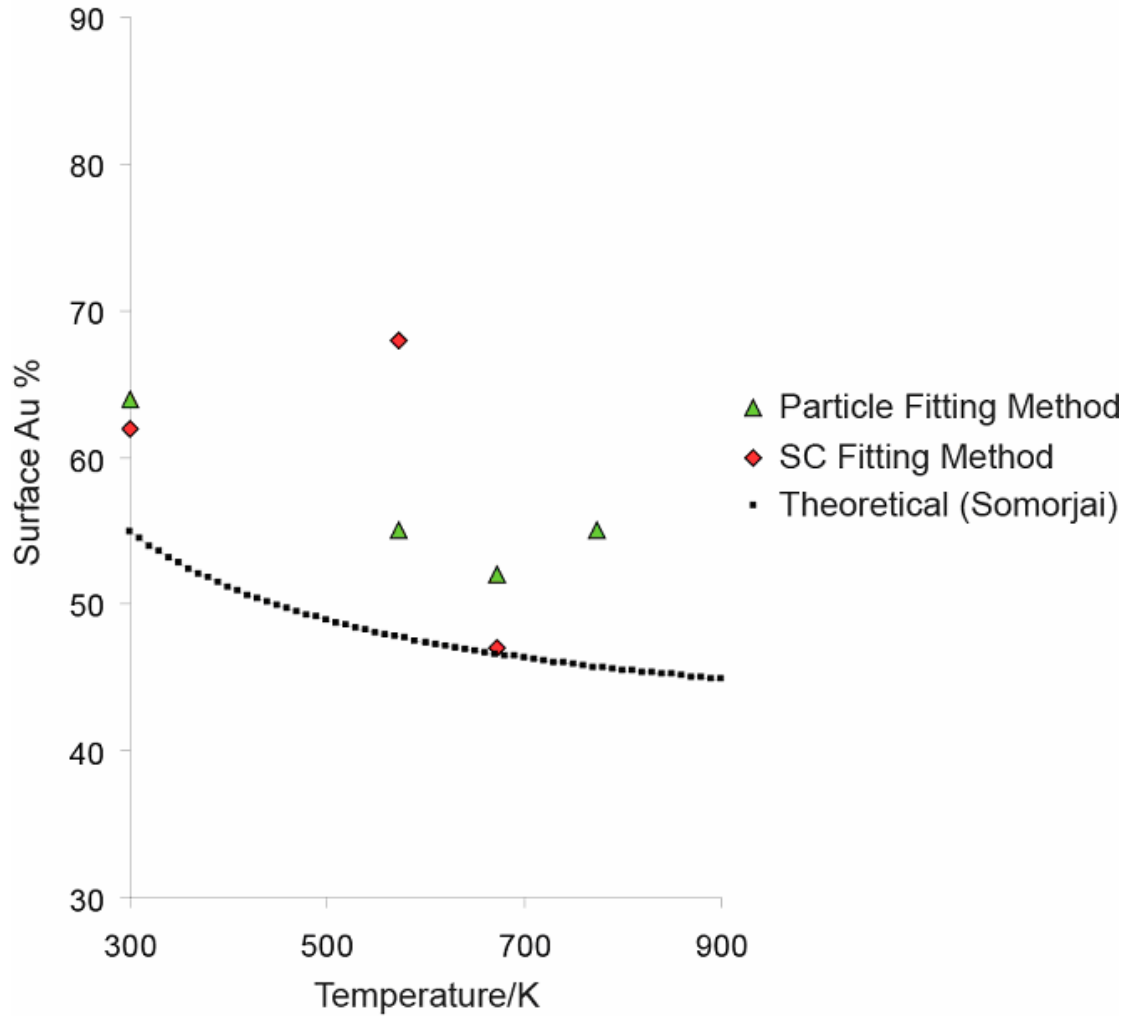


Figure 3.20 – Fitted composition data as a function of pre-annealing temperature and comparison to theoretical predictions from [31].

In order to investigate the possibility of alloying at room temperature and its implications regarding particle structure, we have tested another set of similar samples prepared in the same way as before except that Pd was deposited first this time followed by Au. Figure 3.21 below shows fitted composition data from a $\text{Au}_{40}\text{Pd}_{60}/\text{SiO}_2/\text{Si}\{100\}$ sample created by depositing ~ 0.60 ML Pd followed by ~ 0.40 ML Au onto $\text{SiO}_2/\text{Si}\{100\}$ at 300 K. We have assumed that the particle structure and base diameter are the same as before. As before, the fitted compositions, given as the Au mole fraction, of the surface, core and base regions of the particle are labelled c_{top} , c_{core} and c_{bottom} respectively in table 3.2.

In this case, the surface is slightly more Au rich than before, as would be expected. Otherwise, the composition profile is similar to that shown in figure 3.19, with some

Au migrating into the particle core. Surprisingly, the bottom layer is found to contain a significant concentration of Au, despite Pd being deposited first this time. Again, STM suggests that we are forming mixed PdAu structures so that this observation confirms our finding that Au and Pd are able to intermix even at 300 K. This agrees with the findings of Koel, who observed intermixing of Pd with an Au{111} substrate at 300 K [40].

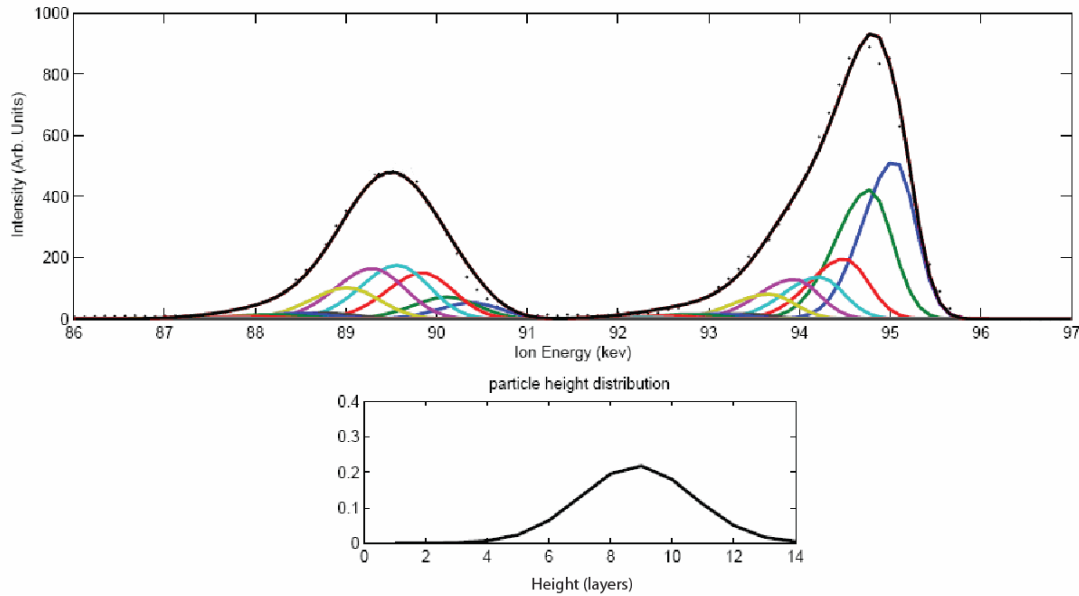


Figure 3.21 – Fitting of data from Au₄₀Pd₆₀/SiO₂/Si{100} showing fitted composition profiles and particle size distributions.

Parameter	Fitted Value
E_{ion}	101.14 keV
$c_{top, core, bottom}$	0.77, 0.22, 0.36

Table 3.2 – Summary of fitted parameters as shown in figure 3.21.

The next step is to investigate the effect of particle size. While our previous samples were created by depositing ~ 1 ML material in total onto SiO₂/Si{100}, we now prepare a new Pd₆₀Au₄₀/SiO₂/Si{100} by depositing 0.2 ML Au followed by 0.3 ML Pd onto SiO₂/Si{100} at 300 K. Figure 3.22 below shows fitted composition data at 300 K. The relevant fitted parameters are given in table 3.3.

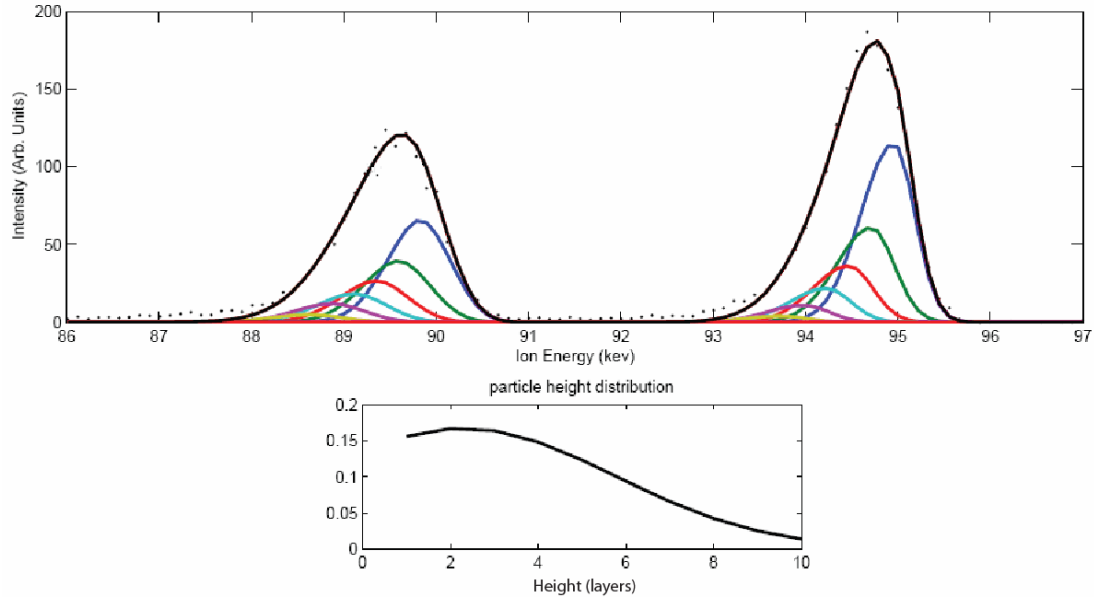


Figure 3.22 – Fitting of data from small $\text{Au}_{40}\text{Pd}_{60}/\text{SiO}_2/\text{Si}\{100\}$ particles showing fitted composition profiles and particle size distributions.

Parameter	Fitted Value
E_{ion}	101.64 keV
$c_{top, core, bottom}$	0.41, 0.41, 0.35

Table 3.3 – Summary of fitted parameters as shown in figure 3.22.

The fit shows that both the surface and the bottom levels of these smaller particles now contain less Au than the ~ 1 ML particles (see figure 3.19 and table 3.1), while the particle core is now enriched in Au compared to figure 3.19. Figure 3.23 below shows plots of the fitted surface Au composition against pre-annealing temperature for $\text{Pd}_{60}\text{Au}_{40}/\text{SiO}_2/\text{Si}\{100\}$ for samples with different metal loadings. While both data sets follow the general trend predicted by Somorjai [31], we find that the surfaces of the larger particles are generally richer in Au than predicted while the smaller particle surfaces are richer in Pd. In addition, we find that core Au composition c_{core} is generally higher for the smaller particles. A similar size-dependent surface composition has previously been observed for oxide supported PdAu alloy nanoparticles, where the surfaces of smaller particles were found to be enriched in Pd. [41]. This is an interesting point and is worth investigating further in the future.

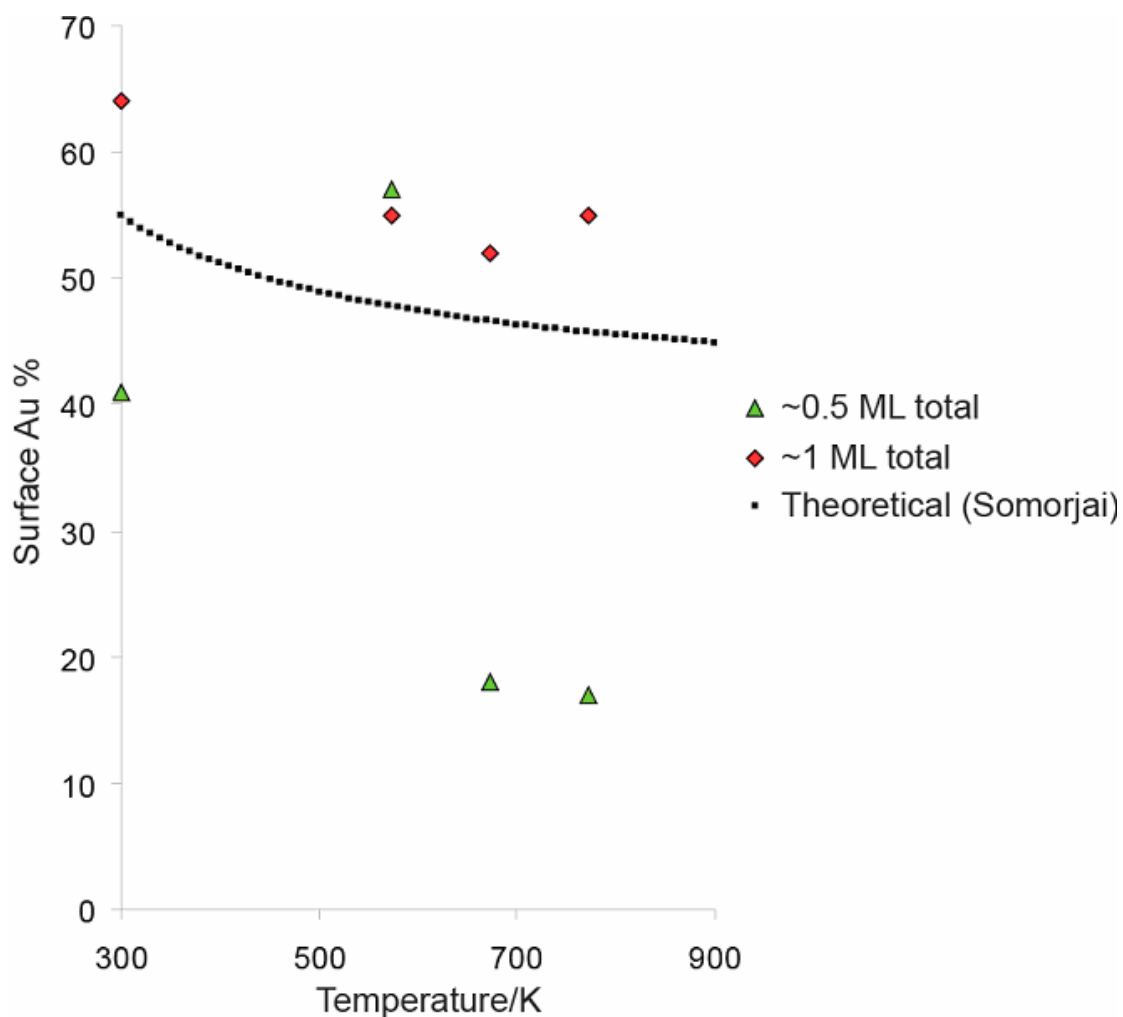


Figure 3.23 – Fitted composition data as a function of pre-annealing temperature for different metal loadings and comparison to theoretical predictions from [31].

Our analysis procedure has so far proved effective in the analysis of MEIS data from $\text{Pd}_{60}\text{Au}_{40}/\text{SiO}_2/\text{Si}\{100\}$. The theory shows that the composition of the particle surface, and hence the catalytic properties, under given conditions is strongly linked to the bulk composition. Using the STM data shown in figure 3.14 above, we will now attempt to extend our analysis to particles of differing compositions.

As we have previously discussed, the z^2 factor means that the MEIS technique is ~ 2.5 times more sensitive to Au than to Pd so we will have a better chance of obtaining good fits from Pd-rich samples than from Au-rich samples. In order to illustrate this point we present data from a $\text{Pd}_{15}\text{Au}_{85}/\text{SiO}_2/\text{Si}\{100\}$ sample created by depositing ~ 0.85 ML Au followed by ~ 0.15 ML Pd onto $\text{SiO}_2/\text{Si}\{100\}$ at 300 K.

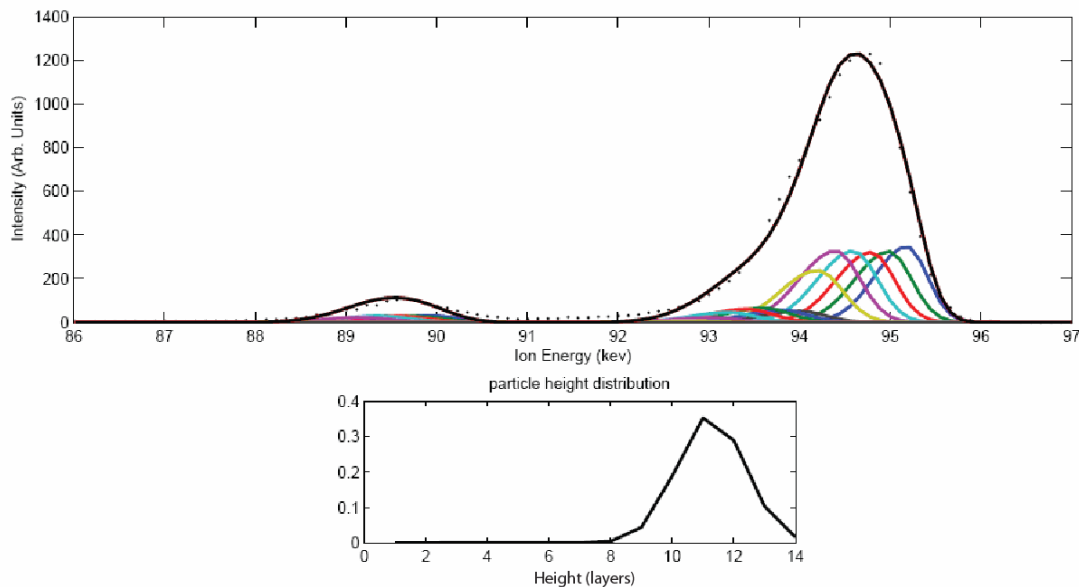


Figure 3.24 – Fitting of data from $\text{Pd}_{15}\text{Au}_{85}/\text{SiO}_2/\text{Si}\{100\}$ particles showing fitted composition profiles and particle size distributions.

In this case, the small size of the Pd peak makes it difficult to obtain consistently reliable fits, giving rise to some unusual trends. Unsurprisingly, it seems that our method is restricted to samples with a higher Pd content where both the Pd and Au features are of reasonable intensity. Fortunately, very Au-rich particles are less interesting from a catalysis perspective so that this is not a significant failing.

Figure 3.25 below shows fitted compositional data from a $\text{Pd}_{90}\text{Au}_{10}/\text{SiO}_2/\text{Si}\{100\}$ sample created by depositing ~ 0.10 ML Au followed by ~ 0.90 ML Pd onto $\text{SiO}_2/\text{Si}\{100\}$ at 300 K. The relevant fitted parameters are summarised in table 3.4.

We observe that, even when a relatively large amount of Pd has been deposited on top of Au, a significant amount of Au is still able to migrate to the particle surface at room temperature. Figure 3.26 shows plots of the fitted surface Au composition against pre-annealing temperature for $\text{Pd}_{90}\text{Au}_{10}/\text{SiO}_2/\text{Si}\{100\}$. Again, our data seem to follow the temperature-dependent trend predicted by the theory.

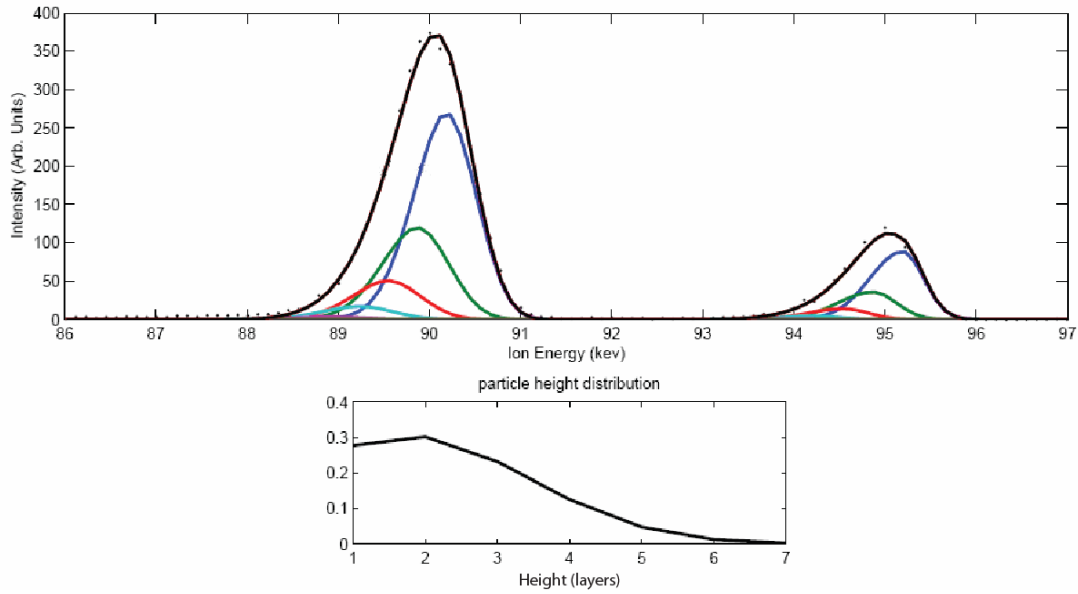


Figure 3.25 – Fitting of data from Pd₉₀Au₁₀/SiO₂/Si{100} particles showing fitted composition profiles and particle size distributions.

Parameter	Fitted Value
E_{ion}	101.73 keV
$C_{top, core, bottom}$	0.11, 0.09, 0

Table 3.4 – Summary of fitted parameters as shown in figure 3.25.

In light of our experimental observations, we propose the following growth mechanism for PdAu clusters on SiO₂/Si{100} at 300 K. First the Au is deposited, creating broad, flat-topped particles on the surface. We know from our STM measurements that Pd deposition results in mixed PdAu particles rather than a distribution of pure Pd and pure Au clusters.

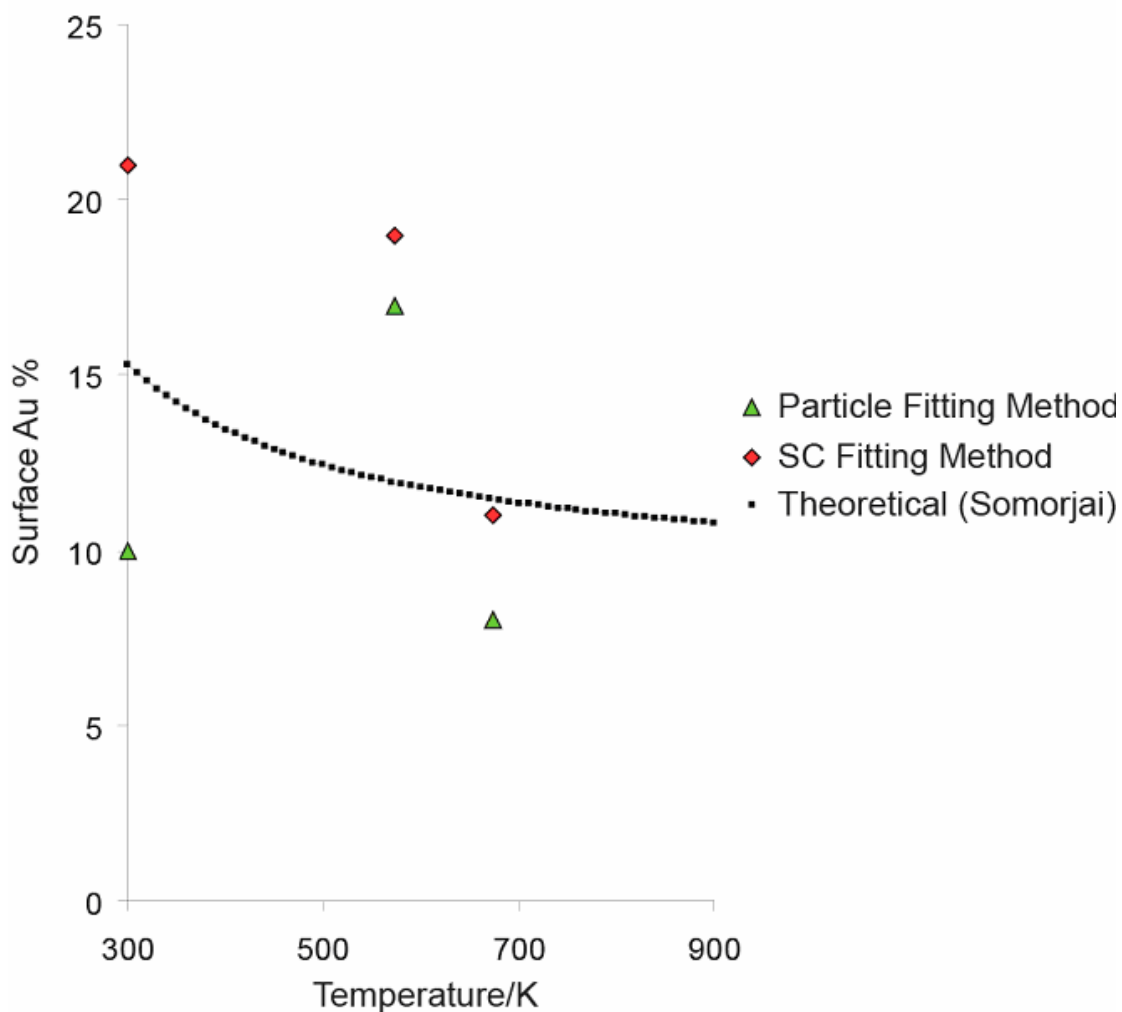


Figure 3.26 – Fitted composition data as a function of pre-annealing temperature and comparison to theoretical predictions from [31].

On the basis of Pd/Au{111} single-crystal investigations [42] we would expect the growth mechanism shown in figure 3.27, where Pd covers the existing Au clusters at 300 K and then begins to intermix on annealing.

If this were the case then we would expect our MEIS measurements to show a Pd-rich outer layer at room temperature, with c_{top} gradually increasing as the particle is annealed and the Pd and Au components intermix. In fact, we consistently observe the exact opposite of this process, even for Pd-rich samples where a relatively large amount of Pd has been deposited on top of Au.

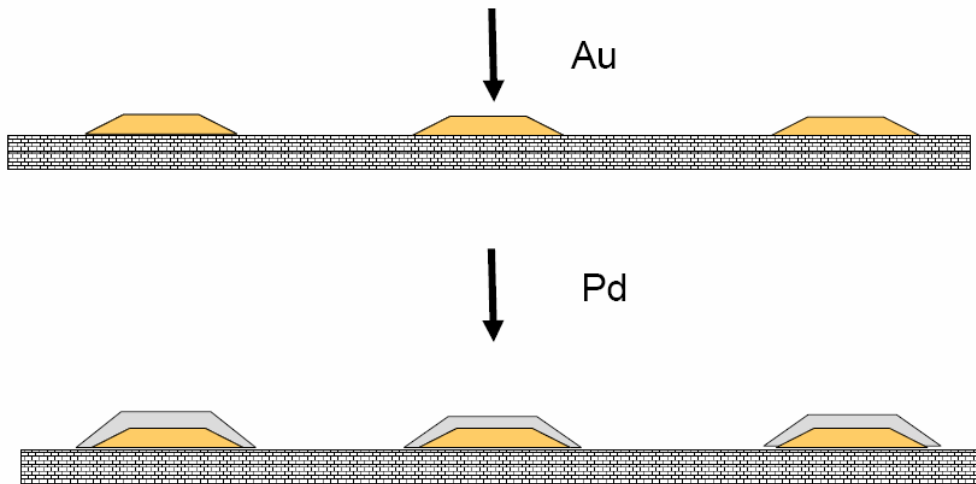


Figure 3.27 – Au-rich cores covered by a Pd-rich shell is the expected growth mechanism based on Pd/Au{111} studies [43].

We propose that the Pd does not grow on top of the existing Au clusters, but is instead encapsulated by Au, creating a core-shell type bimetallic structure with a Pd-rich inner core surrounded by an Au-rich shell at 300 K. This process accounts well for the retention of an Au-rich bottom layer, and seems to be largely independent of particle size or composition or deposition order. As the particles are annealed the Pd and Au regions intermix and the Au surface composition decreases according to Somorjai's model [31].

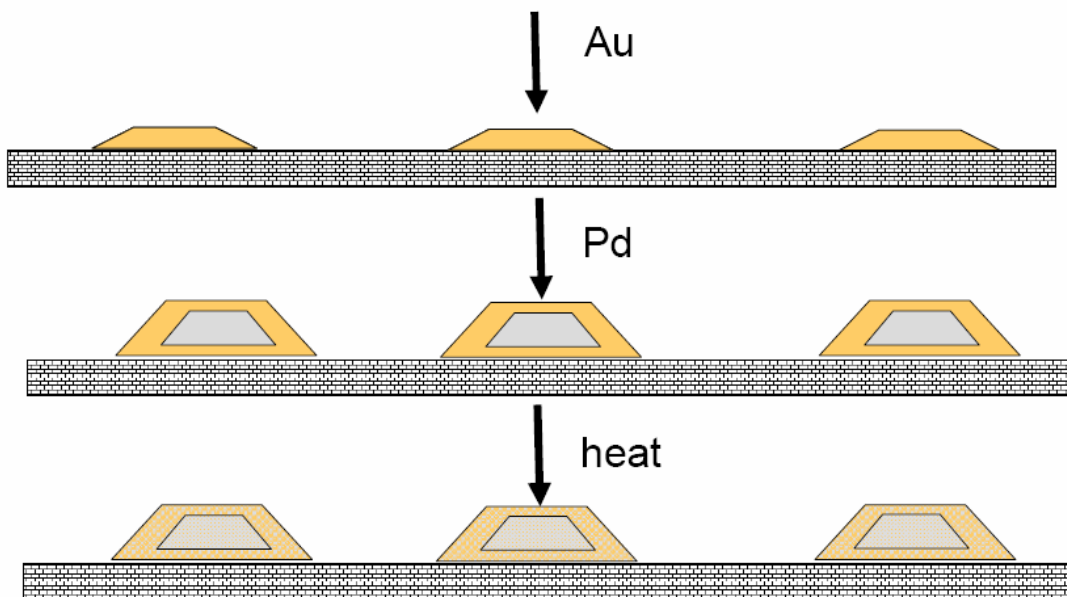


Figure 3.28 – Proposed growth mechanism based on our observations.

3.7 – TPD – CO on Pd/Au/Al₂O₃/NiAl{110}

In an attempt to confirm our findings relating to the composition of the bimetallic particle surface, we have carried out TPD experiments using CO (Aldrich 99.99%) as a probe molecule. For practical reasons, SiO₂/Si{100} was not used as a support in this case. Instead, in order to allow the sample temperature to be controlled more accurately, model PdAu nanoparticles were grown in the same way as before on a thin alumina layer on NiAl{110}. We will show later that the particle structure on Al₂O₃/NiAl{110} is indeed similar to that observed on SiO₂/Si{100}. Figure 3.29 below shows $m/z = 28$ TPD spectra for ~1 ML Pd/Al₂O₃/NiAl{110} and for Pd₇₅Au₂₅/Al₂O₃/NiAl{110} for a number of different pre-annealing treatments.

It has been shown that CO desorbs from alumina well below 300 K [43], so we can assume that the substrate does not contribute to the TPD spectra. The CO feed has been passed through a liquid nitrogen and acetone cold trap prior to dosing so we can assume that contamination due to volatile metal carbonyls is also negligible.

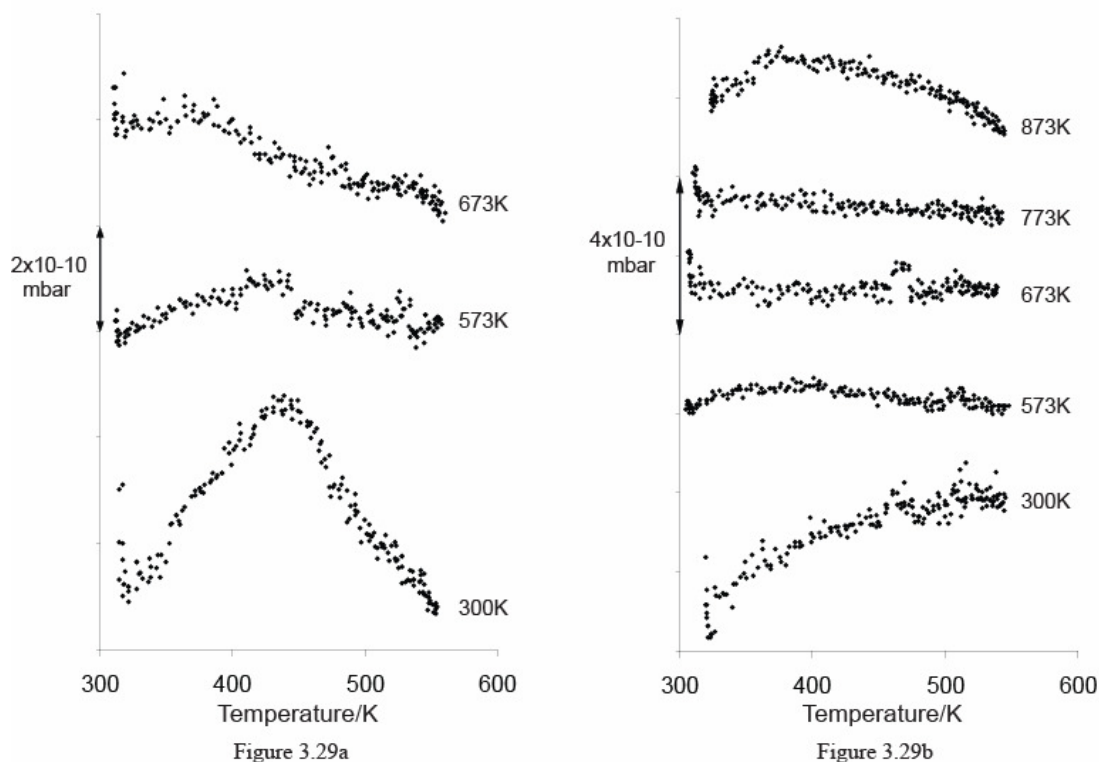


Figure 3.29 – TPD data for 30 L CO dosed at 300 K onto (a) 1 ML Pd/Al₂O₃/NiAl{110} and (b) Pd₇₅Au₂₅/Al₂O₃/NiAl{110} for a series of pre-annealing temperatures.

The TPD trace for the unannealed sample in figure 3.29a shows an initial sharp desorption at ~315 K followed by a broad desorption feature centred at ~445 K with a low T shoulder at 375 K. These are similar to features observed by Goodman and co-workers for CO on Pd/SiO₂ [44] and by Freund and co-workers on Pd/Al₂O₃ [45]. The 315 K feature is assigned to desorption of linearly bound CO from atop sites on the Pd surface while the 465 K feature is assigned to desorption of CO from 3-fold hollow sites on the {111} facets [46]. The desorption feature observed at 375 K is assigned to CO on Pd bridging sites on the {111} and {100} facets [47]. The intensities of all desorptions are significantly reduced when the sample is pre-annealed to 573 K. For samples pre-annealed to 675 K or higher, no evidence of multi-fold sites is observed and only the 315 K desorption is present. This is thought to be due to sintering of the particles leading to reduced surface area [48].

Despite a number of investigations, no evidence has been found for the adsorption of CO on planar Au surfaces at 300 K [49]. Goodman and co-workers investigated the adsorption of CO on Au nanoparticles on thin silica films [44]. No significant adsorption was observed above 200 K, indicating weak CO bonding as had been previously reported [44, 50]. We therefore assume that any desorption features observed are due to CO on Pd sites. The TPD spectra from the Pd₇₅Au₂₅/Al₂O₃/NiAl{110} bimetallic system in figure 3.29b show a low temperature desorption at ~315 K due to CO atop Pd. This feature is attenuated compared to the pure Pd case. For the 873 K pre-annealed sample only, we observe a desorption feature at ~380 K that is similar to features observed in figure 3.29a and is again assigned to CO on Pd bridging sites on the {111} and {100} facets in accordance with [47].

Although it is difficult to draw many conclusions without better quality data, the trends observed seem to fit our model for the growth of PdAu nanoparticles on SiO₂/Si{100}. It has been shown that there is a statistical distribution of multiply coordinating surface sites on the alloy surface [29]. Small concentrations of Au at the surface are enough to quench Pd₂ and Pd₃ ensembles. At low pre-annealing temperatures we form particles with a relatively Au-rich surface so that CO is able to adsorb in atop sites only. As the pre-annealing temperature is increased and Pd

migrates to the particle surface we begin to see some evidence of CO in multi-fold adsorption sites.

Goodman and co-workers investigated the adsorption of CO on 1:1 Pd:Au alloy nanoparticles on silica [44] using IRAS and TPD. For Au deposited first followed by Pd the intensity of all TPD features above 200 K were decreased compared to 1 ML Pd on SiO₂, with the emergence of a new feature at 135 K due to CO on Au. Since the TPD spectra were so similar to the pure Pd case, it was assumed that primary nucleation of Pd was taking place rather than alloy formation. Our STM and MEIS results contradict this assumption – we have presented experimental evidence for the formation of bimetallic clusters comprising a Pd-rich core surrounded by an Au-rich shell and this model appears to be reflected in our TPD data.

3.8 – Interaction With AcOH

We have shown that it is possible to use MEIS in combination with a suitable analysis procedure to obtain layer-by-layer compositional data from model bimetallic nanoparticle systems. However, while estimating the composition of clean bimetallic surfaces is a complex task, modelling the surface composition in the presence of adsorbates adds further complications.

The main goal of heterogeneous catalysis investigations using model bimetallic systems is to attempt to establish the surface composition under reaction conditions and to link the activity and selectivity with the availability of surface ensembles. However, determining the composition of the surface while under the influence of adsorbates is not trivial even on a well defined single crystal surface, despite the number of characterisation methods available.

Currently, MEIS provides one of the most successful methods for studying adsorbate-induced segregation behaviour on single crystal substrates [5, 6, 51-53]. Since the adsorbate generally consists of light atoms (compared to a typical transition metal substrate) and the adsorbate molecules do not generally occupy substrate lattice sites, they are ineffective at shadowing the substrate atoms [51]. This means that, in contrast with many other techniques, the contribution of the adsorbed molecules to the

MEIS spectrum is negligible and can be ignored when calculating the near-surface structure.

Thermodynamic considerations would suggest that segregation due to an adsorbate X at a bimetallic surface of metals A and B would be determined by the relative bonding strength of $A-X$ in comparison to $B-X$. Tomanèk [54] proposed the following modification of Somorjai's original equation [31] to account for adsorbate-induced effects:

$$\chi_B^s/\chi_A^s = \chi_B^b/\chi_A^b \exp [Q_{seg}^{chem}/RT] \quad (\text{Eqn 3.24})$$

where:

$$Q_{seg}^{chem.} = Q_{seg} + (E_A - E_B)\theta \quad (\text{Eqn 3.25})$$

Q_{seg} here is the work done exchanging a surface A atom for a bulk B atom, E_I is chemisorption energy of X on element I and θ is the fractional coverage of X . Clearly, kinetics will also play a role. Hodak et al. [55] investigated interdiffusion in Au/Ag core-shell nanoparticles, finding a diffusion constant D given by:

$$D = D_0 \exp(E_d/kT) \quad (\text{Eqn 3.26})$$

where $D_0 = 0.04 \text{ cm}^2\text{s}^{-1}$ and $E_d = 1.76 \text{ eV}$. The time, t , taken for an atom to diffuse over a distance equal to the radius, R , of the particle is given by [30]:

$$t = R^2/6D \quad (\text{Eqn 3.27})$$

This predicts that the adsorbate induced equilibrium composition can form at elevated temperatures with no diffusion limitation, but that adsorbate induced effects should never be seen at 300 K on a laboratory timescale. The fact that this supposition is contradicted by a number of experimental observations on a range of alloy surfaces suggests that a model created to describe the clean surface structure may not accurately reflect the surface structure under the influence of a reactive gas phase [5, 56-63]. The ability to obtain layer-by-layer compositional data has shown that those segregation effects that have been observed at room temperature may simply involve swapping atoms between the top few layers rather than mass diffusion of atoms from

the bulk. This would explain why such effects are regularly seen on a laboratory timescale despite kinetic arguments to the contrary.

The highly face-selective nature of segregation effects, combined with the fact that real metal surfaces will contain some irregularities means that a number of problems arise when trying to correlate results obtained on single crystal systems with those obtained on bimetallic nanoparticles. A nanoparticle modelled as a truncated octahedron displays {111} facets as well as {100} facets, which have a coordination number of 8, and other edge and corner sites of even lower coordination number as well as various step and kink defects on each of the facets. It has been shown that segregation is favoured at lower coordination sites [64], meaning that segregation effects will be enhanced at the edge and corner sites of alloy nanoclusters compared to sites on flat terraces.

Most attempts to follow segregation in bimetallic nanoparticle systems involve the use of XPS and EXAFS, which are not sufficiently accurate, or CO adsorption, which may itself induce compositional changes [30]. So far, we have chosen to study oxide-supported PdAu model particles as a model of the catalyst used in the vinyl acetate synthesis process. We will now attempt to model the behaviour of the bimetallic nanoparticle surface under the influence of acetic acid. Previous studies carried out by our group have shown that adsorption of acetic acid on Au/Pd{111} causes measurable segregation of Pd to the bimetallic surface at 300 K [5, 15]. In the first reported study of its kind, we have used MEIS experiments in combination with our own analysis model to follow the influence of adsorbed acetic acid on model PdAu bimetallic nanoparticle systems.

Figure 3.30 shows intensity vs. energy profiles for PdAu nanoparticles of different compositions on SiO₂/Si{100}. In each case, the black trace shows the data for the clean surface while the broken red trace shows the result of repeating the MEIS scan after exposing the sample to 30 L AcOH at 300 K.

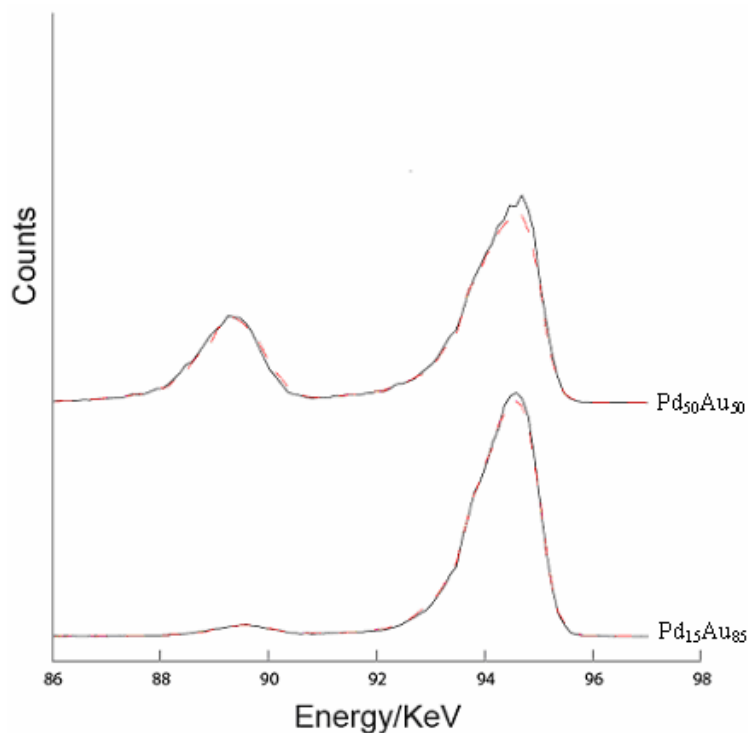


Figure 3.30 – Intensity vs. energy data for PdAu nanoparticles of various compositions on $\text{SiO}_2/\text{Si}\{100\}$ taken before and after modification with AcOH.

A brief examination of the data shows that the high energy (surface) edges of the Pd and Au peaks in the intensity vs. energy profiles are subtly but visibly changed after treatment with AcOH. In our case, we are collecting data from many layers in the particle, so that compositional changes in the very top layers are observed as a small change in the high-energy edges of the Au and Pd peaks.

For comparison, the results in figure 3.31 show similar data for ~ 4 ML Au/Pd{111} taken before and after treatment with AcOH [5]. In this case, the sample has been carefully aligned in the 3-layer geometry. The effects of segregation can be seen more clearly when we are only sampling the top 3 layers.

We have previously shown fitted compositional data for PdAu nanoparticle samples showing thermally-induced segregation. We will now use the same method to investigate adsorbate-induced segregation on similar samples.

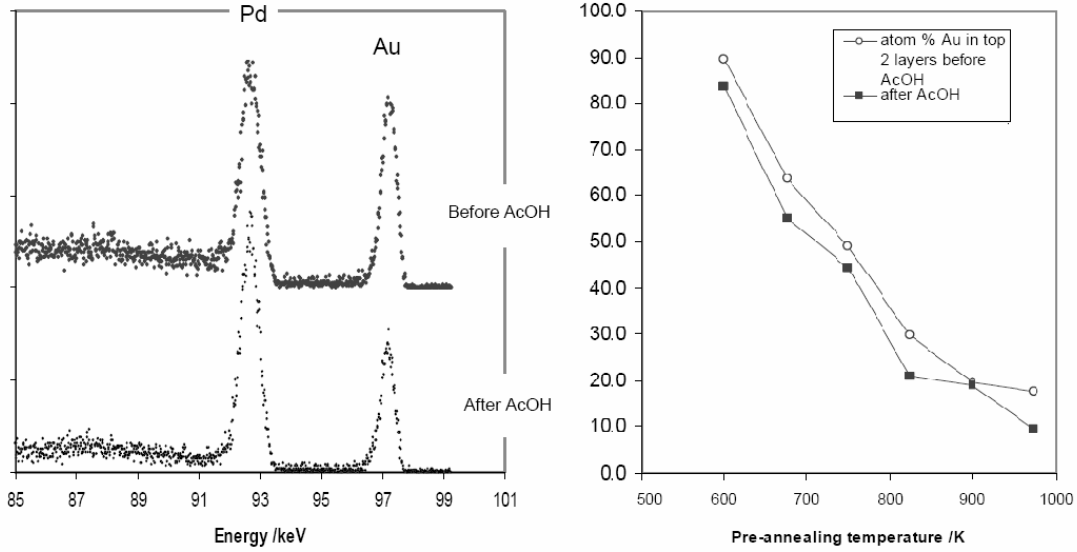


Figure 3.31 – Intensity vs. energy profiles and fitted composition data from ~4 ML Au/Pd{111} showing segregation of Pd to the bimetallic surface after treatment with AcOH [5].

Figure 3.32 below shows fitted compositional data from a Pd₅₀Au₅₀/SiO₂/Si{100} sample created by depositing ~0.50 ML Au followed by ~0.50 ML Pd onto SiO₂/Si{100} at 300 K. The relevant fitted parameters are summarised in table 3.5.

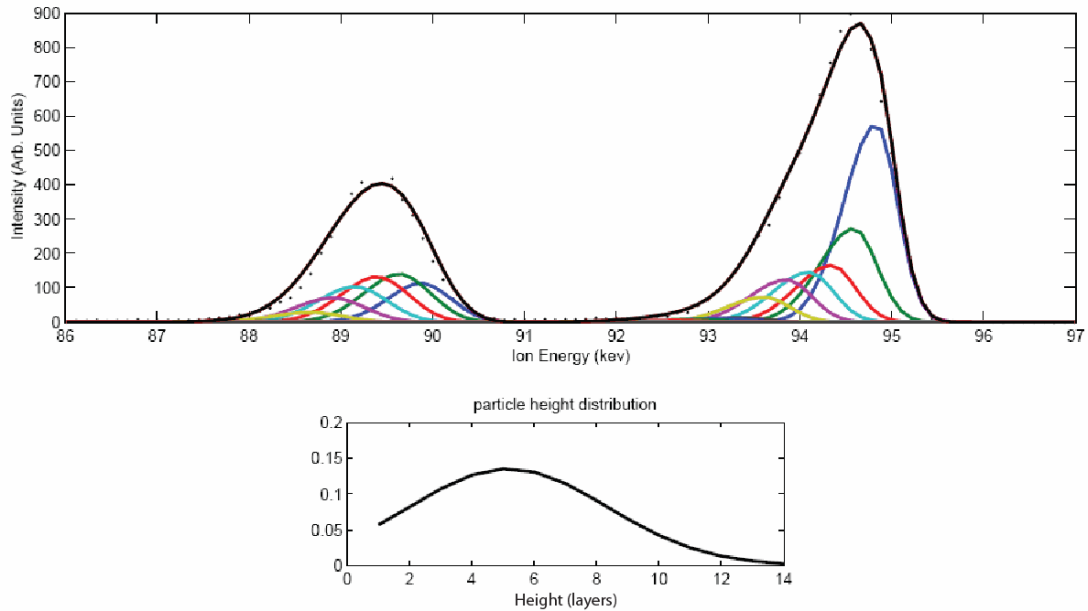


Figure 3.32 – Fitting of data from Pd₅₀Au₅₀/SiO₂/Si{100} particles showing fitted composition profiles and particle size distributions.

Parameter	Fitted Value
E_{ion}	101.30 keV
$c_{top, core, bottom}$	0.81, 0.19, 0.99

Table 3.5 – Summary of fitted parameters as shown in figure 3.32.

We can see that the surface is again Au-rich, consisting of ~81% Au.

Figure 3.33 below shows the result of modifying the sample by dosing 30 L acetic acid (AcOH) at 1×10^{-7} mbar at 300 K and repeating the MEIS scan. We can clearly see that the adsorption of acetic acid has caused measurable depletion of Au in the surface layer (~10%), while the core levels are enriched in Au. This is clear evidence for adsorbate-induced segregation of Pd to the bimetallic particle surface. The sample was discarded after taking the AcOH-treated MEIS data.

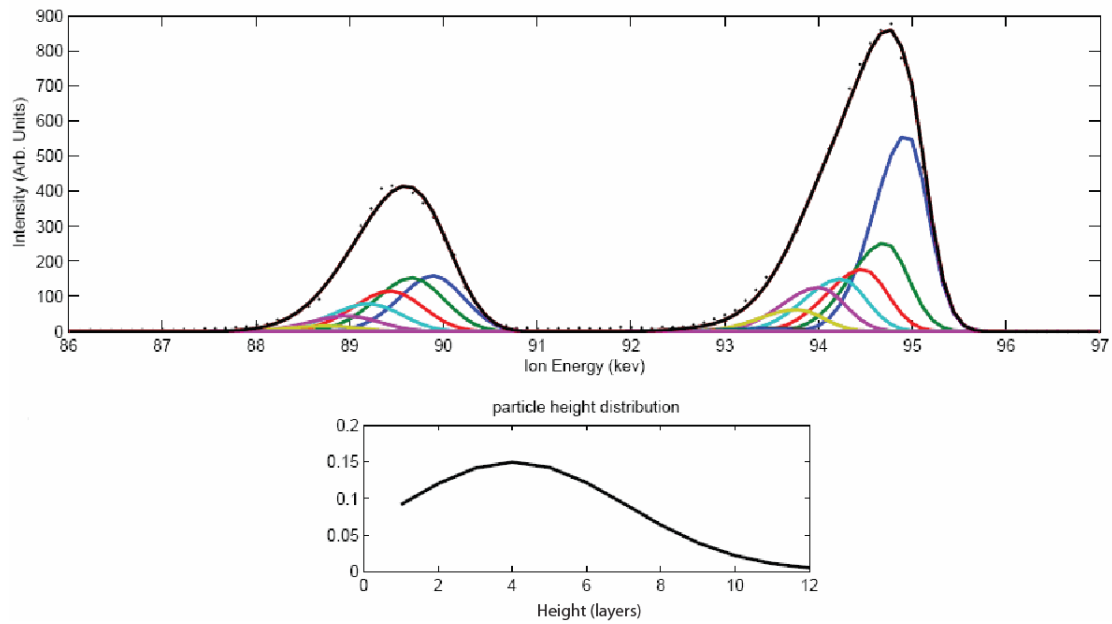


Figure 3.33 – Fitting of data from Pd₅₀Au₅₀/SiO₂/Si{100} particles after adsorption of 30 L AcOH showing fitted composition profiles and particle size distributions.

Parameter	Fitted Value
E_{ion}	101.53 keV
$c_{top, core, bottom}$	0.71, 0.22, 0.99

Table 3.6 – Summary of fitted parameters as shown in figure 3.33.

Figure 3.34 and table 3.7 below show fitted compositional data from a similar Pd₅₀Au₅₀/SiO₂/Si{100} sample that has been annealed to 573 K. c_{top} for this sample is lower than for the unannealed sample in figure 3.30, as expected.

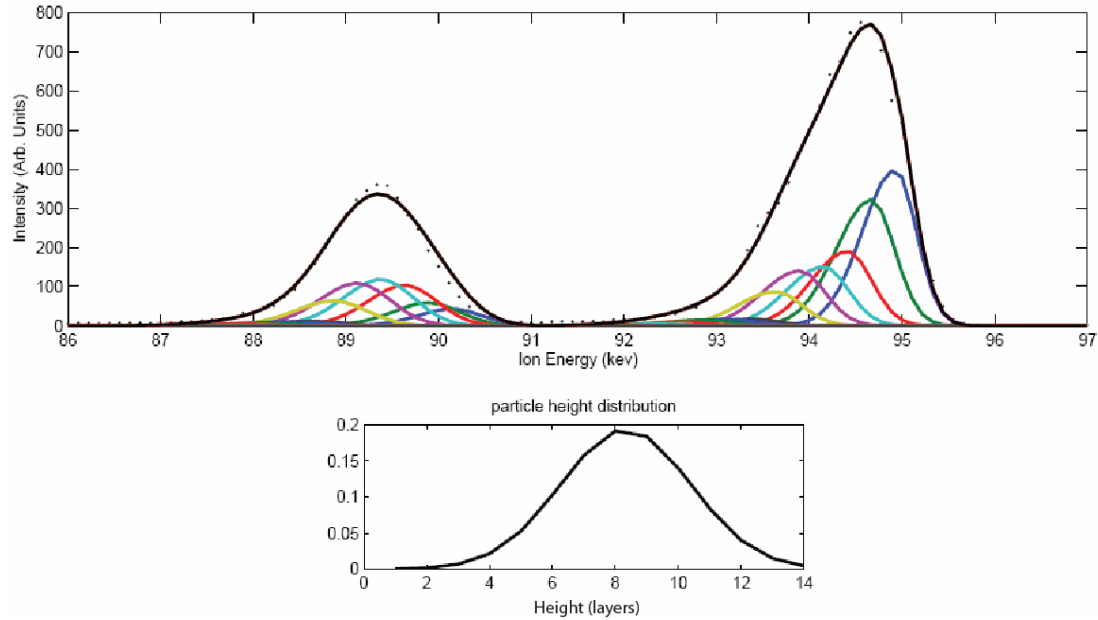


Figure 3.34 – Fitting of data from Pd₅₀Au₅₀/SiO₂/Si{100} particles after annealing to 573 K showing fitted composition profiles and particle size distributions.

Parameter	Fitted Value
E_{ion}	101.17 keV
$c_{top, core, bottom}$	0.77, 0.31, 0.55

Table 3.7 – Summary of fitted parameters as shown in figure 3.34.

This sample was then modified by dosing 30 L acetic acid (AcOH) at 1×10^{-7} mbar at 300 K and the MEIS scan repeated. Figure 3.35 shows the fitted compositional data from the same sample after treatment with AcOH. The relevant fitted parameters are summarised in table 3.8. In this case, we see that the surface Au composition is reduced by ~8% after treatment with AcOH, while the c_{core} is again slightly increased.

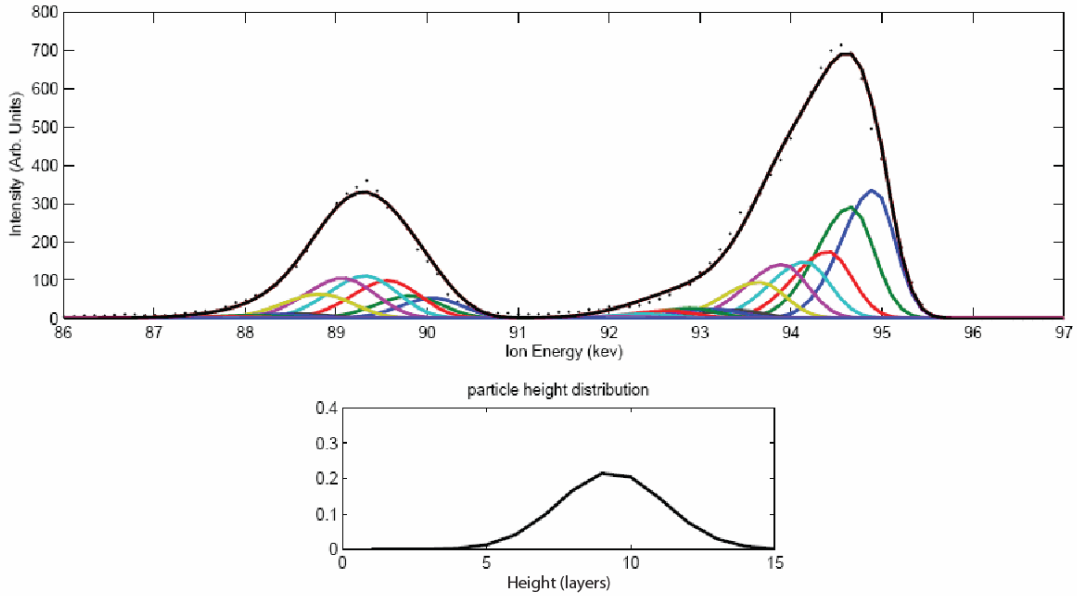


Figure 3.35 – Fitting of data from Pd₅₀Au₅₀/SiO₂/Si{100} particles after annealing to 573 K and then treating with AcOH at 300 K showing fitted composition profiles and particle size distributions.

Parameter	Fitted Value
E_{ion}	101.24 keV
$c_{top, core, bottom}$	0.69, 0.32, 0.75

Table 3.8 – Summary of fitted parameters as shown in figure 3.35.

While we have shown that our analysis method does allow us to obtain reliable composition fits for intermediate Pd compositions of ~30-75% Pd, where both the Pd and the Au peaks are of sufficient intensity, this is not generally the case. As has been mentioned previously, we are not able to obtain reliable fits for Au-rich systems, as it is difficult to fit the small Pd features. As an example, Figure 3.36 below shows the fitted compositional data from Pd₂₀Au₈₀/SiO₂/Si{100} sample that has been annealed to 673 K.

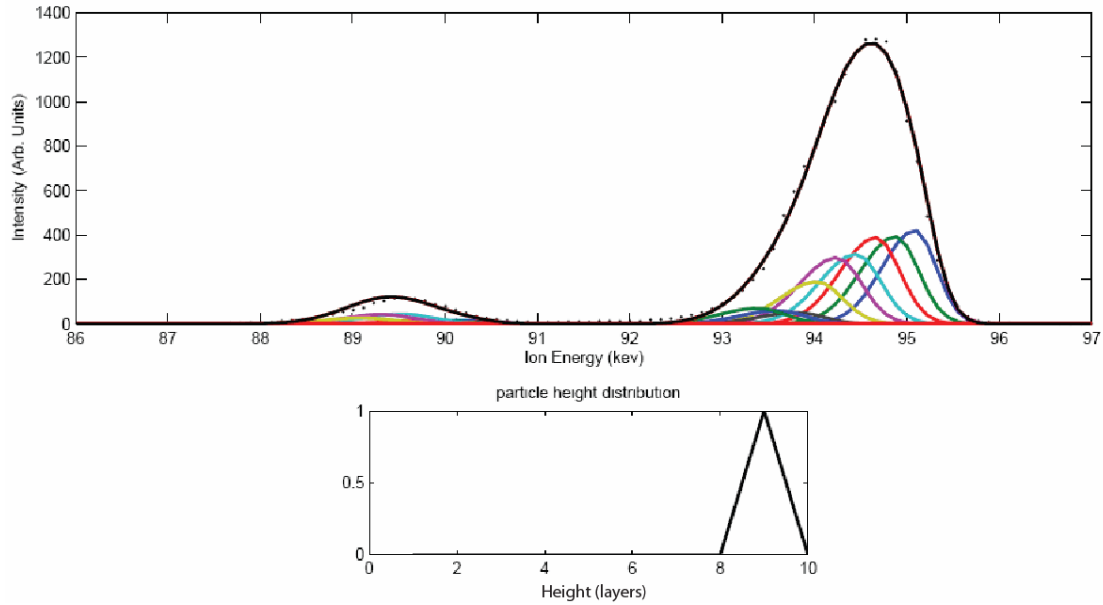


Figure 3.36 – Fitting of data from Pd₂₀Au₈₀/SiO₂/Si{100} particles after annealing to 673 K showing fitted composition profiles and particle size distributions.

Parameter	Fitted Value
E_{ion}	95.09 keV
$c_{top, core, bottom}$	0.92, 0.72, 0.99

Table 3.9 – Summary of fitted parameters as shown in figure 3.36.

Figure 3.37 and table 3.10 below shows the fitted compositional data from the same sample after treatment with 30 L AcOH at 300 K. In this case the small (2%) change in c_{core} after dosing AcOH can be assumed to fall within the error margins of the fitting procedure and it is difficult, and probably not entirely appropriate, to argue that we have observed adsorbate-induced segregation in this case. This is not as serious a problem for Pd-rich particles, since the MEIS technique is ~2.5 times more sensitive to Au than to Pd.

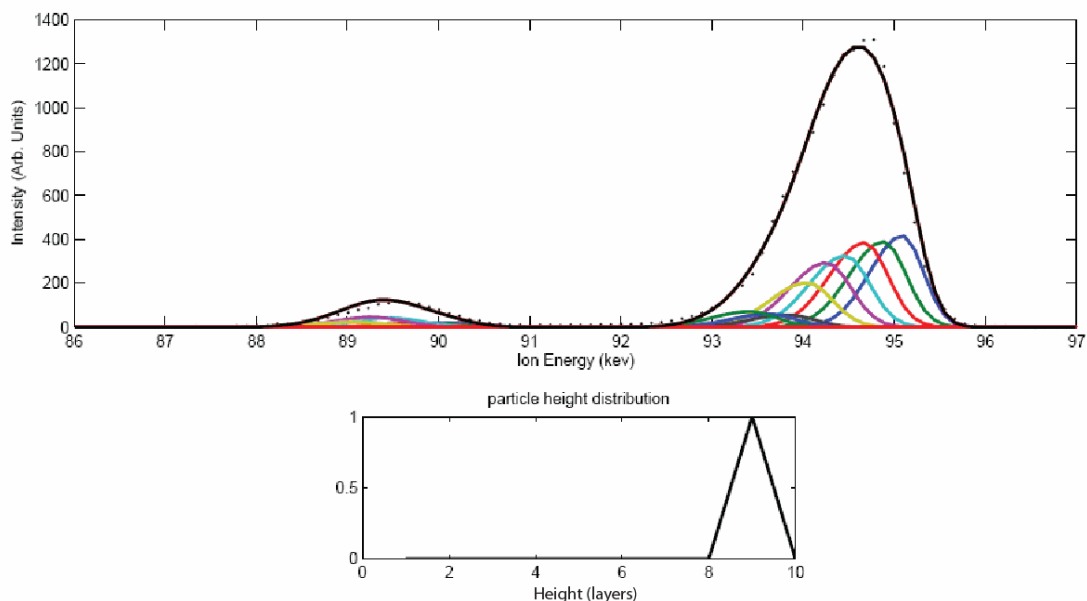


Figure 3.37 – Fitting of data from Pd₂₀Au₈₀/SiO₂/Si{100} particles after annealing to 673 K and then dosing 30 L AcOH at 300 K showing fitted composition profiles and particle size distributions.

Parameter	Fitted Value
E_{ion}	95.09 keV
$C_{top, core, bottom}$	0.90, 0.72, 0.99

Table 3.10 – Summary of fitted parameters as shown in figure 3.37.

Having shown that we can observe adsorbate-induced segregation due to AcOH using MEIS we will now attempt to use a combination of MEIS and TPD experiments to show the effect of heating AcOH on the particle surface. For practical reasons, we have chosen to carry out the next set of experiments using a thin layer of alumina grown on NiAl{110} as our substrate rather than SiO₂/Si{100} since the use of a conducting substrate will allow more accurate control of the sample temperature. Figure 3.38 below shows fitted composition data from a Pd₇₀Au₃₀/Al₂O₃/NiAl{110} sample created by depositing 0.30 ML Au followed by 0.70 ML Pd onto Al₂O₃/NiAl{110} at 300 K and then flash annealing to 573 K. The relevant fitted parameters are summarised in table 3.11.

We observe that the composition profile and size distribution for PdAu particles on Al₂O₃/NiAl{110} are similar to those observed previously on SiO₂/Si{100}. Again,

the particle base is enriched in Au as expected, while the surface composition of 49% Au is higher than the 37% predicted by Somorjai [31].

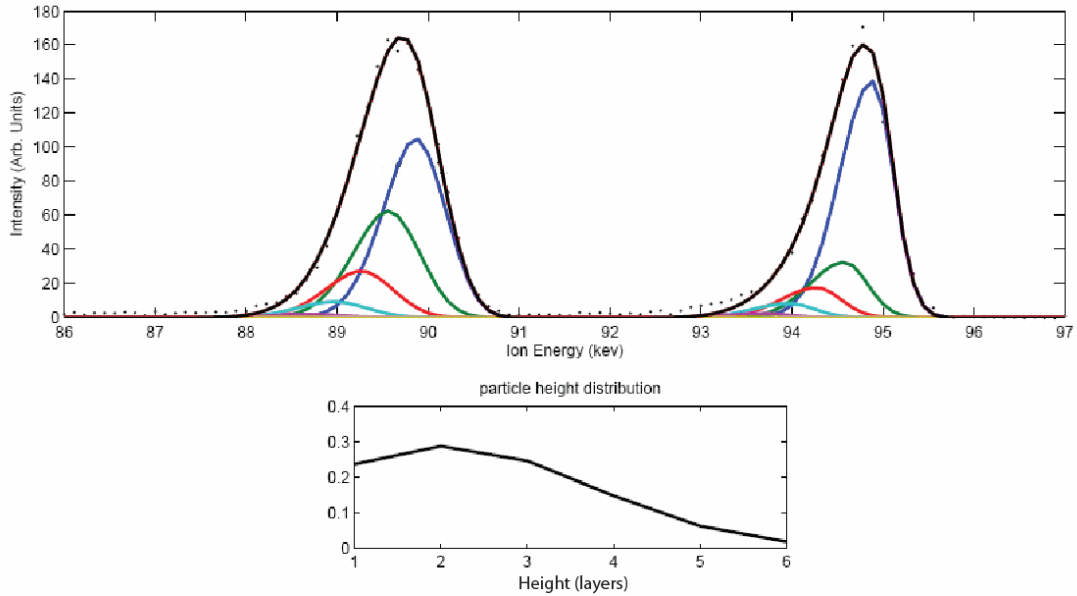


Figure 3.38 – Fitting of data from Pd₇₀Au₃₀/Al₂O₃/NiAl{110} particles showing fitted composition profiles and particle size distributions.

Parameter	Fitted Value
E_{ion}	101.43 keV
$c_{top, core, bottom}$	0.49, 0.11, 0.34

Table 3.11 – Summary of fitted parameters as shown in figure 3.38.

The sample was then modified by dosing 30 L acetic acid at 1×10^{-7} mbar at 300 K and the MEIS scan repeated. Figure 3.39 shows the fitted composition data after treatment with AcOH. The relevant fitted parameters are summarised in table 3.12. As before, we see that the surface Au concentration c_{top} is depleted by ~8% after modification with AcOH. At the same time, the particle base is enriched in Au.

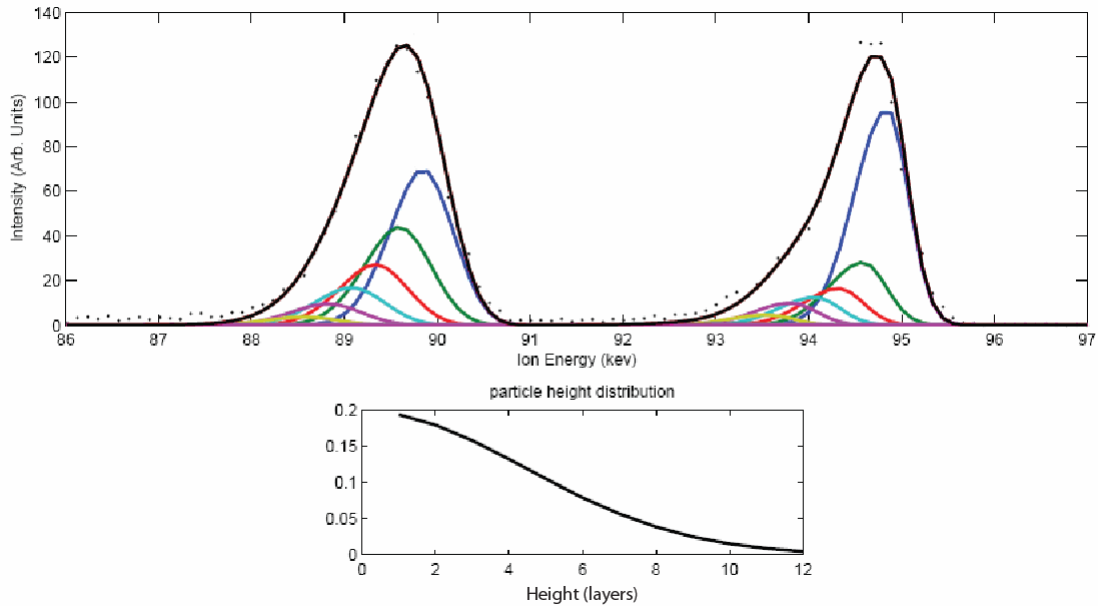


Figure 3.39 – Fitting of data from Pd₇₀Au₃₀/Al₂O₃/NiAl{110} particles after dosing 30 L AcOH showing fitted composition profiles and particle size distributions.

Parameter	Fitted Value
E_{ion}	101.39 keV
$c_{top, core, bottom}$	0.41, 0.09, 0.71

Table 3.12 – Summary of fitted parameters as shown in figure 3.39.

Next, the sample is annealed stepwise up to 430 K following adsorption of acetic acid. MEIS data were taken at a series of annealing temperatures and the resulting fitted c_{top} composition data is plotted as a function of temperature as shown in figure 3.40. The black point shows the original clean-surface composition from figure 3.38 as a reference point. It is difficult to tell whether the adsorbate-induced segregation effect is significantly enhanced by heating the acetic acid on the surface. Following the 450 K anneal, the AcOH is expected to decompose and desorb [65] and the particle surface is now restored to close to its original unmodified state.

In a previous MEIS study of the effects of AcOH on 3-4 ML Au on Pd{111} at 300 K, it was found that the surface Au composition was decreased by ~10% after dosing AcOH, regardless of the starting composition [5, 15]. The fact that we see similar figures here suggests that we can indeed observe evidence of adsorbate-induced segregation of Pd to the nanoparticle surface at 300 K for certain compositions.

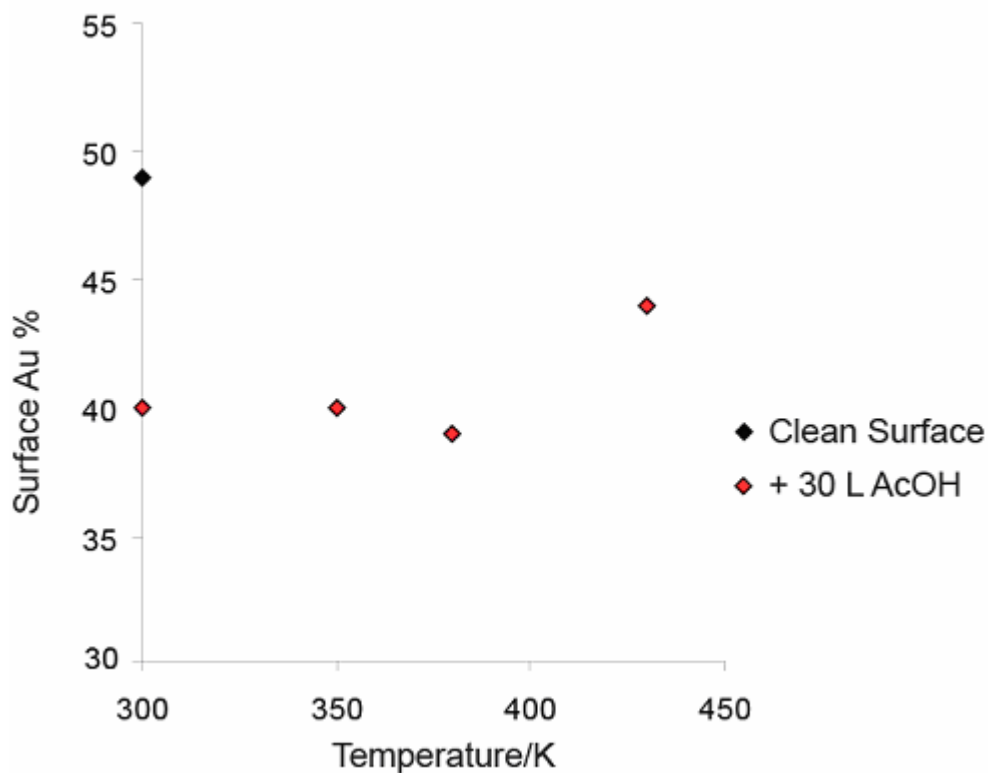


Figure 3.40 – Fitted composition data for AcOH on Pd₇₀Au₃₀/Al₂O₃/NiAl{110} as a function of pre-annealing temperature.

As we have previously discussed, kinetic considerations imply that adsorbate-induced segregation should involve mass diffusion of atoms from the bulk and, as such, should never be observed on a laboratory timescale at 300 K [30]. However, layer-by-layer compositional data obtained by MEIS suggest that segregation can be observed at 300 K [5, 6, 15, 51-53], and that such a process may simply involve the swapping of atoms between the top few layers. The observation that the decrease in the surface Au% for Au/Pd{111} after dosing AcOH is independent of starting composition suggests that segregation takes place mainly at defect sites or step edges on the {111} surface where the near-surface layers are exposed [5]. If this were the case, then we would expect the adsorbate-induced segregation to be enhanced on a defect-rich sample such as a nanoparticle surface. However, we find that this is not true in our case and this may be due to the structure of our particles.

All of our experimental evidence has so far suggested that we are forming broad particles with a height of only a few atomic layers. If this is the case, then the

behaviour of the edge sites is not as significant as would be expected from hemispherical or cuboctahedral particles, for example. This is why we are able to use single-crystal-like structural models to represent our surface to a reasonable approximation as in figure 3.18c. In this case, we would expect adsorbate-induced segregation to largely follow a similar mechanism in our system to that proposed previously for {111} PdAu alloy surfaces [5, 15].

We have investigated the mechanism of acetic acid decomposition on PdAu particles by carrying out TPD experiments on AcOH adsorbed on Pd/Al₂O₃/NiAl{110}, Au/Al₂O₃/NiAl{110} and PdAu/Al₂O₃/NiAl{110} particles created by deposition of Au and Pd onto Al₂O₃/NiAl{110} at 300 K as before.

Figure 3.41 below shows TPD data for 30 L AcOH adsorbed on a blank sample consisting of a thin alumina layer on NiAl{110}. Data for masses 2 (H₂, 3.41a), 18 (H₂O, 3.41b), 28 (CO, 3.41c) and 44 (CO₂, 3.41d) are shown.

The H₂ data in figure 3.41a show a small desorption at 331 K, The H₂O data in figure 3.41b show a small desorption at 331 K, followed by a second broader feature at 497 K. The CO data in figure 3.41c show a small initial desorption at 346 K. The CO₂ data in figure 3.41d show a sharp initial desorption at 331 K, followed by a second broader feature at 500 K.

A second blank experiment was carried out on ~0.3 ML Au/alumina/NiAl{110}, but no significant changes were observed.

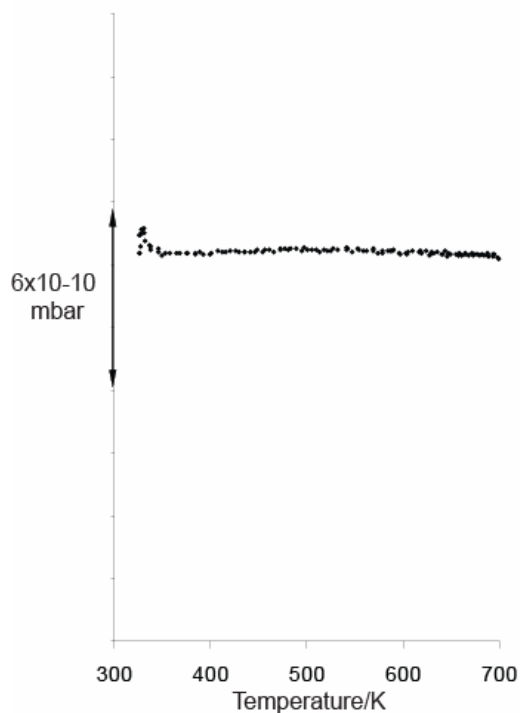


Figure 3.41a

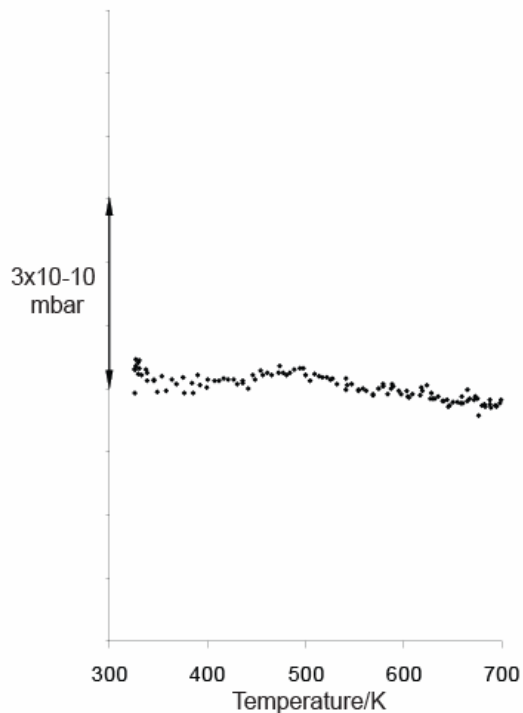


Figure 3.41b

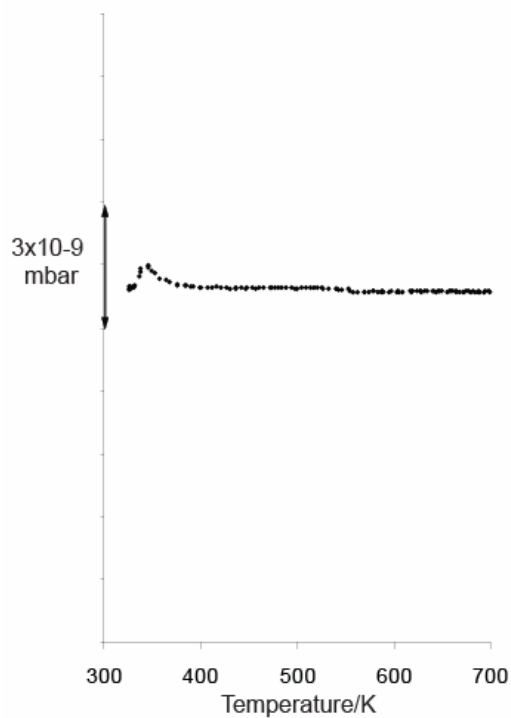


Figure 3.41c

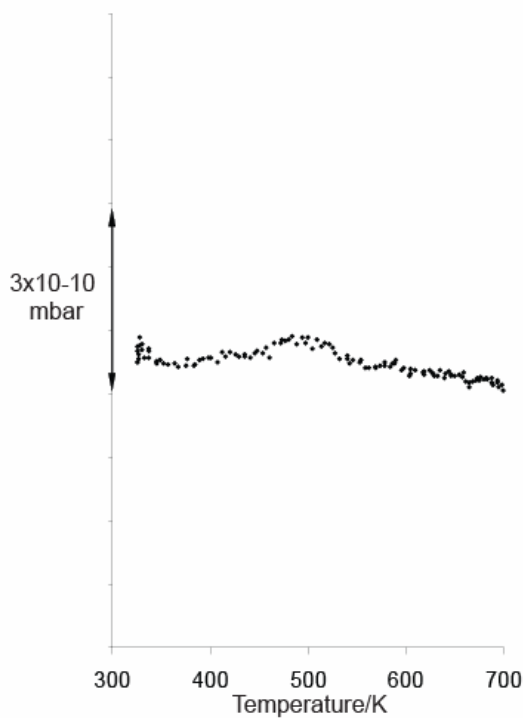


Figure 3.41d

Figure 3.41 – (a) H₂, (b) H₂O, (c) CO and (d) CO₂ TPD data for 30 L AcOH dosed onto alumina/NiAl{110} at 300 K.

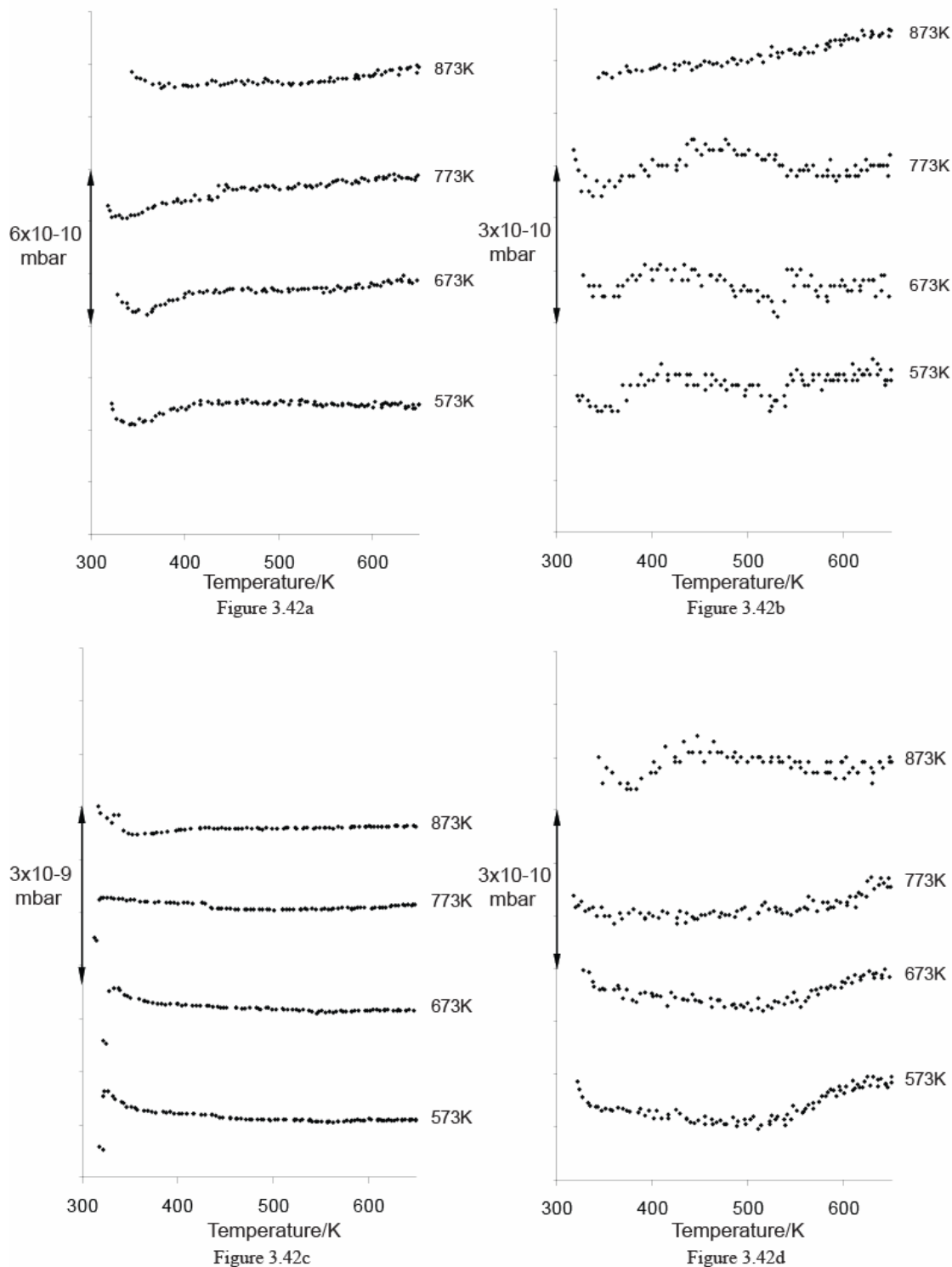


Figure 3.42 – (a) H₂, (b) H₂O, (c) CO and (d) CO₂ TPD data for 30 L AcOH dosed onto ~ 0.3 ML Pd/alumina/NiAl{110} at 300 K.

Figure 3.42 above shows TPD data for 30 L AcOH adsorbed on ~0.3 ML Pd deposited on a thin alumina layer on NiAl{110} for a series of increasing pre-annealing temperatures.

The H₂ data in figure 3.42a show little significant desorption.

The H₂O data in figure 3.42b show a broad desorption feature with an onset at ~360 K and maxima at ~430 K and ~550 K for the 573 K and 673 K annealed samples. For the 773 K annealed sample a single broad feature is observed with a maximum at 480 K. No significant H₂O desorption is observed after the highest annealing treatment.

The CO data in figure 3.42c show an initial broad desorption peaking at around ~330 K with shoulders at ~350 K and ~440 K and a further broad high T feature at ~660 K for all but the 873 K annealed sample, which shows a sharper initial desorption peaking at 317 K followed by a broad feature with an onset at ~360 K and maxima at ~440 and 660 K.

The CO₂ data in 3.42d show a single broad feature with a maximum at ~640 K for the 573-773 K pre-annealed samples. For the 873 K annealed sample only, a desorption maximum is observed at ~440 K that coincides with a similar feature in the CO data from figure 3.42c.

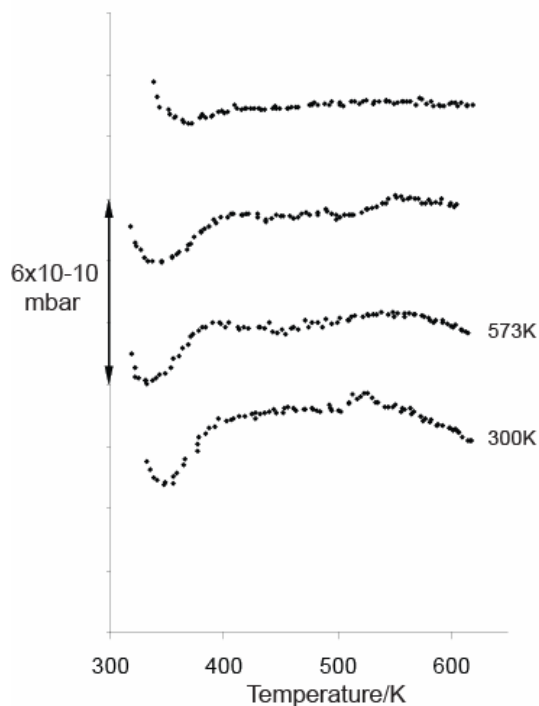


Figure 3.43a

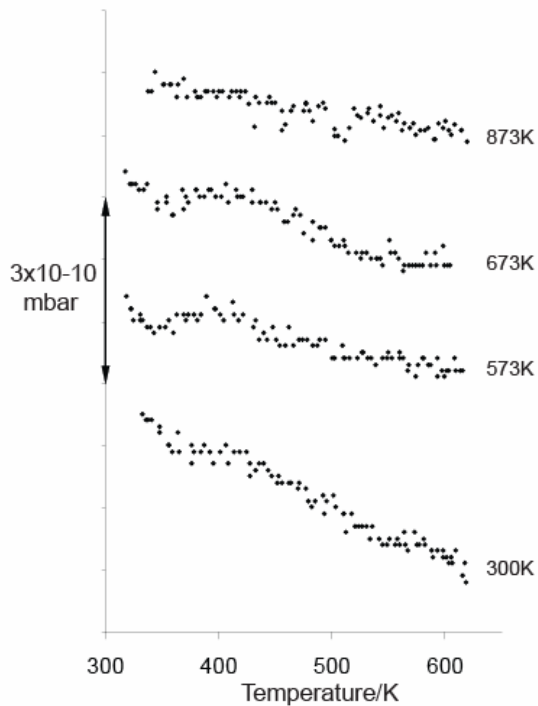


Figure 3.43b

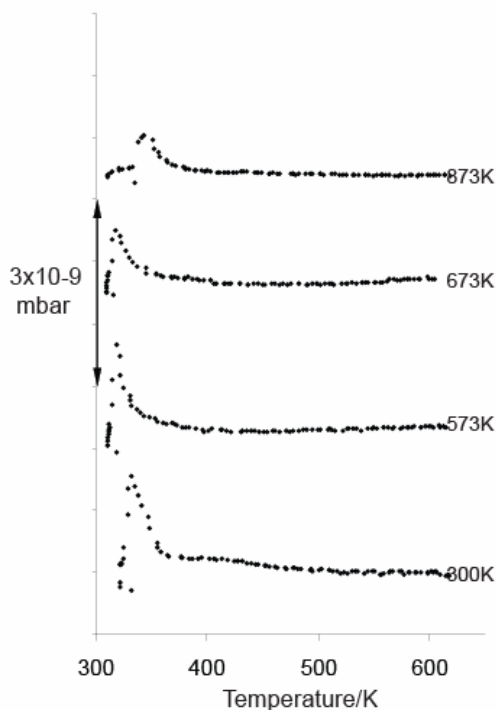


Figure 3.43c

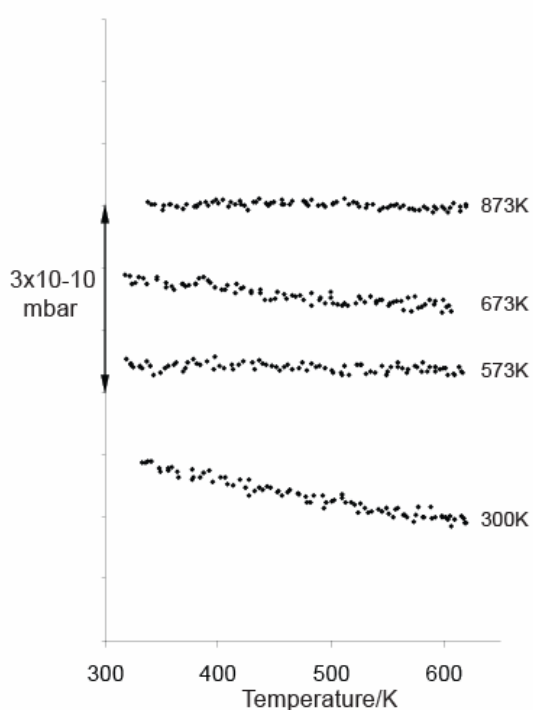


Figure 3.43d

Figure 3.43 – (a) H₂, (b) H₂O, (c) CO and (d) CO₂ TPD data for 30 L AcOH dosed onto Pd₈₀Au₂₀/alumina/NiAl{110} (0.5 ML total metal loading) at 300 K.

Figure 3.43 above shows TPD data for 30 L AcOH adsorbed on Pd₈₀Au₂₀/alumina/NiAl{110} particles created by depositing ~0.1 ML Au followed by

~0.4 ML Pd onto alumina/NiAl{110} at 300 K for a series of increasing pre-annealing temperatures.

The H₂ data is shown in figure 3.43a. For all but the highest pre-annealing temperature, a broad desorption feature is observed between ~360 and 660 K with maxima at ~400 and ~550 K. The intensity of this feature decreases with increasing pre-annealing temperature until it is no longer visible after an 873 K anneal.

The H₂O data in figure 3.43b shows a small feature at 400 K for all but the highest pre-annealing temperature. This coincides with similar features in the H₂ data in figure 40.1 but is of lower intensity.

The CO data in figure 3.43c show an initial desorption peaking at around ~320 K with a sharp onset and an exponentially decreasing tail. The intensity of this feature decreases and T_{max} increases as the pre-annealing temperature is increased. For all but the highest pre-annealing temperature a second small peak is observed at ~610 K.

The CO₂ data in figure 3.43d show little significant CO₂ desorption from any of the samples.

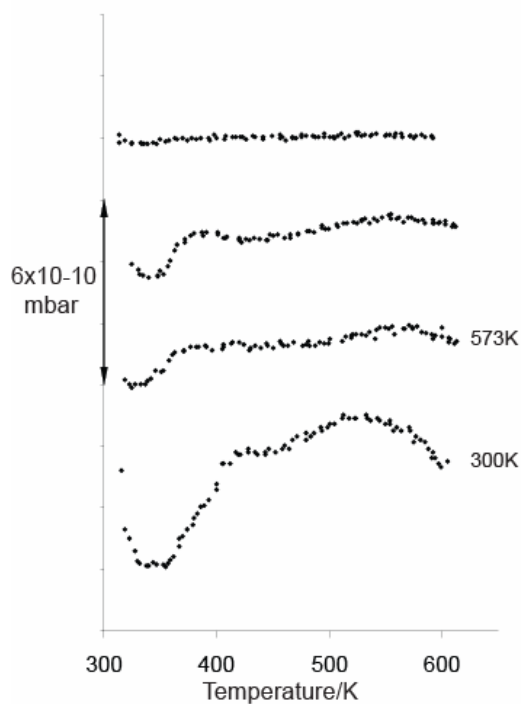


Figure 3.44a

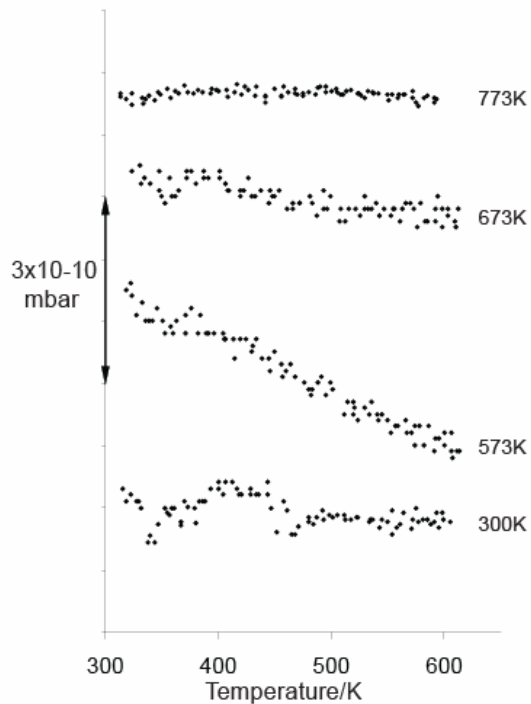


Figure 3.44b

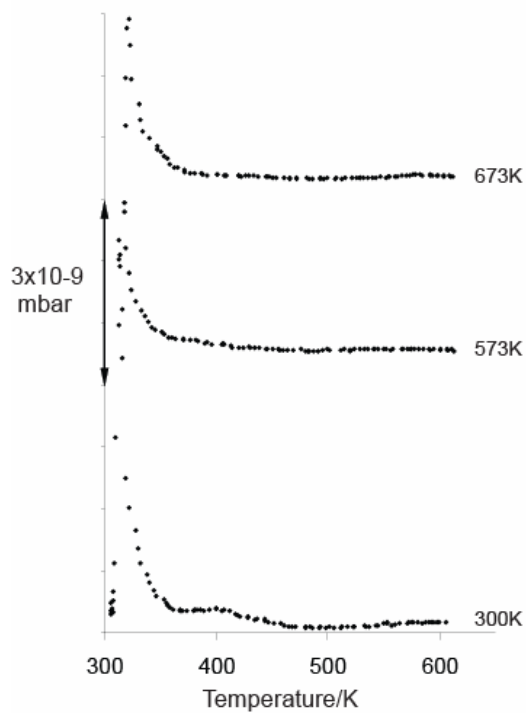


Figure 3.44c

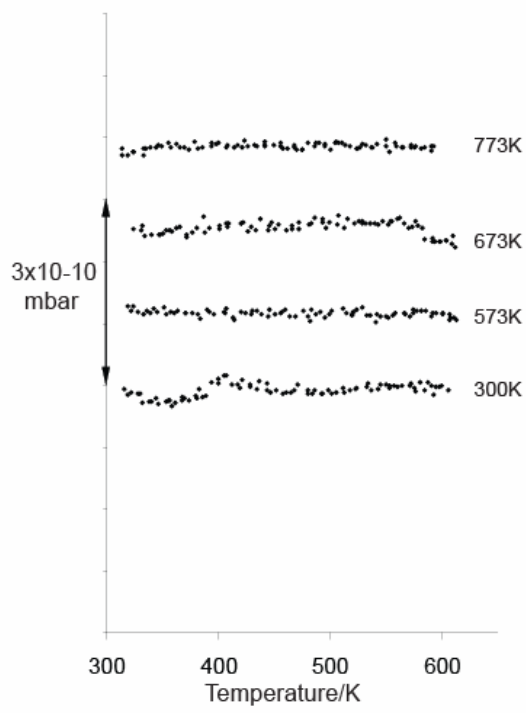


Figure 3.44d

Figure 3.44 – (a) H_2 , (b) H_2O , (c) CO and (d) CO_2 TPD data for 30 L AcOH dosed onto $Pd_{50}Au_{50}/alumina/NiAl\{110\}$ (0.5 ML total metal loading) at 300 K.

Figure 3.44 above shows TPD data for 30 L AcOH adsorbed on $Pd_{50}Au_{50}/alumina/NiAl\{110\}$ particles created by depositing ~ 0.25 ML Au followed

by ~0.25 ML Pd onto alumina/NiAl{110} at 300 K for a series of increasing pre-annealing temperatures.

The H₂ data in figure 3.44a show a broad desorption feature between 350 and 670 K with maxima at ~400 and ~550 K. The intensity of this feature decreases with increasing pre-annealing temperature until it is no longer visible after a 773 K anneal.

The H₂O data is shown in figure 3.44b. For the unannealed sample only we observe a relatively broad desorption feature centred at ~440 K. Few significant features for the higher pre-annealing temperature samples.

The CO data in figure 3.44c show a desorption peaking at around ~320 K with a sharp onset and an exponentially decreasing tail with a FWHM of around 10-12 K. The intensity of this feature decreases as the pre-annealing temperature is increased. For the unannealed sample only, a second lower intensity feature is visible at ~410 K.

The CO₂ data is shown in figure 3.44d. For the unannealed sample only, a small feature is observed at ~410 K. This coincides with the feature observed in the CO data and disappears after pre-annealing the sample. There is little significant evidence for CO₂ desorption from the pre-annealed samples.

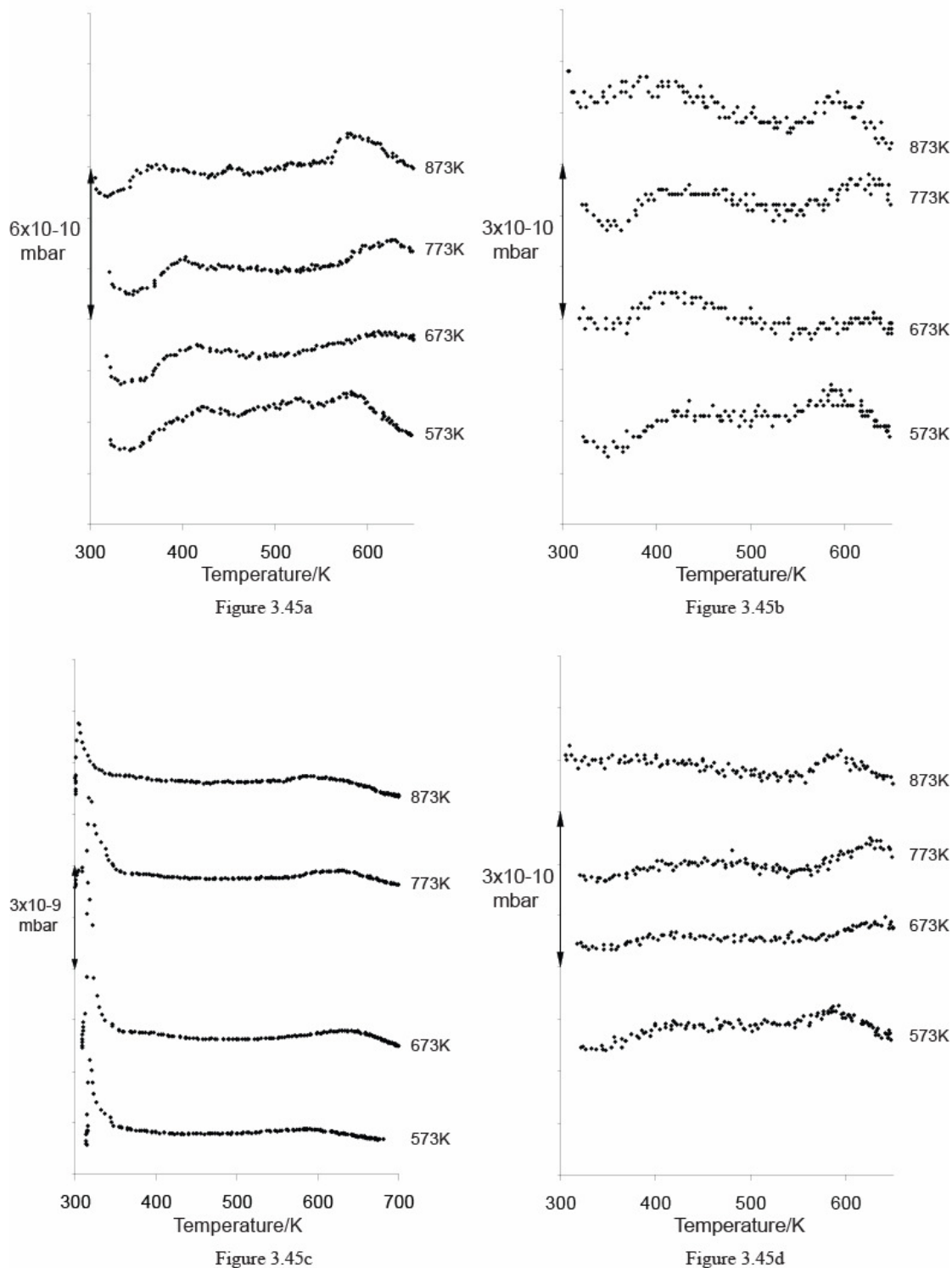


Figure 3.45 – (a) H₂, (b) H₂O, (c) CO and (d) CO₂ TPD data for 30 L AcOH dosed onto Pd₅₀Au₅₀/alumina/NiAl{110} (1 ML total metal loading) at 300 K.

Figure 3.45 above shows TPD data for 30 L AcOH adsorbed on Pd₅₀Au₅₀/alumina/NiAl{110} particles created by depositing ~0.5 ML Au followed by

~0.5 ML Pd onto alumina/NiAl{110} at 300 K for a series of increasing pre-annealing temperatures.

The H₂ data in figure 3.45a show a broad feature with an onset at ~360 K, decreasing to ~340 K for the highest pre-annealing temperature. This broad feature decreases in intensity with increasing annealing temperature and usually displays a pair of maxima. The first is observed at ~430 K for the lowest pre-annealing temperature and shifts gradually to ~370 K for the highest pre-annealing temperature. The second maximum appears at ~590 K for the lowest and highest pre-annealing temperatures and at ~625 K for the intermediate pre-annealing temperatures. For the highest pre-anneal only, a third small feature is visible at ~450 K.

The H₂O data in figure 3.45b show a series of broad, low intensity features that coincide exactly with features observed in the corresponding H₂ spectra, except for the highest pre-annealing temperature, where there is no H₂O peak that coincides with the H₂ desorption feature observed at ~450 K.

The CO data in figure 3.45c show an initial desorption at ~315 K with a high temperature shoulder at ~340 K. A second high temperature feature coincides with peaks observed in the CO₂ spectra in figure 3.45d.

For all but the highest annealing treatment, the CO₂ data in figure 3.45d show a broad desorption feature with an onset at ~360 K with a first maximum appearing at ~420 K and a second that shifts from ~580 K to ~640 K with increasing annealing temperature. For the 873 K annealed sample, this broad feature does not appear and only a single CO₂ desorption at ~595 K is observed.

Like the CO/PdAu/alumina/NiAl{110} TPDs in figure 3.29 above, these are complicated experiments and the desorption yields are small so it is difficult to draw many conclusions here without better quality data. It is more appropriate to give a full discussion of the behaviour of adsorbed acetate and related species on Pd, Au and PdAu alloy surfaces in Chapter 4, which deals with TPD and RAIRS measurements on potassium acetate (AcOK) on Au/Pd{111}, but the relevant points will be summarised here.

It should be noted that, at the time of writing, no evidence is available for the adsorption of acetic acid on Au surfaces at 300 K, so we assumed that AcOH adsorbs on Pd sites that are modified by the presence of Au.

We can assume that adsorption of CO₂ from the residual background gases is negligible so that any CO₂ desorptions observed will be mainly due to decomposition of surface species derived from adsorbed acetic acid. While some adsorption of CO and H₂O from the background gases is to be expected on the pure Pd particles, our CO TPD data in figure 3.29 shows that there is little uptake of CO on PdAu alloy particles at 300 K, presumably due to the formation of an Au-rich outer layer as we have seen from our MEIS data. In contrast, we have presented evidence for adsorption of AcOH on PdAu nanoparticles within the compositional ranges investigated.

Previous studies of acetic acid on Pd single-crystal surfaces have shown that bidentate acetate is usually the preferred surface species at 300 K [66], although there is some evidence for the formation of monodentate acetate [67]. Haley et al. proposed two competing pathways for the decomposition of acetic acid on Pd{111} [67]. Bidentate acetate was found to decompose via a single step to liberate gaseous CO₂ at 400 K. An alternative pathway was proposed to describe the decomposition of monodentate acetate to yield CO(ads). In both cases, CH_x formed on the surface decomposes to yield H₂ at ~380 K.

We propose that the ~320 K temperature CO desorptions observed from the alloy samples in figures 3.33c, 3.34c and 3.35c above are the result of CO formed by the decomposition of monodentate acetate on the surface, rather than CO adsorbed from the background gases.

We have already observed that segregation in our system is most likely to arise from adsorption of acetic acid on step edge sites, presumably at the edges of the particle. In this case, we would expect acetate to form mostly monodentate species rather than bidentate. This model may explain why our ~320 K CO desorption features are much more intense for AcOH dosed onto PdAu/alumina/NiAl{110} than for CO dosed onto similar samples and why we rarely observe significant desorption of CO₂ at ~400 K as would be expected for bidentate acetate [67].

3.9 – Summary and Conclusions.

- We have studied the growth of PdAu nanoparticles on SiO₂/Si{100} using a combination of STM, TPD and MEIS.
- Depositing submonolayer quantities of Au onto SiO₂/Si{100} results in the growth of broad, flat-topped particles with a height of a few atomic layers.
- Depositing Pd on top of Au/SiO₂/Si{100} results in nucleation of Pd on the existing Au particles to create bimetallic clusters – the diameter of these clusters is controlled by the original Au dose.
- Annealing the clusters causes the diameter to increase relative to the Au content but the particle height is not greatly increased.
- We have compared raw MEIS data taken at normal and 15° off-normal incidence and found that the total illumination is not significantly changed. This implies that either all particles are well oriented and just a few layers deep or, more likely, that the particles are not well oriented with respect to the underlying Si substrate.
- Data from much larger particles, created by increasing the Pd and Au doses tenfold, shows that visibility changes significantly between normal and 15° off-normal incidences. This is a direct effect of shadowing and blocking.
- Since traditional single-crystal methods are not appropriate for our sample, we have developed a new computational tool that allows us derive layer-by-layer compositional data from our MEIS data.
- We have fitted experimental MEIS data using a computational mode based on a flat-topped truncated hexagonal pyramid. We have shown that, for the special case of short, broad, flat-topped particles we can use some single-crystal approximations as a shortcut when calculating shadowing and blocking, thus reducing the calculation time and processor workload.
- Our method provides good fits for experimental data obtained from particles containing ~30-90% Pd where both the Pd and Au peaks are of sufficient intensity. Outside this compositional range we have problems obtaining reliable fits.
- We have shown that our PdAu alloy particles consist of a Pd-rich inner core encapsulated by an Au-rich base and surface layer.

- This structure seems to be largely independent of deposition order, suggesting that Pd and Au are able to intermix at 300 K. The data suggest that Au is able to diffuse to cover Pd at 300 K.
- We have examined the surface composition as a function of pre-annealing temperature and have found that our data agrees well with the trend predicted by Somorjai for PdAu alloy systems [31], but the surface Au concentration is systematically higher than the predicted values for all particle compositions tested, regardless of deposition order.
- By halving the Pd and Au doses we have created smaller particles – the surfaces of the smaller particles were found to be systematically richer in Pd than predicted by Somorjai's equations.
- TPD investigations show little uptake of CO at 300 K, supporting our proposal that the particle surface is rich in Au.
- Using our fitting method, we have shown that adsorption of acetic acid on the particle surface causes measurable segregation of Pd to the particle surface. In all cases, the surface Au composition was decreased by ~10% after treatment with AcOH, a similar value to that found on Au/Pd{111} [5, 15].
- Heating to ~430 K causes AcOH to desorb and the surface then reverts to its original state.
- Segregation effects would be expected to be enhanced on particle surface compared to single-crystals, instead we find that segregation effects on our particle surfaces are similar in magnitude to those observed on Au/Pd{111} [5, 15] – we rationalise our findings by proposing that for broad flat-topped particles where edge effects are minimal, adsorbate-induced segregation is likely follow a similar mechanism in our system to that proposed previously for {111} PdAu alloy surfaces where Pd is redistributed between the top few layers by adsorption of AcOH at step-edge sites [5].
- TPD investigations of AcOH on PdAu particles on alumina/NiAl{110} show large CO desorptions – since pure CO was not found to adsorb at significant volume we propose that these CO desorptions are the result of the decomposition of monodentate acetate surface species, as would be expected to form on step-edge sites. Characteristic CO₂ desorption features expected for

the decomposition of bidentate acetate [68] were not generally observed except on pure Pd.

3.10 – References

1. P. Bailey, T. C. Q. Noakes, D. P. Woodruff, Surf. Sci., **426** (1999), 358.
2. M. Yoshitake, B. Mebarki, T. T. Lay, Surf. Sci. **511** (2002), L313.
3. C. J. Baddeley, A. W. Stephenson, R. M. Ormerod, R. M. Lambert, J. Phys. Chem. **99** (1995), 5148.
4. R. M. Tromp, M. P. Seah (eds), “*Practical Surface Analysis Volume 2: Ion and Neutron Spectroscopy, 2nd edition*” D. Briggs, 1992
5. T. G. Owens, T. E. Jones, T. C. Q. Noakes, P. Bailey, C. J. Baddeley, J. Phys. Chem. B **110** (2006) 21152.
6. S. Deckers, F. Habraken, W. F. Vanderweg, A. W. D. Vanderagon, J. F. Van der Veen, J. W. Geus, Appl. Surf. Sci. **45** (1990), 121.
7. P. Bailey, T. C. Q. Noakes, C. J. Baddeley, G. van der Laan, D. Brown, P. D. Quinn, D. P. Woodruff, Current Appl. Phys., **3** (2003), 89
8. D. Brown, P. D. Quinn, D. P. Woodruff, T. C. Q. Noakes, P. Bailey, Surf. Sci. **497** (2002), 1.
9. H.-J. Freund, M. Bäumer, J. Libuda, T. Risse, G. Rupprechter, S. Shaikhutdinov, J. Cat. **216** (2003), 223.
10. Y. Kido, T. Koshikawa, J. Appl. Phys, **67** (1990), 187.
11. T. Okazawa, M. Fujiwara, T. Nishimura, T. Akita, M. Kohyama, Y. Kido, Surf. Sci. **600** (2006), 1331.
12. I. Kononi, S. Hyodo. T. Motohiro, J. Cat., **192** (2000), 11.
13. P. D. Quinn, N. R. Wilson, S. A. Hatfield, C. F. McConville, G. R. Bell, T. C. Q. Noakes, P. Bailey, S. Al-Harhi, F. Gard, Appl. Phys. Lett. **87** (2005) 153110.
14. <http://www.dl.ac.uk/MEIS/stereographs/index.htm>
15. T. G. Owens, Ph. D. Thesis, University of St Andrews, 2006.
16. J. W. Frenken, R. M. Tromp, J. F. van der Veen, Nucl. Instr. Meth. B **17** (1986), 334.
17. J. F. Ziegler, “*Helium Stopping Powers and Ranges in All Elements Vol. 4*”, Pergamon, New York, 1977.

18. A. Hentz, G. S. Parkinson, A. J. Window, P. D. Quinn, D. P. Woodruff, P. L. Grande, G. Schiwietz, P. Bailey, T. C. Q. Noakes, *Phys. Rev. B* **74** (2006), 125408.
19. M. A. Munoz-Marquez, G. A. Parkinson, D. P. Woodruff, A. Hentz, P. L. Grande, G. Schiwietz, T. J. Wood, C. Bonet, S. P. Tear, P. Bailey, T. C. Q. Noakes, *Phys. Rev. B* **72** (2005) 075415.
20. J. B. Marlon, F. C. Young, “*Nuclear Reaction Analysis – Graphs and Tables*”, North-Holland, Amsterdam, 1968.
21. J. Ziegler, J. Biersack, <http://www.srim.org>
22. E. Gusev, H. Lu, T. Gustafsson, E. Garfunkel, *Phys. Rev. B* **52** (1995), 1759.
23. Q. Yang, D. J. O’Connor, *Nucl. Instr. Meth. Phys. Res. B* **61**, (1991), 149.
24. D. Brown, P. D. Quinn, D. P. Woodruff, P. Bailey, T. C. Q. Noakes, *Phys. Rev. B* **61** (2000), 7706.
25. D. A. King, D. P. Woodruff (Eds.), “*The Chemical Physics of Solid Surfaces Vol. 8. Growth and Properties of Ultrathin Epitaxial Layers*”, Amsterdam, Elsevier, 1997.
26. B. K. Min, W. T. Wallace, A. K. Santra, D. W. Goodman, *J. Phys. Chem. B* **108** (2004), 16339.
27. W. Bente, N. Nilus, N. Ernst, H.-J. Freund, *Phys. Rev. B* **72** (2005) 054403.
28. D. Kumar, M. S. Chen, D. W. Goodman, *Cat. Today* **123** (2007), 77.
29. C. J. Baddeley, M. S. Tikhov, C. Hardacre, J. R. Lomas, R. M. Lambert, *J. Phys. Chem.* **100** (1996), 2189.
30. C. J. Baddeley, “*The Chemical Physics of Solid Surfaces, Volume 10, Surface Alloys and Alloy Surfaces*”, Elsevier, 2002.
31. G. A. Somorjai “*Introduction to Surface Chemistry and Catalysis*”, J. Wiley and Sons, 1994.
32. P. Wynblatt, R. C. Ku, *Surf. Sci.* **65** (1977), 511.
33. L. Z. Mezey, *Surf. Sci.* **162** (1985), 510.
34. L. Z. Mezey, *Surf. Sci.* **234** (1990), 210.
35. J. Gustafson, A. R. Haire, A. G. Trant, C. J. Baddeley, *in preparation* (2010).
36. A. G. Trant, T. E. Jones, J. Gustafson, T. C. Q. Noakes, P. Bailey, C. J. Baddeley, *Surf. Sci.* **603** (2009), 571.
37. <http://ie.lbl.gov>
38. <http://www.platinimetalsreview.com>

39. I. Beszeda, E. G. Gontire-Moya, A. W. Imre, *Appl. Phys. A* **81** (2005) 673.
40. B. E. Koel, A. Sellidj, *Phys. Rev. B.* **46**, (1992), 7846.
41. A. A. Herzing, M. Watanabe, J. K. Edwards, M. Conte, Z. R. Tang, G. J. Hutchings, C. J. Kiely, *Farad. Discuss.* **138** (2008) 337.
42. C. J. Baddeley, R. M. Lambert, A. W. Stephenson, M. S. Tikhov, *Surf. Sci.* **398** (1998), 172.
43. T. Dellwig, G. Rupprechter, H. Unterhalt, H.-J. Freund, *Phys. Rev. Lett.* **85** (2000), 776.
44. K. Luo, T. Wei, C.-W. Yi, S. Axnada, D. W. Goodman, *J. Phys. Chem. B* **109** (2005), 23517.
45. N. A. Khan, A. Uhl, S. Shaikhutdinov, H.-J. Freund, *Surf. Sci.* **600** (2006), 1849.
46. X. C. Guo, J. T. Yates Jr., *J. Chem. Phys.* **90** (1989), 6761.
47. A. F. Carlsson, M. Naschitzki, M. Bäumer, H.-J. Freund, *J. Phys. Chem B* **107** (2003), 778.
48. B. K. Min, A. K. Santra, D. W. Goodman *Cat. Tod.* **85** (2003), 113.
49. R. J. Behm, *Appl. Phys. A* **66** (1998) S513.
50. C. Lemire, R. Meyer, S. K. Shaikhutdinov, H.-J. Freund, *Surf. Sci.* **552** (2004), 27.
51. C. J. Baddeley, L. H. Bloxham, S. C. Laroze, R. Raval, T. C. Q. Noakes, P. Bailey, *Surf. Sci.* **435** (1999), 827.
52. C. J. Baddeley, L. H. Bloxham, S. C. Laroze, R. Raval, T. C. Q. Noakes, P. Bailey, *J. Phys. Chem. B* **105** (2001), 2766.
53. T. E. Jones, T. C. Q. Noakes, P. Bailey, C. J. Baddeley, *J. Phys. Chem. B* **108** (2004), 4759.
54. D. Tomanèk, S. Mukherjee, V. Kumar, K. H. Bennemann, *Surf. Sci.* **114** (1982), 11.
55. J. H. Hodak, A. Henglein, M. Giersig, G. V. Hartland, *J. Phys. Chem. B* **104** (2000), 11708.
56. J. Paul, S. Cameron, D. Dwyer, F. Hoffmann, *Surf. Sci.* **177** (1986), 121.
57. A. Dauscher, L. Hilaire, J. Spirlet, W. Muller, G. Maire, *Surf. Sci.* **204** (1988), 161.
58. U. Bardi, P. Ross, G. Rovida, *Surf. Sci.* **205** (1988), L798.
59. G. Hoflund, D. Asbury, *Surf. Sci.* **161** (1985), L583.

60. D. Asbury, G. Hoflund, Surf. Sci. **199** (1988), 552.
61. R. Lad, J. Blakely, Surf. Sci. **179** (1987), 467.
62. S. P. Jeng, P. Holloway, C. Batich, S. Hoffmann, J. Vac. Sci. Tech. A **5** (1987), 650.
63. M. Hegde, T. Sampath Kumar, R. Mallya, Surf. Sci. **188** (1987), 255.
64. J. J. Burton, E. Hyman, D. A. Fedak, J. Cat. **37** (1975), 106.
65. M. Bowker, N. Aas, J. Chem. Soc. Farad. Trans. **89** (1993), 1249.
66. J. James, D. K. Saldin, T. Zheng, W. T. Tysoe, D. S. Scholl, Cat. Today **105** (2006), 74.
67. R. D. Haley, M. S. Tikhov, R. M. Lambert, Cat. Lett. **76** (2001), 125.

Chapter 4 – AcOK on Au/Pd{111}

4.1 - Experimental

All experiments were carried out under ultrahigh vacuum conditions. Two UHV systems were used in this study. These are described in detail in Chapter 2. All TPD experiments were carried out in Chamber 1, while RAIRS measurements were carried out in Chamber 2.

Rather than relying on the use of a number of alloy single crystal samples to simulate different alloy compositions, we refer to the work of Lambert and co-workers, who showed that it is possible to create a range of disordered Pd/Au alloy surfaces on Pd{111} by depositing ~4 ML Au and then varying the annealing temperature [1]. Au was found to intermix with the substrate at around 600 K, while annealing to 1100 K was found to restore the characteristics of Pd{111}.

In all experiments, the Pd{111} single crystal was first cleaned by cycles of Ar⁺ sputtering at 1.0 keV and annealing to 1000 K until a sharp (1x1) LEED pattern was observed and no impurities were detected by AES. ~3-4 ML Au was deposited onto the surface by resistive heating of Au droplets on a tungsten filament. The total Au coverage in each case was estimated from the attenuation of the 330 eV Pd_{MNN} AES signal. A series of Au/Pd alloy surfaces was created by annealing each sample to one of a series of temperatures between 500 and 1000 K to induce intermixing of the metallic components. Samples were allowed to cool to room temperature before exposure to potassium acetate vapour, obtained by heating solid potassium acetate (BDH Chemicals Ltd., 99% purity, melting point 568 K) at 533 K in a small glass tube furnace. This was isolated from the main chamber by means of a gate valve so that the doser could be baked separately in order to minimise contamination. Although the use of a solid doser allows the AcOK dose to be calibrated easily, the actual ratio of potassium and acetate species present on the metal surface at any time may not necessarily be 1:1.

In all cases, AcOK dosage was measured in Langmuir units, where 1 L is the equivalent of 1 monolayer coverage, assuming Langmuir adsorption models with 100% sticking probability (1 L $\sim 10^{-6}$ torr or $\sim 7.6 \times 10^{-7}$ mbar for 1 second). RAIRS data were taken at an ambient temperature of 300 K in all cases.

4.2 - Results

Figures 4.1-4.12 below show TPD spectra for (a) $m/z = 2$ (H_2), (b) $m/z = 28$ (CO), (c) $m/z = 39$ (K) and (d) $m/z = 44$ (CO_2) and (e) RAIRS data taken using a Nicolet Nexus spectrometer with a mercury cadmium telluride detector for AcOK on Pd{111} and on a number of Au/Pd{111} alloy surfaces. Details of the sample preparation conditions are given in each case.

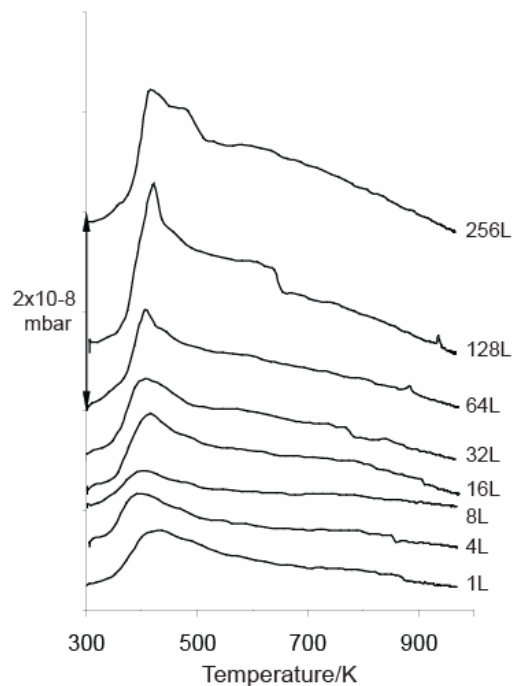
4.2.1 - AcOK on Pd{111}

Figure 4.1a

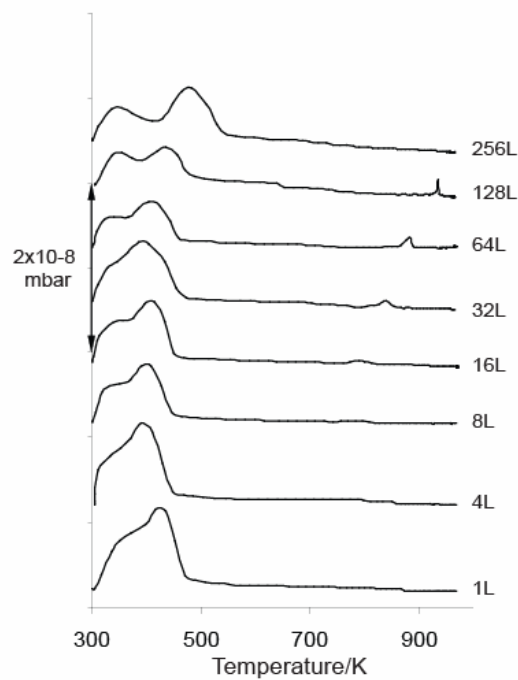


Figure 4.1b

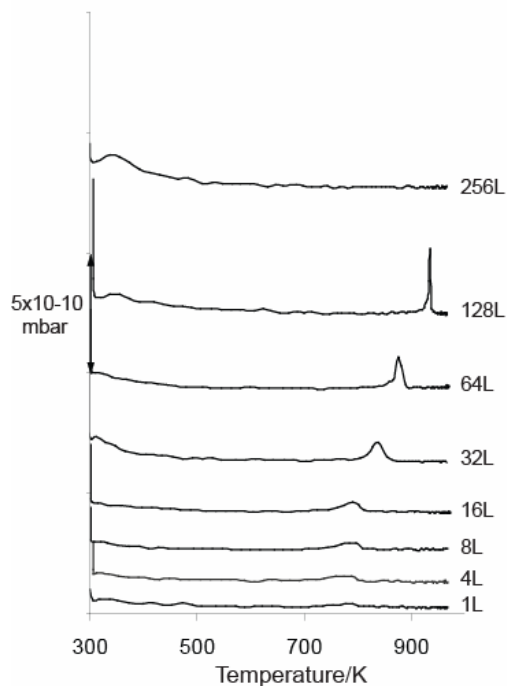


Figure 4.1c

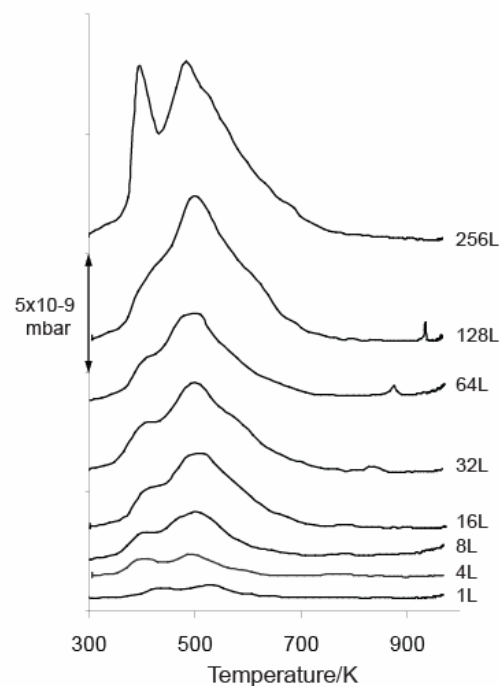


Figure 4.1d

Figure 4.1 - (a) H₂, (b) CO, (c) K and (d) CO₂ TPD data for AcOK dosed at a series of initial exposures at 300 K onto a Pd{111} sample.

Figure 4.1a shows the mass 2 (H₂) TPD data for AcOK on Pd{111} for a series of

increasing initial exposures. The data show a broad desorption feature between ~350 K and ~700 K with a broad maximum at ~415 K. For AcOK exposures of 64 L and above, this is resolved into a major peak at ~410 K and a shoulder at 440 K, increasing to ~480 K with increasing dose.

The mass 28 (CO) TPD data in figure 4.1b show a broad feature at ~400 K that decreases in intensity and increases in T_{\max} with increasing AcOK dose with a low temperature shoulder at around 350 K that becomes more prominent as the AcOK dose is increased. At 265 L AcOK exposure, the low temperature feature is resolved into two peaks at 350 K and 480 K. The high temperature desorption peak appears at higher AcOK exposures only. T_{\max} for this high temperature feature varies smoothly from 800-930 K as AcOK exposure is increased. This feature always coincides with the high temperature desorptions seen in the K and CO₂ TPD spectra in figures 4.1c and 4.1d.

The mass 39 (K) TPD data in figure 4.1c show a high temperature feature that grows sharper as the AcOK dosage is increased, with T_{\max} increasing smoothly from 780-930 K with increasing AcOK exposure. This feature coincides with the high temperature desorptions seen in the CO and CO₂ TPD spectra in figures 4.1b and 4.1d.

The mass 44 (CO₂) TPD data in figure 4.1d shows a broad main peak at around 510 K that increases in intensity as the AcOK dose is increased. A low temperature shoulder is visible at ~430 K, becoming more prominent with increasing AcOK exposure. When AcOK is dosed at 256 L exposure, the low temperature feature is resolved into two separate peaks at 410 K and 480 K. A high temperature CO₂ desorption can be seen for higher AcOK exposures with T_{\max} varying from 830 K to 930 K as AcOK exposure is increased. This feature always coincides with the high temperature desorptions seen in the CO and K TPD spectra in figures 4.1b and 4.1c.

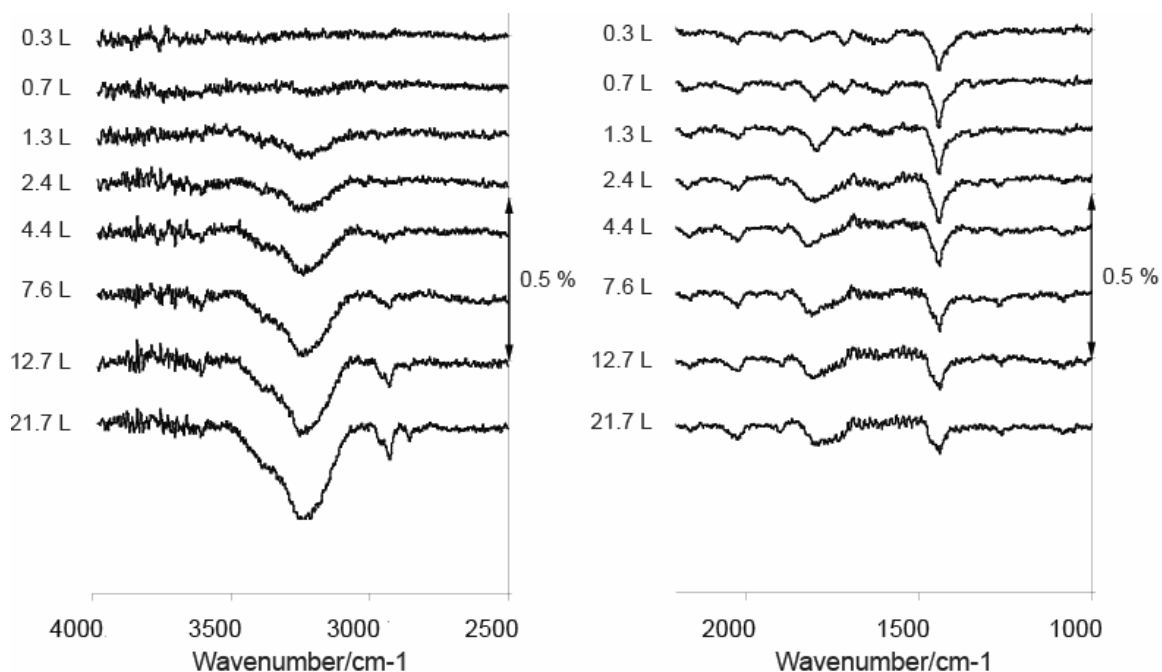


Figure 4.1e – RAIRS data for AcOK dosed at 300 K on Pd{111}.

Figure 4.1e above shows RAIRS spectra for AcOK on clean Pd{111} for a series of increasing exposures. The AcOK exposure time was doubled between successive scans until no significant change was observed in the RAIR spectra. IR absorption features are observed at 1440 cm^{-1} , 1608 cm^{-1} , 1730 cm^{-1} , 1807 cm^{-1} , 1918 cm^{-1} and 2040 cm^{-1} in all of the above spectra. The feature at $\sim 3250\text{ cm}^{-1}$ is attributed to the formation of water ice on the detector, and as such is treated as an experimental artifact. The 1730 cm^{-1} and 1807 cm^{-1} features broaden with increasing AcOK dose, and merge together after 2.4 L AcOK exposure. After 2.4 L exposure new features appear at 1090 cm^{-1} , 1270 cm^{-1} and 2930 cm^{-1} . The 2930 cm^{-1} feature grows with increasing exposure, becoming a double peak with minima at 2930 cm^{-1} and 2970 cm^{-1} after the 12.7 L dose. A further feature at 2860 cm^{-1} becomes apparent after the 7.6 L dose that grows in intensity with increasing exposure. The overall shape of the 1440 cm^{-1} band changes with increasing coverage. At higher exposures, a pair of small shoulders are visible at 1410 cm^{-1} and 1470 cm^{-1} .

4.2.2 - AcOK on 4 ML Au/Pd{111} – Part I

For the first data set, four similar samples were prepared under identical conditions on

the Pd{111} single crystal surface. Each sample was exposed to a different AcOK dose at 300 K and then TPD analysis of the various resulting surface species was carried out. For the RAIRS analysis, the AcOK exposure time was doubled between successive scans.

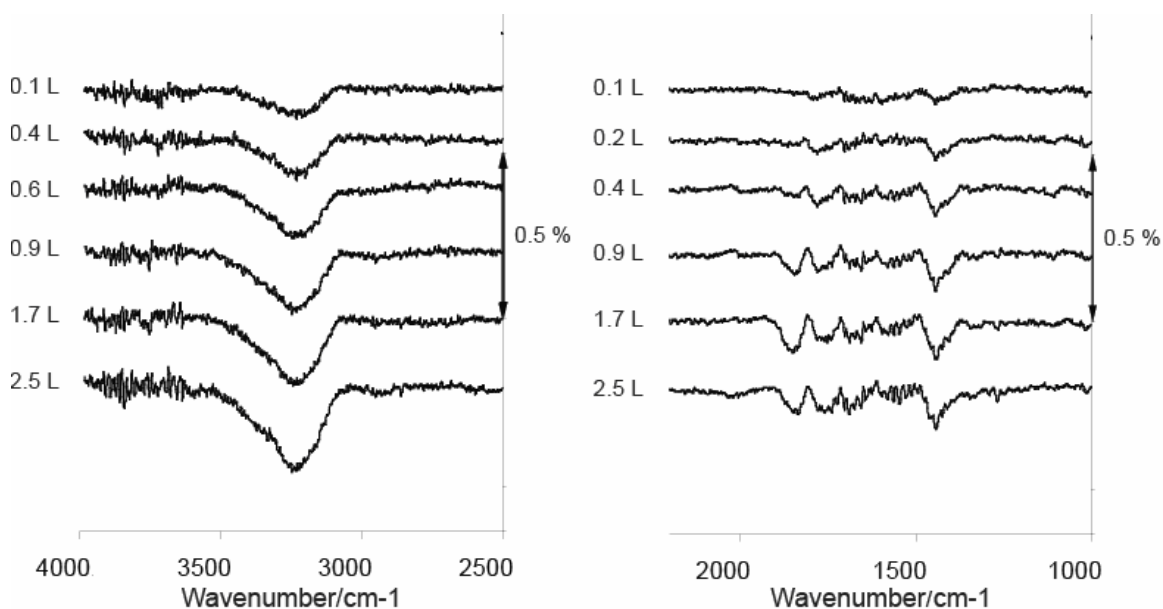


Figure 4.2 – RAIRS data for AcOK dosed at 300 K on ~ 4 ML Au/Pd{111}.

Figure 4.2 above shows RAIRS spectra for AcOK on ~ 4 ML Au/Pd{111} for a series of increasing exposures. Since it has been shown that there is little intermixing of Au with the Pd{111} substrate below ~ 600 K [2-4], it is assumed that the behaviour of AcOK on this surface will be similar to that observed on the 500 K pre-annealed surface and no TPD data is shown for this system. Absorption bands are relatively weak for exposures of < 0.1 L. For 0.1-0.2 L dosage, peaks are observed at 1275 cm^{-1} , 1440 cm^{-1} and 1766 cm^{-1} . For 0.4 L AcOK and above, peaks are observed at 1702 cm^{-1} and 1847 cm^{-1} . After 2.5 L exposure, small features are observed at 2860 cm^{-1} and 2940 cm^{-1} . The intensity of all peaks increases with increasing AcOK dose.



Figure 4.3a

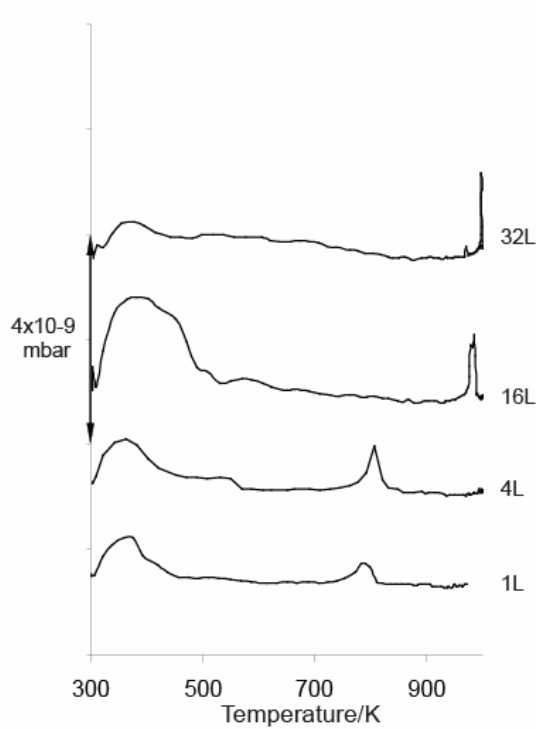


Figure 4.3b

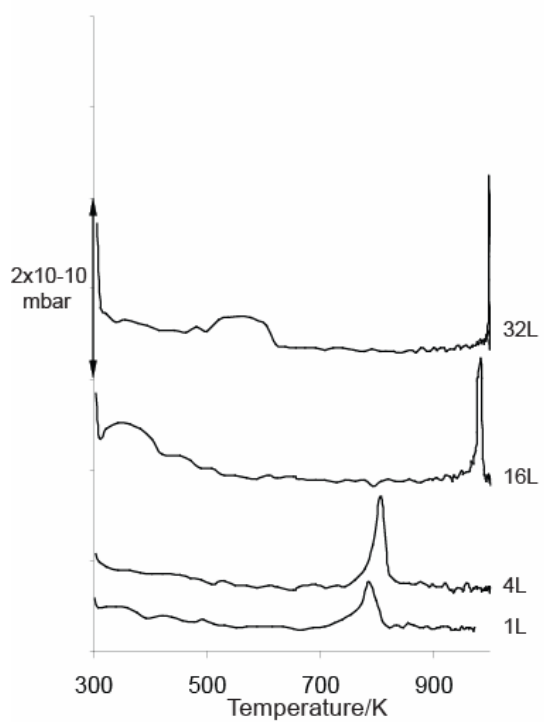


Figure 4.3c

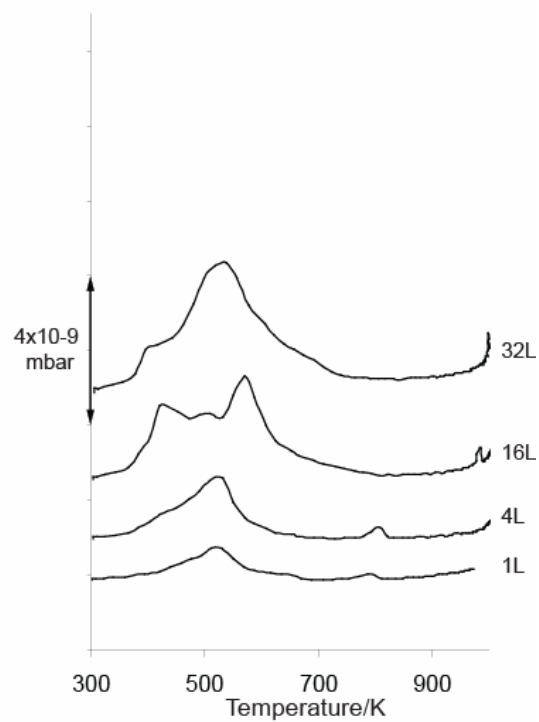


Figure 4.3d

Figure 4.3 - (a) H_2 , (b) CO , (c) K and (d) CO_2 TPD data for AcOK dosed at a series of initial exposures at 300 K onto ~ 4 ML Au/Pd{111} pre-annealed to 500 K.

Figure 4.3a shows the mass 2 (H_2) TPD data for AcOK on ~4 ML Au/Pd{111} pre-annealed to 500 K for a series of increasing initial exposures. For a 1 L exposure a pair of peaks are observed at 376 K and 866 K. for 4 L AcOK exposure, two broad peaks are observed, the first centred at ~471 K with a low temperature shoulder at ~360 K and the second centred at ~867 K. For higher doses, a single broad feature is observed with a low temperature shoulder at ~350 K and maxima at ~450 K, ~605 K, ~850 K and ~990 K.

The mass 28 (CO) TPD data in figure 4.3b show a low temperature desorption peak appearing at about ~380 K that generally increases in intensity as the AcOK dose is increased up to 16 L, with a high temperature shoulder becoming apparent at ~450 K for 4 and 16 L AcOK exposures. The intensity of this feature is significantly reduced after exposure to 32 L AcOK. The high temperature feature increases in intensity and T_{max} with increasing AcOK dose and can be seen to shift from 807 K to 985 K between the 4 L and 16 L AcOK dosed samples. This feature always coincides with the high temperature desorptions seen in the K and CO_2 TPD spectra in figures 4.3c and 4.3d.

The mass 39 (K) TPD data in figure 4.3c show the high temperature feature that increases in intensity and in T_{max} as the AcOK exposure is increased and can be seen to shift from 807 K to 982 K between the 4 L and 16 L AcOK dosed samples. This feature always coincides with the high temperature desorptions seen in the CO and CO_2 TPD spectra in figures 4.3b and 4.3d. For 32 L AcOK, an additional broad feature is visible at 577 K, which coincides with the strong CO_2 desorption peak seen in figure 4.3d.

The mass 44 (CO_2) TPD data are shown in figure 4.3d. A desorption peak usually appears at 530-540 K with a low temperature shoulder at 450 K and increases in intensity with increasing AcOK dose. For the sample dosed with 16 L, this feature is resolved into a pair of peaks at 450 K and 570 K. The broad peak seen at 537 K in the 32 L AcOK exposed sample as well as its shoulder at ~450 K coincide with a similar feature seen in the K TPD data in figure 4.3c above. The high temperature feature increases in height and in T_{max} as the AcOK exposure is increased and can be seen to shift from 807 K to 985 K between the 4 L and 16 L AcOK dosed samples. This

feature always coincides with the high temperature desorptions seen in the CO and K TPD spectra in figures 4.3b and 4.3c.

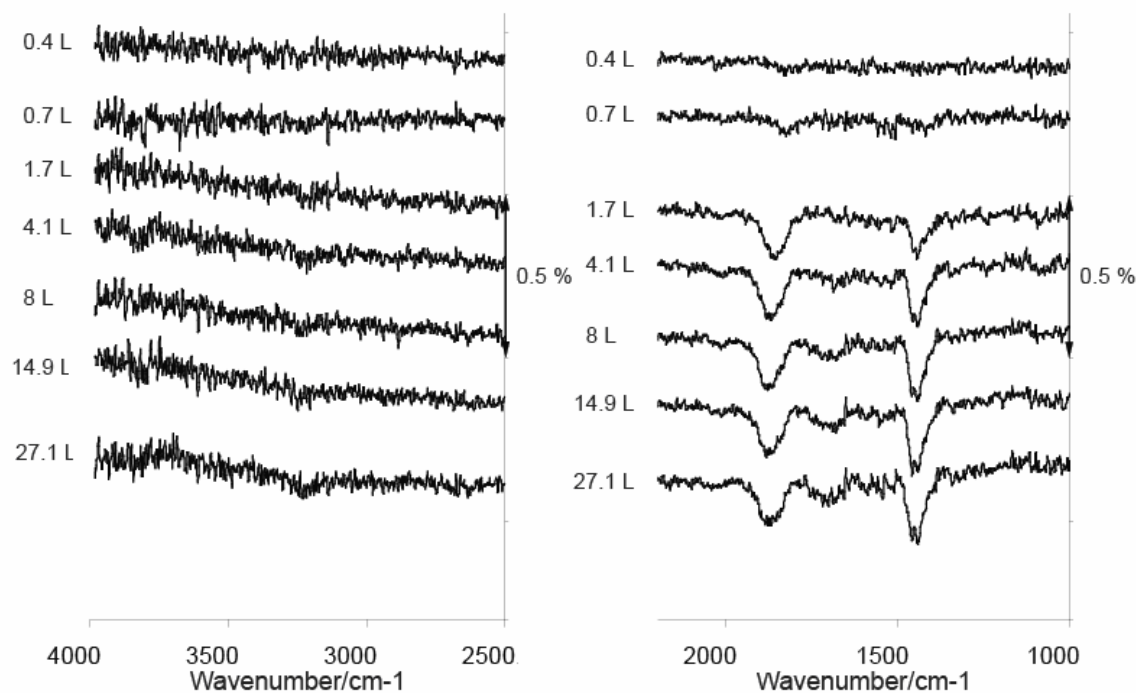


Figure 4.3e – RAIRS data for AcOK dosed at 300 K on ~ 4 ML Au/Pd{111} pre-annealed to 500 K.

Figure 4.3e above shows RAIRS spectra for AcOK on ~ 4 ML Au/Pd{111} pre-annealed to 500 K for a series of increasing exposures. Little adsorption is observed before 0.7 L, where small peaks are observed at 1440 cm^{-1} and 1830 cm^{-1} . At higher coverage, further peaks are observed at 1704 cm^{-1} and 1888 cm^{-1} . The intensity of all peaks increases with increasing AcOK dose.

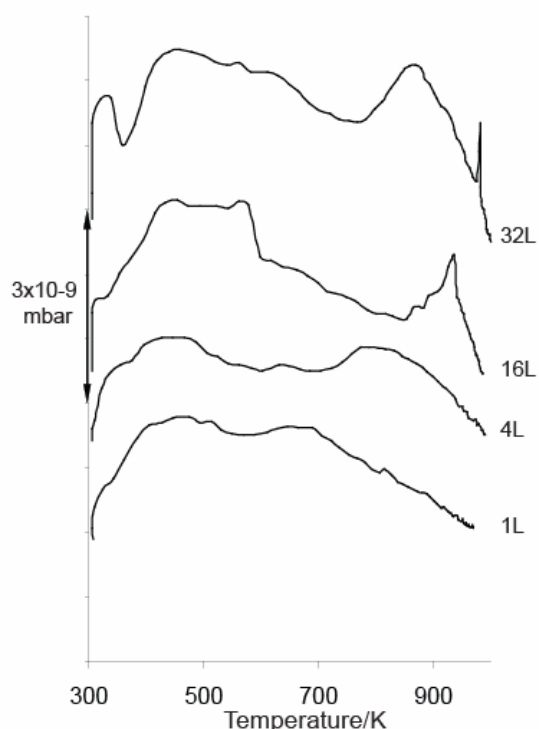


Figure 4.4a

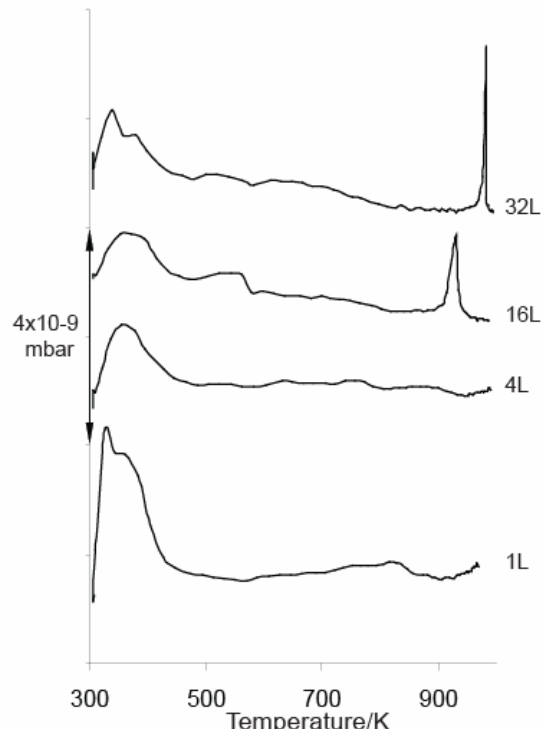


Figure 4.4b

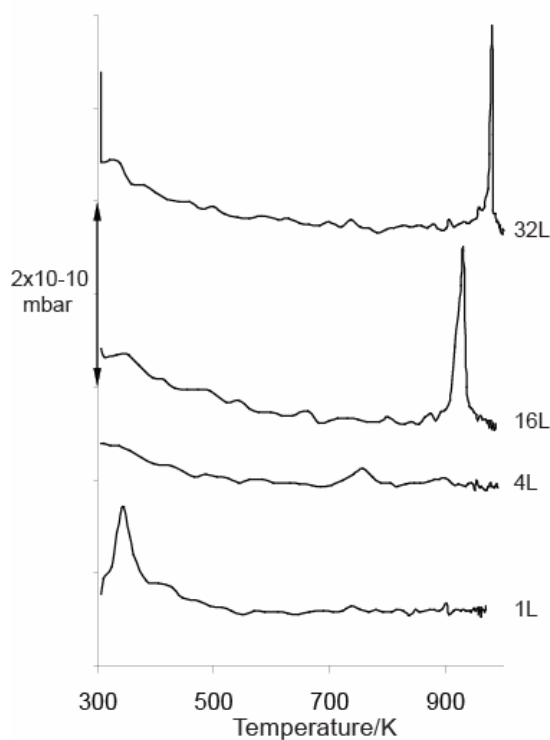


Figure 4.4c

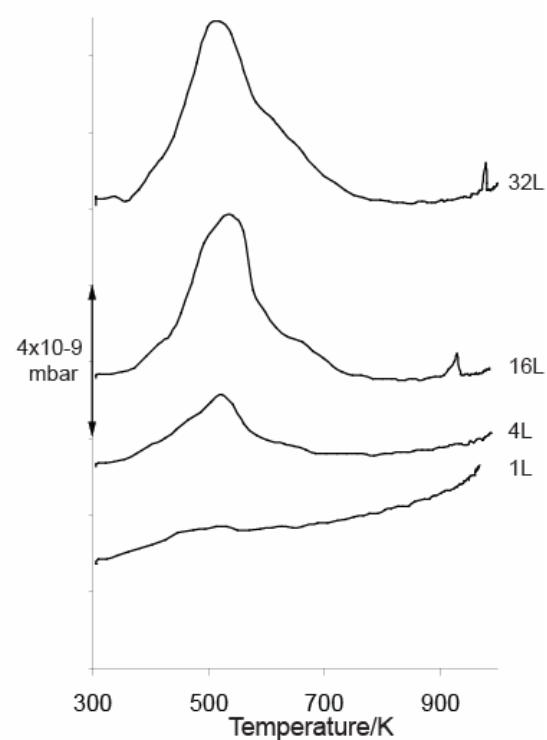


Figure 4.4d

Figure 4.4 - (a) H₂, (b) CO, (c) K and (d) CO₂ TPD data for AcOK dosed at a series of initial exposures at 300 K onto ~4 ML Au/Pd{111} pre-annealed to 600 K.

Figure 4.4a shows the mass 2 (H_2) TPD data for AcOK on ~4 ML Au/Pd{111} pre-annealed to 600 K for a series of increasing initial exposures. For 1 L AcOK, a single broad feature is observed between ~340 and ~850 K with maxima centred at ~440 K and ~650 K. For 4 L exposure, a broad peak is observed at around 440 K with a low temperature shoulder at ~350 K. A second small feature is observed at ~650 K followed by a broad desorption peaking at ~820 K. For greater AcOK exposures, a small feature is observed at 340 K, followed by a broad feature between ~400 and ~650 K with maxima at ~450 K and ~560 K. For 16 L AcOK, a high temperature desorption is observed at 935 K with shoulders at 900 K and 870 K. At 32 L AcOK, this becomes a single broad peak at 870 K followed by a sharp desorption at 980 K.

The mass 28 (CO) TPD data is shown in figure 4.4b. The initial low temperature peak appears at 355 K for a 4 L AcOK dose and at 372 K for a 16 L dose of AcOK. Under the lowest and highest exposure conditions, a double peak structure is observed. This appears at 325 K with a shoulder at 360 K for the 1 L dose and at 339 K with a 380 K shoulder for the 32 L dose. The integrated CO yield decreases with increasing AcOK dose. A high temperature desorption is seen at 756 K for a 4 L AcOK exposure, 930 K for a 16 L dose and at 980 K for a 32 L dose. These features always coincide with the high temperature desorptions seen in the K and CO_2 TPD spectra in figures 4.4c and 4.4d.

Figure 4.4c shows the mass 39 (K) TPD data. The high temperature desorption peaks appear after 4 L AcOK exposure and higher and increase in T_{max} and in height as the AcOK exposure is increased, with a shift from 760 K to 930 K on going from 4 L to 16 L AcOK. This feature always coincides with the high temperature desorptions seen in the CO and CO_2 TPD spectra in figures 4.4b and 4.4d.

The mass 44 (CO_2) TPD data in 4.4d shows a main peak appearing at around 530 K that increases in height with increasing AcOK exposure. A small low temperature shoulder is barely visible at around 470 K for 1-4 L coverage, but this is not observed for higher AcOK exposures. A high temperature desorption is visible at AcOK exposures of 16 L and above, which rises in temperature from 930 K to 980 K between 16 L and 32 L AcOK exposures. This feature always coincides with the high temperature desorptions seen in the CO and K TPD spectra in figures 4.4b and 4.4c.

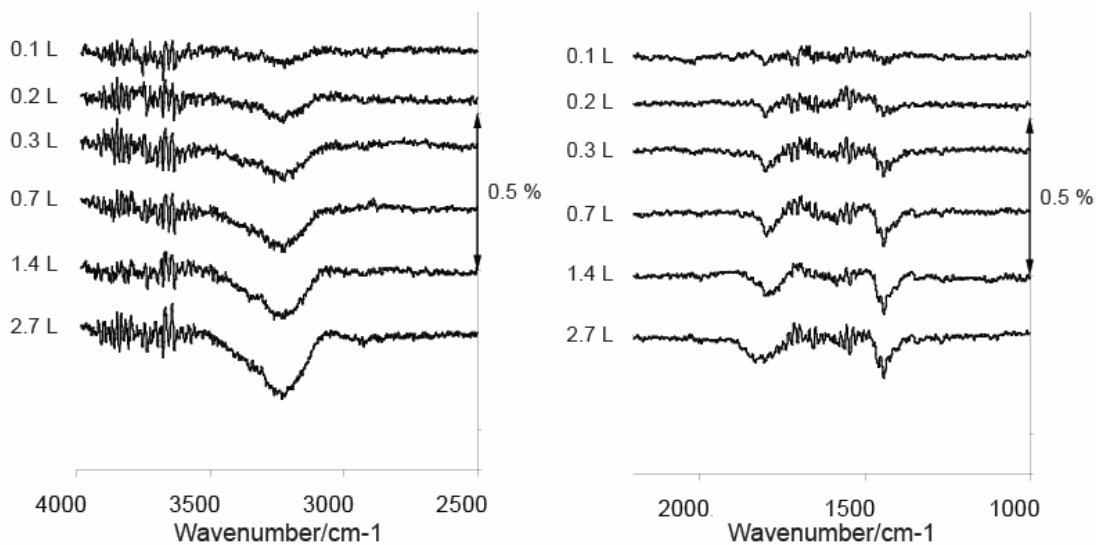


Figure 4.4e – RAIRS data for AcOK dosed at 300 K on ~ 4 ML Au/Pd{111} pre-annealed to 600 K.

Figure 4.4e above shows RAIRS spectra for AcOK on ~ 4 ML Au/Pd{111} pre-annealed to 600 K for a series of increasing exposures. Little adsorption is observed before 0.2 L, where two small peaks are observed at 1440 cm^{-1} and 1805 cm^{-1} . The intensity of both peaks increases with increasing dose until saturation after 2.7 L AcOK. After the 0.3 L dose, further peaks are observed at 1275 cm^{-1} and 1602 cm^{-1} .

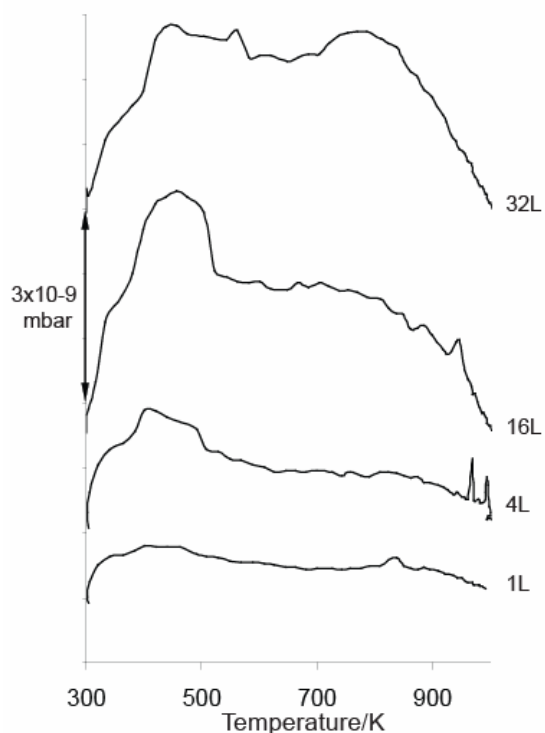


Figure 4.5a

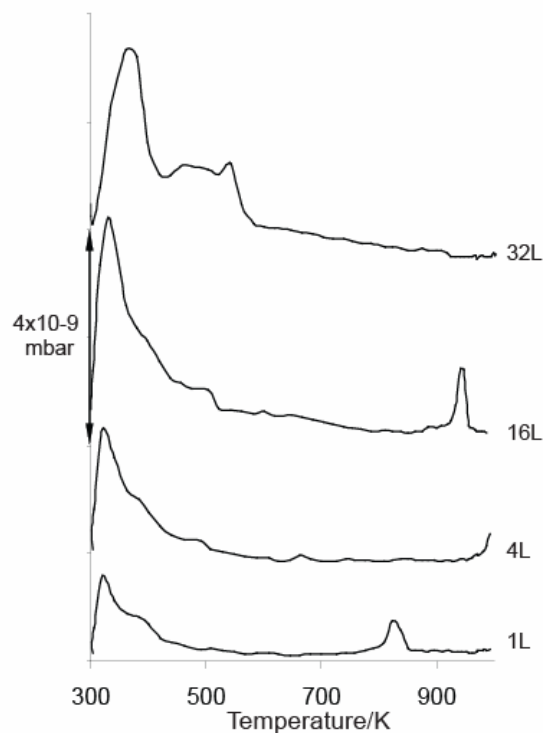


Figure 4.5b

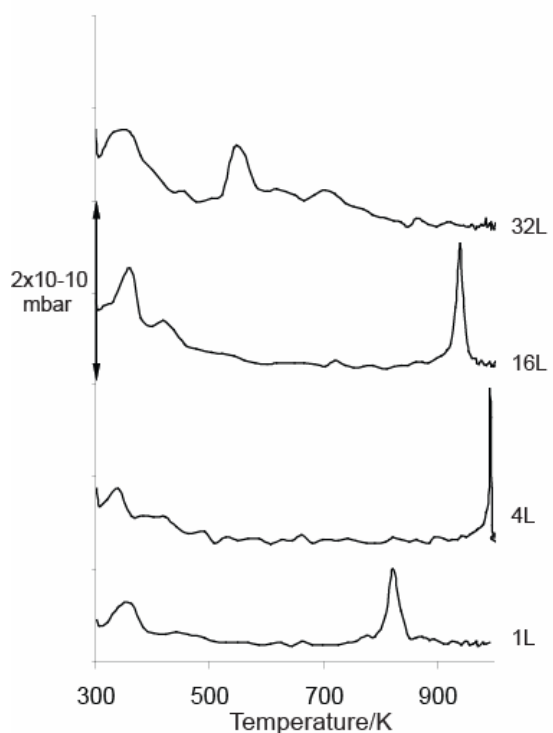


Figure 4.5c

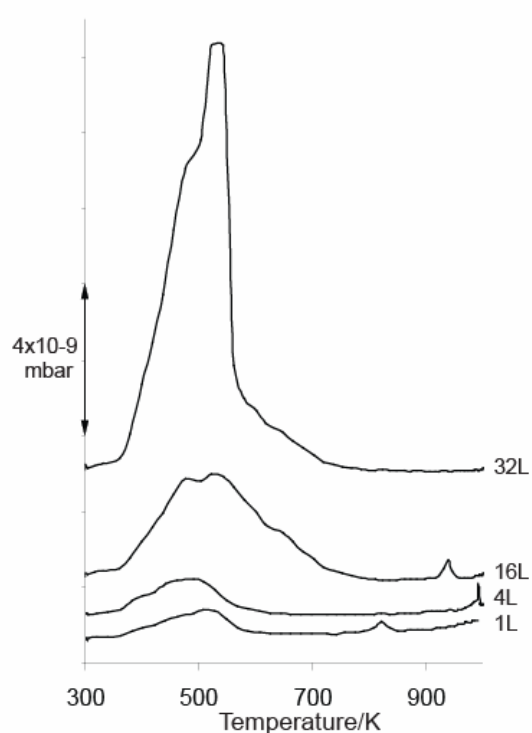


Figure 4.5d

Figure 4.5 - (a) H_2 , (b) CO , (c) K and (d) CO_2 TPD data for AcOK dosed at a series of initial exposures at 300 K onto ~ 4 ML Au/Pd{111} pre-annealed to 700 K.

Figure 4.5a shows the mass 2 (H₂) TPD data for AcOK on ~4 ML Au/Pd{111} pre-annealed to 700 K for a series of increasing initial exposures. In all cases, a broad feature is observed between 300 and 650 K that broadens and increases in intensity with increasing coverage. At 1-4 L exposure, this can be resolved into a triplet of maxima at 340 K, 420 K and 490 K. For 16 L AcOK, a broad, intense feature is observed between 320 and 520 K with a maximum at 450 K and a low temperature shoulder at 340 K. For 32 L AcOK, this feature is further broadened with a third maximum appearing at 560 K. A second broad desorption with a peak at 785 K is observed for the highest AcOK exposure only.

The mass 28 (CO) TPD data in figure 4.5b show a low temperature desorption at 320 K with a high temperature shoulder at 362 K for the lowest AcOK dose. A second high temperature shoulder appears at ~500 K for 4 L AcOK and above. Peak intensity and T_{\max} are seen to rise steadily with increasing AcOK dose, with the main peak appearing at 360 K together with shoulders at 475 K and 542 K for 32 L AcOK exposure. The growth of a peak at ~500 K in the data for the 16 L and 32 L exposures corresponds to the growth of similar peaks in the K and CO₂ TPD spectra in figures 4.5c and 4.5d. A high temperature desorption is visible at all AcOK exposures, with T_{\max} shifting from 882 K for 1 L AcOK to 994 K for 4 L AcOK. This feature always coincides with the high temperature desorptions seen in the K and CO₂ TPD spectra in 4.5c and 4.5d.

The mass 39 (K) TPD data in figure 4.5c show a high temperature desorption peak at 822 K for 1 L AcOK increasing to 992 K for a 4 L AcOK dose. This feature always coincides with the high temperature desorptions seen in the CO and CO₂ TPD spectra in figures 4.5b and 4.5d. For 32 L AcOK, an additional peak appears at 542 K, with another at 703 K. This corresponds to the growth of similar peaks in the CO and CO₂ TPD spectra in figures 4.5b and 4.5d.

The mass 44 (CO₂) TPD data are shown in figure 4.5d. The main peak appears at 460 K for 1 L AcOK with a shoulder at 508 K. T_{\max} rises steadily with increasing AcOK exposure, giving a main peak at 540 K with a shoulder at 504 K for 32 L AcOK. The high T desorption peak appears at 822 K for 1 L AcOK and shifts to 992 K for 4 L AcOK. This feature always coincides with the high temperature desorptions seen in

the CO and K TPD spectra in figures 4.5b and 4.5c. For 32 L AcOK, the main peak at 542 K corresponds to the growth of similar peaks in the CO and K TPD spectra in figures 4.5b and 4.5c.

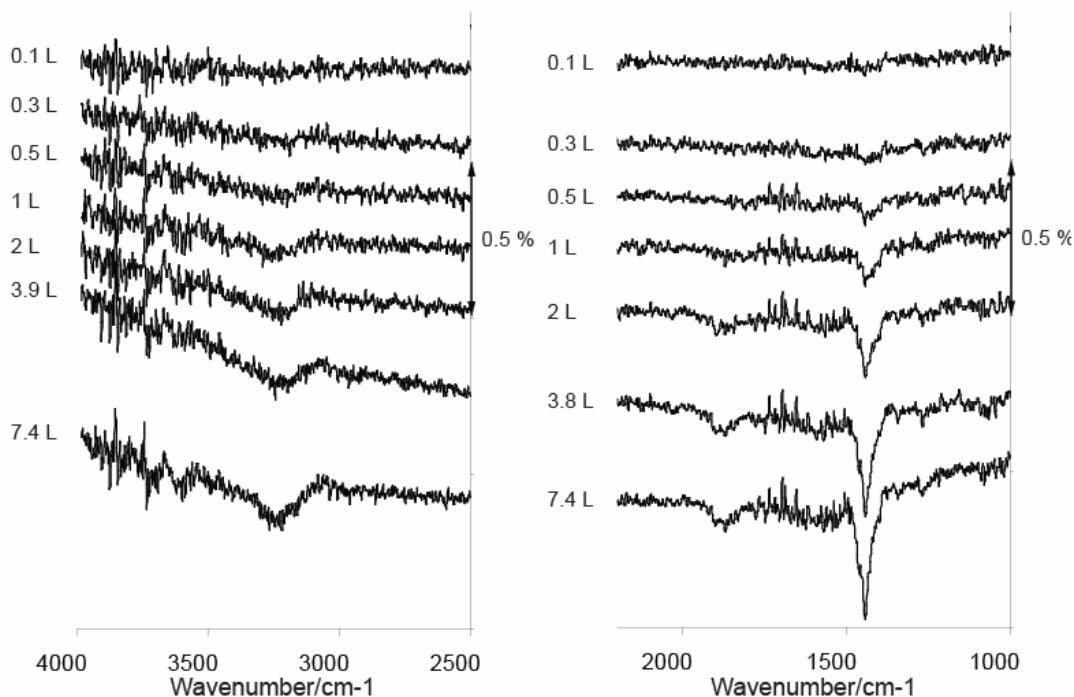


Figure 4.5e – RAIRS data for AcOK dosed at 300 K on ~ 4 ML Au/Pd{111} pre-annealed to 700 K.

Figure 4.5e above shows RAIRS spectra for AcOK on ~ 4 ML Au/Pd{111} pre-annealed to 700 K for a series of increasing exposures. AcOK uptake is first observed at 0.3 L by the appearance of small peaks at 1442 and 1870 cm^{-1} . For 2 L AcOK and above, a new peak is observed at 1500 cm^{-1} . The intensity of all peaks increases with increasing AcOK dose.

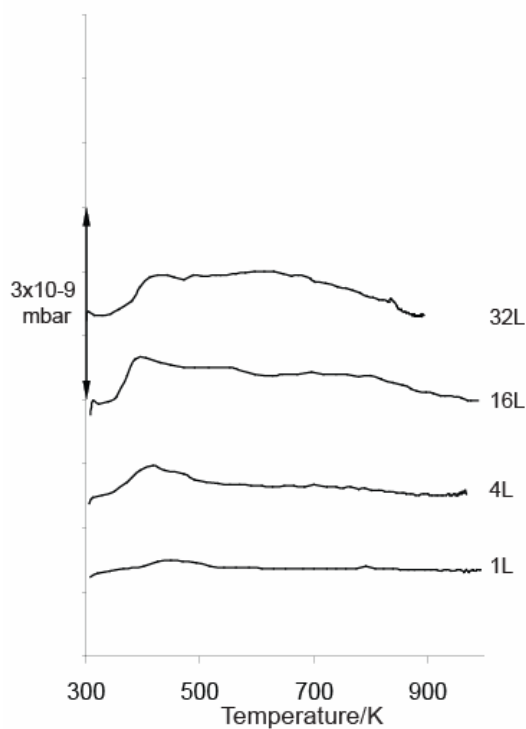


Figure 4.6a

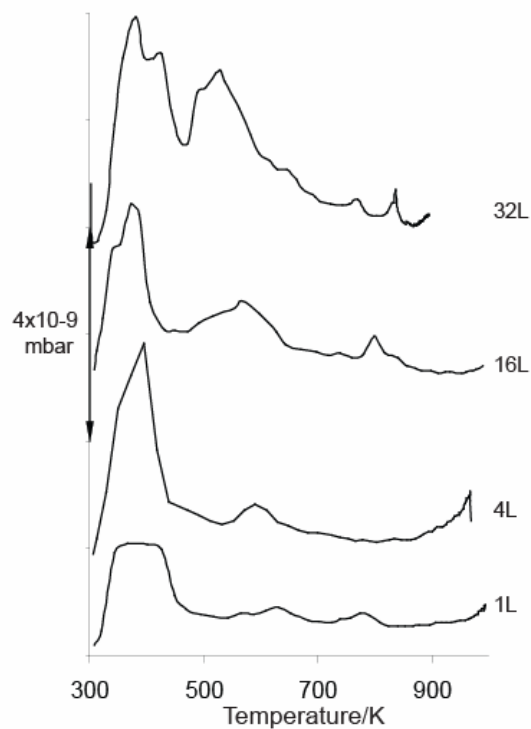


Figure 4.6b

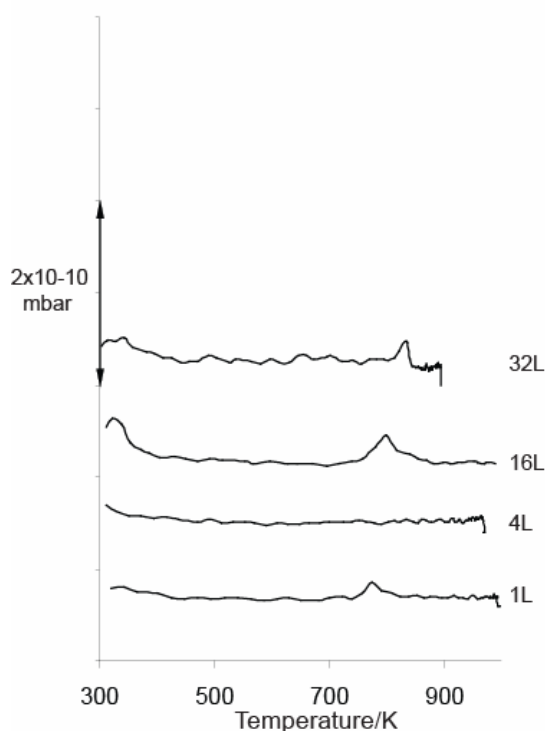


Figure 4.6c

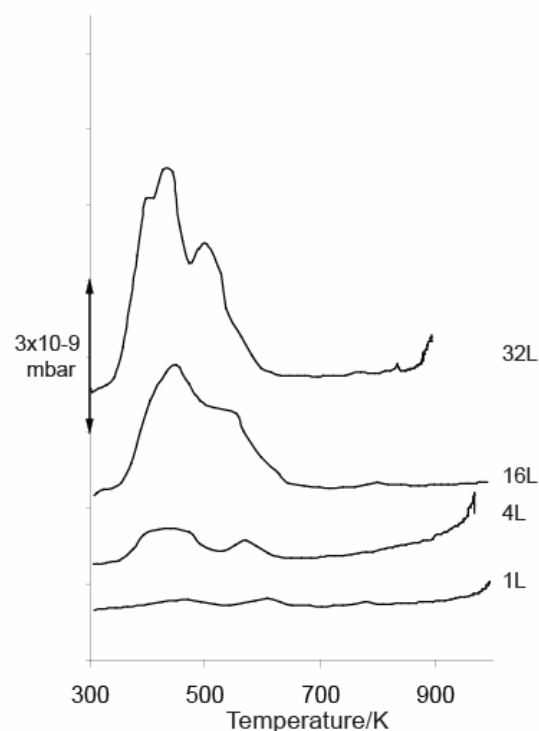


Figure 4.6d

Figure 4.6 - (a) H_2 , (b) CO , (c) K and (d) CO_2 TPD data for AcOK dosed at a series of initial exposures at 300 K onto ~ 4 ML Au/Pd{111} pre-annealed to 800 K.

Figure 4.6a shows the mass 2 (H₂) TPD data for AcOK on 4 ML Au/Pd{111} pre-annealed to 800 K for a series of initial exposures. For 1 L AcOK, a broad desorption feature is at ~480 K. For 4 L AcOK and above, a peak is observed at ~410 K with a shoulder at 480 K. A small high temperature feature observed at ~790-800 K coincides with similar features observed in the CO, K and CO₂ data in figures 4.6b, 4.6c and 4.6d.

The mass 28 (CO) TPD data are shown in figure 4.6b. For the lowest AcOK dose, a broad desorption is observed centred at ~400 K with a low temperature shoulder at 370 K. T_{\max} for this feature decreases with increasing AcOK dose, giving a main peak at 380 K with a shoulder at 350 K for 16-32 L AcOK. After dosing 32 L AcOK a new high temperature shoulder is observed at 430 K. A second CO desorption is observed at 630 K with a shoulder at 570 K. This feature decreases in T_{\max} and increases in intensity with increasing AcOK dose, giving a peak at 530 K with a low temperature shoulder at 500 K for 32 L AcOK. For 1-16 L AcOK, the 630-530 K desorption coincides with features observed in the CO₂ data in figure 4.6d. A third feature is observed at 775 K for 1 L AcOK, increasing to 840 K for 32 L AcOK. This coincides with similar features in the H₂, K and CO₂ data in figures 4.6a, 4.6c and 4.6d.

Figure 4.6c shows the mass 39 (K) TPD data. The main desorption feature is observed at 775 K for 1 L AcOK, rising to 840 K for 32 L AcOK. This coincides with similar features in the H₂, CO and CO₂ data in figures 4.6a, 4.6b and 4.6d.

The CO₂ TPD data are shown in figure 4.6d. For 1 L AcOK, three desorption features are observed at 470, 610 and 775 K. Both the 470 K and the 610 K features decrease in T_{\max} and increase in intensity with increasing AcOK dose, becoming a single feature with a maximum at 450 K and shoulder at 550 K for 16 L AcOK. After a 32 L AcOK dose, a broad feature is observed with a maximum at 440 K and a pair of shoulders at 400 K and 500 K. The 775 K TPD feature shifts to higher T_{\max} with increasing AcOK dose and coincides with similar features in the H₂, CO and K data in figures 4.6a, 4.6b and 4.6c.

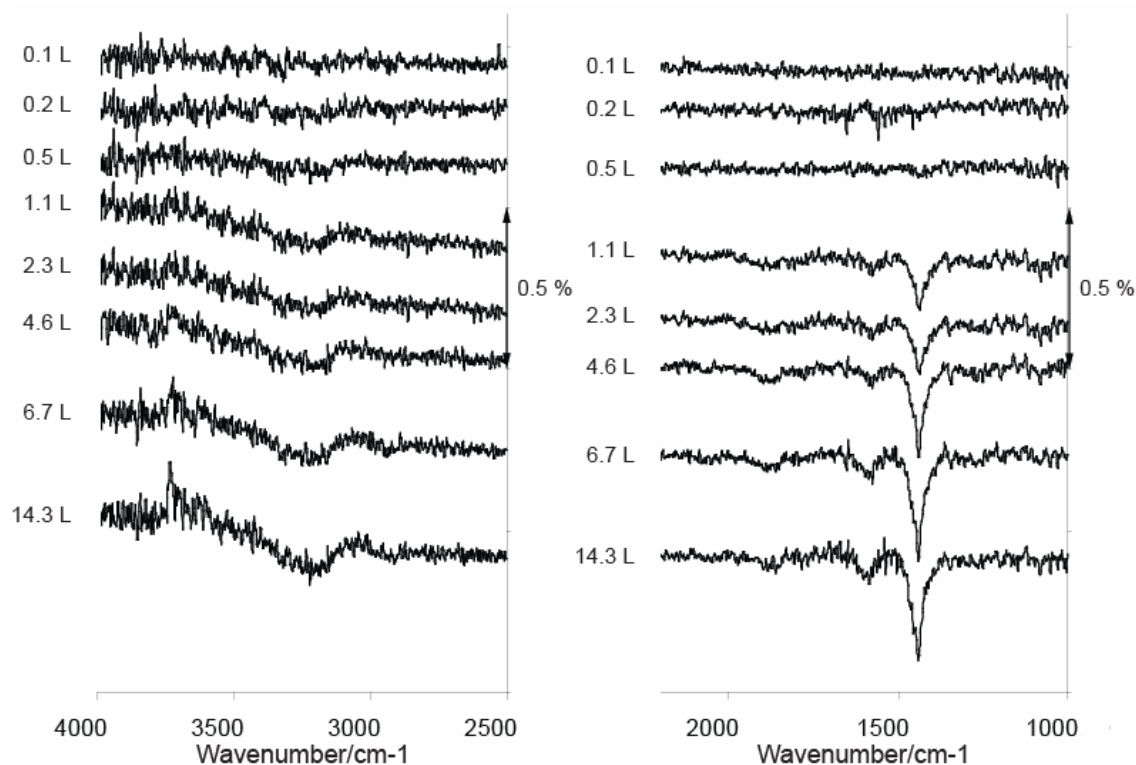


Figure 4.6e – RAIRS data for AcOK dosed at 300 K on ~ 4 ML Au/Pd{111} pre-annealed to 800 K.

Figure 4.6e above shows RAIRS spectra for AcOK on ~ 4 ML Au/Pd{111} pre-annealed to 800 K for a series of increasing exposures. Little adsorption is observed before 0.5 L, at which a small peak is observed at 1440 cm^{-1} . For 1.1 L AcOK and above, further peaks are observed at 1602 and 1880 cm^{-1} . At 6.7 L AcOK and above, a pair of small shoulders are observed at 1410 and 1470 cm^{-1} . The intensity of all peaks increases with increasing AcOK dose.

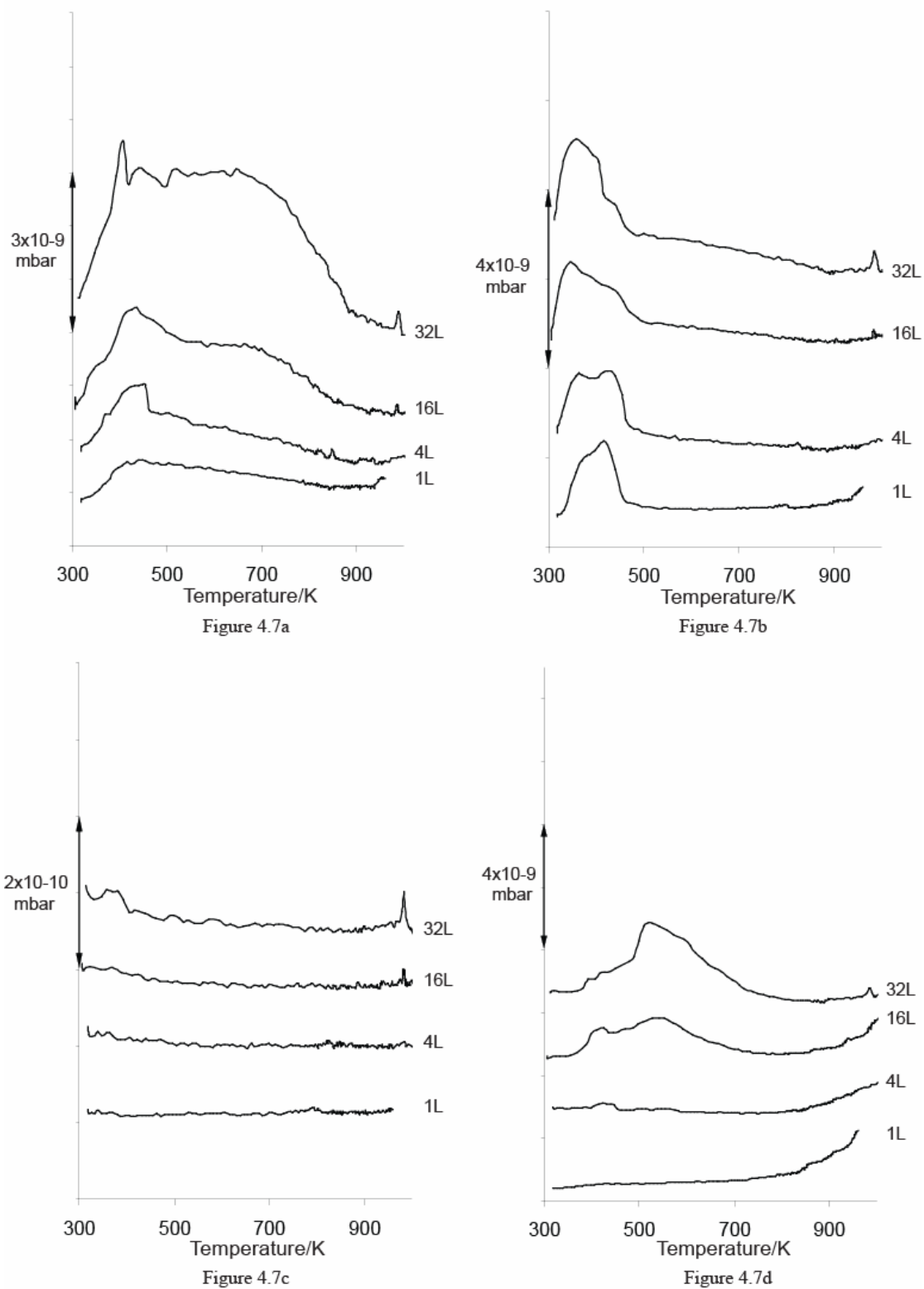


Figure 4.7 - (a) H_2 , (b) CO , (c) K and (d) CO_2 TPD data for AcOK dosed at a series of initial exposures at 300 K onto ~ 4 ML Au/Pd{111} pre-annealed to 900 K.

Figure 4.7a shows the mass 2 (H₂) TPD data for AcOK on ~4 ML Au/Pd{111} pre-annealed to 900 K for a series of initial exposures. For 1-16 L, a broad desorption is observed between 330 and 550 K with a peak at ~440 K and a low temperature shoulder at ~370 K. For 16 L AcOK, a broad high temperature shoulder is observed between 612 and 800 K. For 32 L AcOK exposure, a single broad feature is observed between 330 and 830 K with maxima appearing at 406, 450, 520 and 645 K.

The mass 28 (CO) TPD data is shown in figure 4.7b. At 1 L exposure, a peak is observed at 415 K with a low temperature shoulder at 370 K. The lower temperature feature grows in intensity with increasing coverage, giving two equal peaks at 360 and 430 K after a 4 L dose. For 16-32 L AcOK, the main desorption feature is observed at ~350 K. This feature has a broad tail with high temperature shoulders at ~390 K and ~440 K. A further small feature is observed at 986 K for the two highest doses only. This feature always coincides with the high temperature desorptions seen in the K and CO₂ TPD spectra in figures 4.7c and 4.7d.

Figure 4.7c shows the mass 39 (K) TPD data. No significant peaks are observed for 1-4 L AcOK. A single small peak is visible at 986 K for 16 L AcOK exposure. On increasing the exposure to 32 L, this peak is seen to grow in intensity. This coincides with high temperature features observed in the CO and CO₂ TPD spectra in figures 4.7b and 4.7d. A further peak is observed at 370 K for the highest AcOK exposure only.

Figure 4.7d shows no significant mass 44 (CO₂) desorptions for 1 L AcOK. At 4 L exposure, a single weak desorption feature is observed at 430 K. At 16 L exposure a broad feature is observed between 380 and 650 K with maxima at 430 and 530 K. Further increasing the AcOK exposure to 32 L results in a large desorption at 530 K with a high temperature shoulder at 600 K and a small low temperature shoulder at 430 K. A further small feature is observed at 986 K for the two highest doses only. This feature always coincides with the high temperature desorptions seen in the CO and K TPD spectra in figures 4.7b and 4.7c.

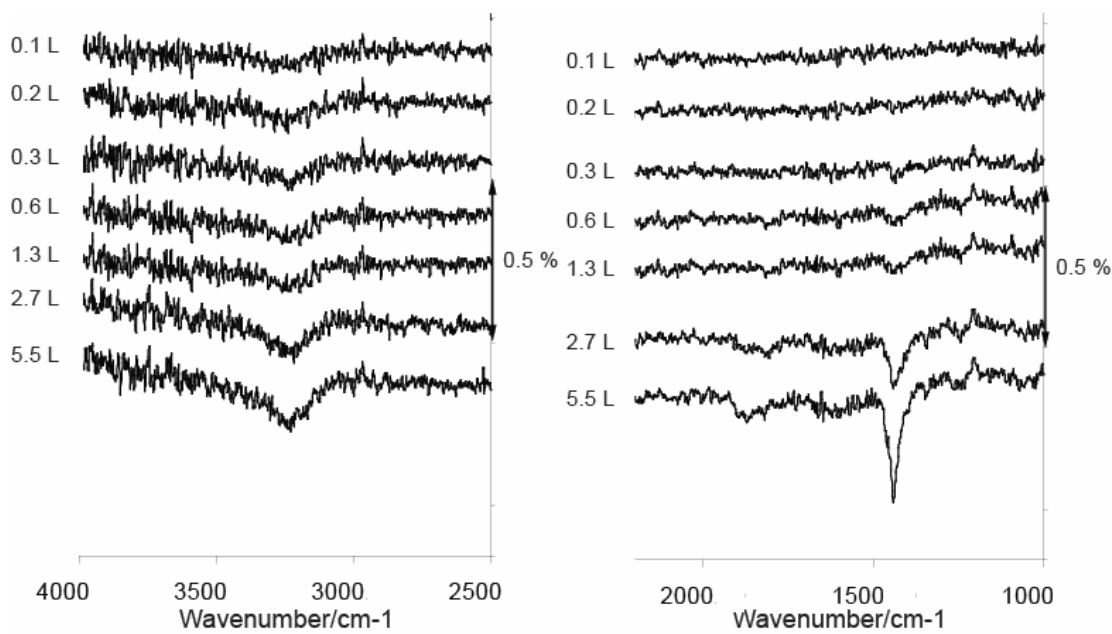


Figure 4.7e – RAIRS data for AcOK dosed at 300 K on ~ 4 ML Au/Pd{111} pre-annealed to 900 K.

Figure 4.7e above shows RAIRS spectra for AcOK on ~ 4 ML Au/Pd{111} pre-annealed to 900 K for a series of increasing exposures. AcOK uptake is observed after 0.3 L, where a small peak is visible at 1442 cm^{-1} . After the 0.6 L dose, further peaks are observed at 1280 cm^{-1} , 1350 cm^{-1} and 1820 cm^{-1} . The intensity of all peaks increases with increasing AcOK dose. After exposure to 2.7 L AcOK a peak is visible at 1880 cm^{-1} . For 5.5 L, both the 1820 cm^{-1} and 1880 cm^{-1} features broaden and increase in intensity. For the 5.5 L AcOK dose only, small features are visible at $2900\text{--}3000\text{ cm}^{-1}$ as well as a pair of small shoulders at 1410 cm^{-1} and 1470 cm^{-1} .

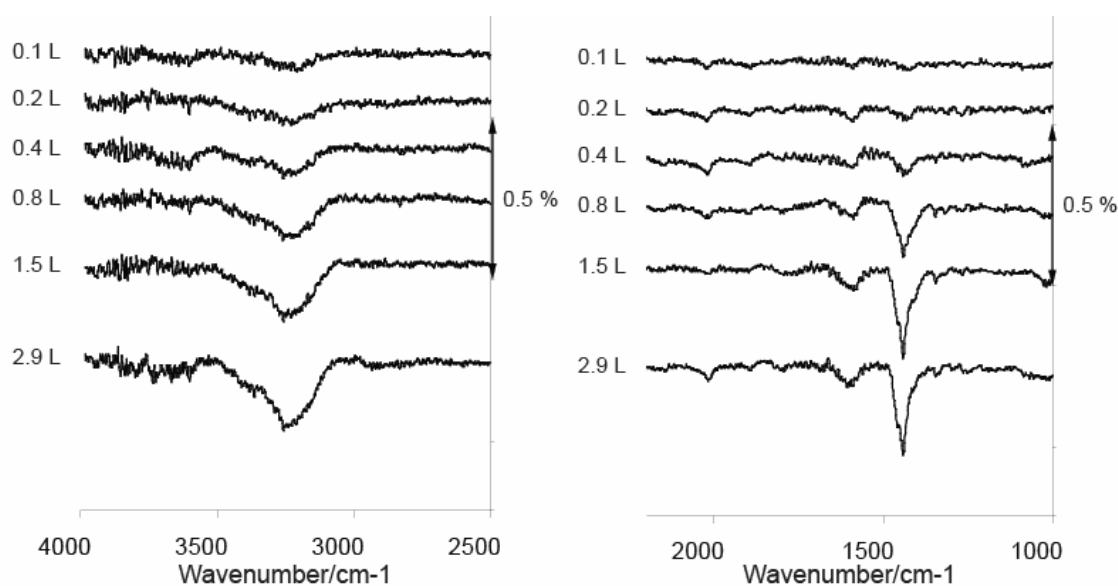


Figure 4.8 – RAIRS data for AcOK dosed at 300 K on ~ 4 ML Au/Pd{111} pre-annealed to 1000 K.

Figure 4.8 above shows RAIRS spectra for AcOK on ~ 4 ML Au/Pd{111} pre-annealed to 1000 K for a series of increasing exposures. Small features are visible at 1810 cm^{-1} , 1910 cm^{-1} and 2020 cm^{-1} in all spectra. Small peaks at 1440 cm^{-1} and 1608 cm^{-1} show uptake after 0.1 L AcOK. The intensity of these three peaks increases with increasing AcOK dose. A small feature is observed at 1350 cm^{-1} for 0.8 L and above. For 2.9 L AcOK, the 1440 cm^{-1} peak is modified by a pair of small shoulders at 1410 cm^{-1} and 1460 cm^{-1} and small features are visible at $2900\text{--}3000\text{ cm}^{-1}$.

4.2.3 - AcOK on 4 ML Au/Pd{111} – Part II

It is obvious that the sample pre-annealing temperature and, hence, the composition of the immediate surface play an important role in determining the surface chemistry of the adsorbed species. For the second data set, six samples were prepared on the Pd{111} single crystal surface. Each sample was pre-annealed to one of a series of varying temperatures. Each was exposed to an identical AcOK dose and then TPD analysis of the various resulting surface species was carried out. Due to time constraints, it was not practical to carry out RAIRS investigations in this manner.

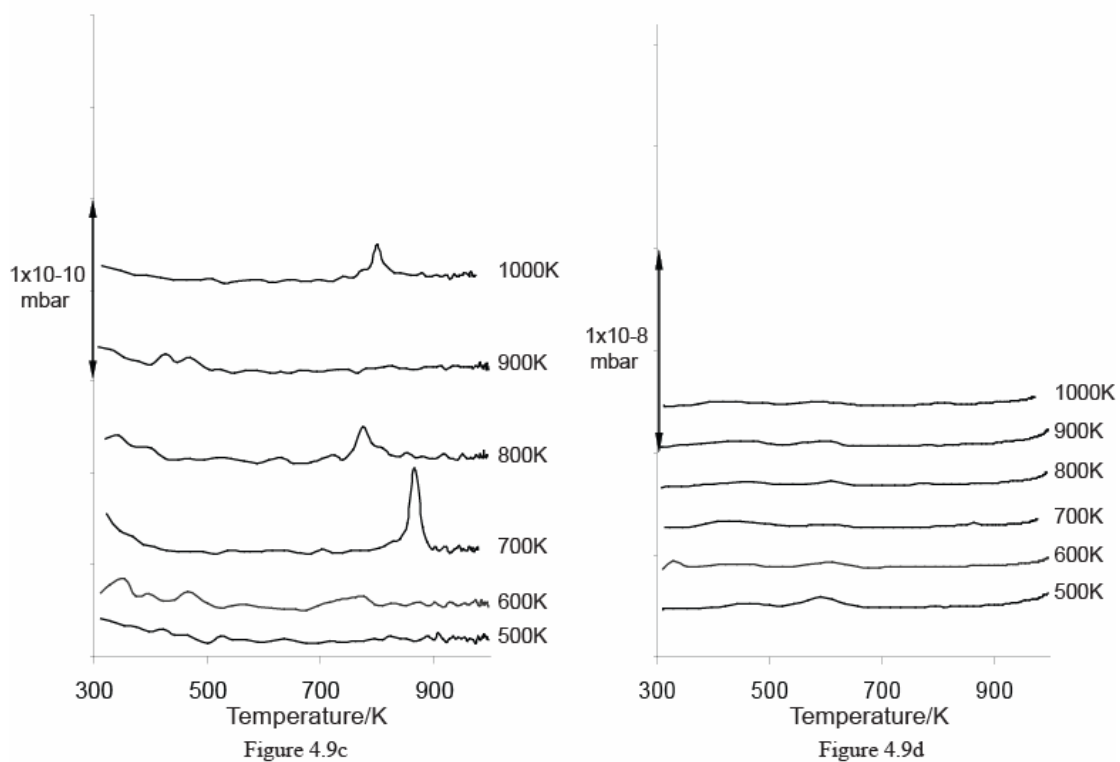
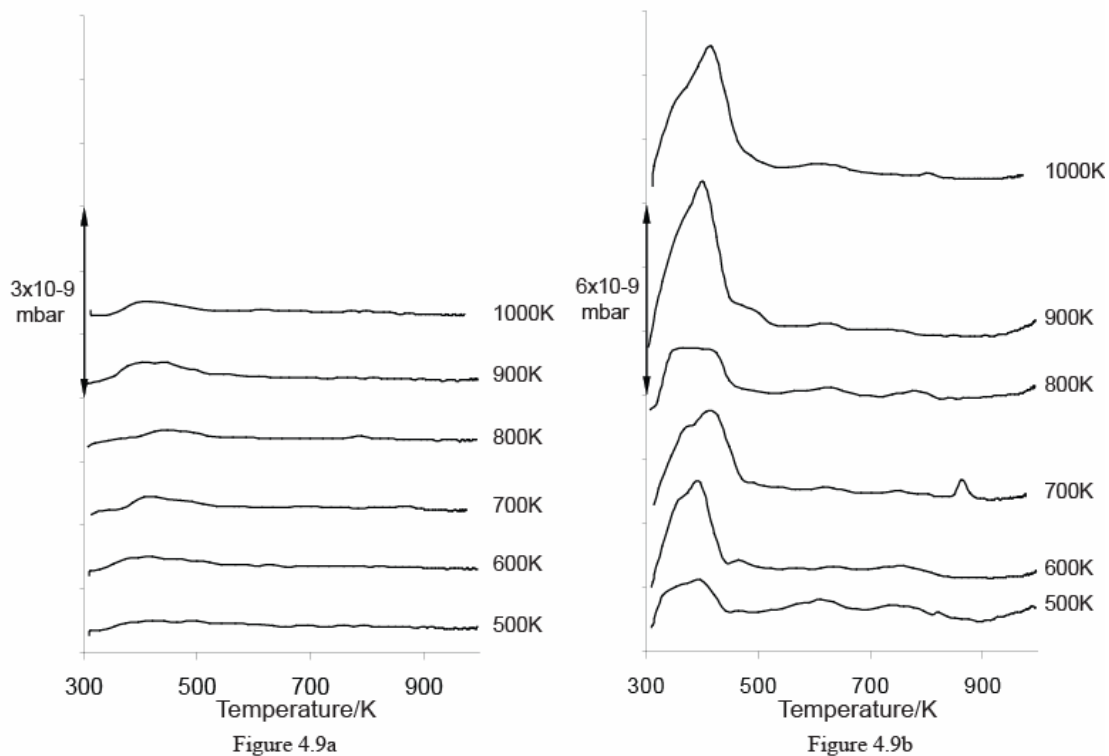


Figure 4.9 - (a) H_2 , (b) CO, (c) K and (d) CO_2 TPD data for 1 L AcOK dosed at 300 K onto ~ 4 ML Au/Pd{111} samples prepared under different pre-annealing conditions.

Figure 4.9a shows mass 2 (H_2) TPD data for a 1 L dose of AcOK on ~ 4 ML

Au/Pd{111} for a series of samples prepared under different pre-annealing conditions. The data show a broad, low intensity feature with a maximum at 430 K. The intensity of this feature increases slightly with increasing pre-annealing temperature.

The mass 28 (CO) data in figure 4.9b show a main feature at ~400 K with a low temperature shoulder at ~370 K. The intensity of both features grows with increasing pre-annealing temperature, with the 400 K peak becoming dominant for 900 K and above. A series of smaller peaks are visible at ~615 K that coincides with features observed in the CO₂ data in figure 4.9d. For the 700 K annealed sample only, a small peak is observed at 865 K. For the 800 K and 1000 K samples, high temperature peaks are visible at 775 K and 800 K respectively. These three high temperature peaks coincide with similar features observed in the K and CO₂ data in figures 4.9c and 4.9d.

Figure 4.9c shows the mass 39 (K) TPD data. Few prominent features are observed except for the peaks at 865 K, 775 K and 800 K peaks coinciding with the CO and CO₂ data in figures 4.9b and 4.9d for the 700 K, 800 K and 1000 K annealed samples respectively.

The mass 44 (CO₂) data in figure 4.9d show a pair of small peaks at ~450 K and ~600 K. Both peaks are broadened with increasing annealing temperature, with the 450 K peak increasing in intensity relative to the 600 K. For the 700 K annealed sample only, a small peak is observed at 865 K. For the 800 K and 1000 K samples, high temperature peaks are visible at 775 K and 800 K respectively. These three high temperature peaks coincide with similar features observed in the CO and K data in figures 4.9b and 4.9c.

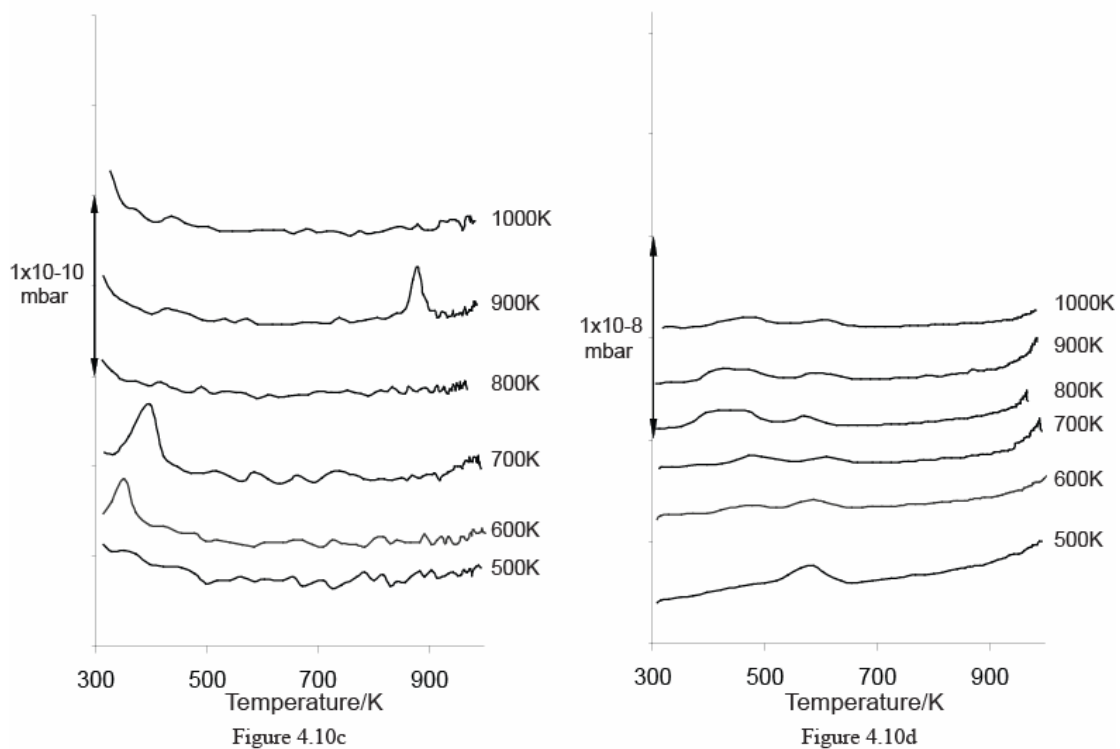
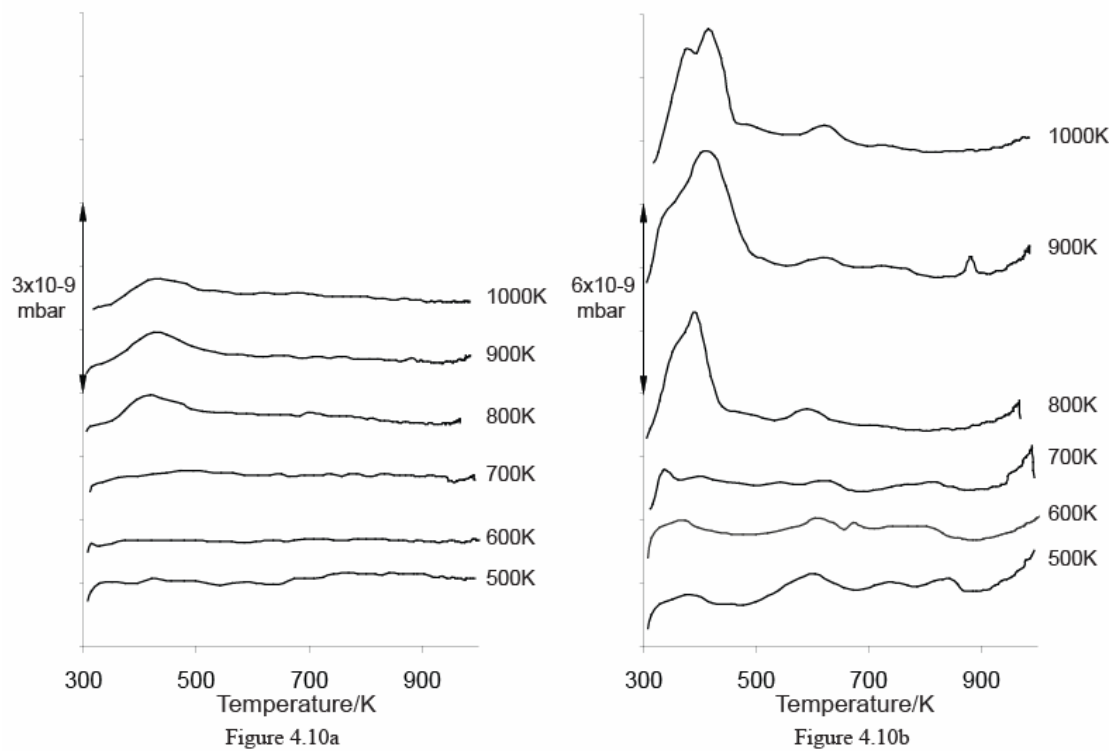


Figure 4.10 - (a) H₂, (b) CO, (c) K and (d) CO₂ TPD data for 4 L AcOK dosed at 300 K onto ~4 ML Au/Pd{111} samples prepared under different pre-annealing conditions.

Figure 4.10 shows TPD data for a 4 L dose of AcOK on ~4 ML Au/Pd{111} for a series of samples prepared under different pre-annealing conditions. In this case, the

AcOK dose is such that the data can be split into two distinct regions relating to the pre-annealing conditions – a low pre-annealing temperature (Au rich) region for samples pre-annealed to 500-700 K and a high pre-annealing temperature (Pd rich) region for sample pre-annealed to 800-1000 K.

Figure 4.10a shows mass 2 (H₂) TPD data. A single broad feature is observed at ~430 K for samples pre-annealed to 800 K or higher. The intensity of this feature is constant with increasing pre-annealing temperature above 800 K.

The mass 28 (CO) data in figure 4.10b show desorption feature at ~370-415 K with a low temperature shoulder at 330-370 K. The intensity of this feature is significantly increased on changing from the 500-700 K pre-annealing temperature region to the 800-1000 K pre-annealing temperature region. Overall intensity and T_{max} for both increase steadily as a function of increasing pre-annealing temperature, with the low temperature shoulder becoming more prominent. A second feature at ~610 K shows the opposite effect, becoming less broad and decreasing in intensity with increasing pre-annealing temperature. This peak coincides exactly with a similar feature observed in the CO₂ data in figure 4.10d. For the 800 K pre-annealed sample only, a small feature is observed at 880 K that coincides with a peak in the K data in figure 4.10c.

The mass 39 (K) TPD data are shown in figure 4.10c. A low temperature feature is observed that increases steadily in T_{max} from 330 K for the 500 K pre-annealed sample up to 470 K for the 1000 K pre-annealed sample. The intensity of this feature increases rapidly with pre-annealing temperature at first, peaking on the 700 K pre-annealed surface and then drops off sharply. For the 800 K pre-annealed sample only, a small feature is observed at 880 K that coincides with a peak in the CO data in figure 4.10b.

The mass 44 (CO₂) data are shown in figure 4.10d. For the 500 K pre-annealed sample, a single desorption peak is observed at 590 K with a small shoulder at 480 K. For increasing pre-annealing temperature up to 700 K, T_{max} values for both features increase steadily to 610 K and 490 K respectively with increasing pre-annealing temperature. The intensity of the ~480 K maximum increases, while the intensity of

the ~600 K maximum decreases steadily with increasing pre-annealing temperature, resolving the feature into two distinct peaks. For the 800 K pre-annealed sample, both features are shifted to lower T_{\max} , appearing at 440 and 570 K, with the 440 K peak now more intense than the 570 K. Again, T_{\max} for both increases with increasing pre-annealing temperature up to 480 K and 600 K respectively.

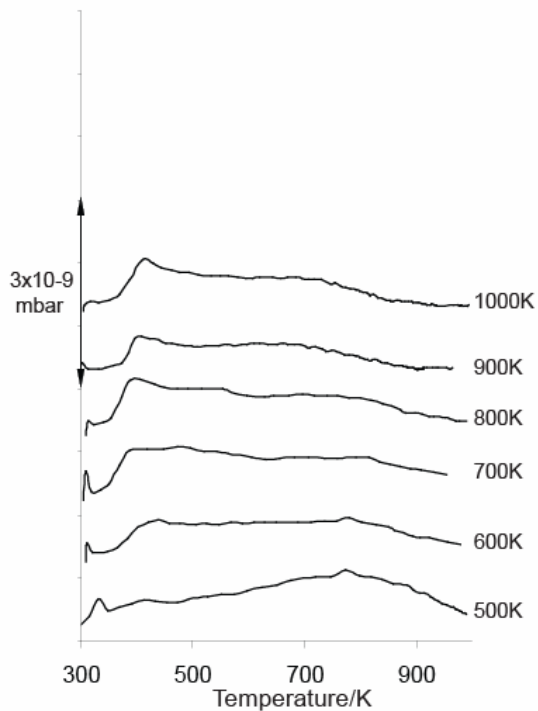


Figure 4.11a

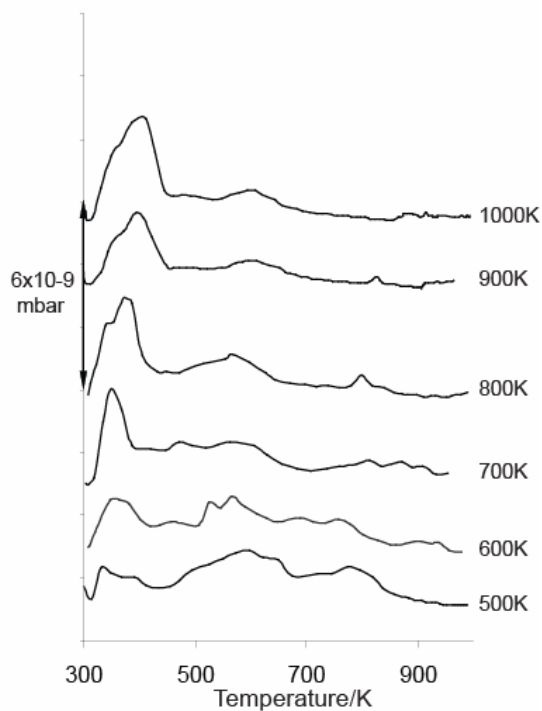


Figure 4.11b

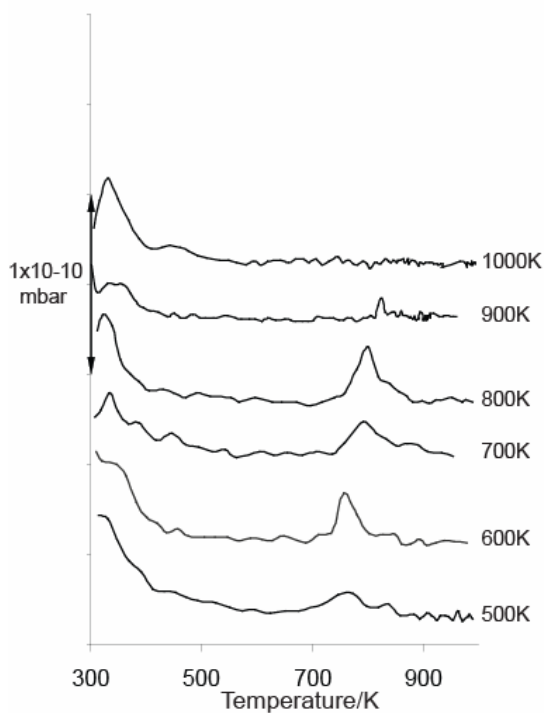


Figure 4.11c

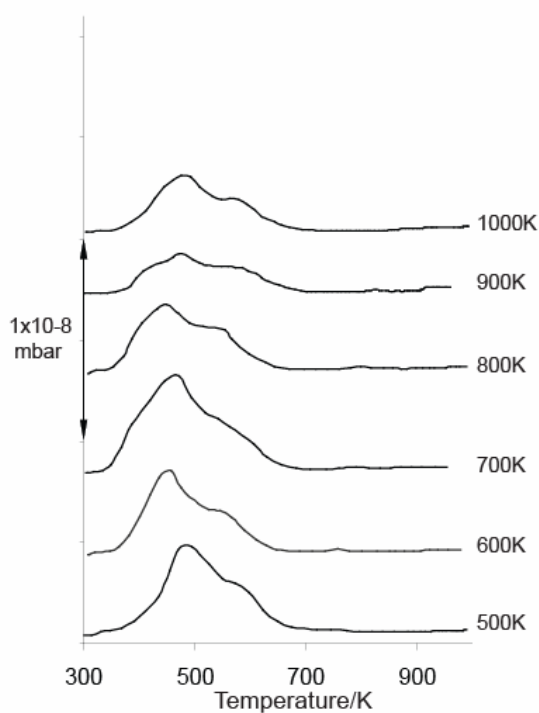


Figure 4.11d

Figure 4.11 - (a) H₂, (b) CO, (c) K and (d) CO₂ TPD data for 16 L AcOK dosed at 300 K onto ~4 ML Au/Pd{111} samples prepared under different pre-annealing conditions.

Figure 4.11a shows mass 2 (H₂) TPD data for a 16 L dose of AcOK on ~4 ML Au/Pd{111} for a series of samples prepared under different pre-annealing conditions.

The data show an initial low temperature feature at 330 K for the 500 K pre-annealed sample decreasing steadily with increasing pre-annealing temperature to 310 K for the 1000 K pre-annealed sample. A broad desorption feature is observed between 350 and 800 K with a low temperature maximum at ~410 K becoming more defined with increasing pre-annealing temperature and a high temperature maximum at ~780 K that decreases in intensity with increasing pre-annealing temperature.

The mass 28 (CO) TPD data is shown in figure 4.11b. On the low pre-annealing T (500-600 K) samples, three broad desorption features are observed – one between ~330-410 K with maxima at 340 K and 390 K, a second between ~520-700 K with maxima at 520 K, 570 K and ~650 K, increasing to ~680 K for the 600 K pre-anneal and a third at around 780 K. As the sample pre-annealing temperature is increased, the low temperature feature becomes first a single peak at 350 K and then a peak at 380-410 K with a shoulder at 350-370 K. T_{\max} for both maxima increases steadily with increasing pre-annealing temperature. The intermediate feature becomes a pair of peaks at 470 K and 600 K on the 700 K pre-annealed sample. As the pre-annealing temperature is further increased the 470 K feature decreases in intensity, giving a single broadened feature peaking at 600 K. The third high temperature desorption feature sharpens and decreases in intensity with increasing pre-annealing temperature. T_{\max} for this peak increases gradually from 780 K to 830 K.

The mass 39 (K) TPD data in figure 4.11c show low temperature and high temperature desorption features corresponding to those in the CO data from figure 4.11b described above. A low temperature feature is observed between with an onset at ~330 K and maxima at 340 K, 390 K and 440 K. The 390 K shoulder decreases in intensity as the sample pre-annealing temperature is increased. A high broad temperature feature is observed at 780 K for the 500 and 600 K pre-annealed samples that sharpens with increasing pre-annealing temperature, with T_{\max} increasing steadily to 830 K.

The mass 44 (CO₂) data in figure 4.11d show a high intensity desorption feature with a peak at ~470 K followed by a high temperature shoulder at ~570 K. T_{\max} for both can be seen to increase slightly with increasing pre-annealing temperature.

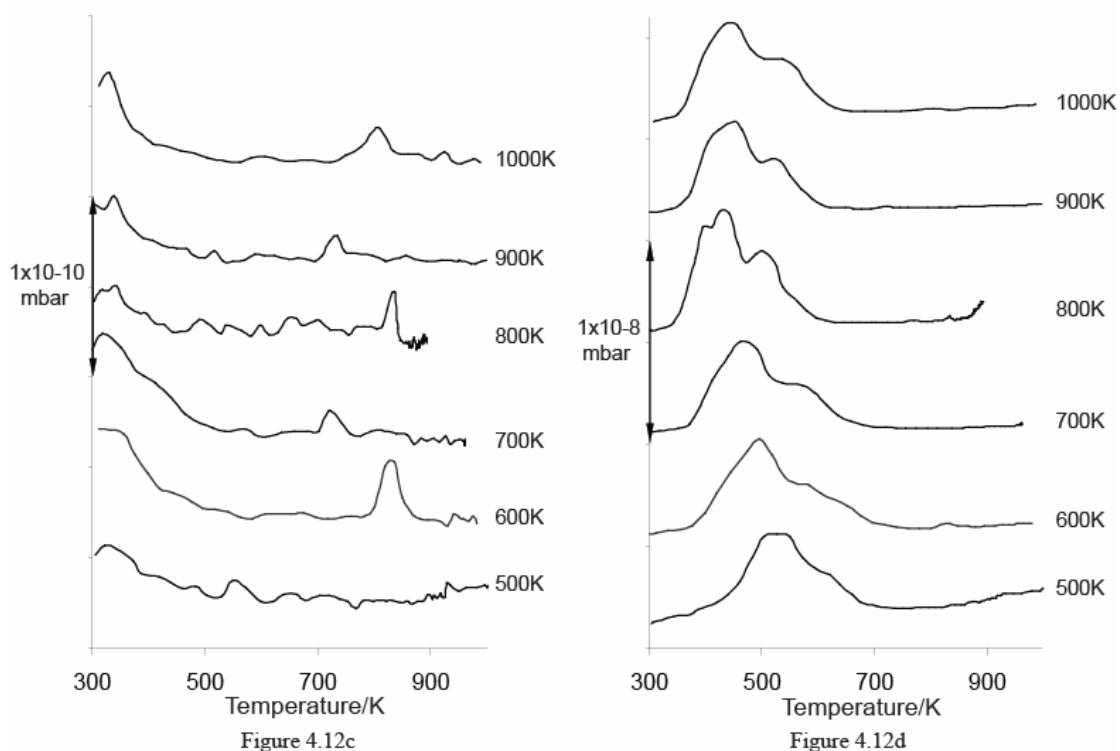
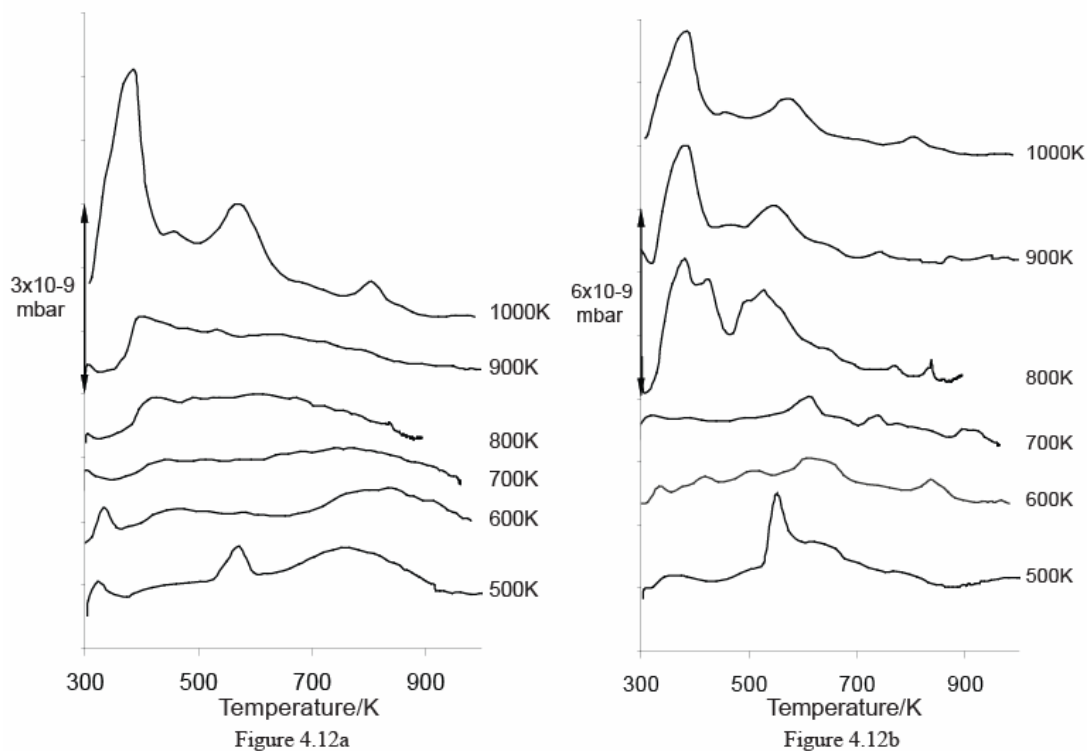


Figure 4.12 - (a) H_2 , (b) CO, (c) K and (d) CO_2 TPD data for 32 L AcOK dosed at 300 K onto ~4 ML Au/Pd{111} samples prepared under different pre-annealing conditions.

Figure 4.12a shows mass 2 (H_2) TPD data for a 32 L dose of AcOK on ~4 ML Au/Pd{111} for a series of samples prepared under different pre-annealing conditions.

The data show a low temperature feature at 330 K for the 500 K pre-annealed sample with intensity and T_{\max} decreasing steadily with increasing pre-annealing temperature to 310 K for the 1000 K pre-annealed sample. A second sharp feature is observed at 570 K, followed by a broad desorption at ~ 770 K. For the 600-900 K pre-annealed samples, a broad desorption feature is observed between 370 and 900 K with a low temperature maximum at ~ 440 K that becomes more intense with increasing pre-annealing temperature with T_{\max} decreasing steadily from 440 K to 390 K and a high temperature maximum at ~ 800 K that decreases in intensity with increasing pre-annealing temperature. On the 1000 K pre-annealed sample, three distinct peaks are observed at 390 K, with a smaller satellite peak at 460 K, and at 580 K and 800 K.

The mass 28 (CO) data in figure 4.12b can be split into two distinct compositional regions relating to the pre-annealing conditions – an Au rich region for samples pre-annealed to 500-700 K and a Pd rich region for samples pre-annealed to 800-1000 K. In the low pre-annealing temperature region, three main features are observed. The first peak is observed at 375 K for the 500 K pre-annealed sample that decreases in intensity with increasing pre-annealing temperature, with T_{\max} decreasing to 315 K on the 700 K annealed sample. The second is a broad feature that appears at ~ 620 K and decreases in intensity and becomes sharper with increasing pre-annealing temperature. A third feature coincides with desorptions seen in the K TPD data in figure 4.12c and is observed at 800 K on the 500 K annealed sample, increasing to 840 K on the 600 K annealed sample together with an increase in intensity. On the 700 K pre-annealed sample, two high temperature peaks are observed at 740 K and 900 K, with the former corresponding to the 740 K potassium desorption in figure 4.12c. For the 500 K annealed sample only, an intense desorption is observed at 550 K. Again, this coincides with the 550 K desorption seen in the K TPD data in figure 4.12c.

For samples pre-annealed to 800 K and beyond, an intense desorption feature is observed at 380 K with a shoulder at 425 K that decreases in intensity with increasing pre-annealing temperature to eventually become a small satellite peak, with T_{\max} increasing steadily up to 460 K on the 1000 K pre-annealed sample. A second feature appears at 525 K, increasing steadily to 580 K on the 1000 K pre-annealed sample. This coincides with K desorptions observed in figure 4.12c. A pair of high temperature peaks are observed at 740 K and 800 K on the 700 K pre-annealed

sample, with the former rising to 800 K and increasing in intensity on the 1000 K pre-annealed sample and the latter rising to 890 K on the 900 K pre-annealed sample and decreasing in intensity and no longer visible on the 1000 K pre-annealed sample. Both features coincide with K desorptions observed in figure 4.12c.

The mass 39 (K) TPD data are shown in figure 4.12c. A broad low temperature feature is observed between with maxima at 340 K, 390 K and 440 K. This feature decreases in intensity as the sample pre-annealing temperature is increased. A second small peak is observed at ~550 K that decreases in intensity with increasing pre-annealing temperature, with T_{\max} increasing steadily up to 600 K on the 1000 K pre-annealed sample. This coincides with the CO desorptions seen in figure 4.12b. On the 600 K pre-annealed sample, a single high temperature desorption peak is observed at 830 K. For samples pre-annealed to 700 K and above, two high temperature desorptions are visible – the first appears at 720 K, increasing to 800 K on the 1000 K pre-annealed sample and the second at 800 K, rising to 920 K on the 1000 K annealed sample. The first peak increases in intensity with increasing pre-annealing temperature, while the second decreases in intensity. Both coincide with desorption features in the CO data in figure 4.12b.

The mass 44 (CO₂) data in figure 4.12d show a single high intensity desorption feature with a peak at ~530 K that decreases steadily with increasing pre-annealing temperature to ~460 K on the 1000 K annealed sample followed by a high temperature shoulder at ~620 K, decreasing to 540 K on the 1000 K pre-annealed sample. A low temperature shoulder becomes apparent at ~440 K on the 600 K pre-annealed sample, decreasing to ~400 K with increasing pre-annealing temperature above 600 K.

4.3 – Discussion

4.3.1 – RAIRS – AcOK on Pd{111} and Au/Pd{111}

Lambert and co-workers monitored the composition of a range of disordered Pd/Au alloy surfaces on Pd{111}, created by depositing ~4 ML Au and then varying the annealing temperature [1]. Surface composition as a function of pre-annealing

temperature is shown below. For low annealing temperatures, they observed that the surface was enriched in Au. For higher annealing temperatures, the surface becomes more Pd-like.

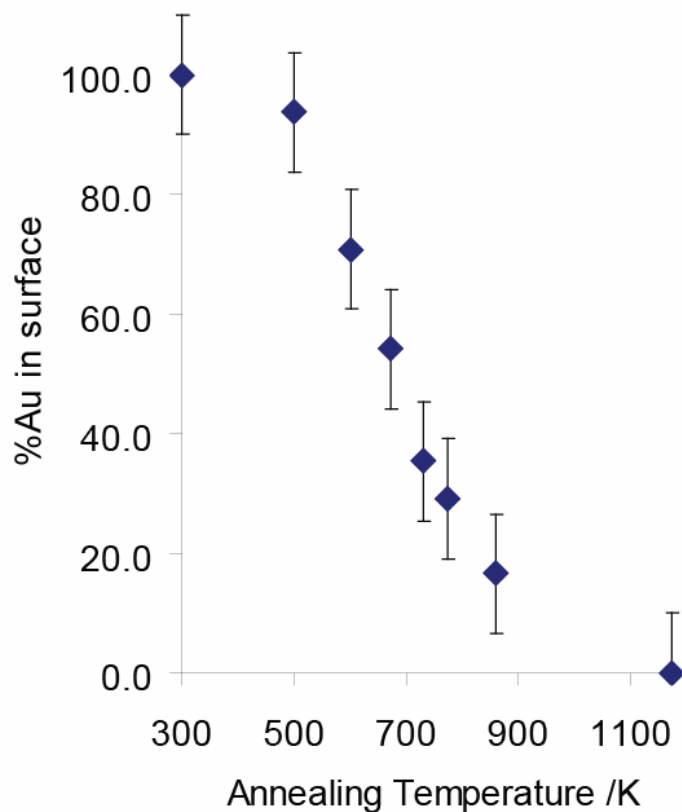


Figure 4.13 – Variation in the Au 69 eV and Pd 330 eV Auger peak intensities for ~4 ML Au on Pd{111} as a function of pre-annealing temperature. Adapted from [1].

Although the co-adsorption of K with acetic acid [2, 5] and formic acid [4, 6-8] has been studied on metal surfaces, no previous studies of AcOK on Pd or Pd alloy surfaces have been reported at the time of writing. In order to better assign our RAIRS features, we have carried out transmission IR measurements on solid AcOK (BDH Chemicals Ltd., 99% purity) and K_2CO_3 (Fischer Scientific, 99.2% purity). The results are shown in figures 4.14 and 4.15 below.

We have assigned RAIRS features as shown in table 4.1 below, using a combination of experimental observations (with references where appropriate) and theoretical spectra calculated using the *Gaussian 03* program with the 6.31 G basis sets and B3-LYP functionals.

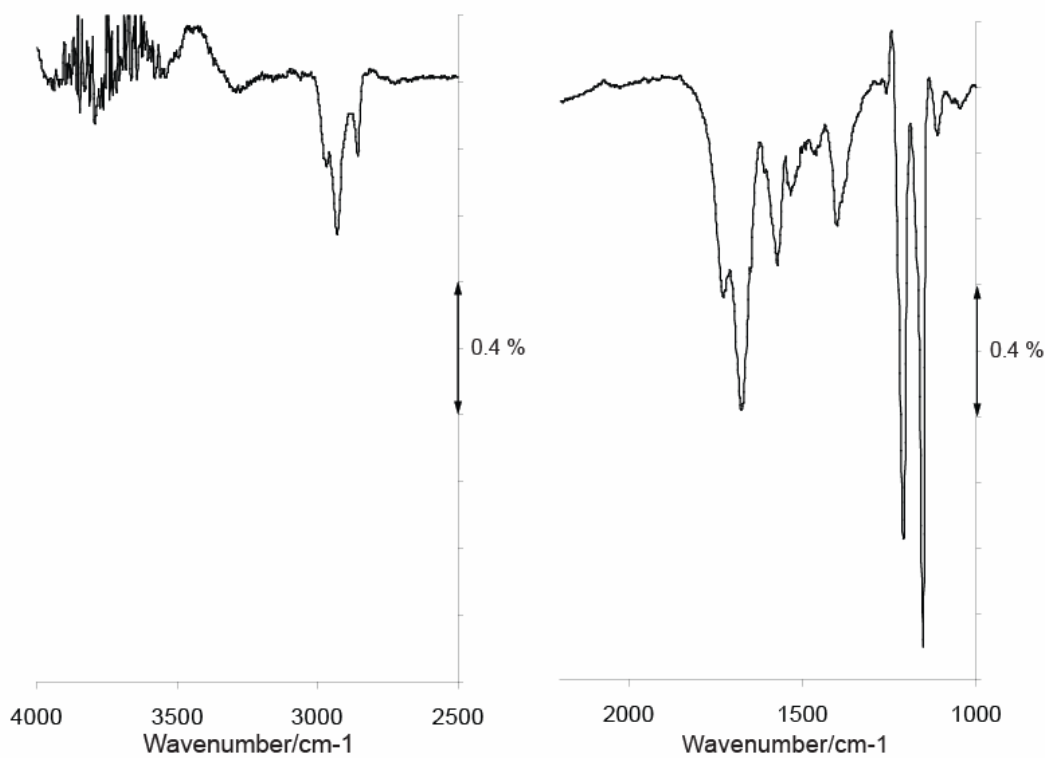


Figure 4.14 – Transmission IR spectrum of solid AcOK.

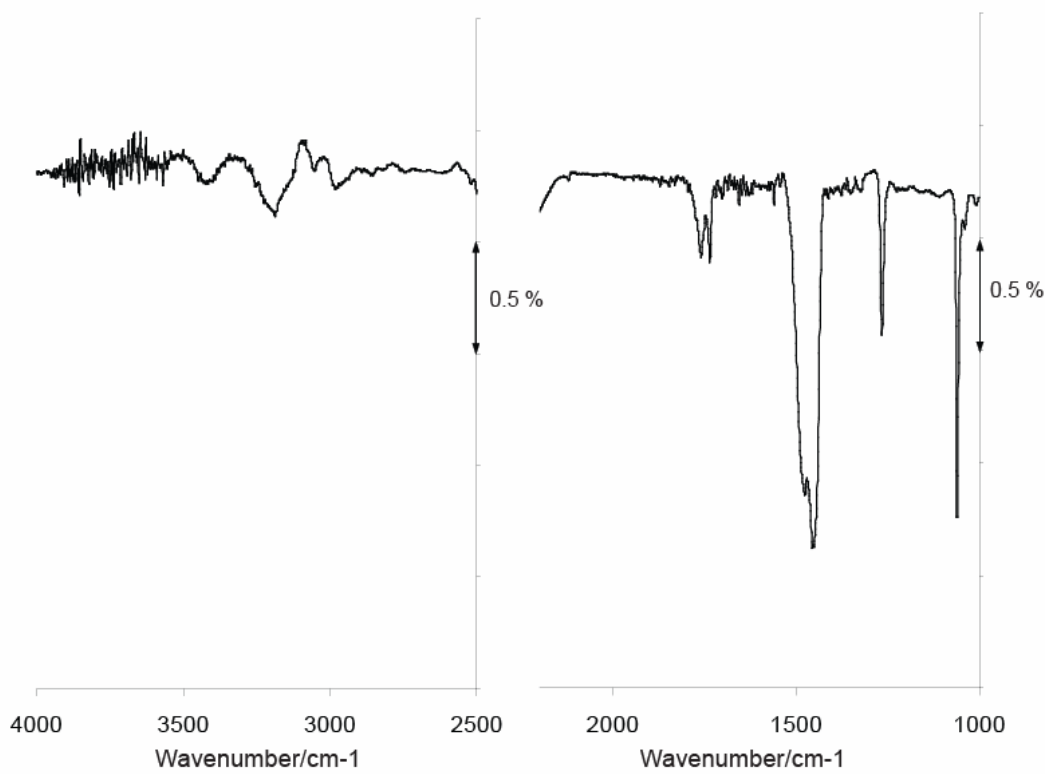


Figure 4.15 – Transmission IR spectrum of solid K₂CO₃.

AcOK (solid)	K ₂ CO ₃ (solid)	AcOK/ Pd{111} [9, 10]	K + CO ₂ /Pd{110} [5]	Au/Pd{111}		Au/Pd{111} 500 K		Au/Pd{111} 600 K		Au/Pd{111} 700 K		Au/Pd{111} 800 K		Au/Pd{111} 900 K		Au/Pd{111} 1000 K		Pd{111}		Assignment
				Low	High	Low	High	Low	High	Low	High	Low	High	Low	High	Low	High	Low	High	
2970	-	2965	-	-	-	-	-	-	-	-	-	-	-	-	-	-	-	-	2970	$\nu(\text{CH}_3)$ [9]
2930	-	-	-	2940	-	-	-	-	-	-	-	-	-	-	-	-	-	-	2930	$\nu(\text{C-H})$
2860	-	-	-	2860	-	-	-	-	-	-	-	-	-	-	-	-	-	-	2860	$\nu(\text{CH}_3)$
-	-	-	-	-	-	-	1888	-	-	-	1870	1880	-	1880	-	1880	1910	2020	2040	$\nu(\text{C-} \alpha \text{) [1]$
-	-	-	-	-	1847	1830	-	1805	-	-	-	-	-	1820	-	1880	1910	1918	2040	$\nu(\text{CO (bridging)}) [1]$
-	1735	-	1770	1766	-	-	-	-	-	-	-	-	-	1820	-	1880	1820	1820	1812	$\nu(\text{CO (3-fold)}) [1]$
1730	1735	1735	-	-	1702	-	1704	-	-	-	-	-	-	-	-	-	-	-	1807	$\nu(\text{C=O}) [5]$
1680	-	1685	1678	-	-	-	-	-	-	-	1590	-	-	-	-	-	-	-	1730	$\nu(\text{C-O}) [9]$
-	-	-	1599	-	-	-	-	-	-	-	-	-	-	-	-	1602	1608	1608	1608	$\nu(\text{C-O}) [5]$
1575	-	-	-	-	-	-	-	-	-	-	-	-	-	-	-	-	-	-	-	-
1535	-	-	1510	-	-	-	-	-	-	-	-	-	-	-	-	-	-	-	-	-
1470	1475	-	-	-	-	-	-	-	-	-	-	-	-	-	-	1470	-	-	-	-
-	1450	-	1440	1440	1440	1440	1440	1444	1444	1442	1442	1442	1442	1442	1442	1440	1440	1440	1440	$\nu(\text{OCO})$
1405	-	1415	-	-	-	-	-	-	-	-	-	-	-	-	-	1420	1410	1410	1410	$\nu(\text{OCO (carbonate)}) [1]$
-	-	-	1352	-	-	-	-	-	-	-	-	-	-	-	-	1350	1350	1350	1350	$\nu(\text{OCO (acetate)}) [10]$
-	1264	1310	-	1275	1275	-	-	-	-	-	-	-	-	-	-	-	-	-	-	$\nu(\text{C-O}) [3]$
1210	-	-	-	-	-	-	-	-	-	-	-	-	-	-	-	-	-	-	-	-
1150	-	-	-	-	-	-	-	-	-	-	-	-	-	-	-	-	-	-	-	-
-	1060	-	-	-	-	-	-	-	-	-	-	-	-	-	-	-	-	-	-	$\nu(\text{C-O}) [2]$

Table 4.1 – Assignment of RAIRS Features for low and high coverage experiments.

It is clear that the presence of Au modifies the surface chemistry of adsorbates on Pd{111}. The decrease in overall intensity of the TPD/RAIRS peaks with increasing Au surface composition for samples exposed to similar AcOK doses suggests that the sticking probability of key adsorbates is reduced by alloying with Au. We observe that the AcOK dose is also a key factor, particularly on the more Pd-rich surfaces so that we will discuss the low coverage and high coverage behaviour separately here.

At low coverage, the main RAIRS band is observed at 1440 cm^{-1} for all surface compositions tested. We observe that the intensity of this feature increases slightly more slowly with increasing AcOK dose on Au-rich surfaces than on Pd-rich surfaces. This feature appears at higher frequency in our data than has previously been reported for acetic acid on Pd{111}, where peaks observed at 1415 cm^{-1} in the HREEL spectra were assigned to the $\nu_s(\text{OCO})$ vibrational mode of a bidentate acetate species [9, 10].

It has been suggested that the presence of co-adsorbed carbon substantially increases the stability of surface acetate species on Pd{111} and Au/Pd{111}, resulting in a higher decomposition temperature and an increase in the $\nu_s(\text{OCO})$ stretching frequency [5, 11]. While it is likely that deposition of surface carbon may result from the adsorption of AcOK on Pd{111} and Pd/Au{111}, giving some stabilization, the dominating influence in our investigations is the presence of co-adsorbed potassium which has been shown to alter the surface chemistry of carboxylate species [4].

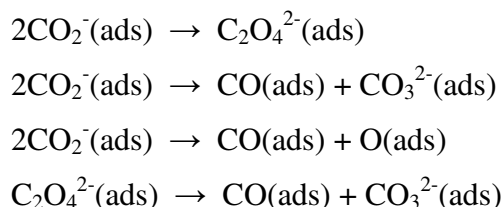
However, in studies of formic acid on Ru{0001} [12], the position of the $\sim 1360\text{ cm}^{-1}$ $\nu_s(\text{OCO})$ vibrational mode was not significantly changed by the co-adsorption of potassium. We cannot therefore assume that the $\nu_s(\text{OCO})$ acetate feature has been blue-shifted from 1415 cm^{-1} to 1440 cm^{-1} due to the presence of potassium on the surface in our case. Furthermore, while Barteau et al. observed a methyl stretching mode at 2990 cm^{-1} for AcO on Pd{111} [10], we do not observe significant features in this region on any surface tested at low coverage.

In light of these observations, we propose that the 1440 cm^{-1} band is not due to surface acetate, and that we do not form surface acetate at low coverage on Pd-rich

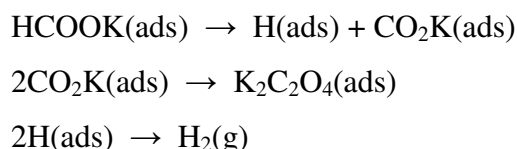
samples or at any coverage tested on Au-rich samples. Instead, the supplied AcOK is reacting with the surface to form another species.

The most likely scenario involves the reaction of potassium acetate with the surface to form adsorbed carbonate species. The co-adsorption of CO₂ and potassium metal on Pd{110} has been shown to result in a characteristic CO₂ desorption feature that was assigned to a carbonate decomposition [4].

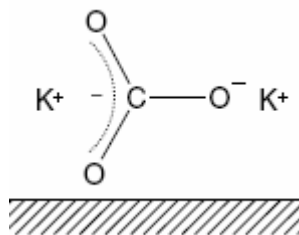
Chemisorption of CO₂ on alkali metal promoted surfaces has been found to lead to the formation of many surface species including oxalate, carbonate and CO as shown below [13].



King and co-workers studied the decomposition of formic acid on potassium pre-covered Co{1010}, concluding that the adsorbed potassium formate reacts on the surface to form oxalate by the following sequence [6].

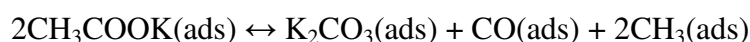


The formation of CO₃²⁻ from CO₂⁻ and C₂O₄²⁻ in the presence of co-adsorbed CO then proceeds as above. A RAIRS band observed at 1440 cm⁻¹ was assigned to the asymmetric stretch of carbonate, suggesting that the molecular plane is perpendicular to the substrate with one of the C-O bonds approximately parallel to the surface as shown in figure 4.16 [6]. This geometry is thought to arise from bidentate and monodentate coordination of the carbonate with two K atoms as shown in figure 4.15 below, so that the ν_a(OCO) is the only one of the IR active vibrations that gives rise to a strong band in the RAIRS spectrum.

Figure 4.16 – Configuration of K_2CO_3 on Pd{110} from [6].

We propose that our low coverage RAIRS data points to the formation of carbonate on the surface. Hence, we assign the 1440 cm^{-1} RAIRS to the $\nu_a(\text{OCO})$ mode of carbonate in agreement with [6].

In agreement with [4], we propose the following mechanism for the decomposition of AcOK(ads) to K_2CO_3 (ads), CO(ads) and CH_3 (ads) on Pd{111} and Au/Pd{111}.



Wiesel et al. have previously proposed that the formation of carbonate from formate on Ru{001} is reversible [12] and our high coverage data suggests this is also the case for acetate as will be discussed. In addition to our assignment of the 1440 cm^{-1} RAIRS feature, it is necessary to discuss the behaviour of adsorbed CO on our surfaces.

IR stretching frequencies for CO on the various adsorption sites on Pd{111} have previously been assigned as follows; $2110\text{-}2018\text{ cm}^{-1}$ for linearly bound CO in atop sites, $1965\text{-}1900\text{ cm}^{-1}$ for CO on 2-fold bridging sites and $1900\text{-}1800\text{ cm}^{-1}$ for CO bound in 3-fold hollow sites [1, 14-16]. Again, despite a number of investigations, no evidence has been found for the adsorption of CO on planar Au surfaces at 300 K. Although features relating to the adsorption of CO atop Au have been observed on Pd/Au alloy surfaces, such species were found to desorb well below 300 K so will not be discussed further here [1, 17].

While we expect to produce some CO by reaction of AcOK with the surface at 300 K, we must also consider the possibility that CO has adventitiously adsorbed onto the surface before or during the AcOK exposure. As has been stated in the procedures

section in Chapter 2, the residual gas pressure in the vacuum chamber must be in the range of around 10^{-10} mbar in order to maintain a clean surface for up to one hour. However, the reactivity of the Pd{111} surface as well as the time-consuming nature of these experiments means that some adsorption of unwanted background species, particularly CO, is inevitable. Secondly, it is likely that some of the CO adsorbed on the walls of the vacuum chamber will be displaced and released into the background on dosing AcOK.

The low-coverage data for AcOK on Pd{111} and our 900-1000 K pre-annealed samples show clear features at $\sim 1810\text{ cm}^{-1}$, $\sim 1910\text{ cm}^{-1}$ and $\sim 2040\text{ cm}^{-1}$ that have been assigned to CO in 3-fold coordinating, bridging coordinating and atop coordinating sites on Pd respectively in agreement with [15]. For the more Au-rich samples, only weak features are observed in the $1800\text{-}1890\text{ cm}^{-1}$ region at low coverage.

As the AcOK dosage is increased, we begin to observe a number of striking differences in the behaviour of the Au-rich and Pd-rich surfaces.

A new vibrational feature observed at $\sim 1600\text{ cm}^{-1}$ for higher coverage on most of our samples and for $K + CO_3$ on Pd{110} [4] has been assigned to a potassium-perturbed CO vibration. As the surface becomes more Pd-rich, the intensity of the $\sim 1600\text{-}1700\text{ cm}^{-1}$ feature decreases and the $\sim 1810\text{ cm}^{-1}$ feature grows in intensity. While we would not expect to detect much CO adsorption on Au-rich surfaces at 300 K, it is more likely that CO is bound to surface potassium on the Au-rich surfaces. This feature does not appear at lower coverages, presumably because the surface coverage of potassium is too low. As the surface becomes more Pd-rich and the density of Pd ensembles increases, adsorption of CO on Pd sites becomes more favourable and the expected $\sim 1810\text{-}2040\text{ cm}^{-1}$ bands become more intense.

For higher AcOK doses on Pd{111} and Pd-rich alloy surfaces only, the 1440 cm^{-1} feature is modified by the appearance of a pair of shoulders at 1410 cm^{-1} and 1470 cm^{-1} . The origin of the 1470 cm^{-1} feature is ambiguous, since IR spectra of solid AcOK and K_2CO_3 both show $\nu(\text{OCO})$ features at $1470\text{-}1475\text{ cm}^{-1}$. However, the 1410 cm^{-1} vibration is very similar to one that has previously been observed for acetate on Pd{111} [10]. Therefore, in agreement with [10], we assign the 1410 cm^{-1} feature to

the $\nu_s(\text{OCO})$ stretching mode of bidentate acetate.

On the Pd{111} surface, we observe a set of bands at 2860-2970 cm^{-1} for higher AcOK doses only. The appearance of a band at 2970 cm^{-1} agrees well with previous studies of acetate on Pd{111} and is assigned to a $\nu_s(\text{CH}_3)$ stretching mode [9]. Additional features observed at 2860 cm^{-1} and 2940 cm^{-1} in our data are not observed in [9], but are both observed in the IR spectra of solid AcOH and AcOK. The 2860 cm^{-1} band is assigned to a $\nu_a(\text{CH}_3)$ stretching mode, while the 2930 cm^{-1} band is assigned to $\nu_a(\text{C-H})$ mode. Our *Gaussian 03* calculations show that the dynamic dipole moments of these vibrations would be parallel to the surface for acetate in the expected bidentate conformation.

It is possible that we are forming $K(\text{ads}) + \text{AcO}(\text{ads})$ and that interaction with surface potassium causes the bidentate surface acetate to tilt such that the 2860 cm^{-1} and 2930 cm^{-1} vibrations, which would normally be parallel to the surface, are now visible in the RAIRS. Alternatively, it may be that exposing the surface to high doses of AcOK results in the formation of islands of AcOK(ads) on the surface.

An additional smaller feature observed at $\sim 1730 \text{ cm}^{-1}$ is assigned to a $\nu(\text{C=O})$ stretch in agreement with a similar feature that was observed in [9]. In DRIFTS studies of a working VAM catalyst surface, Augustine and Blitz [13] observed absorption features relating to bidentate acetate as well as a further absorption feature at 1735 cm^{-1} . They were able to confirm that this additional feature was not due to either physisorbed or condensed acetate, but described the presence of what was termed a Pd-ester distinct from bidentate acetate. Formally, this assignment corresponds to the presence of monodentate surface acetate, a species that has been proposed as a reaction intermediate in the formation of vinyl acetate.

In our case, the assignment of the 1730 cm^{-1} RAIRS feature is ambiguous, since a similar feature would be expected either from tilted acetate or from potassium carbonate in the configuration shown in figure 4.16 [4]. Our TPD data does not seem to show significant evidence for the presence of monodentate acetate, as will be discussed in section 4.3.2. The 1730 cm^{-1} band is more likely associated with surface carbonate, in agreement with our assignment of the 1440 cm^{-1} feature.

The RAIRS spectrum for the unannealed Au film in figure 4.2 shows C-H stretching features at $\sim 2860\text{-}2970\text{ cm}^{-1}$, that are similar to those observed on the Pd-rich surfaces. Previous studies have shown that a $\sim 3\text{-}4$ ML thick Au film is not sufficiently homogeneous to completely cover the Pd{111} surface at 300 K, but forms a continuous alloy layer after annealing beyond ~ 600 K [1, 5], so that this feature may simply be indicative patches of bare Pd exposed by cracks in the Au overlayer.

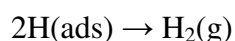
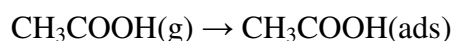
In order to better collate our RAIRS findings with our TPD data, it would be useful to repeat the RAIRS measurements after heating the AcOK covered surface. Unfortunately, it was not possible to measure reliable RAIR spectra after annealing the sample. This is an obvious area for further investigation.

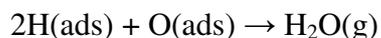
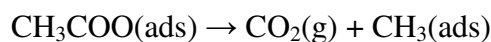
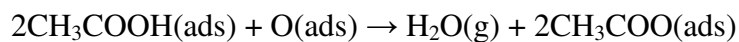
4.3.2 – TPD – AcOK on Pd{111} and Au/Pd{111}

The desorption processes observed above are complex and may involve the formation and decomposition of a number of different surface species as well as multiple-layer desorptions, meaning that a simple treatment in terms of desorption energies may not be appropriate.

Although the adsorption of AcOK on Pd surfaces has not previously been studied, the behaviour of the three key surface species AcO(ads), K(ads) and CO(ads) on various surfaces has been well documented as is summarized below.

Bowker and Aas carried out the first detailed study of AcOH on Pd{110} [11]. Acetic acid was found to adsorb onto the surface and remain stable up to ~ 350 K. This is similar to results obtained for the AcOH/Rh{111} system where AcOH was found to be stable up to ~ 380 K [18]. Adsorption results in deprotonation of the O-H group, giving a bidentate bridging acetate species where both oxygen atoms are equivalent. From analysis of the TPD data, the adsorption, desorption and decomposition mechanisms were assigned as follows:





The C(ads) left behind on the surface acts as a site-blocking adatom, increasing the temperature of some of the desorption steps. Bowker and co-workers found that the co-adsorption of atomic C, N or O resulted in the stabilisation of surface acetate on Rh{110}, offering three possible explanations for this [18]. The first assumes that a surface reconstruction, similar to the Cu{110}-(2x1)O reconstruction [19], changes the nature of the adsorption sites, affecting the available bridging options. Secondly, it may be that adsorbed carbon is acting as a catalytic poison by blocking sites adjacent to the acetate which would be required for its decomposition.

A third possible explanation involves the concept of adsorbate-induced ordering. For the AcOH on Rh{110} system, this was explained as follows [18]. Initial adsorption on the clean surface is random and the acetate is unstable at room temperature. The attractive interaction between the acetate and the adjacent adatoms forces the acetate to arrange itself in an ordered pattern as shown in figure 4.16 below. This ordering of the acetate blocks the decomposition sites, increasing the thermal stability of the overlayer. This was taken to be the most likely explanation since it best fitted the proposed rate equations and fitted well with the explosive kinetics observed during autocatalytic decomposition at higher temperatures.

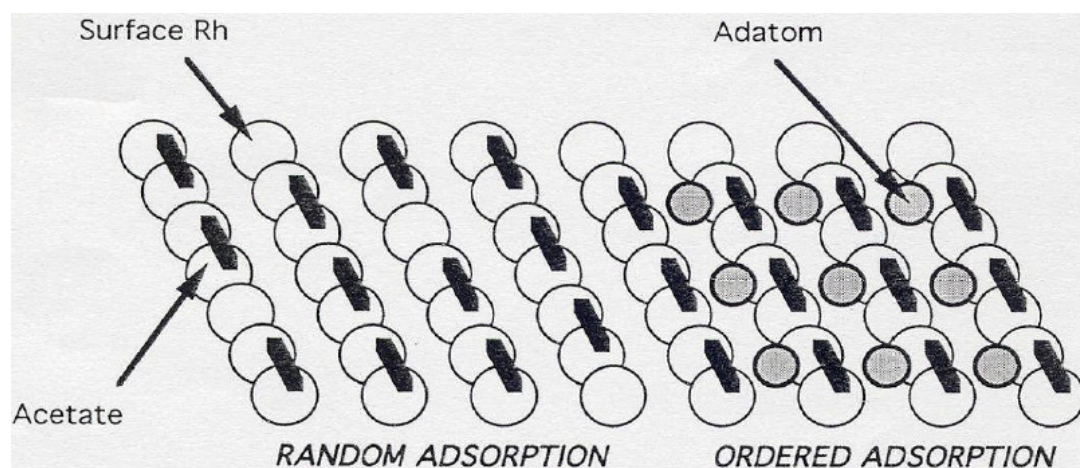
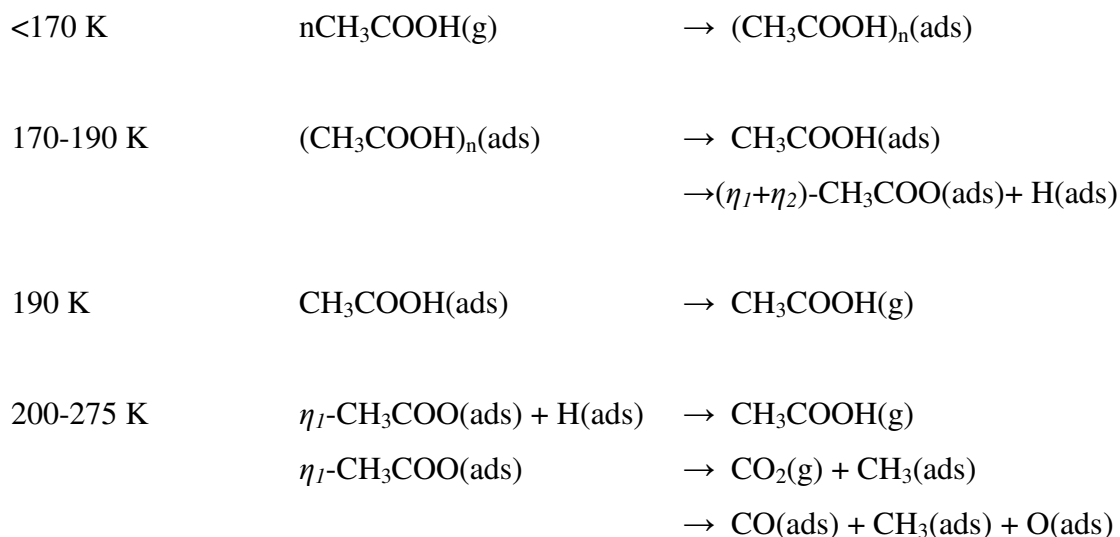


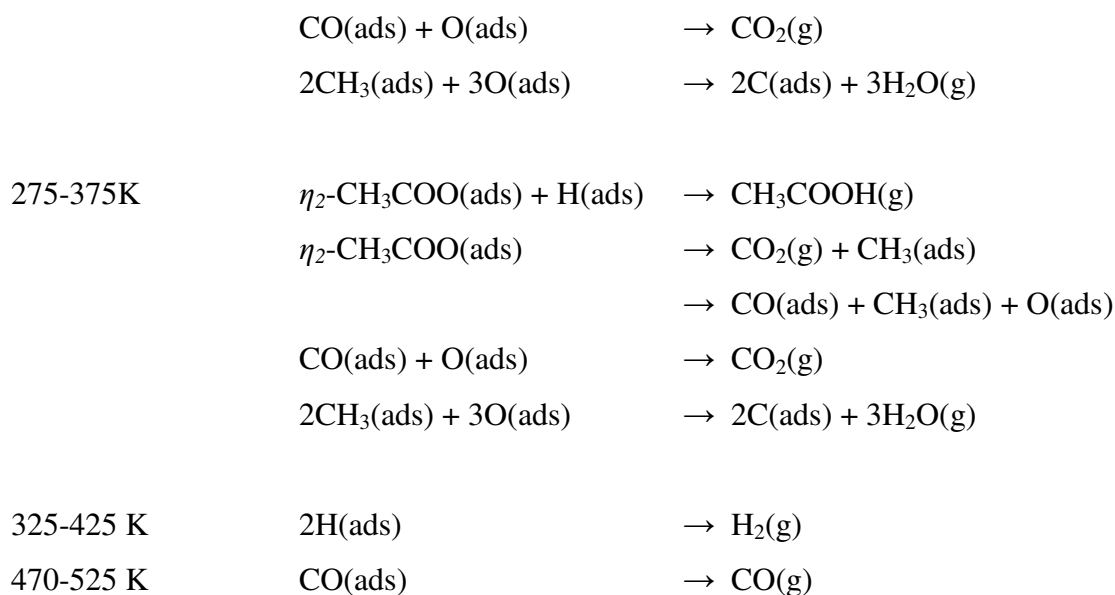
Figure 4.16 – Co-adsorbate induced ordered adsorption on Rh{110}. Image taken from [18].

Davis and Barteau found that the mechanism for acetic acid decomposition on clean Pd{111} is different to that seen on Pd{110} [10]. The adsorbed acetic acid was found to decompose between 350 K and 375 K to give CO₂ and H₂, analogous to the behaviour observed on Rh{110} [18]. Pre-adsorption of oxygen to form a Pd{111}-(2x2)O overlayer was found to stabilize the acetate up to 400 K, delaying the onset of autocatalytic decomposition to higher temperatures [20].

Acetic acid adsorbs molecularly on Pd{111} at low temperatures, usually forming bidentate acetate on heating to ~300 K, although there is some evidence of for the formation of monodentate species [9]. The bidentate acetate species adsorbs with acetate oxygen atoms approximately atop Pd sites and the OCO plane aligned along the surface normal [21]. Theoretical calculations have shown that the bidentate species thermally decomposes at ~400 K by rocking about the OCO group until the methyl group can reach a free Pd site on the surface and dehydrogenate [22, 23]. This process has been shown to occur explosively on carbon-covered Pd{110} [24] and oxygen-covered Pd{111} [20].

Haley et al. carried out TPD experiments on acetic acid adsorbed on Pd{111} at 170 K and proposed the existence of two competing decomposition pathways, as shown in the reaction scheme below [9], corresponding to the decomposition of mono (η_1) - and bidentate (η_2) acetate species. Acetic acid desorption was observed at ~230 K and ~310 K, with the major decomposition products consisting of CO₂ at 200-400 K, CO at ~490 K H₂ at ~380 K and water.

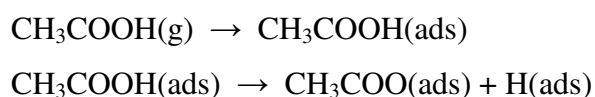


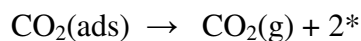
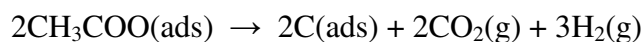
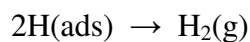


The observation of TPD features at ~400-500 K for CO and ~410 K for H₂ in our investigation is in agreement with the above mechanism, but, in our study, CO₂ desorption was not generally seen until higher temperatures. There are effectively two competing pathways for acetic acid decomposition. In the first, acetic acid decomposes via a single step to liberate gaseous CO₂ while the second pathway results in the formation of CO(ads). In both cases, CH₃(ads) eventually breaks down in stages giving a series of three H₂(g) desorptions and C(ads). Haley et al. proposed that the pathway 1 was associated with bidentate acetate, while pathway 2 was initiated via a monodentate surface acetate [9].

The adsorption of acetic acid at 300 K on Pd{110} [24] and Rh{111} [25] is found to occur via two dissociative pathways, one leading to adsorbed acetate and hydrogen and the other leading to adsorbed CH_x, hydrogen, CO and oxygen. Desorption of CO, CO₂, H₂ and H₂O is observed on annealing, with a significant amount of carbon left behind on the surface.

One of the main sources of CO₂ production during VAM synthesis is thought to be the autocatalytic decomposition of surface palladium acetate species. The mechanism for such a process is thought to be as follows:





The * here represents a vacant active site, which in this case would be a palladium ensemble. A simplified version of this process is shown in figure 4.17.

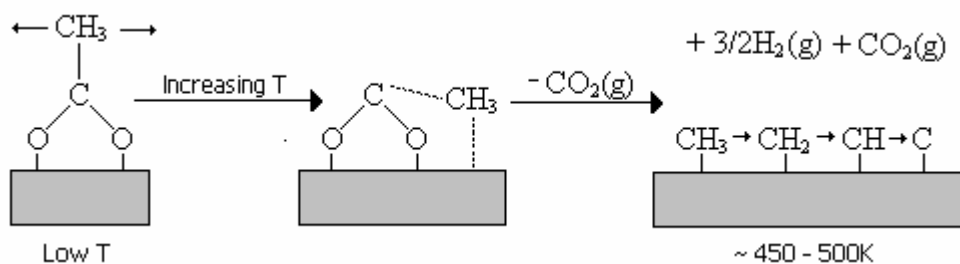


Figure 4.17 – Autocatalytic decomposition of AcOH on the metal surface.

In TPD studies of acetate species on Pd surfaces, a peak relating to the production of CO₂ by autocatalytic processes is observed at around 350 K. Studies of model Pd/Au VAM catalysts has shown stabilisation of surface acetate to higher temperatures, with the CO₂ peak appearing at 450 K [26].

At the time of writing, no evidence is available for the adsorption of acetic acid on Au surfaces at 300 K. Tysoe and co-workers found that AcOH desorbed intact from Au rich alloy surfaces with a given activation energy of ~52 kJmol⁻¹ [3], which is close to the value of 54 kJmol⁻¹ found for formic acid on gold [27]. The key difference between adsorption of potassium acetate and acetic acid on Au is the mass. As the mass increases, the van der Waals interactions will increase, so it is feasible that AcOK could adsorb intact on Au at 300 K.

Previous experimental [14] and theoretical [22] studies have suggested that the decomposition of surface acetates by autocatalytic processes requires the presence of large Pd ensembles. As the surface Au composition is increased, the number of such ensembles decreases so that the autocatalytic decomposition process is inhibited. The

implication for VAM synthesis is that the addition of Au to the Pd catalyst acts to stabilise the surface acetate species against decomposition by unselective reaction pathways which would otherwise take place under reaction conditions at 450 K.

As has been noted, the decomposition of surface acetate is not necessarily the only source of surface CO and H₂ here. Our RAIRS data shows evidence of adsorbed CO, especially on Pd-rich surfaces, but the origin of this is ambiguous. We have already discussed TPD of CO on PdAu alloy surfaces in Chapter 3. In agreement with Baddeley et al. [1], we assign the lower temperature CO desorptions observed in the range 300-450 K to molecular CO, either adsorbed onto the surface from the background gases or from the decomposition of surface species at lower temperatures.

The higher temperature (>450 K) CO desorption features are the direct result of reaction-rate limited decomposition of surface species. Similarly, in the case of H₂, while low temperature desorptions may indicate the presence of co-adsorbed H₂, any desorptions above 350 K are due to reaction-rate limited breakdown of surface species, the most likely candidates being AcO and CH_x [28].

In contrast, adsorption of CO₂ from the residual background gases is not expected to be significant on the clean surface, however, CO₂ has been found to react with K pre-dosed Pd surfaces to form surface carbonates [4]. It is unclear whether this process is taking place in our experiments, since we are dosing potassium in the form of AcOK here and not potassium metal as in the previous studies. The increase in the 430 K and 510 K CO₂ peak intensities and subsequent decrease in the ~350 K and ~410 K CO peak intensities with increasing dosage points to displacement of CO from the surface due to uptake of AcOK and the subsequent decomposition of the resulting surface species to produce CO₂.

We have observed from our RAIRS data that the surface chemistry is dependent on both the surface coverage and the surface composition. In order to study the effects of surface coverage, we will first discuss the data in figure 4.1 for AcOK on Pd{111}.

Figure 4.1b above shows that, for up to 64 L coverage, molecular CO desorption from AcOK on Pd{111} was observed in a peak at around 400-425 K with a low

temperature shoulder appearing at around 340-350 K. These are thought to correspond with the IR features at 1910 cm^{-1} and 2040 cm^{-1} and are assigned to CO in 3-fold hollow sites and in atop sites respectively. As the AcOK dose is increased and the available surface sites are filled, the $\sim 350\text{ K}$ TPD and 2040 cm^{-1} RAIRS features grow in intensity relative to the $\sim 410\text{ K}$ and 1910 cm^{-1} , supporting this assignment. For 128 L AcOK and more on Pd{111}, a broad peak is observed at $\sim 360\text{ K}$ followed by a second peak at 440-480 K. This may be due to the formation of multiple layers at high AcOK exposure or it may indicate the stabilization of CO by co-adsorbed K as reported in [4].

The data in figure 4.1d shows CO_2 desorption occurs at $\sim 510\text{ K}$ with a low temperature shoulder at $\sim 430\text{ K}$. The $\sim 510\text{ K}$ desorption is higher than would be expected from acetate on Pd{111}. Haley et al. reported that the desorption of CO_2 as a result of acetate decomposition was complete by $\sim 400\text{ K}$ [9, 10]. We propose that this feature is a result of the decomposition of surface carbonate [29], in agreement with our assignment of the 1440 cm^{-1} RAIRS feature [4]. At higher AcOK coverages, the growth of the RAIRS features at around 1410 cm^{-1} and $2900\text{-}3000\text{ cm}^{-1}$ and the CO_2 desorption feature at $\sim 430\text{ K}$ points to the formation of bidentate acetate on the surface [26].

Figure 4.1c shows that K desorption from AcOK on Pd{111} occurs in a peak at 790 K for low coverage. The position of this feature varies smoothly from 790 K to 940 K as the initial AcOK dose is increased. The kinetics of this desorption process are strongly dependent on the surface coverage with the peak narrowing with increasing coverage. This feature always coincides with peaks observed in the corresponding CO and CO_2 data sets. It is known that multilayer potassium on Pd{110} will give a peak at around 313 K, while monolayer K^+ ions desorb in the region 900-1000 K [30]. Bulk potassium carbonate is known to decompose at around 1064 K, a higher temperature than has been observed for carbonates of other alkali metals [31]. TPD features relating to the decomposition of potassium carbonates have previously been observed in the range 800-1000 K [30, 31]. We propose that the high temperature features in our data are indicative of the formation of islands of carbonate or acetate, or most likely a mixture of both species, on the surface.

In order to illustrate the effect of island formation on the desorption kinetics consider two scenarios. In the first case, molecules are distributed across the surface in the form of a large number of small islands. In the second case, a similar number of molecules are distributed in a small number of large islands. We assume that molecules in the centre of the islands are unable to desorb as they are held very strongly via ionic interactions with neighbouring species. Species at the edges of islands are less strongly bound and the probability of desorption of edge species is proportional to $\exp[-E_d/kT]$, where E_d is the desorption enthalpy, k is Boltzmann's constant and T is the absolute temperature. In a small temperature window between T and $T + \Delta T$, the number of desorbing species will be given by N_{edge} (the number of edge located species) multiplied by the exponential term.

In the first scenario, since N_{edge} is relatively large, a sizeable desorption occurs even at relatively low temperature, but the rate of desorption increases only slightly as the temperature is increased since the exponential term varies only weakly at low temperature. Hence there will be a measurable desorption rate at low temperature and the desorption trace will be relatively broad. In contrast, in the second scenario, where N_{edge} is small, the desorption rate is very small at low temperatures and only becomes sizeable when T is high enough for the exponential term to be significant. Since this exponential term increases dramatically at higher temperatures, the desorption rate increases very rapidly resulting in a higher temperature desorption peak which is significantly narrower.

The formation of mixed carbonate and acetate islands on the surface fits well with our assignment of the 2940 cm^{-1} and 2970 cm^{-1} RAIRS features as C-H stretching frequencies that cannot come from surface carbonate alone. In this case, it is possible that an adsorbate-induced ordering effect, as has been described in [18], results in the high temperature K, H₂, CO and CO₂ peaks seen at around 900-1000 K.

In agreement with [4], we propose the following mechanism for the decomposition of AcO(ads) to CO₃(ads), CO(ads) and CH₃(ads) in the presence of K(ads) on Pd{111}.



This appears to be the main surface process at low coverage on Pd{111}, giving rise to the ~510 K CO₂ desorption. The appearance of the strong 1440 cm⁻¹ band in our RAIRS data suggests that this process occurs at 300 K. The CO produced, as well as the adventitiously adsorbed CO species, then desorb between 300 K and 450 K as expected. A fraction of the adsorbed species react with K(ads) to form small islands of K₂CO₃, although the coincident H₂ desorption suggests this is mixed with either AcOK or KHCO₃, that give rise to the high temperature H₂, CO, K and CO₂ features observed at ~790 K. As we supply the surface with more AcOK we observe two main processes. First, the formation of bidentate acetate on the surface becomes more favourable, as evidenced by the growth of the ~430 K CO₂ desorption feature and the 1410 cm⁻¹ and 2900-3000 cm⁻¹ RAIRS features. Secondly, the increase in the profile and intensity of the high temperature feature and its continuous shift to higher temperature suggests the formation of larger islands.

It is clear from both the TPD and the RAIRS data that the surface chemistry is strongly dependent on the surface composition. The structure of Au/Pd{111} alloy surfaces are discussed in detail in Chapters 1 and 3. The literature shows intermixing of Au with the substrate on annealing to ~600 K, giving rise to an Au-rich alloy region at pre-annealing temperatures below ~700 K and a Pd-rich region above ~800 K [1, 5]. This compositional change is mirrored in the TPD/RAIRS data, especially for lower AcOK doses. It should be noted that, while we have already shown in Chapter 3 that adsorption of AcOH on PdAu alloy surfaces has been shown to cause measurable segregation of Pd to the bimetallic surface, the presence of co-adsorbed potassium as has been found to counter this effect [5]. Hence, we do not expect the adsorption of AcOK to significantly alter the composition of our bimetallic surfaces.

We will first consider the effects of surface composition if the low dosage (1-4 L AcOK) region.

For the most Au-rich surfaces, our TPD and RAIRS data show little evidence for the formation of acetate for up to 4 L AcOK. Instead, only the 600 K CO₂ TPD and 1440 cm⁻¹ RAIRS features are observed. Previous studies carried out by our group [5] have shown that the presence of Au quenches the formation of surface carbonates. In agreement with our previous observation that the 1440 cm⁻¹ peak grows more slowly

on Au-rich surfaces, we find that the intensity of all TPD features is decreased on Au-rich surfaces compared to Pd-rich surfaces. For samples in the low pre-annealing temperature range, molecular CO is either not detected in the TPD data or appears as a weak feature at ~340 K that is assigned to CO atop Pd singleton sites. We observe a distinct change in the surface chemistry of CO between the 700 K and 800 K pre-annealed samples that points to a greater availability of Pd surface sites. In relation to the above mechanism, the reduced sticking probabilities of AcOK and the fact that any CO(ads) formed is likely to instantly desorb mean that it is harder to form AcO(ads) on such surfaces at lower doses.

We find that the more Pd-rich alloy surfaces behave similarly to Pd{111} in the low dosage regime. The increase in T_{\max} and intensity of both the ~300-350 K and the ~390-440 K peaks, relating to adsorbed CO, with increasing pre-annealing temperature points to increased stabilisation and increased capacity for CO on Pd rich surfaces. This is supported by studies carried out by Goodman and co-workers of CO adsorbed on 1:1 Pd/Au alloy films [14, 32], where integration of the peaks showed that the capacity for CO adsorption was reduced by 1/3 on the PdAu alloy surface compared to Pd alone [14]. The increase in the intensity of the ~390-440 K feature relative to the ~300-350 K feature with increasing surface Pd composition agrees with our RAIRS observation that the abundance of multiply-coordinating CO is increased on more Pd-like surfaces.

On the Pd-rich alloy surfaces, we observe two distinct CO₂ desorption features for up to 4 L AcOK doses. For 1 L AcOK, the major CO₂ desorption feature appears at ~550-600 K for all compositions and is assigned to carbonate, although there is some evidence for a second smaller acetate feature at ~440 K for the 800-1000 K pre-annealed samples only. For 4 L AcOK on Au/Pd{111} (figure 4.10d) we can clearly see the carbonate feature at ~550-600 K for all compositions. For samples pre-annealed to 700 K and higher, we observe an acetate feature at ~440 K that increases in intensity relative to the ~550-600 K feature as the pre-annealing temperature is increased and the surface becomes more Pd-like. This is in good agreement with our RAIRS data and supports our proposal that we are form carbonate on all surfaces, but we are only able to form acetate on Pd-rich surfaces at low dosage.

We have discussed the possibility of island or cluster formation on the surface. If the pre-annealing temperature is kept constant and the initial AcOK dose is increased incrementally, then the high temperature K, CO and CO₂ peaks are discontinuously shifted from ~800 K to ~1000 K between 4 L and 16 L doses on the more Au-rich surfaces. Again, we attribute this change in desorption kinetics to the formation of larger islands of adsorbate on the surface. These are more likely to be composed mostly of K₂CO₃ on Au-rich surfaces and a mixture of K₂CO₃, KHCO₃ and AcOK on Pd-rich surfaces as evidenced by the high temperature H₂ desorption observed for higher pre-anneals.

Otherwise, we find that the behaviour of higher (16-32 L) doses of AcOK on Au/Pd{111} is largely similar for all compositions tested. For 16 L AcOK on Au/Pd{111} (figure 4.11d), we observe an intense acetate CO₂ desorption at ~470 K. Carbonate CO₂ desorption is observed as a high temperature shoulder at ~570 K. The slight increase in T_{max} for both with increasing pre-annealing temperature above 600 K points to increased stabilization of both species on Pd-rich alloys but the intensities of both features remain largely unaffected by surface composition. Similarly, for the 32 L AcOK dose (figure 4.12d) we observe a large acetate CO₂ desorption feature at 460-500 K followed by a carbonate CO₂ desorption feature at ~540-620 K, but the intensities of both features remain nearly constant with changing surface composition. No RAIRS data are available for the 16-32 L AcOK dosing range on alloy surfaces, but we can see a set of strong C-H vibrations for 21 L AcOK on Pd{111} that confirm the presence of intact acetate on the surface.

4.4 - Summary

We observe that the uptake of AcOK and the surface chemistry of the resulting surface species on Au/Pd{111} is strongly affected by the surface composition for low (1-4 L) doses of AcOK.

It is possible to draw some conclusions in reference to the reaction mechanism proposed above.



The main driving force behind such an equilibrium in our case will be the relative strength of adsorption of each component on each of the various surfaces tested. In all cases, the decrease in the intensity of the CO TPD peaks together with the increase in intensity of the CO₂ TPD peaks with increasing AcOK dose suggests that CO(ads) is more weakly bound than either AcO(ads) or K₂CO₃(ads) and is partially displaced from the surface at higher coverage.

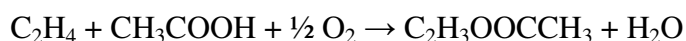
On the lowest annealing temperature, Au-rich alloy surfaces, the sticking probability of AcOK is low and there is little or no pre-adsorbed CO present at 300 K. Any CO(ads) produced by the above will be weakly bound to the surface and is likely to immediately desorb at 300 K. It is likely that the equilibrium lies to the right and K₂CO₃(ads) will be the main surface species as evidenced by the 1440 cm⁻¹ and 1730 cm⁻¹ RAIRS features and the ~550-600 K TPD peaks at low coverage.

As the pre-annealing temperature is increased and the sample surface becomes more Pd-like the sticking probabilities of both CO and AcOK are increased. This results in the presence of surface CO at 300 K as evidenced by RAIRS features at 1910 cm⁻¹ and 2040 cm⁻¹ and the CO TPD features at ~300-450 K, which would be expected to push the equilibrium to the left. However, uptake of AcOK results in displacement of some of this pre-adsorbed CO. This means that, for lower AcOK doses, carbonate is again the major surface species but integration of the TPD/RAIRS peaks show that K₂CO₃(ads) is present in greater quantities on Pd-rich surfaces than on Au-rich surfaces. For samples pre-annealed to 700 K and above, our TPD/RAIRS data shows some evidence for acetate formation in the ~2-4 L KOAc range in the form of an OCO vibrational feature at 1410 cm⁻¹ and C-H vibrations at ~2860 cm⁻¹, 2940 cm⁻¹ and 2970 cm⁻¹ together with CO₂ desorption features at 400-500 K.

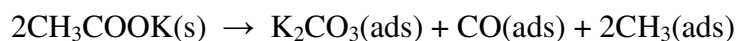
For higher AcOK doses of 16-32 L, our TPD data show evidence of adsorbed CO on Au-rich surfaces. This is most likely in the form of CO bound to surface potassium as evidenced by the ~1600 cm⁻¹ RAIRS feature. The behaviour of the CO₂ desorption spectrum is largely independent of the initial surface composition. In all cases, we observe a strong CO₂ desorption at ~400-500 K followed by a weaker desorption feature at ~550-600 K, which, along with the 2860-2970 cm⁻¹ RAIRS features,

suggests that acetate is the major surface species in this case even though we still have some carbonate present. The coincident high temperature H₂, CO, K and CO₂ desorptions observed at ~800-1000 K are much higher than we would expect from either AcO(ads) or CO₃(ads) and are instead attributed to the formation of islands of solid AcOK, K₂CO₃ and possibly KHCO₃ on the surface. The change in T_{max} and in the peak profile on increasing the AcOK dose or the starting surface Pd composition points to the formation of larger islands in either case.

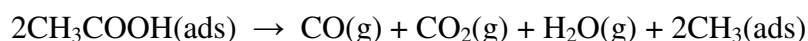
The effect of surface carbonates on the vinyl acetate synthesis reaction is unclear. The AcOK/PdAu catalysed reaction is known to follow the equation shown [33]:



It is conceivable that K₂CO₃(ads) will react with the acetic acid feed as shown.



The net reaction in this case is the consumption of acetic acid and the liberation of CO, CO₂ and H₂O which are all known to be unselective by-products of the vinyl acetate synthesis reaction [24, 25, 34].



At higher AcOK loadings, we propose that acetate is the major surface species. Since the reaction order of the vinyl acetate synthesis reaction is proposed to be positive in AcOH [35, 36], the presence of acetate species on the catalyst surface is likely to be beneficial to the vinyl acetate synthesis reaction.

4.5 – Conclusions

- The surface chemistry of all major adsorbates is strongly dependent on surface composition and on surface coverage.

- At low coverage potassium acetate reacts reversibly with the surface to form carbonate and CO. The presence of adsorbed CO is more evident on Pd-rich surfaces than on Au-rich surfaces – on Au it is likely to be stabilized by co-adsorbed K.
- For intermediate doses of ~4 L we begin to see evidence of acetate formation on Pd-rich surfaces only. The observation of RAIRS peaks at 2860 cm⁻¹ and 2930 cm⁻¹ in addition to the 2970 cm⁻¹ feature suggests this is not in the expected bidentate AcO(ads) form. The surface acetate may be tilted due to interaction with surface potassium or may be present as AcOK(ads).
- As the potassium surface coverage increases, we begin to see evidence for K-stabilised CO, on the surface. On Au-rich surfaces this is the major CO species, while we observe features relating to CO in atop, bridging and 3-fold coordinating sites on more Pd-rich surfaces.
- At higher doses of 16-32 L, acetate is the major surface species on all surfaces tested. The appearance of high temperature features in the TPD data suggest that we are forming mixed islands of K₂CO₃, AcOK and possibly KHCO₃ on the surface. The size and stability of these islands for a given dose increases with increasing Pd composition.
- Surface carbonates are likely to be detrimental to the vinyl acetate synthesis reaction, while surface acetates are likely to increase the vinyl acetate selectivity.

4.6 – References

1. C. J. Baddeley, M. S. Tikhov, C. Hardacre, J. R. Lomas, R. M. Lambert, *J Phys. Chem.* **100** (1996) 2189.
2. T. G. Owens, T. E. Jones, T. C. Q. Noakes, P. Bailey, C. J. Baddeley, *J. Phys. Chem. B* **110** (2006) 21152.
3. Z. Li, F. Calaza, F. Gao, W. T. Tysoe, *Surf. Sci.* **601** (2007) 1351.
4. S. J. Pratt, D. A. King, *Surf. Sci.* **540** (2003) 185.
5. T. G. Owens, Ph. D. Thesis, University of St Andrews, 2006.
6. R. L. Toomes, D. A. King, *Surf. Sci.* **349** (1996) 43.
7. G. J. Millar, C. H. Rochester, K. C. Waugh, *J. Cat.*, **155** (1995) 52.

8. P. M. Miller, P. J. Godowski, J. Onsgaard, *Vacuum* **54** (1999), 36.
9. R. D. Haley, M. S. Tikhov, R. M. Lambert, *Cat. Lett.* **76** (2001) 125.
10. J. L. Davis, M. A. Barteau, *Langmuir* **5** (1989), 1299.
11. M. Bowker, N. Aas, *J. Chem. Soc. Farad. Trans.* **89** (1993), 1249.
12. M. D. Weisel, J. L. Robbins, F. M. Hoffmann, *J. Chem. Phys.* **97** (1992), 9396.
13. S. M. Augustine, J. P. Blitz, *J. Cat.* **142** (1993), 312.
14. M. S. Chen, K. Luo, T. Wei, Z. Yan, D. Kumar, C.-W. Yi, D. W. Goodman, *Cat. Today* **117** (2006), 37.
15. X. C. Guo, J. T. Yates Jr., *J. Chem. Phys.* **90** (1989), 6761.
16. E. Ozensoy, D. W. Goodman, *Phys. Chem. Chem. Phys.* **6** (2004), 3765.
17. P. J. Schmitz, H. Kang, W. Y. Lang, P. A. Thiel, *Surf. Sci.* **248** (1991), 287.
18. M. Bowker, Y. Li, *J. Cat.* **142** (1993), 630.
19. S. Haq, F. M. Liebsle, *Surf. Sci.* **355** (1996), L345.
20. J. L. Davis, M. Barteau, *Surf. Sci.* **256** (1991), 50.
21. J. James, D. K. Saldin, T. Zheng, W. T. Tysse, D. S. Sholl, *Cat. Today* **105** (2006), 74.
22. M. Neurock, *J. Cat.* **216** (2003), 73.
23. E. Hansen, M. Neurock, *J. Phys. Chem. B* **105** (2001), 9218.
24. M. Bowker, C. Morgan, J. Couves, *Surf. Sci.* **555** (2004), 145.
25. G. Hoogers, D. C. Papageorgopoulos, Q. Ge, D. A. King, *Surf. Sci.* **340** (1995).
26. N. Macleod, J. M. Keel, R. M. Lambert, *Appl. Cat. A* **261** (2004), 37.
27. D. A. Outka, R. J. Madix, *Surf. Sci.* **179** (1987), 361.
28. R. J. Behm, V. Penka, M.-G. Cattania, K. Christmann, G. Ertl, *J. Chem. Phys.* **78** (1983), 7486.
29. E. V. Thomsen, B. Jorgensen, J. Onsgaard, *Surf. Sci.* **304** (1994), 85.
30. S. J. Pratt, D. K. Escott, D. A. King, *Phys. Rev. B*, **68** (2003), 235.
31. P. Herrera-Fierro, K. Wang, F. T. Wagner, T. E. Moylan, G. S. Chottiner, D. A. Scherson, *J. Phys. Chem.* **96** (1992), 3788.
32. Y.-F. Han, J.-H. Wang, D. Kumar, Z. Yan, D. W. Goodman, *J. Cat.* **232** (2005), 467.
33. M. Neurock, W. D. Provine, D. A. Dixon, G. W. Coulston, J. J. Lerou, *Chem. Eng. Sci.* **51** (1996), 1691.

34. R. J. Madix, J. L. Falconer, A. M. Suszko, Surf. Sci. **54** (1976), 6.
35. W. K. Kuhn, J. Szanyi, D. W. Goodman, Surf. Sci. **274** (1992) L611.
36. W. K. Kuhn, J. Szanyi, D. W. Goodman, Surf. Sci. **303** (1994) 377.

Chapter 5 – Summary, Further Work and Publications

5.1 – Summary

We have studied the growth of PdAu nanoparticles on SiO₂/Si{100} using a combination of STM, TPD and MEIS. We find that depositing submonolayer quantities of Au onto SiO₂/Si{100} results in the growth of broad, flat-topped particles with a height of a few atomic layers. Depositing Pd on top of Au/SiO₂/Si{100} results in nucleation of Pd on the existing Au particles to create bimetallic clusters – the diameter of these clusters is controlled by the Au content.

While we have no way of measuring particle heights directly from the STM data, we have compared raw MEIS data taken at normal and 15° off-normal incidence and found that the total illumination is not significantly changed. This implies that either all particles are well oriented and just a few layers deep or, more likely, that the particles are not well oriented with respect to the underlying Si substrate. Annealing the clusters causes the diameter to increase relative to the Au content but the particle height is not greatly increased.

Data from much larger particles, created by increasing the Pd and Au doses tenfold, shows that visibility changes significantly between normal and 15° off-normal incidences. This is a direct effect of shadowing and blocking.

Since traditional single-crystal analysis methods are not directly applicable in our case, we have developed a new computational tool that allows us to derive layer-by-layer compositional data from our MEIS data. We have fitted experimental MEIS data using a computational mode based on a flat-topped truncated hexagonal pyramid. We have shown that, for the special case of short, broad, flat-topped particles we can use some single-crystal approximations as a shortcut when calculating shadowing and blocking, thus reducing the calculation time and processor workload.

Our method provides good fits for experimental data obtained from particles containing ~30-90% Pd where both the Pd and Au peaks are of sufficient intensity.

Within this compositional region, we are able to show that our PdAu alloy particles consist of a Pd-rich inner core encapsulated by an Au-rich base and surface layer but we are not able to reliably fit data from Au-rich samples. The composition profile seems to be largely independent of deposition order, suggesting that Pd and Au are able to intermix at 300 K. Our data suggest that Au is able to diffuse to cover Pd at 300 K, so that the surface and base layers of our particles are always enriched in Au.

We have examined the surface composition as a function of pre-annealing temperature and have found that while our data agrees well with the trend predicted by Somorjai for PdAu alloy systems, the surface Au concentration is systematically higher than the predicted values for all particle compositions tested, regardless of deposition order. The surfaces of smaller particles, created by halving the Pd and Au doses were found to be systematically richer in Pd than predicted by Somorjai's equations. TPD experiments carried out on similar samples show little uptake of CO at 300 K, supporting our proposal that the particle surface is rich in Au.

In the first study of its kind, we have used MEIS together with our analysis procedure to investigate the interaction of acetic acid with the nanoparticle surface. We have shown that adsorption of acetic acid causes measurable segregation of Pd to the bimetallic particle surface. In all cases, the surface Au composition was decreased by ~10% after treatment with AcOH, a similar value to that found on Au/Pd{111}. Heating the surface to ~430 K causes AcOH to desorb and the surface then reverts to its original state.

While segregation effects would be expected to be enhanced on particle surface compared to single-crystals, instead we find that segregation effects on our particle surfaces are similar in magnitude to those observed on Au/Pd{111} – we rationalise our findings by proposing that for broad flat-topped particles where edge effects are minimal, adsorbate-induced segregation is likely follow a similar mechanism in our system to that proposed previously for {111} PdAu alloy surfaces where Pd is redistributed between the few layers by adsorption of AcOH at step-edge sites.

TPD investigations of AcOH on PdAu particles on alumina/NiAl{110} show large CO desorptions. Since pure CO was not found to adsorb at significant volume we

propose that these CO desorptions are the result of the decomposition of monodentate acetate surface species, as would be expected to form on step-edge sites. Characteristic CO₂ desorption features expected for the decomposition of bidentate acetate were not generally observed except on pure Pd particles.

In order to investigate the promoting role of potassium acetate in the vinyl acetate synthesis reaction, we have carried out TPD and RAIRS measurements of AcOK on Pd{111} and on a series of Au/Pd{111} alloy surfaces. We find that the surface chemistry of all major adsorbates is strongly dependent on both surface composition and surface coverage.

At low coverage potassium acetate reacts reversibly with the surface to form carbonate and CO. The presence of adsorbed CO is more evident on Pd-rich surfaces than on Au-rich surfaces. On Au rich surfaces, CO is likely to be stabilized by co-adsorbed K. For intermediate doses of ~4 L AcOK, we begin to see evidence of acetate formation on Pd-rich surfaces only. The observation of RAIRS peaks at 2860 cm⁻¹ and 2930 cm⁻¹ in addition to the 2970 cm⁻¹ feature suggests this is not in the expected bidentate AcO(ads) form and may be present as AcOK(ads).

As the potassium surface coverage increases, we begin to see evidence for K-stabilised CO, on the surface. On Au-rich surfaces this is the major CO species, while we observe features relating to CO in atop, bridging and 3-fold coordinating sites on more Pd-rich surfaces. At higher doses of 16-32 L, acetate is the major surface species on all surfaces tested. The appearance of high temperature features in the TPD data suggest that we are forming mixed islands of K₂CO₃, AcOK and possibly KHCO₃ on the surface. The size and stability of these islands for a given dose increases with increasing Pd composition.

The presence of surface carbonates is likely to be detrimental to the vinyl acetate synthesis reaction, while the presence of acetates on the surface is likely to increase the vinyl acetate selectivity.

5.2 – Suggested Further Work

Possible future work resulting from this study may include:

- Further refinement of our MEIS analysis method to allow faster and more efficient fitting of experimental data.
- STM/MEIS investigations of PdAu nanoparticles on oxide surfaces other than SiO₂ and Al₂O₃.
- Investigation of the influence of K or AcOK on the AcOH-induced segregation of Pd to the nanoparticle surface using MEIS.
- MEIS investigations of the behaviour of the particle surface under the influence of other VAM synthesis feedstocks, including O₂ or ethylene or mixtures.
- Extension of our method to allow investigation of oxide-supported metallic and bimetallic nanoparticle systems other than PdAu using STM/MEIS. This may or may not require reconfiguration of our existing particle model.
- RAIRS investigations of AcOK on Au/Pd{111} at higher coverage.
- RAIRS investigations of AcOK on Au/Pd{111} as a function of temperature to allow direct comparison with our TPD data.
- TPD/RAIRS investigations of AcOK on oxide-supported PdAu nanoparticle systems for comparison with our single-crystal data from Chapter 4.

5.3 – Publications

1. J. Gustafson, A. R. Haire, A. G. Trant, C. J. Baddeley, “*Depth Profiling of Bimetallic Nanoparticles Using MEIS*” (2010), in preparation.
2. A. R. Haire, J. Gustafson, A. G. Trant, C. J. Baddeley, “*Adsorbate-Induced Segregation at Bimetallic Nanoparticle Surfaces Studied Using MEIS*” (2010), in preparation.